Half-Heusler thermoelectrics: studying new paradigms via defects, entropy, and band engineering

विद्या वाचस्पति की
उपाधि की अपेक्षाओं की आंशिक पूर्ति में प्रस्तुत
शोध प्रबंध

A thesis submitted in partial fulfillment of the
requirements of the degree of Doctor of Philosophy

द्वारा / By
अंकित कुमार / Ankit Kumar

पंजीकरण सं. / Registration No.: 20193694

शोध प्रबंध पर्यवेक्षक / Thesis Supervisor:

प्रो. सुरजीत सिंह / Prof. Surjeet Singh
डॉ. प्रसेनजीत घोष / Dr. Prasenjit Ghosh

भारतीय विज्ञान शिक्षा एवं अनुसंधान संस्थान
पुणे
INDIAN INSTITUTE OF SCIENCE EDUCATION AND RESEARCH PUNE

2024

Certificate

Certified that the work incorporated in the thesis entitled **"Half-Heusler thermoelectrics: studying new paradigms via defects, entropy, and band engineering"** submitted by **Ankit Kumar** was carried out by the candidate, under my supervision. The work presented here or any part of it has not been included in any other thesis submitted previously for the award of any degree or diploma from any other university or institution.

Date: April 28, 2025 (Supervisor) (Co-Supervisor)

Declaration by student

Name of Student:	Ankit Kumar
Reg. No.:	20193694
Thesis Supervisor(s):	Prof. Surjeet Singh & Dr. Prasenjit Ghosh
Department:	Physics
Date of joining program:	August 1 2019
Date of Pre-Synopsis Seminar:	August 26, 2024

Title of Thesis: Half-Heusler thermoelectrics: studying new paradigms via defects, entropy, and band engineering

I declare that this written submission represents my idea in my own words and where others' ideas have been included; I have adequately cited and referenced the original sources. I declare that I have acknowledged collaborative work and discussions wherever such work has been included. I also declare that I have adhered to all principles of academic honesty and integrity and have not misrepresented or fabricated or falsified any idea/data/fact/source in my submission. I understand that violation of the above will be cause for disciplinary action by the Institute and can also evoke penal action from the sources which have thus not been properly cited or from whom proper permission has not been taken when needed.

The work reported in this thesis is the original work done by me under the guidance of

Prof. Surjeet Singh & Dr. Prasenjit Ghosh

Date: April 28, 2025

Signature of the student: Ankit Kumar

Acknowledgments

Completing this PhD journey has been a profound and transformative experience, marked by both challenges and triumphs. There were times when motivation waned, and the road ahead felt daunting. Yet, through perseverance and determination, I pushed forward, ultimately achieving what once seemed like an insurmountable goal.

I am immensely grateful to my supervisors, Prof. Surjeet Singh and Prof. Prasenjit Ghosh. Their unwavering support, guidance, and insightful feedback were instrumental in shaping my research and helping me navigate the complexities of this process. Their encouragement during difficult moments kept me focused and inspired, and I cannot thank them enough for their dedication and belief in my potential. The contributions of my Research Advisory Committee members, Prof. Umesh Waghmare and Prof. Sunil Nair, were critical to my progress during the research period.

I would like to express my heartfelt gratitude to our Engineer Nilesh Dumbre and Kartik for their unwavering support in maintaining and fixing the instruments throughout my PhD tenure. Their expertise, patience, and quick response to any technical issues I encountered were invaluable in ensuring that my research progressed smoothly. Whether it was troubleshooting complex equipment or offering insightful solutions to problems, Nilesh and Kartik's dedication to keeping everything running efficiently made a significant difference in the quality and consistency of my work. Their help has been crucial in enabling me to focus on my research without the added stress of technical setbacks. I would also like to thank our technical staff, Mr. Anil and Mr. Sudhir, for performing electron microscopy with great enthusiasm and dedication.

I also wish to acknowledge the generous financial support provided by the Prime Minister's Research Fellowship (PMRF). Opportunities to participate in multiple international conferences would not have been possible without the PMRF support. I am also thankful to SERB for providing me with a travel grant. The backing from these agencies allowed me to focus on my research without the constant concern of funding limitations, and their support has been instrumental in advancing the scientific goals of this work. I am deeply grateful for

their belief in my project and their investment in the future of scientific discovery.

Lastly, IISER Pune has provided me with the best infrastructure to carry out my research. I never had to seek resources elsewhere for measurements. Even IISER provided me with one of the fastest in-house supercomputers, “Param Brahma” for DFT calculations. My institute has helped me in many ways that can’t be expressed.

Lastly, my heartfelt thanks to my lab members and friends, whose camaraderie and support made this journey so much more enjoyable. Dr. Kumar Saurav, my senior and friend, is like a guide to me. He taught me everything in the initial days of my PhD. I can’t thank him enough for making my journey smoother. Dr. Dibyata Raut, one of the finest researchers I have ever met, helped me through intricate concepts and taught me the correct way to solve any problem. I learned a lot from her dedication to science. I am very much thankful to Dr. Navita and Mr. Dinesh K. Kedia for assembling a high-temperature Hall measurement setup. I could not have completed my projects without the Hall setup. I would like to thank Latit and Vishak, BS-MS students, for their contribution to my thesis. Lalit was there with me during the toughest times, encouraging me not to lose hope. Vishak helped me with material synthesis. Together, we managed to synthesize 200 samples in a very short span of time, and all was possible because of his perfect punctuality. I would also like to thank other members of my group, Pankaj Gupta and Prabhu, who kept me updated on my measurements when I was not in the lab. A special thanks to my colleagues from the theory group, Dr. Gautam Sharma, Dr. Vineet Pandey, Rajeev, Sarika, and Pallavi, for their support and meaningful discussions. Your encouragement and collaboration provided both motivation and a sense of belonging.

A very special thank you to my best friend, Manisha Rajput. I just wanted to take a moment to thank you from the bottom of my heart for being there for me during this challenging phase of my research. Your support, encouragement, and unwavering belief in me have meant more than words can express. There were times when I felt overwhelmed, stuck, and ready to give up, but your presence –whether it was offering advice, lending a listening ear, or simply distracting me with a laugh –helped me push through. I truly couldn’t have

made it this far without you by my side. You're not just a friend; you're a constant source of strength and inspiration, and I'm so grateful for everything you've done.

Finally, to my family –thank you for your unconditional love and belief in me, even during the toughest times. Your faith fueled my resolve and reminded me of the importance of perseverance. This accomplishment is as much yours as it is mine.

Date: April 28, 2025 (Ankit Kumar)

The joy of discovery is certainly the liveliest that the mind of man can ever feel

- Claude Bernard

This thesis is dedicated to my mother

Abstract

Thermoelectric research focuses on materials that convert temperature differences directly into electrical energy, offering a promising pathway for sustainable energy production. By harnessing waste heat from industrial processes, vehicles, and even renewable sources, thermoelectric devices can enhance energy efficiency and reduce greenhouse gas emissions. Recent advancements in material science, particularly in nanostructured and complex materials, have significantly improved the efficiency of thermoelectric systems. The integration of these technologies has the potential to support a transition to cleaner energy, promote energy independence, and drive innovation in various sectors, including automotive and consumer electronics. As the global demand for clean energy solutions intensifies, thermoelectric research stands at the forefront of addressing environmental challenges while fostering economic growth. This thesis work mostly focus on developing materials for high temperature application. Half Heusler (hH) materials exhibit high melting temperatures which makes them suitable for mid-to-high temperature range extending from about 500 K to 1200 K.

In Chapter 1 of this thesis, we have pointed out the importance of thermoelectric research and the chalenges asociated. We have extensivly discused the scientific background and reseach which have been done till date specially in half-Heusler based thermoelectric materials. Chapter 2 describes the computational method which has been used in this research. We have outlined the fundamentals of Density Functional Theory (DFT) as well as methods to calculate transport coefficients. In Chapter 3, we have outlined the experimental techniques that were used for sample synthesis, structural characterization, and transport measurments. The following chapters deals with the various projecte we have exicuted towards thermoelectric research.

In Chapter 4, we show a dramatic improvement in the thermoelectric performance of TiCoSb by introducing 3-D modulation doping and synergistic band engineering in the composites of the form $(1 - f)$A + fB, where A and B refers to the phases $Ti_{1-x}Nb_xCoSb$ and $Nb_{0.8+\delta}CoSb$, respectively, and f is the volume fraction of phase B. We show that the electrical conductivity and Seebeck coefficient of these composites increase simultaneously

due to modulation doping, giving rise to a colossal power factor (PF) enhancement from $0.3\ \mu\mathrm{W\ cm^{-1}\ K^{-2}}$ (TiCoSb) to $18\ \mu\mathrm{W\ cm^{-1}\ K^{-2}}$ ($x = f \approx 0.05$) at 300 K, and exceeding $25\ \mu\mathrm{W\ cm^{-1}\ K^{-2}}$ over a broad temperature range (T $>$ 600 K). Due to Ti-Nb point-mass fluctuation in phase A, high concentration of defects in phase B, and interfacial phonon scattering between A and B, these composites also exhibit very low lattice thermal conductivity (κ_L), resulting in a high zT of 0.81 near 970 K. The simulation of κ_L using the Klemens model successfully describes the significant reduction of κ_L for these composites, observed experimentally. Our ab-initio DFT calculations show that $Ti_{1-x}Nb_xCoSb$ exhibits band convergence as x increases, which contributes to improving the charge transport. Thus, benefitting from the synergistic effect of band convergence and 3-D modulation doping, a high zT is obtained.

In chapter 5, we focus on double half-Heusler (dhH) alloys ($XY_{0.5}Y'_{0.5}Z$), a subject of extensive research as an alternate to hHs for high temperature thermoelectric applications due to low lattice thermal conductivity due to random Y and Y' mixing at the Y site. In this work, using a combination of density functional theory (DFT) based calculations and semiclassical Boltzmann transport theory, we elucidate the role of hierarchical bonding, reduction of electronegativity of X and chemical pressure induced by variation in its atomic size on the electronic properties, transport and thermoelectric properties, of a family of dhH compounds, namely, $XFe_{0.5}Ni_{0.5}Sb$ (where X=Ti, Zr and Hf). Compared to the parent compounds, we observe a larger variation in the nature of bonds in dhHs lattice that aids in the reduction of their lattice thermal conductivity. Our calculations show that electronegativity in the X and the chemical pressure due to size mismatch together influence the band convergence observed in the conduction band of these materials in a reverse way. While reduction of electronegativity favors band convergence, tensile strain induced in the lattice due to the larger size of X is detrimental for the same. However, electronegativity has a much stronger effect. We observe that $HfFe_{0.5}Ni_{0.5}Sb$, which shows the largest band convergence, has the highest value of zT for n-type charge carriers amongst the three materials considered in our work. Moreover, hole doped (p-type) $HfFe_{0.5}Ni_{0.5}Sb$ also exhibits $zT > 1$. Therefore, we

envisage that $HfFe_{0.5}Ni_{0.5}Sb$ can be a good candidate for both the n and p legs of a thermoelectric device.

Chapter 6 deals with High-entropy alloys (HEAs) which have gained significant attention recently due to their exceptional properties. Among HEAs, entropy-stabilized alloys where the high configurational entropy drives the structural stability are of considerable interest in new materials discovery. Here, we combine theoretical and experimental approaches to design very low lattice thermal conductivity (κ_l) high-entropy alloys $(TiHf)_{1/2}(Fe_{1-x}CoNi_{1+x})_{1/3}Sb$ belonging to the half Heusler family. We demonstrate that $(TiHf)_{1/2}(FeCoNi)_{1/3}Sb$ is entropy-stabilized, with κ_l at 300 K suppressed by over 80% with respect to the parent compound TiCoSb, which has an unfavorably high thermal conductivity of 18 W m^{-1} K^{-1}. Further reduction in κ_l is achieved by tuning the Fe/Ni ratio. The lowest κ_l is observed in the alloy $(TiHf)_{1/2}(Fe_{0.5}CoNi_{1.5})_{1/3}Sb$, where it approaches the theoretical minimum value of $\kappa_{\min}$ $\approx$ 1 W m^{-1} K^{-1} at 973 K. Tuning Fe/Ni ratio also optimizes carrier concentration simultaneously, thus significantly enhancing electronic properties. The electrical conductivity increased almost five-fold and power factor rose from 7 μW cm^{-1} K^{-2} to 16 μW cm^{-1} K^{-2} as x increased from 0 to 0.5 at 973 K, making the alloy $(TiHf)_{1/2}(Fe_{0.5}CoNi_{1.5})_{1/3}Sb$ achieve a zT of 0.51 at 973 K without further optimization.

In Chapter 7, we exploite the effect of defects in the thermoelectric properties. TaFeSb is reported to show good thermoelectric properties when 16% Ta is substituted with Ti, resulting in a maximum zt of 1.4 at 973 K. Here, we obtained a higher zT of 1.55 for the same amount of Ti substitution by using a different synthesis approach. We show that the enhancement in the zT is not just an effect of the carrier optimization, the role of antisite disorder is shown to be important as well. To demonstrate this, we prepared samples with controlled stoichiometry to tune the disorder. The thermoelectric power factor was suppressed in samples with less disorder, which also enhanced the lattice thermal conductivity, leading to a low zT of 0.98. However, with Fe deficiency, which is shown to increase the antisite disorder, we observed an increase in the Seebeck effective mass, leading to enhanced power factor and reduced lattice thermal conductivity, resulting in a zT of 1.35, i.e., a 35% enhancement.

These findings provide valuable insights for optimizing the thermoelectric performance of half-Heusler materials through controlled defect engineering.

List of publications

- *Defect-assisted ultrahigh zT of TaFeSb based Half-Heuslers;*
  Ankit Kumar, S. S. Vishak, Prasenjit Ghosh, and Surjeet Singh
  To be Submitted

- *Elucidating the role of hierarchical bonding, electronegativity and chemical pressure on thermoelectric properties of double Half Heuslers;*
  Ankit Kumar, and Prasenjit Ghosh
  ACS Appl. Energy Mater. 2025, 8, 3, 1507-1517

- *Entropy-stabilized half-Heusler alloys (TiHf)$_{1/2}$(Fe$_{1-x}$CoNi$_x$)Sb with ultralow lattice thermal conductivity;*
  Ankit Kumar, S. S. Vishak Prasenjit Ghosh, and Surjeet Singh
  Chem. Mater. 2025, 37, 4, 1370-1381

- *Simplified approach to estimate Lorenz number using experimental Seebeck coefficient for non parabolic band;*
  Ankit Kumar
  AIP Advances 14, 105216 (2024)

- *Band engineering and synergistic modulation doping for excellent thermoelectric performance in composite Ti$_{1-x}$Nb$_x$CoSb - Nb$_{0.8}$CoSb composite;*
  Ankit Kumar, Dinesh K. Kedia, Prasenjit Ghosh, and Surjeet Singh
  ACS App. Energy Mat. 06, 20, 10694 (2023)

Additional Publications:

- *Grain boundary engineering in metavalent SnTe: A simplified approach;*
  Navita Jakhar, Dinesh Kumar Kedia, **Ankit Kumar**, and Surjeet Singh
  Appl. Phys. Lett. 123, 173901 (2023)

- *Enhanced thermoelectric figure of merit in defective half-Heusler '$Nb_{0.83}CoSb$';*
  Kumar Saurabh, Vineet Pandey, **Ankit Kumar**, Prasenjit Ghosh, and Surjeet Singh
  Mat. Today Phys. Volume 38, November 2023, 101236

- *Reproducible high zT in Ag_2Se;*
  Navita Jakhar, Dinesh Kumar Kedia, **Ankit Kumar**, Kumar Saurabh, and Surjeet Singh
  ACS App. Energy Mat. 06, 20, 10694 (2023)

- *Structural, electronic and thermoelectric properties of SnTe with dilute co-doping of Ag and Cu;*
  Gaurav Jamwal, **Ankit Kumar**, Mohd Warish, Shruti Chakravarty, Saravanan Muthiah, Asokan Kandasami, and A. Niazi
  Journal of Alloys and Compounds 954, 170182 (2023)

- *Enhancement in the thermoelectric figure of merit of ZrNiSi by doping;*
  Kumar Saurabh, **Ankit Kumar**, Prasenjit Ghosh, and Surjeet Singh
  Phys. Rev. Materials 6, 065401 - Published 3 June 2022

- *Low thermal conductivity and semimetallic behavior in some TiNiSi structure-type compounds;*
  Kumar Saurabh, **Ankit Kumar**, Prasenjit Ghosh, and Surjeet Singh
  Phys. Rev. Materials 5, 085406 - Published 23 August 2021

List of Symbols & Abbreviations

Symbol	Description
S	Seebeck coefficient
π	Peltier coefficient
σ	Electrical conductivity
κ	Thermal conductivity
κ_e	Electronic contribution to thermal conductivity
κ_l	Lattice contribution to thermal conductivity
κ_b	Bipolar contribution to thermal conductivity
J	Current density
J_Q	Thermal current density
zT	Material figure of merit
ZT	Device figure of merit
T	Absolute temperature (K)
e	Elementary charge (1.602×10^{-19} C)
h	Planck's constant (6.626×10^{-34} Js)

Symbol	Description
$\hbar$	Reduced Planck's constant ($h/2\pi$)
κ_B	Boltzmann constant (1.381×10^{-23} J/K)
m_e	Free electron mass (9.109×10^{-31} kg)
E_g	Band gap energy (eV)
μ	Chemical potential
E_F	Fermi energy
V	Voltage (V)
$\mu_{(h/e)}$	Hole / electron mobility
μ_H	Hall mobility
v_d	Drift velocity
τ	Carrier Relaxation time
τ_q	Phonon Relaxation time
C	Specific heat
B_H	Bulk modulus
G_H	Shear modulus
γ	Gruneisen parameter
Θ_D	Debye temperature
$v_{(T/L/av)}$	Sound velocity (Transverse/Longitudnal/average)
n	Carrier density
n_H	Hall carrier density
μ_w	Weighted mobility
L	Lorenz number
η	Reduced fermi energy
$m^*_{(d/D)}$	Carrier or density of state effective mass
m^*_b	band effective mass

Abbreviation	Description
TE	Thermoelectrics
HH / hH	Half-Heusler
VEC	Valence Electron Count
RTGs	Radioisotope Thermoelectric Generators
SPB	Single Parabolic Band
SKB	Single Kane Band
ADP	Acoustic Deformation Potential
EF	Energy Filtering
BTE	Boltzmann Transport Equation
ΔH	Formation energy
ΔG	Gibbs free energy of formation
AM	Arc Melting
PS	Powder Synthesis
XRD	X-ray Diffraction
BM	Ball Milling
HP	Hot pressing
SEM	Scanning Electron Microscope
TEM	Transmission Electron Microscope
SAED	Selected Area Electron Diffraction
SE	Schrondinger Equation
DFT	Density Functional Theory
GGA	Generalized Gradient Approximation
LDA	Local Density Approximation
XC	Exchange Correlation
PBE	Perdew-Burke-Ernzerhof functional
BZ	Brillouin Zone
CBM / VBM	Conduction Band Minima / Valence Band Maxima

List of Figures

List of Tables

Contents

Chapter 1

Introduction

1.1 Why Thermoelectrics

The history of thermoelectrics is intrinsically linked to the escalating global demand for energy, a phenomenon primarily fuelled by a burgeoning population and industrialization. In particular, emerging economies like India exemplify this trend, where energy demand has exhibited remarkable growth. Therefore, it is important to discover efficient and renewable energy production methods to reduce reliance on fossil fuels. The energy consumption distribution depicted in Figure 1.1 illustrates the current global energy landscape [1]. As of 2022, a substantial (84.3 %) of our energy needs are fulfilled by finite natural resources, namely oil, coal, and natural gas. These resources face the risk of depletion within the next century. Consequently, there is a pressing need to intensify research on renewable energy sources. Currently, our reliance on renewable options is confined to hydro power, nuclear energy, wind power, solar energy, biofuels, and similar alternatives. As per the U.S. energy flow record [9], approximately 65 % of energy gets dissipated in the form of heat every year. If even 10 % of this heat could be harnessed to generate clean electricity, it would significantly enhance overall energy system efficiency and contribute in mitigating the environmental impact of rising temperatures. Thermoelectric (TE) technology proves beneficial in recovering heat from various sources, including automobiles, utilities (such as the combustion of coals

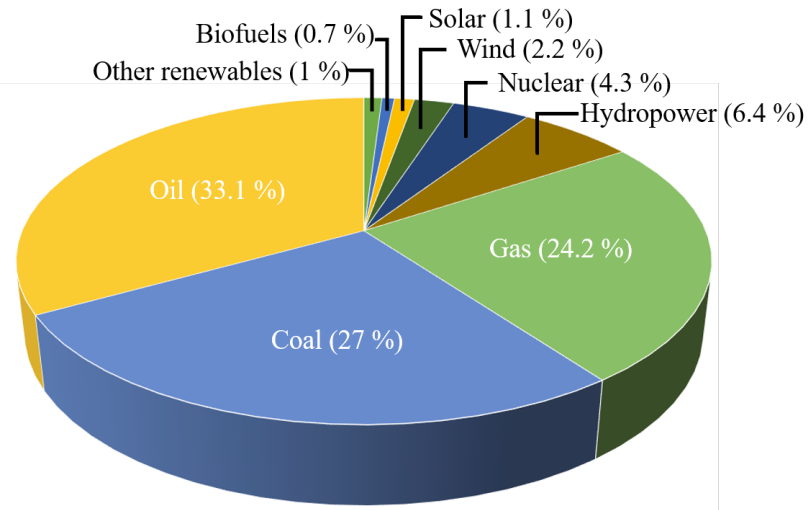

Figure 1.1: 2022 global energy consumption. Data taken from Ref. [1]

and natural gas), and chemical plants.

TE energy harvesting offers several advantages, including a compact design, robustness, emissions-free operation, noiselessness, and maintenance-free functionality. These attributes render TE devices an appealing option as a renewable energy source. Notably, NASA has incorporated TE generators in their deep space projects, utilizing Radioisotope Thermoelectric Generators (RTGs) capable of producing nearly 300 W of power, with uninterrupted operation for the past 40 years [10]. The absence of moving parts and the resulting vibration-free operation make TE devices suitable for applications such as cooling units in sensitive scientific instruments like laser systems.

1.2 Thermoelectrics

Thermoelectrics refers to the relation and interconversion of heat and electricity also called thermoelectricity. The documented discovery of thermoelectricity can be traced back to the 19^{th} century when Italian scientist Alessandro Volta discovered the voltaic pile, an early electrochemical cell, in 1800. This observation laid the foundation of thermoelectricity. Later, in the year 1821, generation of electric current in a closed loop of different metals when subjected to a temperature gradient, was observed by Thomas Johann Seebeck [11]. In

1834, Jean Charles Athanase Peltier, a French physicist, discovered the inverse of this effect, now known as the Peltier effect, which occurs when an electric current passes through a circuit of two different conductors, causing a temperature gradient at the junction [12]. The extension of the aforementioned effect was discovered by Lord Kelvin in 1851 known as the Thomson effect [13]. The transport equations which are commonly used after the above discoveries can be written as:

$$J = \sigma E - (\sigma s)\frac{dT}{dx} \tag{1.1}$$

$$J_Q = \pi J - (\kappa_l + \kappa_e)\frac{dT}{dx} \tag{1.2}$$

where J, σ, E, S, and T are the current density, electrical conductivity, applied electric field, Seebeck coefficient, and temperature respectively. The derivative of temperature is along the gradient of temperature. The equation represents the current density in the presence of an external electric field and temperature gradient. Equation 1.2 represents the heat flow in the presence of external electric fields and temperature gradient. J_Q, π, κ_l, and κ_e are the thermal current density, Peltier coefficient, Lattice thermal conductivity and electronic thermal conductivity respectively. All the transport coefficients will be discussed one by one in the following paragraphs.

1.2.1 Seebeck Coefficient

Generation of voltage across a material as as consequence of temperature gradient is termed as Seebeck effect. The voltage generation is quantified as Seebeck coefficient (S).

$$S = -\lim_{\Delta T \to 0} \frac{\Delta V}{\Delta T} \tag{1.3}$$

Where ΔV and ΔT are the measured voltage and temperature difference respectively across the material. It was clear from the discovery that temperature gradients can also drive the current to flow. The situation is similar to that of current flow when external potential is applied across a material which results in the Fermi level misalignment across the sample

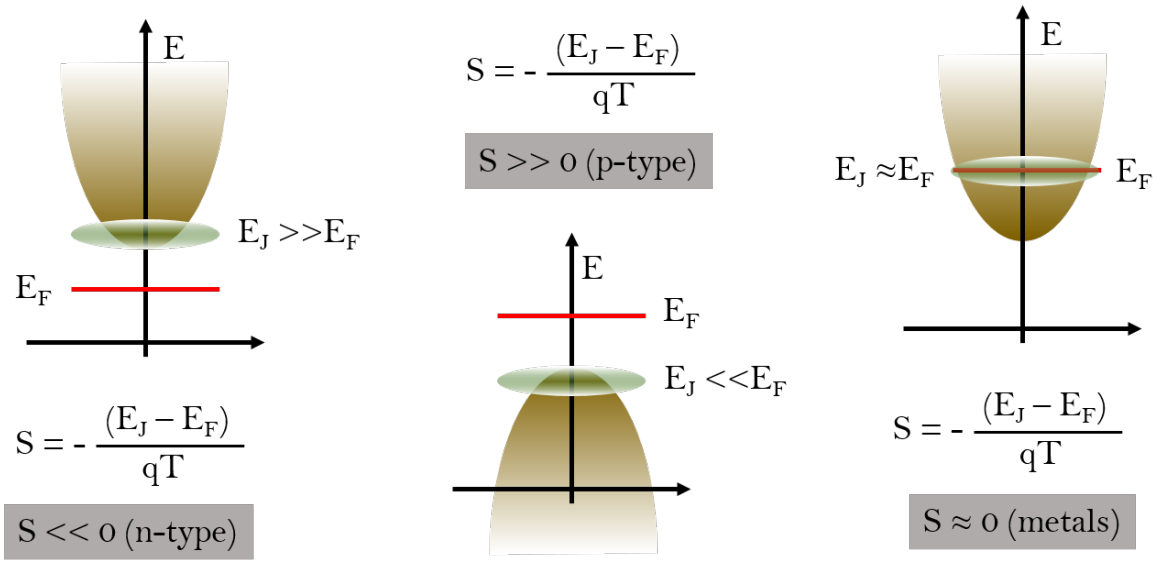

Figure 1.2: Electronic bands and relative position of Fermi energy and average charge flow in n-type semiconductor (left), p-type semiconductor (middle), and metals (right).

that drives the current. Here, the chemical potential rises at the hotter end as the Fermi Dirac distribution function is also dependent on temperature. After solving Boltzmann transport equation one can derive an expression of S as a function of energy as [14]:

$$S = -\left(\frac{E_J - E_F}{qT}\right) \tag{1.4}$$

where q is the electronic charge, T is temperature, E_J and E_F are average energy at which current is flowing and Fermi energy respectively. This can be demonstrated using the following Figure 1.2. The difference between E_j and E_f is more in case of Semiconductor, hence it has better S compared to metals which are bad thermoelectrics due to minimal S. It is also clear from the picture that for n-type materials S will be negative whereas for p-type, it will be positive. It is also clear why semiconductors are the desired material for better Seebeck coefficients. For degenerate semiconductors or metals, the Seebeck coefficient can be formulated through Mott's relation as [15]:

$$S = \frac{\pi^2 k^2 T}{2e}\left(\frac{1}{\mu}\frac{d\mu}{dE} + \frac{1}{n}\frac{dn}{dE}\right)_{E_F} \tag{1.5}$$

here k_B, e, μ, E, n and E_F represent the Boltzmann constant, electronic charge, carrier mobility, energy, carrier concentration and Fermi energy.

1.2.2 Peltier Coefficient

Jean Charles Athanase Peltier first discovered the Peltier effect in 1834. [12]. It was found that heat can be transferred from one junction to another with electrical assistance. In other terms, it is the opposite of the Seebeck effect. It is quantized as the Peltier coefficient as mentioned earlier in the transport equation. Although it is property of Semiconductor, not an interface property but requires a junction. Since Peltier effect is inverse phenomenon of Seebeck effect there is a well-defined relationship between S and π as:

$$\pi = ST \tag{1.6}$$

1.2.3 Electrical conductivity

Electrical conductivity (σ) is a measure of charge carrying capacity of a material. In the simplest form it can be defined as:

$$\sigma = en\mu \tag{1.7}$$

where e, n and μ are electronic charge, carrier concentration and mobility respectively. In case of bipolar system where both holes (h) and electrons (e) are available for conduction, the conductivity because of each can be added linearly as:

$$\sigma = en_e\mu_e + en_h\mu_h \tag{1.8}$$

The electrical conductivity has direct relation with both n and μ. The n can be tuned by doping mechanism, it is the μ which is complex and depends on electronic structure and scattering mechanism of the conducting material. Mobility can also be expressed in terms of drift velocity of carriers (υ_d) as $\mu = \upsilon_d/E$, where E is the electric field. Drift velocity can also be expressed as $\upsilon_d = eE\tau/m_e$ where τ is the relaxation time and m_e is band effective

Table 1.1: Temperature dependence of mobility

Scattering mechanism	Temperature dependence
Acoustic phonon scattering	$T^{-3/2}$
Optical phonon scattering	$T^{-1/2}$
Ionised Impurity scattering	$T^{3/2}$
Point defect scattering	T^{0}

mass of the carriers. From both the equation we can have mobility as $\mu = e\tau/m_e$. It is clear from the mobility expression that it is inversely proportional to band effective mass which means sharper band will will produce high mobility. Other factor is the relaxation time which is related to the strength and type of carriers scattering. In case of multiple scattering centres, relaxation time from each factor is added according to Matthiessen's rule and so as the mobility since it is directly proportional to relaxation time. Using the Matthiessen's rule one can add τ and μ as [16]:

$$1/\tau = 1/\tau_1 + 1/\tau_2 + 1/\tau_3 + ... \tag{1.9}$$

$$1/\mu = 1/\mu_1 + 1/\mu_2 + 1/\mu_3 + ... \tag{1.10}$$

There are various scattering mechanisms through which carriers are scattered and behaves differently as a function of temperature. The table shows the temperature dependence of mobility for various scattering mechanism.

If the carrier concentration of the system does not change with temperature, the temperature dependence of conductivity will be same as that of mobility.

1.2.4 Weighted mobility

Wieghted mobility (μ_w) is defined as the electronic mobility weighted over density of states. In most of the cases Hall measurement is done till 300 K, which provide information of electrical mobility. But at high temperatures hall measurements are quite difficult. In order to understand the electronic transport behaviour, G. J. Snyder *et.al* came up with an equation to

quantify the μ_w using Seebeck coefficient (S) and electrical conductivity (σ). As measuring these transport coefficient is relatively easier at high temperatures, μ_w can be calculated till high temperatures. The expression is given as [17]:

$$\mu_w = \frac{3h^3\sigma}{8\pi e(2m_e\kappa_B T)^{3/2}} \left[\frac{exp(\frac{|S|}{\kappa_B/e} - 2)}{1 + exp(\frac{-5|S|}{\kappa_B/e} + 5)} + \frac{\frac{3}{\pi^2}\frac{|S|}{\kappa_B e}}{1 + exp(\frac{5|S|}{\kappa_B/e} - 5)} \right] \tag{1.11}$$

where e, h, κ_B, m_e, and T represent the electronic charge, Planck's constant, Boltzmann constant, free electron mass, and temperature, respectively.

1.2.5 Thermal conductivity

Thermal conductivity (κ) is the heat carrying capacity of a material. It can be written as the sum of electronic thermal conductivity (κ_e) and lattice thermal conductivity (κ_l) as $\kappa = \kappa_e + \kappa_l$. The κ_e is the fraction of heat transported by the charge carriers. A clear correlation between electronic conductivity (σ) and κ_e is given by Weidemann-Franz relation as [18]:

$$\kappa_e = L\sigma T \tag{1.12}$$

where L is called the Lorenz number. L is estimated to be 2.44 10^{-8} W Ω K^{-2} for the metals and degenerate semiconductors. For light doped semiconductors Lorentz number deviates significantly from its natural value. The calculation method for such case is explained in the next section.

After estimating the κ_e the remaining quantity is the κ_l and bipolar contribution (κ_b) in the thermal conductivity. We can write the equation as:

$$\kappa_l + \kappa_b = \kappa - L\sigma T \tag{1.13}$$

The κ_l is dependent on the specific heat (C), sound velocity (υ_s) and mean free path (λ_{mfp}) or phonon relaxation time (τ_q) as:

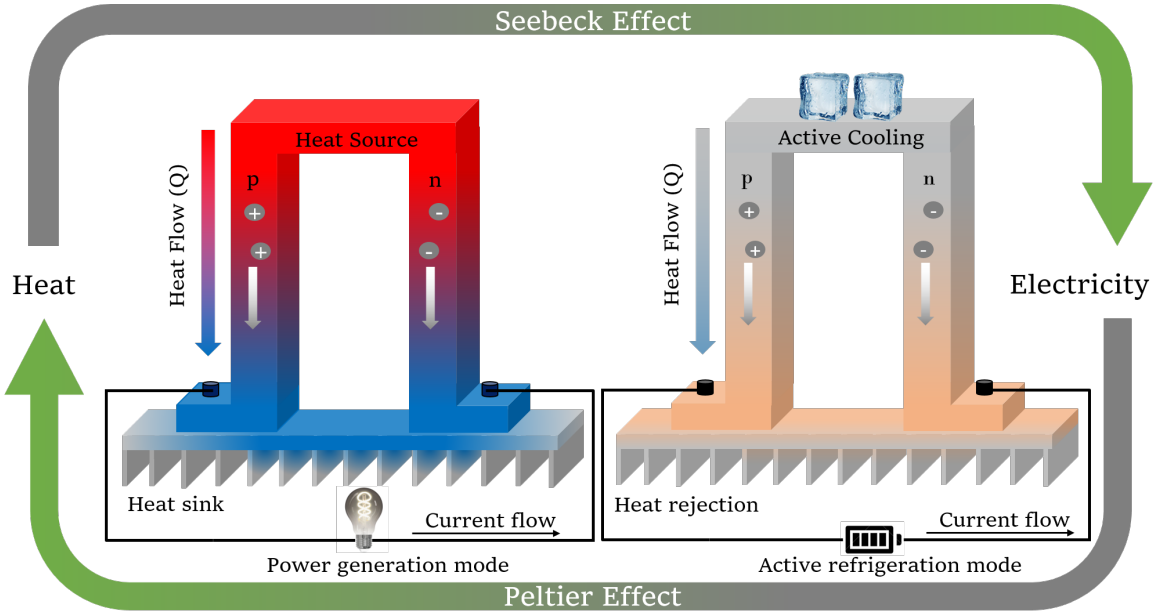

Figure 1.3: Cartoon of thermoelectric two leg device

$$\kappa_l = \frac{1}{3} C v_s \lambda_{mfp} = \frac{1}{3} C v_s^2 \tau_q \tag{1.14}$$

The relaxation time or mean free path depends on the scattering mechanism of phonons. A detailed analysis of calculation and scattering mechanism will be explained in chapter 2. A general estimate of the bipolar contribution to thermal conductivity can be expressed as:

$$\kappa_b = T \frac{\sigma_n \sigma_p}{\sigma_n + \sigma_p} (S_p - S_n)^2 \tag{1.15}$$

Bipolar contribution will be considerable if σ_n and σ_p are comparable [19].

1.3 Thermoelectricity: Basic mechanism and formulation

Thermoelectric devices operate based on the principles of the Seebeck and Peltier effects. A cartoon of a thermoelectric generator and a Peltier cooler is shown in Figure 1.3. The cartoon shows a two-leg device with n-type and p-type material each connected in series. The left cartoon in Figure 1.3 is a thermoelectric generator converting heat into electricity

under a thermal gradient. The device's top surface is in thermal contact with the heat source, while the bottom surface is connected to a heat sink to maintain a temperature gradient. The reverse effect is shown in the right cartoon in the image. With applied current, the top surface is actively cooling, and the bottom surface is acting as a heat rejector. The maximum efficiency of a thermoelectric generator can be expressed as [20]:

$$\eta = \frac{T_h - T_c}{T_h} \frac{\sqrt{1 + zT_m} - 1}{\sqrt{1 + zT_m} + \frac{T_c}{T_h}} \tag{1.16}$$

where zT_m is a dimensionless quantity called material figure of merit (zT). For a practical device the figure of merit is represented as ZT, which is average zT of both legs. T_h and T_c represent the temperatures of the hot and cold ends, respectively. The efficiency depends on zT, defined as [20, 21]:

$$zT = \frac{S^2 \sigma T}{\kappa_e + \kappa_l} \tag{1.17}$$

As discussed earlier the transport coefficients are closely interdependent to each other. For example, κ_e is directly proportional to electrical conductivity. The relationship between Seebeck coefficient and electrical conductivity is not direct, rather entangled through carrier concentration (n) and scattering mechanism. The next few paragraphs deal with discussion on the interdependencies of all the transport coefficients and their correlation with carrier concentration.

Single parabolic and Ken band model

Under the assumption of thermoelectric materials being heavily doped semiconductors, electrical transport of materials with complex band structures can be modelled using single band structure [22]. Within the assumption one can have single parabolic or non-parabolic bands. In the case of multiple bands, once can incorporate more than one band into the model. Transport equations for the single-band model are based on the Boltzmann transport equation. The carrier concentration (n), Seebeck Coefficient (S), and Lorentz number (L) can be expressed as follows for the SPB band model.

$$n = \frac{2m_d^* k_B T}{3\pi^2 \hbar^3} F_{r+\frac{1}{2}}(\eta) \tag{1.18}$$

$$S = \frac{k_\mathrm{B}}{e}\left[\frac{\left(r+\frac{5}{2}\right)F_{r+\frac{3}{2}}(\eta)}{\left(r+\frac{3}{2}\right)F_{r+\frac{3}{2}}(\eta)} - \eta\right] \tag{1.19}$$

$$L = \left(\frac{k_B}{e}\right)^2\left[\frac{\left(r+\frac{7}{2}\right)F_{r+\frac{5}{2}}(\eta)}{\left(r+\frac{3}{2}\right)F_{r+\frac{1}{2}}(\eta)} - \left(\frac{\left(r+\frac{5}{2}\right)F_{r+\frac{3}{2}}(\eta)}{\left(r+\frac{3}{2}\right)F_{r+\frac{1}{2}}(\eta)}\right)^2\right] \tag{1.20}$$

where η is reduced Fermi energy defined as $(E_F)/\kappa_B T$. m_d^*, κ_B, r, T, and e are the carrier effective mass, Boltzmann coefficient, scattering factor, temperature, and electronic charge. The function $F_k(\eta)$ is Fermi integral given as:

$$F_k(\eta) = \int_0^\infty \frac{x^k dx}{1 + exp(1-\eta)} \tag{1.21}$$

The scattering mechanism decides the r value to be used in the above expressions [23]. In case of non-parabolic band model also known as Single Kane Band (SKB) Model, the above equations are modified [24]. An additional term of nonparabolicity α defined as $\kappa_B T/E_g$, where E_g is the band gap, is included. The modified expressions for the Acoustic Deformation Potential (ADP) scattering are as follows:

$$n = \frac{1}{3\pi^2}\left(\frac{2m_d^* k_B T}{\hbar^2}\right)^{3/2}\left[{}^0F_{-2}^{3/2}(\eta,\alpha)\right] \tag{1.22}$$

$$S = \frac{k_\mathrm{B}}{e}\left[\frac{{}^1F_{-2}^1(\eta,\alpha)}{{}^1F_{-2}^1(\eta,\alpha)} - \eta\right] \tag{1.23}$$

$$L = \left(\frac{k_B}{e}\right)^2\left[\frac{{}^2F_{-2}^1(\eta,\alpha)}{{}^0F_{-2}^1(\eta,\alpha)} - \left(\frac{{}^1F_{-2}^1(\eta,\alpha)}{{}^0F_{-2}^1(\eta,\alpha)}\right)^2\right] \tag{1.24}$$

$${}^nF_k^m(\eta,\alpha) = \int_0^\infty -\left(\frac{\partial f}{\partial \varepsilon}\right)\varepsilon^{\mathrm{n}}(\varepsilon+\varepsilon^2)^{\mathrm{m}}(1+2\alpha\varepsilon^2)^{\mathrm{k}} \tag{1.25}$$

where ε is the reduced energy E/k_BT, and f is the Fermi distribution function. The parameter n, m and k are the indices of the integral whose value depend on the transport property and scattering mechanism. The scattering factor is also incorporated into the equation. Depending on the scattering mechanism the italicized value will change and expressions can be readjusted accordingly.

In order to estimate Lorenz number using non parabolic band model, one has to solve the above equation which has Fermi integrals. We have given a new expression that can easily be used to estimate L using experimental Seebeck coefficient, band gap, and absolute temperature [25]. The details can be found the Appendix A. The expression is given as:

$$L = 1.1 + 1.35exp\left[\frac{-|S|}{\left[162 + 128exp\left(-\frac{Eg}{0.614}\right)\right]\left[\frac{15.71}{\sqrt{T}} + 0.0925\right]}\right] \tag{1.26}$$

where L is in 10^{-8} WΩK^{-2} and S in μVK^{-1}.

1.4 Power factor optimization

1.4.1 Carrier concentration optimization

For ADP (r = -0.5), the predominant scattering mechanism in thermoelectric materials, the Seebeck coefficient can be expressed in a simplified form, commonly referred to as the Pisarenko equation [26].

$$S = \frac{8\pi^2 k_B^2 T}{3eh^2} m_d^* \left(\frac{\pi}{3n}\right)^{3/2} \tag{1.27}$$

We can clearly see that the S is inversely proportional to $n^{3/2}$ and conductivity has direct correlation. So in order to increase the power factor, carriers must be tuned. Figure 1.4 shows the optimization of power factor which is defined as $S^2\sigma$, as a function of carrier concentration. The approach shows a method to increase the numerator of zT just by adjusting the carriers.

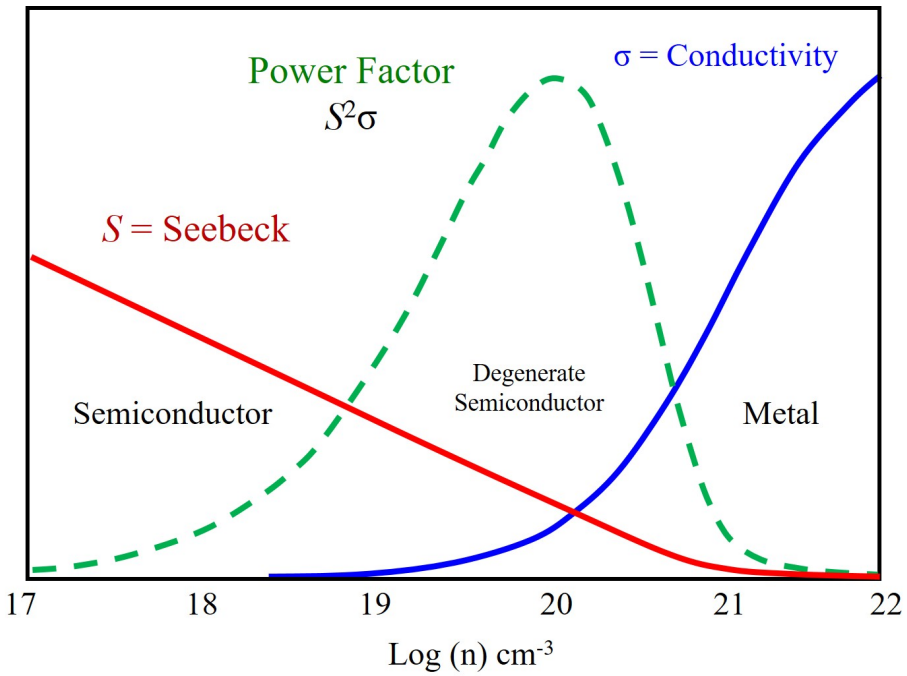

Figure 1.4: A general trend of Seebeck, conductivity, and power factor with carrier concentration

1.4.2 Band engineering

Band engineering refers to the modification of electronic bands in favour of thermoelectric properties. The Seebeck coefficient has direct correlation to the band curvature that decides the carrier effective mass. Modifying the band such that the curvature decreases or bands becoming degenerate helps the case of Seebeck enhancement. The band effective mass (m_b^*) is estimated from band curvature as:

$$\left(\frac{1}{m_b^*}\right)_{ij} = \frac{1}{\hbar^2}\frac{\partial E_{edge}(k)}{\partial k_i \partial k_j}, \qquad i,j = x,y,z \tag{1.28}$$

In case of multiple degenerate bands, the Seebeck effective mass or density of states effective mass is estimated as:

$$m_d^{*3/2} = m_{b1}^{*3/2} + m_{b2}^{*3/2} + m_{b3}^{*3/2} + ... \tag{1.29}$$

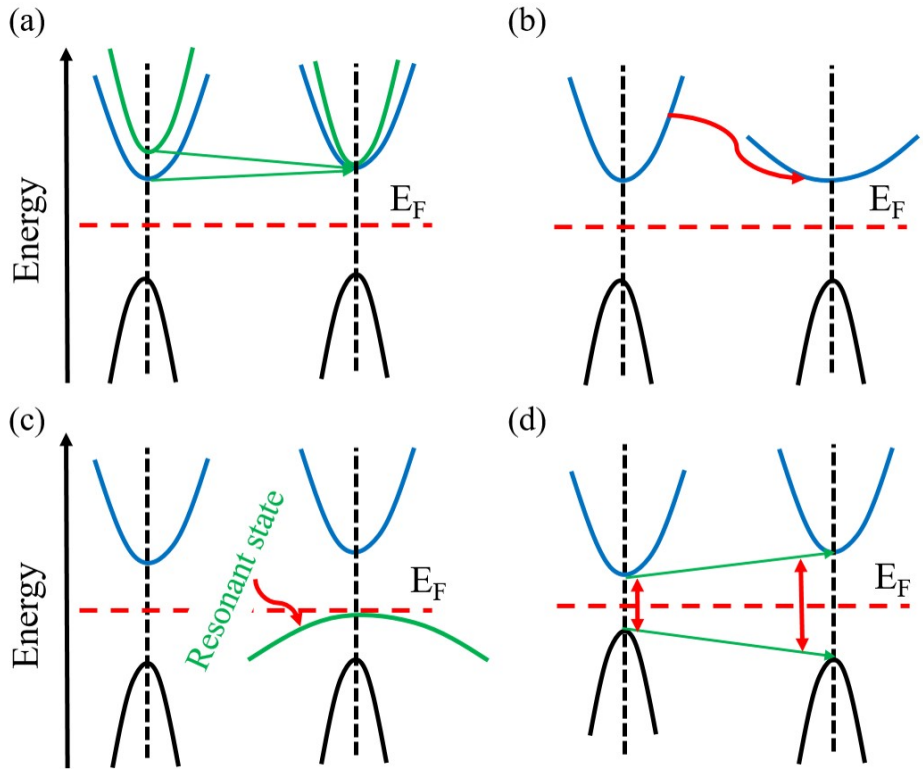

Figure 1.5: Cartoon representing (a) band convergence, (b) band flattening, (c) Resonant state and (d) band gap opening. E_F is the Fermi level.

When all the bands have same band effective mass then the expression reduces to [27]:

$$m_d^* = N^{2/3} m_b^* \tag{1.30}$$

From the expression it is clear that having multiple degenerate band leads to higher Seebeck coefficient. This concept has been widely used in various class of materials form half-Heuslers to chalcogenides. In many systems the degeneracy is achieved with suitable doping [28–30]. One of the best examples is of PbTe where Na doping leads to band convergence [31]. A cartoon of band convergence is shown in Figure 5.2a. A similar change in the effective mass in favour of Seebeck coefficient can be achieved by band flattening as shown in figure 5.2b. Another way of modifying the bands is with resonant doping [32–35]. A suitable dopant which brings a new state called resonant state at Fermi level, hence modifying

the band structure and density of states as shown in Figure 5.2c. A few cases like Indium doping in SnTe results in resonant state [36]. Materials with small band gap tend to show bipolar transport i.e both type of carriers participate in the transport which result in overall lower Seebeck coefficient. Tuning the band gap to higher value is one of the ways to get rid of the bipolarity (see Figure 5.2d).

1.4.3 Tuning carrier scattering

The scattering of carriers is an integral part of electrical transport. Scattering mechanism like electron-phonon scattering (from both acoustic and optical), impurity scattering (both neutral and ionized) , energy barrier scattering etc is detrimental to the relaxation time. The relaxation time can be expressed in terms of energy independent pre-factor τ_0 and energy (E) with index r called scattering factor.

$$\tau(E) = \tau_0 E^r \tag{1.31}$$

For different scattering mechanism the scattering factor is different. Scattering parameter r = -1/2 for acoustic phonons scattered charge carriers, whereas r = 3/2 for ionised impurity scattering. Carrier mobility which is directly proportional to relaxatation time can be tuned by either the intensity of the scattering (τ_0) events or by changing its energy dependence (r). This is called scattering engineering. A few important concepts of scattering engineering will be discussed in the following paragraphs.

Energy Filtering:

The concept of Energy Filtering (EF) was first introduced by Ioffe [37] and further analyzed by Row and Min [38]. They observed the effect of a barrier on Seebeck coefficient and electrical conductivity. The introduced potential barrier filters the low energy carriers led to an increase in Seebeck value. There are many ways to introduce energy filtering. Internal phases and grain boundaries, nanoporous media, superlattice and heterostructure are some of the common examples. The basic understanding of the EF can be understood from the solution of Boltzmann Transport Equation (BTE). The Seebeck coefficient (S), differential

electrical conductivity (σ) and "conductivity weighted average" Seebeck coefficient can be written as [39]:

$$S = \frac{1}{eT}\frac{\int_0^\infty E\tau(E)(E-E_F)g(E)\frac{\partial f_o}{\partial E}dE}{E\tau(E)g(E)\frac{\partial f_o}{\partial E}dE} \tag{1.32}$$

$$\sigma = \frac{2e^2}{3m^*}E\tau(E)g(E)\frac{\partial f_o}{\partial E} \tag{1.33}$$

$$S = \frac{3m^*}{2e^3T} < E - E_F >_\sigma \tag{1.34}$$

where $\tau(E)$, E_F, $g(E)$, and E are the energy dependent relaxation time, Fermi energy, density of states and charge carrier energy respectively. f_o and T represents equilibrium Fermi-Dirac distribution and absolute temperature. It is clear from the above equation that S is dependent on Fermi energy and an asymmetric form of $g(E)$ will with respect to Fermi energy will result in large S. Modifying energy dependent relaxation time in such cases increases the extent of asymmetry of $\tau(E)g(E)$ resulting in the increases S. EF can be a tool to modify the $\tau(E)$ that eventually increases the Seebeck coefficient. Figure 1.6a shows the physical picture of energy barrier acting as a charge filter.

Charge Modulation:

Charge Modulation is a technique for doping carriers by spatially separating from the donors. It helps to maintain high mobility in the system by eliminating the presence of external impurity. It has been widely used in layered materials where there is doping layer and conducting layer where charges are modulated as shown in Figure 1.6b. In bulk thermoelectric, three-dimensional (3D) modulation has been used to enhance power factor by increasing electrical conductivity [40]. Initially nanoparticles of electron or hole rich material is doped as impurity into the bulk thermoelectric where carriers are modulated from the impurity without disturbing the mobility (See Figure 1.6b). The modulation can also be done from electron rich impurity phase of micron size as demonstrated in TiNiSn hH [41]. 3D modulation doping has also been reported in TiCoSb based hH [42]

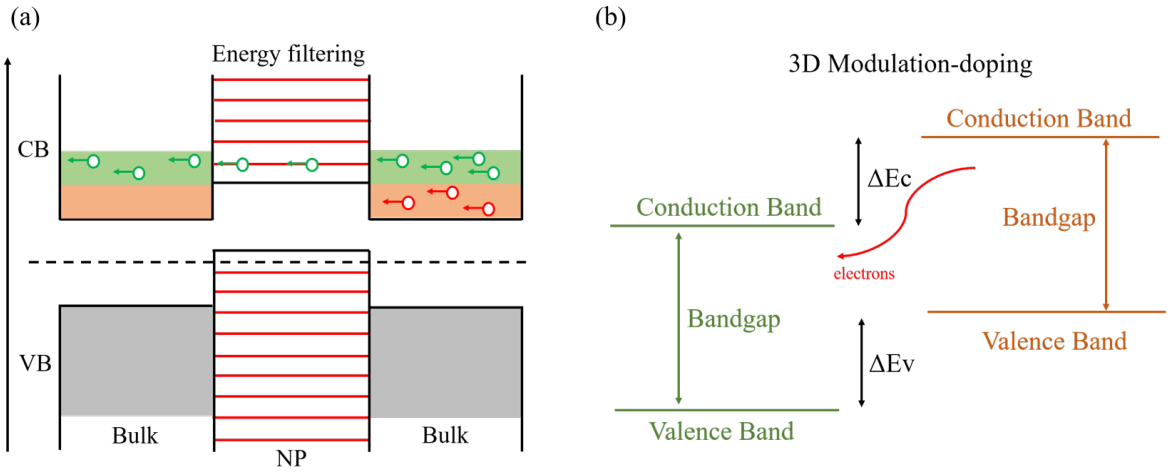

Figure 1.6: (a) energy filtering and (b) 3D modulation doping. CB and VB represents Conduction and Valence band respectively. Nano Particle is denoted as NP. ΔEc and ΔEv represents the difference in the conduction and valence band respectively.

1.5 Lattice thermal conductivity optimization

The heat transported by phonons is referred to as lattice thermal conductivity. By inhibiting the phonon transport, κ_l can be reduced. Apart from the phonon-phonon scattering which is a material intrinsic properties that depend on complexity of crystal structure, some additional source of scattering can be introduced as follows.

Grain boundary Scattering: The propagation of phonon is mediated by the regular arrangement of atoms in the system. At the grain boundary the arrangement breaks down leading to the scattering of phonon. Smaller the grains more will be the scattering as phonon will encounter the grain boundary more frequently. Therefore, nano-structuring has been widely used exploiting the grain boundary scattering effect to reduce the κ_l [43]. The quantitative estimation is discussed in chapter 2. Up untill now the scattering because of the grain boundary is estimated by comparing the κ_l of single crystal and polycrystalline sample. A new method of probing the κ_l at microscopic level has been developed by Eleonora Isotta et.al where probing κ_l at the grain boundary lead to further understanding of scattering mechanism [44]. They found that all grain boundaries are not same rather scattering tendency depends on the grain boundary mis-oriantation angle.

Point defect: The other way of scattering phonon is by creating point defect, which is done by doping a foreign element with significant mass difference. The change in mass leads to difference in the phonon frequency locally acting as an additional scattering centre. The quantificantion is explained in Chapter 3, where it is shown that larger the mass difference larger is the scattering. In case of polycrystalline samples where grain size is large such that effect of grain boundary scattering is not significant, the difference in the κ_l is because of vacancy or anti-site disorder which act as point defect centre [42]. Point defect can be maximized by placing multiple elements at the same site, as in High Entropy alloys which tend to have low κ_l because of extreme point defect scattering. A similar approach is shown in Chapter 6.

1.6 Thermoelectric Materials

Oxides

Oxide thermoelectric have gained some attention due to their low cost and application in atmospheric conditions. The major challenge was the low electric conductivity and high thermal conductivity [45]. Despite having unfavourable transport properties, a few notable materials are mentioned. N-type ZnO, $SrTiO_3$, and $CaMnO_3$ [46], as well as p-type $Ca_3Co_4O_9$ are one of the most promising materials in this class. A zT of 0.9 was reported for a single crystal of Bi-doped $Ca_3Co_4O_9$ [46]. Cu doped $NaCo_2O_4$ in polycrystalline form shows maximum zT of 0.5 at 573 K [47]. The environment friendly nature of the oxide thermoelectric makes it a viable candidate for further investigation.

Chalcogenides

A family of compounds with anions belongs to the chalcogen group (S, Se, Te). Chalcogenides offer a variety of crystal structure for simplest cubic (PhTe, SnTe) to rhombohedral (GeTe) to Orthorhombic (SnSe). This class of compounds have been studied rigorously as an excellent thermoelectric material in the low to mid temperature range. Having low thermal conductivity due to presence of heavy elements, high anharmonicity and soft bonding favours the thermoelectric properties. Many binary compounds such as PbTe, PbSe, Cu_2Se,

SnSe, and Bi_2Te_3 [48–52] have zT close to 2. However, some exceptional material like $AgSbTe_2$ has shown a zT of 2.6 [53].

1.7 Heuslers

A class of intermetallic materials discovered in the early 20^{th} century by a German mineralogist Fritz Heusler and is named after him. However, it was not until the latter part of the century that Heusler compounds has gained considerable interest, especially due to their potential applications in thermoelectric and magnetic materials. Heusler compounds are characterized in various subgroups on the basis of atomic occupation and electronegativity of the occupying element. The most explored among all is half-Heusler, classified as intermetallics having 1:1:1 stoichiometry of three interpenetrating face-centered cubic sublattices ($F\bar{4}3m$). We will be using a general formulation of hH as XYZ, where X(most electropositive), Y(intermediate electropositive), and Z(most electronegative) occupies the position 4a(0,0,0), 4c(1/4,1/4,1/4), and 4b(1/2,1/2,1/2) respectively. The Wycoff positions 4a and 4b are equivalent and generally occupied by X and Z resulting in NaCl type structure whereas the 4c site (tetrahedrally coordinated) is occupied by Y. In case of X and Y occupying 4c and 4a sites respectively yield ZnS type structure. Overall, three variations of XYZ hH structure could be possible according to the 4c site occupation of elements (X/Y/Z). The full Heusler is represented as XYYZ. All the classifications of the Heusler family are shown in Figure 1.7. Among all hH shows the most explored and interesting from thermoelectric point of view. The intricate properties, advantages and disadvantages are discussed below.

1.7.1 Half Heusler:

Most of the hH are semiconductor with band gap between 0 to 1 eV. The semiconducting behaviour can be released based on valence electron count (VEC) which also provides a thumb rule for the stability of any hH [54]. VEC is the total number of electrons participating in the bonding or in other word, total valence electrons. An example of TaFeSb, with a total number of 18 electrons, 5 from Ta, 8 from Fe and 5 from Sb making it a total of 18. It has

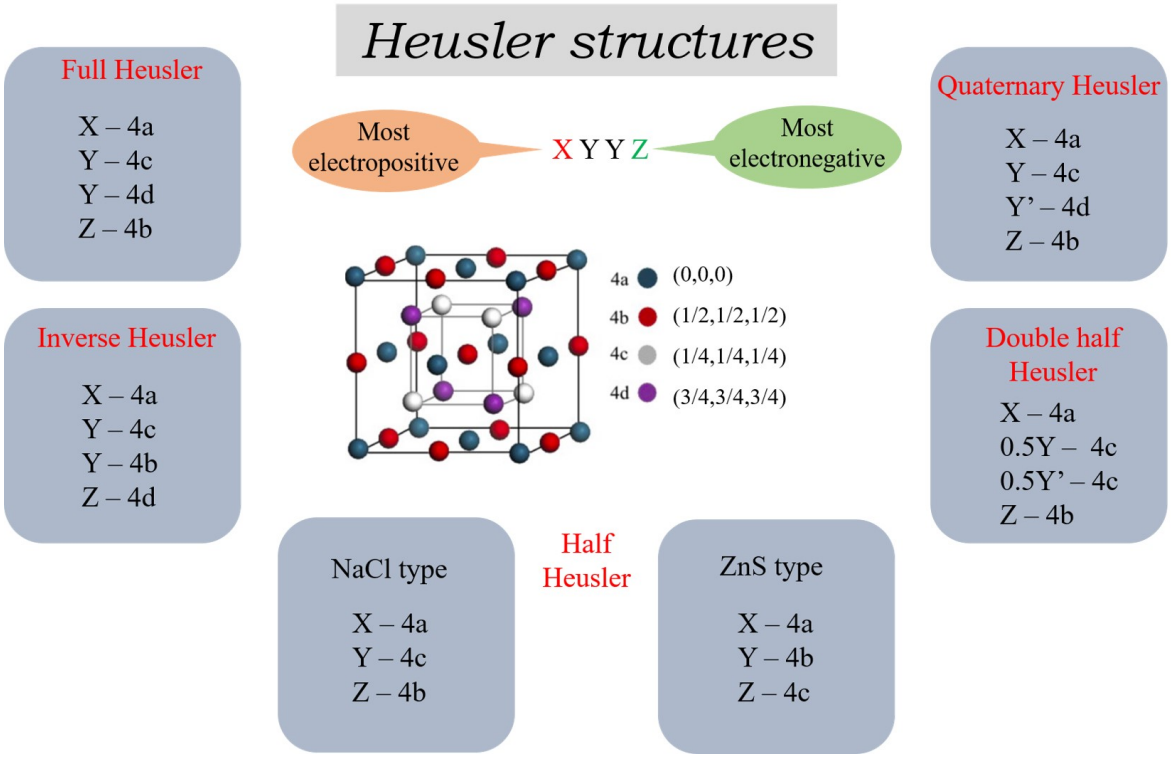

Figure 1.7: Heusler structures. X, Y, Y', and Z represents different elements. 4a, 4b, 4c, and 4d are the Wyckoff notations.

been found that hH with 18 electrons are stable and show semiconducting properties. In the case of 18 VEC, all the bonding orbitals are filled, and antibonding orbitals are empty. A detailed analysis is done in chapter 5. A few exceptional hH with 17 and 19 VEC are also stable. TiFeSb with VEC of 17 becomes stable with excess Fe as $TiFe_{1.33}Sb$ [55]. The excess Fe provides the extra electron to fill the bonding orbitals. Similarly, NbCoSb, a 19 VEC hH stabilizes with Nb vacancy to remove one electron from the antibonding orbitals. It forms with Nb vacancy as $Nb_{0.8}CoSb$ [56]. A few double hH (dhH) are also reported which are formed by mixing 17 and VEC materials to achieve 18 VEC. For example, $TiFe_{0.5}Ni_{0.5}Sb$ is one the wll known dhH which has been realised experimentally [57]. The ideal dHH are generally represented as $X_2YY'Z_2$ where the Y and Y' shows 1 : 1 ordering.

Table 1.2: zT of a few reported state of the art hH

Material	T (K)	Peak zT	references
$Ti_{0.5}Zr_{0.25}Hf_{0.25}NiSn_{0.998}$ $Sb_{0.002}$	824	1.21 (n-type)	[59]
$Hf_{0.6}Zr_{0.4}NiSn_{0.98}Sb_{0.02}$	1030	1.01 (n-type)	[60]
$Ti_{0.25}Hf_{0.75}CoSb_{0.85}Sn_{0.15}$	981	1.15 (p-type)	[61]
$Zr_{0.5}Hf_{0.5}Co_{0.9}Ni_{0.1}Sb$	1074	1.02 (n-type)	[62]
$Nb_{0.8}Ti_{0.2}FeSb$	1100	1.09 (p-type)	[63]
$Nb_{0.88}Hf_{0.12}FeSb$	1200	1.45 (p-type)	[64]
$(Nb_{0.6}Ta_{0.4})_{0.8}Ti_{0.2}FeSb$	1200	1.60 (p-type)	[65]
$Ta_{0.74}V_{0.1}Ti_{0.16}FeSb$	973	1.52 (p-type)	[66]
$ZrCo_{0.9}Ni_{0.1}Bi_{0.85}Sb_{0.15}$	972	1.04 (n-type)	[67]
$ZrCoBi_{0.65}Sb_{0.15}Sn_{0.20}$	973	1.42 (p-type)	[68]
$Nb_{0.85}CoSb_{0.9}Sn_{0.1}$	1073	1.04 (n-type)	[69]

1.7.2 Reported literature:

HH as thermoelectric materials come to focus in last 2 decades. During the end of 20th century intermetallic MNiSn was found to exhibit semiconducting properties [58]. Having semiconducting properties open the opportunity to exploit these materials for their thermoelectric properties. This paragraph deals with discovery and performance of some of the well known p-type and n-type hH thermoelectric materials. A few well known hH are listed in the Table 1.2 with peak zT and temperature.

Over the last 20 years, MNiSn-based HH compounds have advanced to become the most effective n-type hH thermoelectric materials with peak zT exceeding unity [59,70–72]. Since 2000, researchers have focused on MCoSb, p-type thermoelectric with a zT approximately equal to one [61, 73]. Recent research indicates that n-type MCoSb has comparable high zT values to p-type MCoSb [62, 74], makes it the first hH to exhibit good thermoelectric performance in both types. Thermoelectric characteristics of XFeSb were studied as early as MNiSn and MCoSb [75], but received little attention due to its poor performance. Since 2014, the heavy-band XFeSb-based hH system has been engineered as a high-performance p-type thermoelectric material, reaching a peak zT of approximately 1.5 through careful

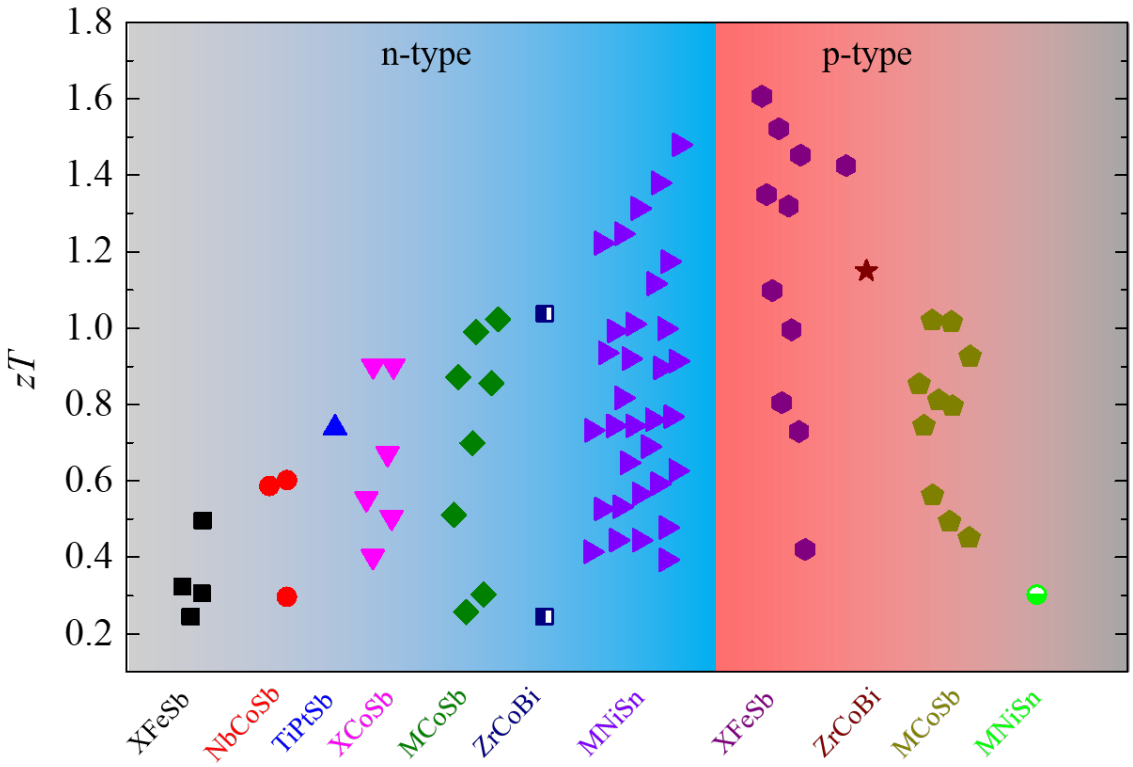

Figure 1.8: Peak zT of few reported hH thermoelectric materials. Data taken from Ref. [2].

compositional tuning and optimal doping. [63–66]. Prototype eight-pair HH thermoelectric modules, constructed using n-type MNiSn and p-type XFeSb, demonstrated a maximum conversion efficiency of 10.5 % and a power density of 3.1 W cm^{-2} under a temperature difference of 680 K [76]. This highlights the potential of HH compounds for power generation. Peak zT of a few notable hH are shown in Figure 1.8 [2].

1.8 Synopsis of the thesis work

This thesis focuses on understanding and further improving thermoelectric properties of half Heusler systems. The objective was to design new hH based materials along with find new methods to improve the existing ones. The First chapter introduces the the fundamental concepts of thermoelectricity, the challenges and the ways it can be improved. Chapter 2 deals with the computational method used to estimate the thermodynamic stability, electronic ground state and transport properties. The experimental techniques required to synthesize, characterize and transport properties measurements are explained in chapter 3. The next chapters deal with new approaches used in this study in enhancing the thermoelectric properties of half Huesler based materials as detailed below.

In chapter 4, we investigated the effect of band degeneracy and modulation doping on the thermoelectric properties of TiCoSb. Conduction bands of TiCoSb was modified by suitable doping and further optimization of carriers were done using charge modulation by making composite samples using TiCoSb and $Nb_{0.8}CoSb$. The phonon transport calculation was done to explain the reduction in the observed lattice thermal conductivity.

Chapter 5 shows the concept of Zintl chemistry to understand the bonding mechanism of some double half Heusler with the help of density functional theory based calculation. Furthermore, transport properties of the systems were calculated to predict the maximum zT in both p and n type region at optimum carrier concentration and temperature.

Chapter 6 has an experimental implementation of calculated results from chapter 5. A new double half Heusler ($HfFe_{0.5}Ni_{0.5}Sb$) was synthesized and further reduction of lattice thermal conductivity was done by adding more components at Hf and Fe/Ni site. Finally

the compound was transformed from double half Heusler to a high entropy alloy by adding Co at Fe/Ni site, $Ti_{1/2}Hf_{1/2}(FeCoNi)_{1/3}Sb$ having mixing entropy having mixing entropy of 1.79R. The effect of entropy on structural stabilization was also proved experimentally. By tuning the Ni and Fe concentration we optimized the thermoelectric figure of merit.

In chapter 7, we have investigated the role of antisite defects on the electron and phonon transport of Ti doped TaFeSb. We discovered the Ti/Ta-Fe anti-site disorder increases the density of state effective mass and reduces the lattice thermal conductivity. A maximum zT of 1.55 at 973 K was observed which is so far the highest among p-type hHs in this temperature range.

Chapter 2

Computational Methods

The identification of thermoelectric materials has historically depended on a trial-and-error approach. However, recent advancements in theoretical simulations, which allow for the prediction of new phase structures, as well as their thermodynamic stability and functional characteristics, have paved the way for the inverse design method. This approach, in contrast to traditional discovery methods, holds the potential to greatly reduce the experimental workload involved in finding compounds with specific desired properties. It is now possible to calculate physical properties of a material by solving many-body Schrodinger equation (SE) [77]. Exact solution of the SE is not practically possible without some approximation. This chapter deals with the challenges, tips and tricks to solve many-body SE. This chapter also deals with methodologies for calculating the transport properties by solving the semiclassical Boltzmann transport equation.

2.1 Many Body Schrodinger Equation

Many body systems (Matter) consist of positively charged nuclei (N) and electrons (n) that are bonded together via coulomb interaction. The time independent SE for the system can be written as:

$$\hat{H}_{tot}\wp(\mathbf{R}_I, \mathbf{r}_i) = E_{tot}\wp(\mathbf{R}_I, \mathbf{r}_i) \tag{2.1}$$

where, $\wp(\mathbf{R}_I,\ \mathbf{r}_i)$ is the many-body wave function and is a function of position of all the nuclei ($\mathbf{R}_I$) and electrons ($\mathbf{r}_i$) in the system. $\hat{H}_{tot}$ is the total Hamiltonian of the system. Symbols written in bold are vector quantities. $\hat{H}_{tot}$ can be expressed by adding the potential and kinetic energy of many-body system. The kinetic energy of nuclei and electrons can be expressed as:

$$-\sum_{I=1}^{n}\frac{\hbar^2}{2M_I}\nabla_I^2-\sum_{i=1}^{n}\frac{\hbar^2}{2M_e}\nabla_i^2 \tag{2.2}$$

where $\hbar$ is the reduced Planck's constant, M_I and M_e are the masses of I^{th} nuclei and i^{th} electron respectively. The potential energy corresponding to electron-electron(e-e) repulsion, nucleus-nucleus (N-N) repulsion and electron-nucleus (e-N) attraction can be expressed as:

$$\frac{1}{2}\sum_{I,J=1}^{N}\frac{e^2}{4\pi\epsilon_o}\frac{Z_IZ_J}{|\mathbf{R}_I-\mathbf{R}_J|}+\frac{1}{2}\sum_{i,j=1}^{n}\frac{e^2}{4\pi\epsilon_o}\frac{1}{|\mathbf{r}_i-\mathbf{r}_j|}-\frac{e^2}{4\pi\epsilon_o}\sum_{I=1}^{N}\sum_{i=1}^{n}\frac{Z_I}{|\mathbf{R}_I-\mathbf{r}_j|} \tag{2.3}$$

Now $\hat{H}_{tot}$ can be expressed as:

$$\hat{H}_{tot}=-\sum_{I=1}^{N}\frac{\hbar^2}{2M_I}\nabla_I^2-\sum_{i=1}^{n}\frac{\hbar^2}{2M_e}\nabla_i^2+\frac{1}{2}\sum_{I,J=1}^{N}\frac{e^2}{4\pi\epsilon_o}\frac{Z_IZ_J}{|\mathbf{R}_I-\mathbf{R}_J|} \tag{2.4}$$

$$+\frac{1}{2}\sum_{i,j=1}^{n}\frac{e^2}{4\pi\epsilon_o}\frac{1}{|\mathbf{r}_i-\mathbf{r}_j|}-\frac{e^2}{4\pi\epsilon_o}\sum_{I=1}^{N}\sum_{i=1}^{n}\frac{Z_I}{|\mathbf{R}_I-\mathbf{r}_i|} \tag{2.5}$$

where, Z_I represents the nuclear charge of I^{th} nucleus, e and ϵ are the electronic charge and vacuum permittivity. The nonlocal potential term in the above equation makes it difficult to solve; hence, further approximations are needed. In addition to that, one has to solve the SE for both electrons and nucleus as well with the given form of Hamiltonian above. Moreover because of the much heavier mass of the nucleus, its dynamics will not affect the dynamics of electrons, and they can be treated separately.

According to Born-Oppenheimer (BO) approximation [78], $\wp(\mathbf{R}_I,\mathbf{r}_i)$ can be decoupled as a product of nuclear wave function $(\Psi(\mathbf{R}_I))$ and electronic wavefunction $(\Phi(\mathbf{r}_i;\mathbf{R}_I))$, where $\Phi(\mathbf{r}_i;\mathbf{R}_I)$ has only parametric dependence on the nuclear coordinates. Mathemati-

cally,

$$\wp(\mathbf{R}_I, \mathbf{r}_i) = \Psi(\mathbf{R}_I)\Phi(\mathbf{r}_i; \mathbf{R}_I) \tag{2.6}$$

Now all electron Hamiltonian ($\hat{H}_e$) can be expressed in a nutshell as (in Hartree atomic units, $\hbar$ = e = $4\pi\epsilon_o$ = M_e = 1):

$$\hat{H}_e = -\sum_{i=1}^{n} \frac{\nabla_i^2}{2} + \frac{1}{2}\sum_{i,j=1}^{n} \frac{1}{|\mathbf{r}_i - \mathbf{r}_j|} - \sum_{i=1}^{n} \frac{Z_I}{|\mathbf{R}_I - \mathbf{r}_i|} \tag{2.7}$$

2.1.1 Independent electron approximation

The above SE still have nonlocal e-e interaction term, hence further approximation is required. If the e-e term were negligible, the Hamiltonian can be broken down into a series of N independent Hamiltonians, each corresponding to a single electron, which significantly simplifies the problem. The e-e interaction term, however, prevents this decomposition by ensuring that the Hamiltonian for each electron will include terms for the position of every other electron in the system. If the electron-electron interaction term is sufficiently small, however, the Coulomb interactions terms can be approximated by an effective potential term, which neglects e-e interactions. This is called the "Independent electron approximation". Under this assumption all electron wave function (Φ) can be expressed in terms of individual electron wave function $\phi_i(\mathbf{r}_i)$. For the sake of simplicity, we are not mentioning the nuclear position $\mathbf{R}_I$ in the expression.

$$\Phi(\mathbf{r}_i) = \phi_1(\mathbf{r}_1)\phi_2(\mathbf{r}_2).....\phi_n(\mathbf{r}_n) \tag{2.8}$$

Here, the independent particle Hamiltonian (H_o) has only two terms the kinetic energy and the nuclear potential energy $V_n(\mathbf{r})$

$$\hat{H}_o(\mathbf{r})\phi_i(\mathbf{r}) = \varepsilon\phi_i(\mathbf{r}), \quad and \quad \hat{H}_o(\mathbf{r}) = -\frac{\nabla_i^2}{2} + V_n(\mathbf{r}) \tag{2.9}$$

where, V_n is electronic interaction due to nuclei. The next section deals with a method to incorporate the nonlocal e-e interaction term.

2.1.2 Hartree's self-consistant field approximation

The excluded e-e interaction can be estimated by "Mean Field approximation" which uses the electron density $[n(\mathbf{r})]$ to determine the electrostatic field generated by electrons. So, now we have the SE after Independent electron approximation as:

$$\left[-\frac{\nabla_i^2}{2} + V_n(\mathbf{r})\right]\phi_i(\mathbf{r}) = \varepsilon_i\phi_i(\mathbf{r}) \tag{2.10}$$

with electron density given as:

$$n(\mathbf{r}) = \sum_{i=1}^{n} |\phi_i(\mathbf{r})|^2 \tag{2.11}$$

From mean field theory, the e-e interaction can be approximated which is in general known as Hartree potential.

$$V_H(\mathbf{r}) = \int d\mathbf{r}' \frac{n(\mathbf{r}')}{|\mathbf{r} - \mathbf{r}'|} \tag{2.12}$$

now the updated SE with e-e interaction as Hartree potential can be expressed as:

$$\left[-\frac{\nabla_i^2}{2} + V_n(\mathbf{r}) + V_H(\mathbf{r})\right]\phi_i^{new}(\mathbf{r}) = \varepsilon_i^{new}\phi_i^{new}(\mathbf{r}) \tag{2.13}$$

After solving the updated SE with V_H a new electronic wave function is obtained. With new ϕ_i^{new}, a new $V_H(\mathbf{r})$ is estimated and using it again a new ϕ_i. This is Hartree's self-consistent field approximation which was proposed in 1928 [79]. It does not require many-body wave function but require iterative solution.

2.1.3 Exchange energy

The Hartree approximation does not incorporate the constraint on the anti-symmetry of many-body wavefunction $\Psi(\mathbf{r}_1, \mathbf{r}_2) = -\Psi(\mathbf{r}_1, \mathbf{r}_2)$. Hartree-Fock came up with an idea to use the Slater determinant as a wavefunction instead of the Hartree product of electron's

wavefunction [80]. A Slater determinant takes care of the anti symmetricity of the electronic wavefunction with respect to the exchange of the coordinates, which is a consequence of Pauli exclusion principle. Incorporating this constrain in the mean field equation leads to a new potential energy contribution, known as the "Fock exchange" expressed as:

$$V_X(\mathbf{r},\mathbf{r}') = -\sum_{j\in occ} \frac{\phi_j^*(\mathbf{r})\phi_j(\mathbf{r})}{|\mathbf{r}-\mathbf{r}'|} \tag{2.14}$$

The Fock potential enforces Pauli's principle by making sure that same spin electrons repel each other and opposite spin attracts. The Fock potential is non-local. After the incorporation of exchange potential the new SE has one additional term.

$$\left[-\frac{\nabla_i^2}{2} + V_n(\mathbf{r}) + V_H(\mathbf{r}) + \int d\mathbf{r}' V_X(\mathbf{r},\mathbf{r}')\right]\phi_i(\mathbf{r}) = \varepsilon_i\phi_i(\mathbf{r}) \tag{2.15}$$

2.1.4 Correlation energy

So far it was assumed that electrons are independent, in other word uncorrelated. Such assumption is not accurate as electrons energy depends on the position of other electrons, therefore, the wavefunction can not be expressed as Slater determinant. But so far all the formulation is developed Slater determinant is very useful in practical solution, it can be kept with an inclusion of a correction energy term into the Hamiltonian as $V_C(\mathbf{r})$. Now the SE has evolved into a form which later takes a form which is commonly known as Kohn-Sham Equation.

$$\left[-\frac{\nabla_i^2}{2} + V_n(\mathbf{r}) + V_H(\mathbf{r}) + \int d\mathbf{r}' V_X(\mathbf{r},\mathbf{r}') + V_C(\mathbf{r})\right]\phi_i(\mathbf{r}) = \varepsilon_i\phi_i(\mathbf{r}) \tag{2.16}$$

Solving the above equation is still non practical as one has to deal with 3n dimensional problem. Each electron has 3 degree of freedom which result in a calculation with 3n dimension with total n number of electrons.

2.2 Density Functional Theory (DFT)

DFT, introduced by Hohenberg and Kohn, offers an alternative approach to solving many-body quantum systems by using the electron charge density [n(**r**)] as the fundamental variable instead of the many-body wavefunction. This framework is built on the idea that the ground-state energy of a system of interacting electrons is a functional of the electron density, making the problem significantly more manageable computationally compared to dealing with the full wavefunction. It will shrink the 3n dimensional problem to just 3 dimensional. DFT is based on the following two theorems [81].

Theorem 1: "For any system of interacting particles in an external potential $V_{ext}(\mathbf{r})$, the potential $V_{ext}(\mathbf{r})$ is determined uniquely, except for a constant, by the ground state particle density $n_0(\mathbf{r})$".

Theorem 2: "A universal functional for the energy $E[n]$ in terms of the density $n(\mathbf{r})$ can be defined, valid for any external potential $V_{ext}(\mathbf{r})$. For any particular $V_{ext}(\mathbf{r})$, the exact ground state energy of the system is the global minimum value of this functional, and the density $n(\mathbf{r})$ that minimize the functional is the exact ground state density $n_0(\mathbf{r})$".

The first theorem establishes that two distinct external potentials can not give rise to the indistinguishable ground state (GS) charge density $n_0(\mathbf{r})$). Specifically, V_{ext} is known uniquely through $n_0(\mathbf{r})$. The second theorem tells that $E[n]$ can be minimized with respect to variations in $n(\mathbf{r})$. The value of density that minimizes $E[n]$ gives the GS density $n_0(\mathbf{r})$ and the corresponding value of energy is the GS energy (E_{min}). In summary, if $n_0(\mathbf{r})$ is specified, all properties can be uniquely characterized. The functional described by the Hohenberg-Kohn theorem is in terms of the single-electron wave functions which collectively construct the density.

For an unknown $V_{ext}(\mathbf{r})$, the energy functional ($E_{HK}[n]$)) can be written as:

$$E_{HK} = F_{HK} + \int d\mathbf{r} n(\mathbf{r}) V_{ext}(\mathbf{r}) \tag{2.17}$$

where F_{HK} is the sum of the K.E. of the electrons ($T[n]$) and the electron-electron inter-

action ($E_{ee}[n]$ =) terms, can be written as:

$$F_{HK} = T[n] + E_{ee}[n] \tag{2.18}$$

If F_{HK} is given, it implies the information of the GS properties is known for the system. HK theorem predicts existence of a universal functional form of $F_{HK}[n]$ that could give all the GS properties of the system. However, it does not give a recipe to calculate it. In the next section, we have briefly discussed a practical way to find F_{HK} suggested by Kohn and Sham.

2.2.1 The Kohn-Sham (KS) Ansatz

KS tackled this problem of unknown functional ($F_{HK}[n]$) [82] in 1965 by resolving it numerically by replacing interacting electrons with an auxiliary system of non-interacting electrons. Kohn and Sham proposed the following ansatz [83]:

- The GS density of the fictitious system is same as that of actual system.
- The calculations can be performed on a fictitious independent-particle systems defined by Hamiltonian ($\hat{H}_s$) for single electron having the kinetic energy (KE) term and subjected to an effective local potential ($V_{eff}(\mathbf{r})$). (Again, we adopt Hartree atomic units $\hbar$ = m = e = $4\pi\epsilon_o$= 1).

$$\hat{H}_s = -\frac{\nabla^2}{2} + V_{eff}(\mathbf{r}) \tag{2.19}$$

Using above two ansatzes, the KS suggested to rewrite expression of $F_{HK}[n]$ functional in the following manner:

$$F_{KS}[n] = T_s[n] + E_H[n] + E_{XC}[n] \tag{2.20}$$

where $T_s[n]$ denotes the ground state KE of non-interacting electrons of the supplementary system and $E_H[n]$ is the Hartree energy.

$$T_s[n] = \frac{1}{2}\sum_{i}^{n}\int d\mathbf{r}|\nabla\phi_i(\mathbf{r})|^2 \tag{2.21}$$

$$E_H[n] = \frac{1}{2}\int\int d\mathbf{r}d\mathbf{r}'\frac{n(\mathbf{r})n(\mathbf{r}')}{|\mathbf{r}-\mathbf{r}'|} \tag{2.22}$$

and the $E_{KS}[n]$ can be written as:

$$E_{KS}[n] = F_{KS}[n] + \int d\mathbf{r}n(\mathbf{r})V_{ext}(\mathbf{r}) \tag{2.23}$$

Kohn-sham equation can again be written as:

$$\left[-\frac{\nabla_i^2}{2} + V_{ext}(\mathbf{r}) + V_H(\mathbf{r}) + V_{XC}(\mathbf{r})\right]\phi_i(\mathbf{r}) = \varepsilon_i\phi_i(\mathbf{r}) \tag{2.24}$$

where V_{ext} + V_H +V_{XC} = KS potential V_{KS} and is expressed as:

$$V_{KS}[n](\mathbf{r}) = V_{ext}(\mathbf{r}) + \int d\mathbf{r}'\frac{n(\mathbf{r}')}{|\mathbf{r}-\mathbf{r}'|} + V_{XC}(\mathbf{r}) \tag{2.25}$$

KS equations for a system of independent electrons moving in local effective potential can be derived by the minimizing $E_{KS}[n]$. This property is known as "Hohenberg-Kohn variational principle" and can be written as follows:

$$\left[\frac{\delta E_{KS}[n]}{\delta n}\right]_{n_o} = 0 \tag{2.26}$$

The unknown term of the V_{KS}(**r**) can also be represented as:

$$V_{XC}(\mathbf{r}) = \frac{\delta E_{XC}}{\delta n(\mathbf{r})} \tag{2.27}$$

Thus, if we know V_{KS} (local effective potential), we can solve the set of single electrons Kohn-Sham equations (2.24) and obtain information of GS of the system of interacting electrons. The calculation starts with an initial guess of density. The complete iterative loop is shown in the Figure 2.1.

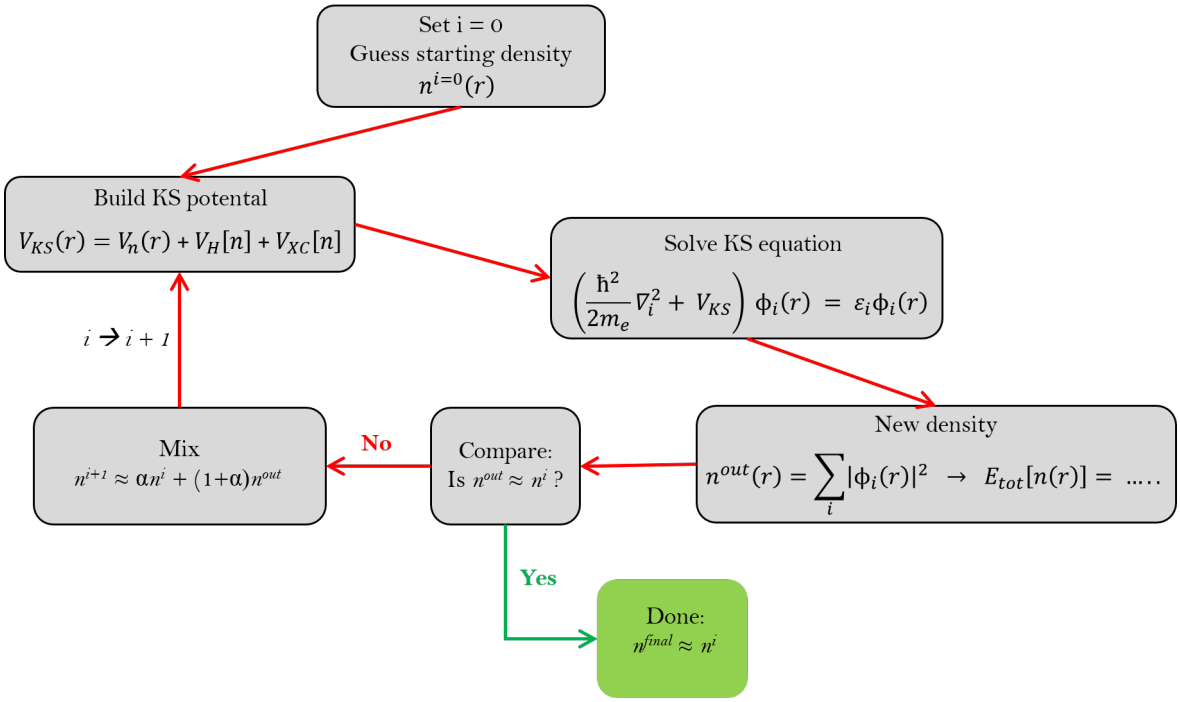

Figure 2.1: Self consistent cycle

2.2.2 Exchange Correlation Functional

The unknown term of exchange correlation (V_{XC}), as described earlier section, has not been discovered. There are many approximation techniques that have been used so far with least to highest accuracy. The accuracy comes at a cost of large computational cost. This section will deals with a few most common forms of the functional used. In this thesis, we have not gone beyond commonly used approximations.

Local Density Approximation (LDA):

LDA is the widely used approximation for the exchange-correlation energy (E_{XC}). Energy functional is assumed to be function of electron density at point r in space and is expressed as:

$$E_{XC}^{LDA} = \int n(\mathbf{r})\epsilon_{XC}^{H}[n(\mathbf{r})]d\mathbf{r} \tag{2.28}$$

where $\epsilon_{XC}^{H}[n(\mathbf{r})]$ denotes exchange-correlation energy per particle for a homogeneous elec-

tron gas with density n(**r**) at a point **r**. LDA provides exact functional form of exchange-correlation energy for homogeneous electron gas and thus it performs well for systems with minimal variation in electron density in space. It has produced correct results in many cases but fails in other situations. One of the most noted failures is the correct cancellation of electron self interaction that is introduced by Hartree potential [84]. In fact, this is true for all approximations of the exchange correlation functionals. The XC potential far from a finite system decays exponentially in an LDA, rather than following the Coulomb-like -r^{-1} decay present in the exact V_{XC} [85–87]. These failings lead to errors in the KS orbital [88]. It imperative to use more accurate approximation to estimate xc energy.

Generalized Gradient Approximation (GGA):

GGA considers both local distribution as well as gradient of electron density (Δn(**r**)) into account. It can be expressed as:

$$E_{XC}^{GGA} = \int n(\mathbf{r})\epsilon_{XC}[n(\mathbf{r}), |\Delta n(\mathbf{r})|]d\mathbf{r} \tag{2.29}$$

Various approximations of GGA functional are available, for e.g., Becke (B88) [89], Perdew and Wang (PW91) [90] etc. In this thesis, we use the GGA functional parameterized by Perdew, Burke, and Ernzerhof (PBE) as it offers a more accurate description of many-body electron systems compared to the LDA [91]. Like LDA, the XC potential far from a finite system decays exponentially in this case as well. It fails to estimate the XC energy in case of Mott insulators. GGA fails for Mott insulators because it doesn't capture strong on-site electron-electron repulsion, leading to an incorrect prediction of metallic behaviour instead of an insulating state.

2.3 Periodicity

In the paragraph above, it was demonstrated that a single electron SE equation can replace the many-body interacting system with a non-interacting system subject to V_{KS}. But there are two daunting obstacles waiting to be solved. The first involves solving the KS equations

for an infinite number of independent electrons traveling in $V_n(\mathbf{r})$ (ionic potential) as a result of an endless number of nuclei. The second problem involves using impractically large basis sets while representing each wavefunction. In the following section, we explain how the periodic nature of crystals can be incorporated to address both of these issues.

2.3.1 Bloch's theorem

For an electron in periodic potential generated by atomic periodicity, the electronic wave function can be written as plane wave modulated by a periodic function for a given crystal momentum vector k.

$$\phi_{n\mathbf{k}}(\mathbf{r}) = e^{i\mathbf{k}.\mathbf{r}} u_{n\mathbf{k}}(\mathbf{r}) \tag{2.30}$$

where $u_n(\mathbf{r})$ is the periodic function related to the crystal periodicity which resulted in the periodic potential at the first place. The periodic function can be expanded with a discrete basis set of plane waves:

$$u_{n\mathbf{k}}(\mathbf{r}) = \frac{1}{V} \sum_G (C_{n,\mathbf{G}}) e^{i\mathbf{G}.\mathbf{r}} \tag{2.31}$$

where G indicates the reciprocal lattice vector (with **G.T** = 2πn, where T is the translation lattice vector in real space and n is an integer.) Using above two equations, we can expand $\phi_n(\mathbf{r})$ as the sum of plane waves as shown below.

$$\phi_{n\mathbf{k}}(\mathbf{r}) = \frac{1}{V} \sum_G (C_{n,\mathbf{k}+\mathbf{G}}) e^{i(\mathbf{k}+\mathbf{G}).\mathbf{r}} \tag{2.32}$$

First challenge is to describe the given wave function in terms of limited number of plain wave basis. Ideally one should consider infinite number of plane wave basis. In order to limit the number of basis needed to describe the wavefunction, a cutoff is decided based on the radial distribution of an orbital. In practice G_{max} cutoff is done by setting a cutoff kinetic

energy (E_{cut}) as:

$$E_{cut} = \frac{\hbar^2 G_{max}^2}{2m} \tag{2.33}$$

With the fixed cutoff, the KS orbitals can be expressed in terms of finite number of plain wave basis.

$$\phi_{n\mathbf{k}}(r) = \frac{1}{V} \sum_{|\mathbf{k}+\mathbf{G}|<G_{max}} (C_{n,\mathbf{k}+\mathbf{G}}) e^{i(\mathbf{k}+\mathbf{G}).\mathbf{r}} \tag{2.34}$$

2.3.2 k-point sampling

In order to sample the irreducible Brillouin zone (BZ) and determine physical parameters such as total energy, numerical integrations utilising an infinite number of k-points are required. In actuality, we are limited to using a small number of k-points for computations by choosing specific k-points within BZ. We used the approach described by Monkhorst $et\ al.$ in this thesis to assemble a k-point finite grid. This technique produces k-points evenly dispersed throughout the BZ [92].

$$k_j = x_{1j} b_1 + x_{2j} b_2 + x_{3j} b_3 \tag{2.35}$$

where b_i represents reciprocal lattice vector and

$$x_{ij} = \frac{(2j - q - 1)}{2q}, j = 1, 2, 3, ..., q \tag{2.36}$$

where q is an integer which determines the size of set of k-points.

2.3.3 Pseudopotentials

Bonding between any atoms is governed by its valence electrons and the core electrons do not take part in the reaction. Thus, ignoring the core electrons will be computationally efficient without affecting the accuracy of the calculation. The radial part of the orbital wave function can be of many forms as shown in the Figure 2.2. The wave function could have multiple nodes or fast oscillation in the region very close to nuclei where no reaction is taking place.

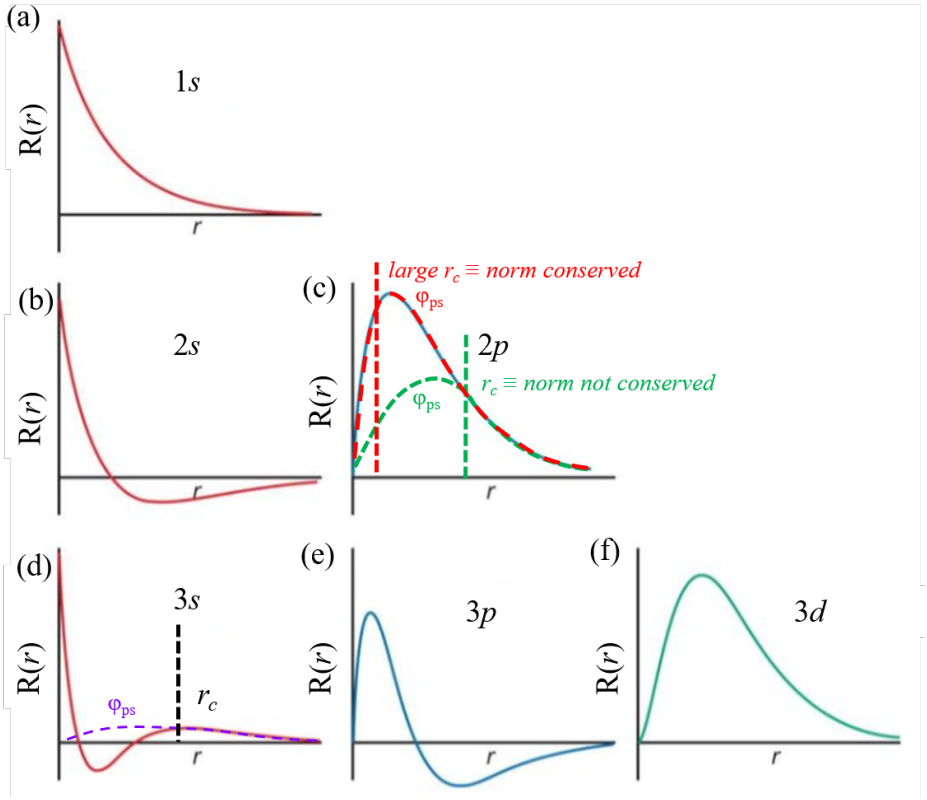

Figure 2.2: Radial wave functions

It is the exponentially decaying tail of the wavefunctions of the individual atoms that overlap with each other and get modified. Representing the full radial part of a wavefunction in terms of plain wave basis will require E_{cut}. The concept of pseudopotentials is to replace the exact coulomb potential with a alternate potential which will produce a wave function exactly like the real one beyond a cutoff r_c and have a smooth form with no oscillation near the nuclei (see Figure 2.2d). In such case a low kinetic energy cutoff is required. In the calculation, two types of pseudopotentials are used: (a) norm-conserving and (b) ultrasoft [93, 94]. The former require that the condition of Norm-conservation needs to be satisfied. It is given as:

$$\int_0^{r_c} \phi_{ae}(\mathbf{r})^* \phi_{ae}(\mathbf{r}) d\mathbf{r} = \int_0^{r_c} \phi_{ps}(\mathbf{r})^* \phi_{ps}(\mathbf{r}) d\mathbf{r} \tag{2.37}$$

The norm-conservation is very efficient for orbitals having multiple nodes but require high E_{cut} in case of orbitals with no nodes like 1s, 2p, 3d, 4f etc. To further lower the kinetic energy cutoff, beyond norm-conservation approach was taken by Vanderbilt to create ultrasoft pseudopotential which has no constrain of norm conservation as shown in the Figure 2.2c. But without the constrain an additional term is added in the charge density, which is augmented charge localized close to nucleus that account for the missing norm. The new expression for charge density becomes:

$$n(\mathbf{r}) = \sum_{i=1}^{n} \phi_i(\mathbf{r})^* \phi_i(\mathbf{r}) d\mathbf{r} + n^{aug}(\mathbf{r}) \tag{2.38}$$

As a result, a large kinetic energy cutoff for the density has to be used for accurate calculation.

2.4 Lattice dynamics from electronic-structure theory

The fundamental approximation that enables the separation of vibrational and electronic degrees of freedom in a solid is the adiabatic approximation proposed by Born and Oppenheimer in 1927. In this framework, the lattice-dynamical properties of a system are governed by the eigenvalues ξ and eigenfunctions Ψ of the Schrodinger equation:

$$\left(-\sum_{I} \frac{\hbar^2}{2M_I} \frac{d^2}{d\mathbf{R}_I^2} + E(\mathbf{R}) \right) \Psi(\mathbf{R}) = \xi \Psi(\mathbf{R}) \tag{2.39}$$

where $\mathbf{R}_I$ is the position of I^{th} nucleus , M_I the mass, and $E(\mathbf{R})$ the clamped-ion energy of the system, which is sometimes referred to as the Born-Oppenheimer energy surface. It has been discussed in the previous section that position of the nuclei ($\mathbf{R}_I$) changes the energy surface. The system will be in equilibrium if forces (F_I) on individual nuclei vanishes

$$\mathbf{F}_I = -\frac{dE(\mathbf{R})}{d\mathbf{R}_I} = 0 \tag{2.40}$$

whereas the vibrational frequencies ω are determined by the eigenvalues of the Hessian of

the Born- Oppenheimer energy, scaled by the nuclear masses:

$$\det \left| \frac{1}{\sqrt{M_I M_J}} \frac{\partial^2 E(\boldsymbol{R})}{\partial \boldsymbol{R}_I \partial \boldsymbol{R}_J} - \omega^2 \delta_{IJ} \right| = 0 \tag{2.41}$$

Solving this equation yields the phonon frequencies ω and their associated eigenvectors, which describe vibrational modes of the lattice.

The calculation of the equilibrium geometry and of the vibrational properties of a system thus, amounts to computing the first and second derivatives of its Born-Oppenheimer energy surface. One of the most important tools to achieve this goal is the **Hellmann-Feynman theorem**. The first derivative of eigenvalue of a Hamiltonian, H_λ which is dependent on some parameter λ, is given by the expectation value of the derivative of the Hamiltonian.

$$\frac{E_\lambda}{d\lambda} = \left\langle \Psi_\lambda \left| \frac{dH_\lambda}{d\lambda} \right| \Psi_\lambda \right\rangle \tag{2.42}$$

here Ψ_λ is the nuclear eigenfunction with eigenvalue E_λ.

With BO approximation, nuclear positions act as parameters in the electronic Hamiltonian (H_o) The force on the I^{th} nucleus in the electronic ground state is thus

$$\mathbf{F}_I = -\frac{dE(\mathbf{R})}{d\mathbf{R}_I} = -\left\langle \psi(\mathbf{r}, \mathbf{R}) \left| \frac{dH_o}{d\mathbf{R}_I} \right| \psi(\mathbf{r}, \mathbf{R}) \right\rangle \tag{2.43}$$

The wave function $\psi(\mathbf{r}, \mathbf{R})$, is dependent on position of ions through electron-ion interaction that couples the electronic degree of freedom only through the electron charge density. Solving the above equation will give

$$\mathbf{F}_I = -\int n_{\mathbf{R}}(\mathbf{r}) \frac{dV_{\mathbf{R}}(\mathbf{r})}{d\mathbf{R}_I} dr - \frac{dE_N(\mathbf{R})}{d\mathbf{R}_I} \tag{2.44}$$

where $V_{\mathbf{R}}(\mathbf{r})$ is the electron-nucleus interaction given as:

$$V_{\mathbf{R}}(\mathbf{r}) = -\sum_{iI} \frac{Z_I e^2}{|\mathbf{r}_i - \mathbf{R}_I|} \tag{2.45}$$

$n_{\mathbf{R}}(\mathbf{r})$ is the charge density for nuclear configuration $\mathbf{R}$, and $E_N(\mathbf{R})$ the electrostatic interaction between nuclei. Now further derivation of the force will give:

$$-\frac{d\mathbf{F}_I}{d\mathbf{R}_I} = \frac{d^2E(\mathbf{R})}{d\mathbf{R}_I d\mathbf{R}_J} = \int \frac{dn_{\mathbf{R}}(\mathbf{r})}{d\mathbf{R}_J}\frac{dV_{\mathbf{R}}(\mathbf{r})}{d\mathbf{R}_I}dr + \int n_{\mathbf{R}}(\mathbf{r})\frac{d^2V_{\mathbf{R}}(\mathbf{r})}{d\mathbf{R}_I d\mathbf{R}_J}dr + \frac{d^2E_N(\mathbf{R})}{d\mathbf{R}_I d\mathbf{R}_J} \tag{2.46}$$

Above equation states that to calculate the Hessian of Born-Oppenheimer energy surface requires the calculation of ground-state electron charge density ($n_{\mathbf{R}}(\mathbf{r})$) along with its liner response to a distortion of the nuclear geometry, $dn_{\mathbf{R}}(\mathbf{r})/d\mathbf{R}_J$ [95, 96].

The calculation of the linear response is done using a well defined procedure called **density functional perturbation theory** (DFPT). The charge density response can be evaluated by linearizing electron density as:

$$\Delta n(\mathbf{r}) = 4Re\sum_{n=1}^{N/2}\psi_n^*(\mathbf{r})\Delta\psi_n(\mathbf{r}) \tag{2.47}$$

The finite difference operator is defined as:

$$\Delta^{\lambda}F = \sum_i \frac{\partial F_\lambda}{\partial\lambda_i}\Delta\lambda_i \tag{2.48}$$

λ was removed from the expression 2.48 for simplicity.

The variation of the Kohn-Sham orbitals, $\Delta\psi_n(\mathbf{r})$, is obtained by standard first-order perturbation theory [97]:

$$(H_{SCF} - \epsilon_n)|\Delta\psi_n > \ = -(\Delta V_{SCF} - \Delta\epsilon_n)|\psi_n > \tag{2.49}$$

where

$$H_{SCF} = -\frac{\hbar^2}{2m}\frac{\partial^2}{\partial\mathbf{r}^2} + V_{SCF}(\mathbf{r}) \tag{2.50}$$

is the unperturbed Kohn-Sham Hamiltonian. Expression 2.49 is known as Sternheimer equation. The first term of the equation represents how the unperturbed system acts on the per-

turbed wavefunction. In other words, how much change in energy because of the perturbed wavefunction.

The first-order correction to self-consistent potential is given as:

$$\Delta V_{SCF}(\mathbf{r}) = \Delta V(\mathbf{r}) + e^2 \int \frac{\Delta n(\mathbf{r}')}{|\mathbf{r} - \mathbf{r}'|} d\mathbf{r}' + \left(\frac{dv_{xc}(n)}{dn} \right)_{n=n(\mathbf{r})} \Delta n(\mathbf{r}) \tag{2.51}$$

and

$$\Delta \epsilon_n = < \psi_n | \Delta V_{SCF} | \psi_n > \tag{2.52}$$

is the first-order variation of Kohn-Sham eigenvalue ϵ_n. The above set of equations for the perturbed system is completely analogous to unperturbed self-consistent Kohn-Sham equations. The full details of the analogy can be found in reference [98].

2.5 Electron Transport calculation

To gain insight of the transport properties of real materials, Boltzmann theory is proved to be a useful tool. The electrical current (j) in a material in the presence of electric field (E), magnetic field (B), and thermal gradient (∇T) can be written in terms of conductivity tensors (σ) as:

$$j_i = \sigma_{ij} E_j + \sigma_{ijk} E_j B_k + \nu_{ij} \nabla_j T + ... \tag{2.53}$$

First term in the right hand side of the expression represents the Ohm's law, a liner response to the applied electric field. Second represents magnetoresistance or Hall effect. Third term is the thermoelectric term where contribution in current is because of temperature gradient and the coefficient ν_{ij} is Seebeck or Nernst coefficient. The conductivity tensor is a function of group velocity (υ) and relaxation time (τ), given as:

$$\sigma_{\alpha\beta}(i, \mathbf{k}) = e^2 \tau_{i,\mathbf{k}} \upsilon_\alpha(i, \mathbf{k}) \upsilon_\beta(i, \mathbf{k}) \tag{2.54}$$

where $\tau_{i,\mathbf{k}}$ is the relaxation time of electrons with band index i and state $\mathbf{k}$ (crystal momentum).The group velocity along α-direction can be computed from electronic band structure as:

$$\upsilon_\alpha(i,\mathbf{k}) = \frac{1}{\hbar}\frac{\partial \epsilon_{i,\mathbf{k}}}{\partial k_\alpha} \tag{2.55}$$

Now, the only remaining quantity is the relaxation time which depends on several factors. τ is dependent on the electron scattering mechanism such as, electron-phonon, point defect, alloy scattering etc. It will be much easier to estimate the relaxation time after estimating the transport properties assuming the τ to be constant. This approximation is generally called Constant Relaxation time approximation (CRTA). We can also write the conductivity tensor in terms of energy by projecting the density of states with conductivity tensor as follows.

$$\sigma_{\alpha\beta}(\epsilon) = \frac{1}{N}\sum_{i,\mathbf{k}} \sigma_{\alpha\beta}(i,\mathbf{k})\frac{\delta(\epsilon - \epsilon_{i,\mathbf{k}})}{\partial\epsilon} \tag{2.56}$$

This is called transport distribution function. All the transport coefficients like conductivity (σ), Seebeck coefficient (S), and electronic thermal conductivity (κ) can be written as a function of chemical potential (μ) and temperature (T) as [99]:

$$\sigma_{\alpha\beta}(\mu,T) = \frac{1}{V}\int \sigma_{\alpha\beta}(\epsilon)\left[\frac{-\partial f_o(\epsilon,\mu,T)}{\partial\epsilon}\right]d\epsilon \tag{2.57}$$

$$S_{\alpha\beta}(\mu,T) = \frac{1}{eT\sigma_{\alpha\beta}(\mu,T)}\int \sigma_{\alpha\beta}(\epsilon)(\epsilon-\mu)\left[\frac{-\partial f_o(\epsilon,\mu,T)}{\partial\epsilon}\right]d\epsilon \tag{2.58}$$

$$\kappa_{\alpha\beta}(\mu,T) = \frac{1}{e^2TV}\int \sigma_{\alpha\beta}(\epsilon)(\epsilon-\mu)^2\left[\frac{-\partial f_o(\epsilon,\mu,T)}{\partial\epsilon}\right]d\epsilon \tag{2.59}$$

where f_o is the Fermi Dirac occupation, V indicates the volume of the unit cell. The absolute value of conductivity and thermal conductivity can be calculate by explicitly calculating relaxation time.

2.6 Phonon Transport calculation

Lattice thermal conductivity is related the phonon transport. A general form of κ_l can be expressed as:

$$\kappa_l = \frac{1}{3\Omega N_0} \sum_{qs} v_{qs}^2 \tau_{qs} \hbar \omega_{qs} \frac{\partial n_{qs}}{\partial T} \tag{2.60}$$

where ω is volume of unit cell, N_0 is the number of unit cell, $\sum_{qs}$ is summation over all phonon wavevectors q and phonon branches s, τ_{qs} is the relaxation time (lifetime) of the phonon mode (q, s), ω_{qs} is the phonon frequency, and $\frac{\partial n_{qs}}{\partial T}$ is the derivative of the Bose-Einstein phonon distribution with respect to temperature. In a more simplified expression of κ_l, it dependent on the specific heat (C), sound velocity (υ_s) and mean free path (l) or phonon relaxation time (τ_q) as:

$$\kappa_l = \frac{1}{3} C \upsilon_s l = \frac{1}{3} C \upsilon_s^2 \tau_q \tag{2.61}$$

The relaxation time or mean free path depends on the scattering mechanism of phonon. So by solving Boltzmann transport equation for phonon, lattice thermal conductivity can be estimated [100–103]. One of the most effective scattering mechanisms found at high temperature is the phonon-phonon scattering also known as 3 Phonon (3P) process. The next segment will briefly discuss the 3P process.

3 Phonon process (3P)

Heat carried by the phonon (lattice thermal conductivity) is highly dependent on the transport of phonon in the system. There are several scattering mechanisms like phonon-phonon scattering, electron-phonon scattering, phonon-impurity scattering, phonon-boundary scattering. Phonon-phonon scattering is the intrinsic mechanism present for all the system. All process require involvement of 3 phonon, therefore termed as 3 phonon process.

Figure 2.3 shows the two possibilities of the 3P process. The three phonon wave vectors are represented as q, q', and q''. The scattering of phonon that result in resultant wave vector within the BZ ($q + q' = q''$) is called Normal (N) Process. In the N-process the crystal

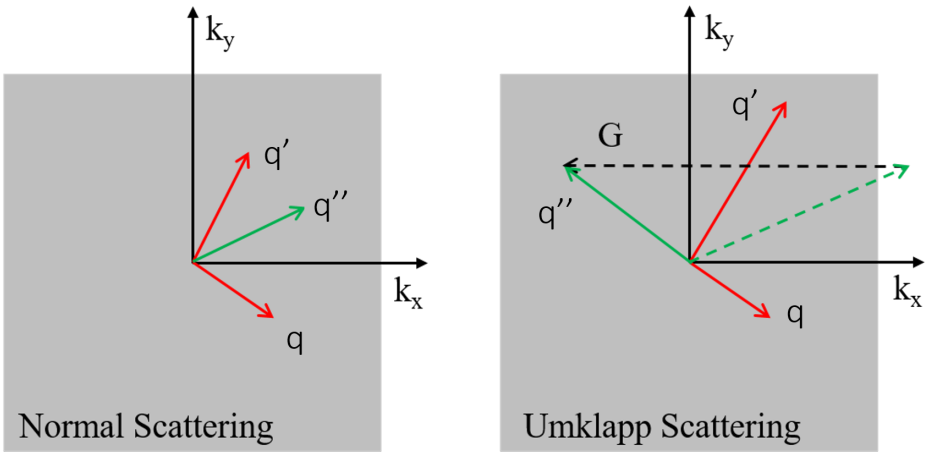

Figure 2.3: (a) Normal scattering process and (b) Umklapp scattering process

momentum is conserved. The other case is Umklapp (U) process where the wave vector of the scattered phonon lie outside the BZ is mapped into the BZ because of periodicity of the system ($q + q' = G + q''$). In this case the crystal momentum is not conserved. The relaxation time of phonon undergoing the 3P process can be calculated by solving the Boltzmann transport equation where phonon properties including frequencies, velocities, and scattering rates are determined by inter-atomic force constants. Here no relaxation time approximation is considered. The relaxation time can be calculated using the third order force constant implemented using phono3py package [104, 105]. The detailed theory of calculation method is given in by Laurent Chaput [106].

Calculations using Slack's Model

An alternate method to estimate the lattice thermal conductivity is using Slack's equation [107]. It is a phenomenological approach to estimate κ_l^0. The model assumes only the contribution from acoustic phonon modes. The mathematical formulae used were:

$$\kappa_l^0 = A\frac{\Theta_D^3 V_a^{1/3} m_{av}}{\gamma^2 n^{2/3} T}, \tag{2.62}$$

where Θ_D, V_a, m_{av}, γ and n are the Debye temperature, the volume per atom (in Å), average atomic mass (in amu), the Gruneisen parameter and n is number of atoms in unit cell. Each parameters can be estimated as:

$$A = \frac{2.43 \times 10^{-6}}{1 - \frac{0.514}{\gamma} + \frac{0.228}{\gamma^2}} \tag{2.63}$$

$$\Theta_D = \frac{\hbar}{k_B} v_{av} \left(\frac{6\pi^2 n}{V}\right)^{\frac{1}{3}} \tag{2.64}$$

where V is the lattice volume, v_{av} is the average sound velocity which can be estimated from longitude and transverse velocities v_L and v_T which depend on Bulk (B_H) modulus, Shear modulus (G_H) and material densities (ρ). v_{av} can be computed using the following equations:

$$v_L = \left[\frac{B_H + (4/3)G_H}{\rho}\right]^{1/2}, v_T = \left[\frac{G_H}{\rho}\right]^{1/2} \tag{2.65}$$

$$v_{av} = \left[\frac{1}{3}\left(\frac{1}{v_L^3} + \frac{2}{v_T^3}\right)\right]^{-1/3} \tag{2.66}$$

The Gruneisen parameter (γ) estimation can be done as:

$$\gamma = \frac{3}{2}\left(\frac{1+u}{2-3u}\right), \tag{2.67}$$

where u, the Poisson ratio is given as:

$$u = \frac{1 - 2\left(\frac{v_T}{v_L}\right)^2}{2 - 2\left(\frac{v_T}{v_L}\right)^2} \tag{2.68}$$

So far, any defect in the system has not been considered. In the practical scenario, effect like grain boundary (GB) and point defect (PD) play an important role in scattering phonon and reducing κ_l. It is important to discuss a few methods to incorporate the effect on the κ_l. The contribution of each effect can be included by combining the scattering rates of each factor using Matthiessen's rule:

$$\tau_{tot}^{-1} = \tau_{3P}^{-1} + \tau_{GB}^{-1} + \tau_{PD}^{-1} + ... \tag{2.69}$$

Grain Boundary (GB)

Relaxation time due to GB is dependent on the sound velocity (υ) and size of the grain (L_{GB}).

$$\tau_{GB}^{-1} = \frac{\upsilon}{L_{GB}} \tag{2.70}$$

When the contribution of grain boundary scattering is accounted for in addition to the intrinsic lattice thermal conductivity (κ_L^0), the lattice thermal conductivity, including the effect of the grain boundaries, can be expressed as:

$$\kappa_{GB} = \frac{\kappa_L^0}{1 + \frac{\lambda_{mfp}}{L_{GB}}} \tag{2.71}$$

where λ_{mfp} is the phonon mean free path.

Using a single value for λ_{mfp} is not justified, as phonons can have different velocity, relaxation time, and contribute uneven to the intrinsic lattice thermal conductivity (κ_l^0). The more accurate way is to express the κ_L^0 with respect to λ_{mfp} than use the above expression of each λ_{mfp} and integrating back to obtain κ_{GB} [108]

Point Defect (PD)

Materials with point defect, κ_{PD} is given by $\kappa_l = \eta(T)\kappa_l^0$ where $\eta(T) < 1$ is a temperature-dependent attenuation factor which depends on the nature of defects present in the sample. In an ingot sample, the point defects, e.g., antisite disorder, off-stoichiometry, etc., are more effective in suppressing κ_l. The factor $\eta(T)$ for the point defects can be estimated using the Klemens model [109]:

$$\eta(T) = \left[\left(\frac{\omega}{\omega_D}\right) tan^{-1}\left(\frac{\omega_D}{\omega}\right)\right], \tag{2.72}$$

where κ_l^0 is the lattice thermal conductivity of an idealized lattice or it can be κ_{GB}, after considering GB effect. ω_D is the Debye cut-off frequency and ω is the cut-off due to point defects given by:

$$\omega = \left[\frac{4\gamma^2\omega_D^2 k_B T}{3\pi G_H V_a x_a}\right]^{1/2} \frac{M}{\Delta M}, \tag{2.73}$$

here, G_H, γ, V_a, and x_a represent the shear modulus, the Grüneisen parameter, the volume per atom and the doping concentration per atom in the unit cell, respectively. The mass of the host atom is represented as M, and ΔM represents the mass difference between the host and the dopant.

Chapter 3

Experimental Techniques

The sample synthesized in this thesis are obtained using various synthesis methods. In this chapter we will discuss each synthesis steps one by one. This is followed by a detailed description of the structural characterization techniques, including powder x-ray diffraction and the associate structure refinement technique, Field-emission scanning electron microscopy and associated qualitative elemental analysis using the energy dispersive method, and high-resolution transmission electron microscopy. Subsequently, we describe the various experimental techniques for the measurement of thermoelectric properties.

3.1 Arc melting

A method which uses electric arc to melt the pure elements to make alloys. It is one of the easiest and fastest ways to synthesize alloys, as all the constituent elements are melted together to create ingots. Figure 3.1 displays a arc melting machine on the left, while an interior view is shown on the right. Tungsten tip and copper hearth are subjected to an AC potential of 2000 volts and at least 15 amperes (amp) in order to form an arc. Grooves cast into a copper hearth hold the sample. By adjusting the current, one may control the temperature. The arc melting machine's temperature range is approximately 2300 K to 5000 K, and its current tuning ranges from 15 to 200 amp. A vacuum pump is fitted to the chamber to keep the sample from oxidising while being treated at such a high temperature. The

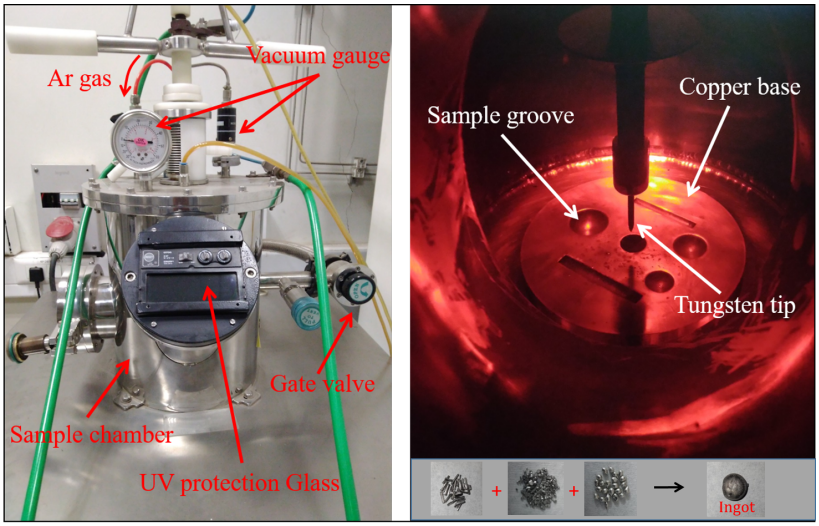

Figure 3.1: Arc melting (let), Inner view of the chamber (right).

environment is rendered inert by argon gas purging the room. Prior to initiating the arc, the chamber is vacuumed and purged five times. Before melting the sample, zirconium price is melted for one minute to ensure that there is no oxygen present. The melted arc ingot from the starting composition is depicted in Figure 3.1(right bottom).

3.2 Ball Milling (BM)

BM is primarily used for mixing and reducing particle size (making fine powder). This step is required mostly to reduce grain size in order to achieve lower thermal conductivity. Furthermore, samples synthesized using arc melting may or may no be pure, in that case BM is used to for homogeneous mixing before further treatment. The ball milling setup consists of a stainless steel jar where the sample is kept with agate or stainless steel balls for milling as shown in Figure 3.2. The loaded jar is then subjected to a high frequency shaker for fine milling. To maintain the grain size uniform for a family of compounds, the mass ratio of balls and sample is kept constant. By changing the mass ratio, frequency and time of milling, the particle size can be tuned. Effect on the transport properties due to grain boundary or grain size can be realized by tuning the size precisely.

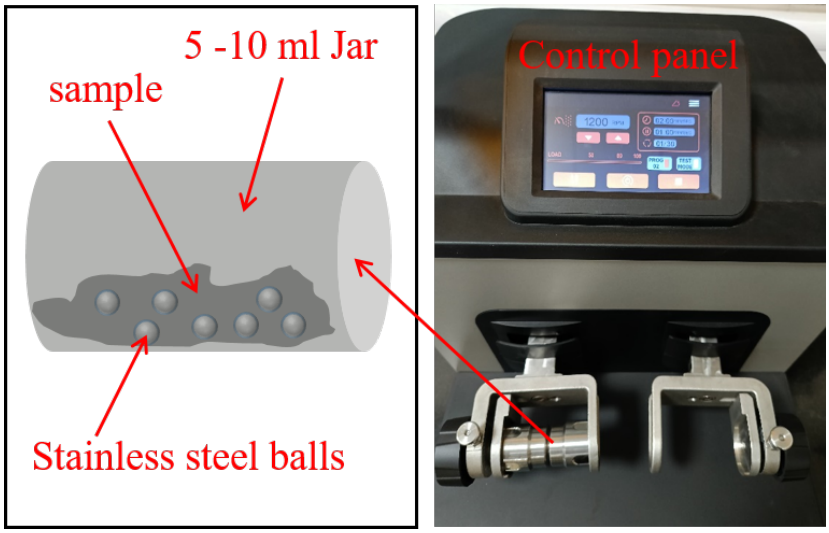

Figure 3.2: The ball milling apparatus used in this work. (Right) An image showing the control panel and the two vibrational arms. The left arm shows the milling jar that holds the material to be milled along with milling balls (a schematic zoomed-in view of the same is shown in the left frame). The right arm of the mill is loaded with an empty jar to counter the weight of the left jars.

3.3 Hot Pressing (HP)

For transport properties to be measured correctly the sample density should be close to its theoretical value. In other words, the porous material will have an additional porosity factor in their transport coefficient and the correct value can not be determined precisely. HP is particularly used for this purpose where arc melted sample is pure. In various cases sintering using HP help sample stabilize in desired phase. It has two important functionalities, one is to apply pressure using a hydraulic press to densify the powder sample into dense pellets, and second maintain desired temperature while applying pressure. Graphite diesets are used to consolidate the sample. The temperature of the die set is maintained by a RF generator by inducing eddy current using water cooled copper coils as shown in the Figure 3.3(right). It provides very rapid heating, and the sintering time is usually 2 to 10 min. The maximum temperature and pressure that could be achieved is 400 MPa and 1600 ^{o}C respectively. Powder samples are loaded into 10 mm diameter die sets which are then kept under the hydraulic press in a vacuum chamber. The temperature of the sample is measured by an attached

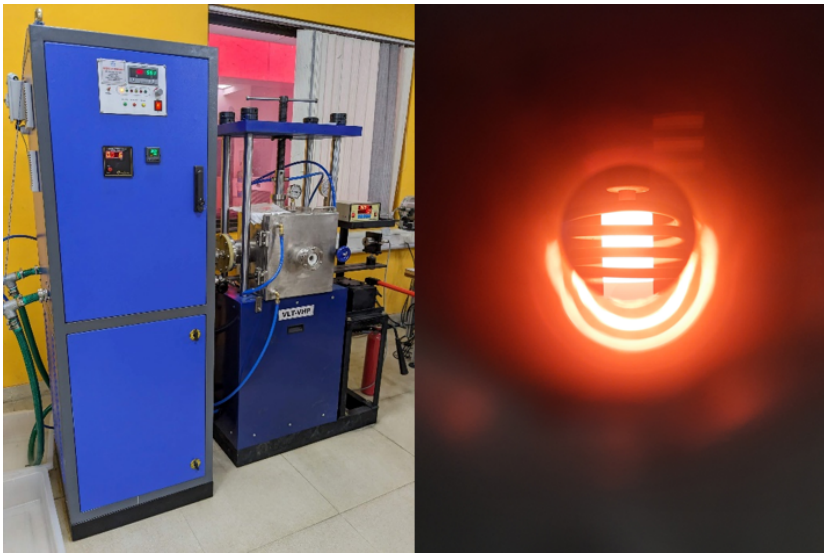

Figure 3.3: Hot Press (let), Heating coils and graphite die inside the chamber (right).

pyrometer.

3.4 Annealing

Most of the alloys form just by arc melting but some need rapid sintering in HP to form in pure phase. Still, there are some alloys that need further long annealing. It is a process of keeping the sample at high temperatures for a long time. Since the synthesized samples are alloys they get oxidized at high temperature, so 10 mm diameter quartz tubes were used to seal them in a dynamic vacuum of 10^{-5} torr pressure. The quartz tubes were preheated for 24 hrs at 900 ^{o}C in order to remove any absorbed moisture. The annealing is usually done for 7 days or more with multiple stages of temperature profiles and is optimized from system to system.

3.5 Post Processing

The shape and size of as synthesized samples can't be used for characterization or measurements. Some post processing is required before further analysis.

cutting and polishing: In order to do electrical conductivity measurement, sample with finite dimension is required as shown in Figure 3.4. The typical dimension of 2 mm $\times$ 3

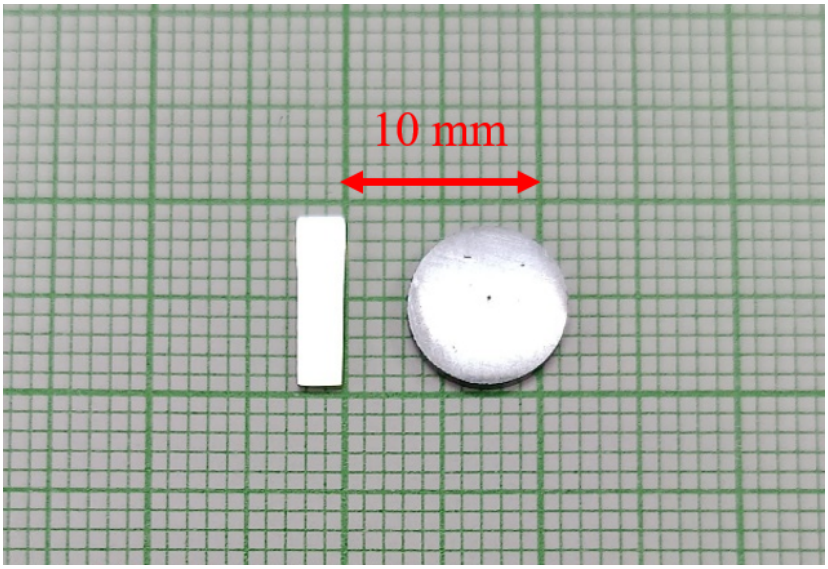

Figure 3.4: Rectangular and disc shaped samples prepared for measuring Resistivity/Seebeck (left), and thermal diffusivity (right).

mm $\times$ 7 mm. For the thermal diffusivity measurement circular sample of 6 mm or 8 mm diameter is required. In order to get better quality data, the thickness of the sample was reduced below 0.5 mm. Fine polishing of the sample surface is needed to get better quality Image from electron microscope.

3.6 Structural Characterization

The purity and final composition of a sample plays a crucial role in the transport properties. This section deals with the techniques used in this thesis for sample structural and compositional characterization.

3.6.1 Powder X-ray diffraction (XRD)

A non-destructive technique that is used to understand the atomic arrangement inside a crystal. It works on the principle of X-ray diffraction by electron clouds of atom to form interference pattern when the atoms are arranged in a periodic manner. The interference pattern usually called X-ray diffraction pattern depends on the crystal structure and orientation. Figure 4.3 shows the X-ray instrument, cartoon of x-ray diffraction and the final data from the

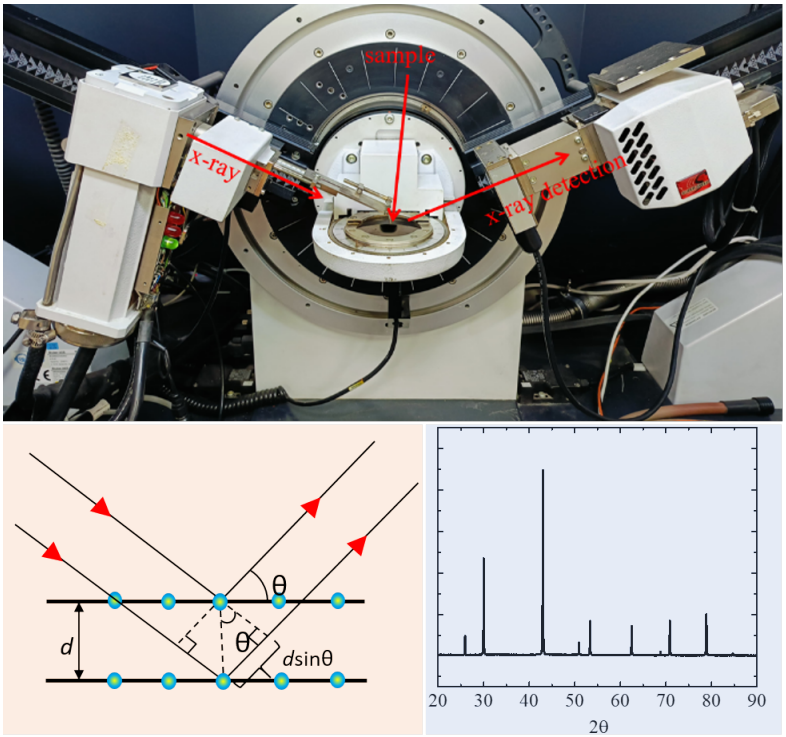

Figure 3.5: X-ray diffraction instrument (top) from IISER Pune central facility, cartoon of the x-ray diffraction (bottom left), and collected data, intensity as a function of 2θ (bottom right).

measurement. The position (angle, 2θ) of the interference depends on the wavelength (λ) of X-ray and the inter planer distance (d) of plains in the crystal. The relation is known as Braggs's law:

$$2dsin\theta = n\lambda \tag{3.1}$$

In addition to crystal structure information, analysis of the XRD pattern reveals many intricate details such as phase purity, strain, grain size, atomic occupation, etc. In-house XRD having X-ray produced by bombarding accelerated electrons on Cu/Fe/Mo targets, will have a low purity detection limit. Impurities below 1% are outside the detection range. Usually synchrotron X-ray is used for further fine detection of impurities. The shape (broadening: Full-width half maxima) and intensity of an XRD peak is related to grain size and occupation of atoms, respectively. Lattice strain due to defects can also change the shape of the peak. Rietveld refinement is done to extract all the structural information. The details are explained here.

Rietveld refinement: Rietveld refinement technique is used to analyze the X-ray diffraction data by fitting it with theoretical model. It works on the principle of one-to-one correspondence between the experimental pattern and theoretical pattern. Since, refinement is about finding the best fit between theoretical and experimental pattern, it is necessary then to quantify the quality of fit. The goodness of fit is determined by three parameters in the refinement process, χ^2, R_{wp}, and R_{exp}. If $Y_{O,i}$ is is the intensity observed at $2\Theta_{O,i}$ with an uncertainty of $\sigma[Y_{O,i}] = \sqrt{\langle(Y_{O,i} - \langle Y_{O,i}\rangle)^2\rangle}$. Similarly, $Y_{C,i}$ is the calculated intensity at $2\Theta_{C,i}$. Then the goodness of fit parameters obtained from the refinement are given by equations below.

$$\chi^2 = \frac{1}{N}\frac{\sum_i w_i(Y_{C,i} - Y_{O,i})^2}{\sigma^2[Y_{O,i}]} \tag{3.2}$$

$$R_{wp} = \frac{\sum_i w_i(Y_{C,i} - Y_{O,i})^2}{\sum_i w_i(Y_{O,i})^2} \tag{3.3}$$

$$R_{exp} = \frac{N}{\sum_i w_i (Y_{O,i})^2} \tag{3.4}$$

where w_i is given by $\frac{1}{\sigma^2[Y_{O,i}]}$. χ^2 can also be written as $\frac{R_{wp}}{R_{exp}}$. And a χ^2 value of ≈ 1 is usually considered to be best quality fit. But the best to confirm the fitting quality of experimental is by visual analysis of fit by plotting the experimental and calculated patterns on the same scale. In that case, even higher values of χ^2, 4 - 5 are acceptable for correctly analyzing the crystal structure.

3.6.2 Electron Microscopy

The optical image resolution depends on the wavelength of the visible light which is not small enough to resolve features in the sample like grain size varying in the range from micron to nm. Using the wave nature of electron when accelerated to high velocity is a best alternative. The electron interaction with matter provide much more information than just imaging. This section deals with two of the most used techniques based on electron microscopy. Following are the common steps used in any electron microscopy techniques:

- Electron generation using a filament or field emission cathode, then accelerated in vacuum using very high electric field for high speed and small de Broglie wavelength.
- The electron beam is focused using electromagnetic lenses onto the desired area.
- The scattered or transmitted electron are detected using electron detector. Furthermore the electron matter interaction produced many more observable quantities which is detected using suitable detectors.

Scanning Electron Microscope (SEM) SEM is a surface scanning probe where sample are usually thick and the electron interacts only with the surface of the specimen. The electron energy is usually between 3 KV to 30 KV. Image magnification of 200 KX is possible with SEM. The samples are mounted onto a aluminium stub using adhesive carbon tape. For non conducting sample, a thin gold layer is deposited to reduce charging effect. Electron iteraction with the sample produces secondary electrons (SE), back scattered electrons

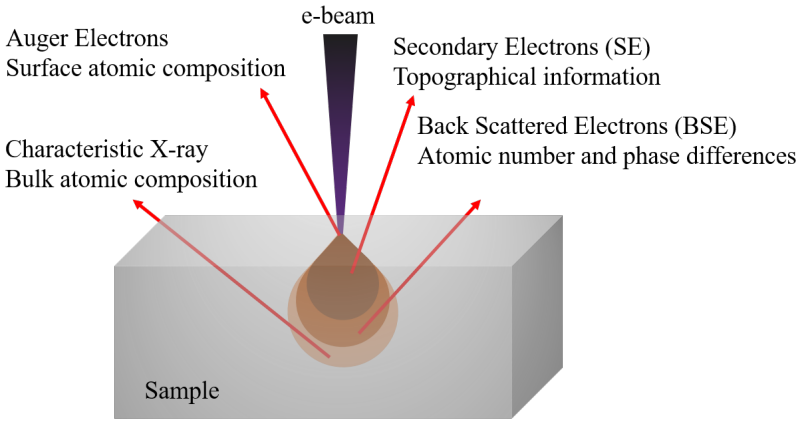

Figure 3.6: The possible outcomes during the interaction of an incident electron beam with the sample in a scanning electron microscope.

(BSEs), X-rays, Auger electrons, and photons etc as shown in the cartoon in the Figure 3.6. Each of the above mentioned quantities have different information. The BSEs electrons are the elastic scattered electrons which has the information of the surface morphology. The SE originate from the atoms of the sample after inelastic interaction of electron beam and sample. They have the information of the atomic constituent of the sample. The colour contrast in the SEM image with different atomic number can be recorder using SE. The x-ray produced have the information of the atomic number as they are characteristic to individual element present in the sample. Analysing the energy and intensity of characteristic X-ray the type and percentage of element present in the sample is determined. It is also known as Energy Dispersive X-ray spectroscopy or EDX.

Transmission Electron Microscope (TEM)

As the name indicates, transmitted electrons are collected and analysed. Additionally, it produced high resolution by using high energy electrons (more than 200 KeV). Figure 3.7 shows the setup (left) and the schematic (right) of TEM. The magnified image of the specimen is collected in the real space where the resolution can be up angstrom. Diffraction pattern can also be captured in the reciprocal space also known as Selected Area Electron Diffraction (SAED) pattern as shown in the Figure 3.7. A fast furrier transformation of the real image will transform into diffraction pattern similar to SAED pattern. In this thesis

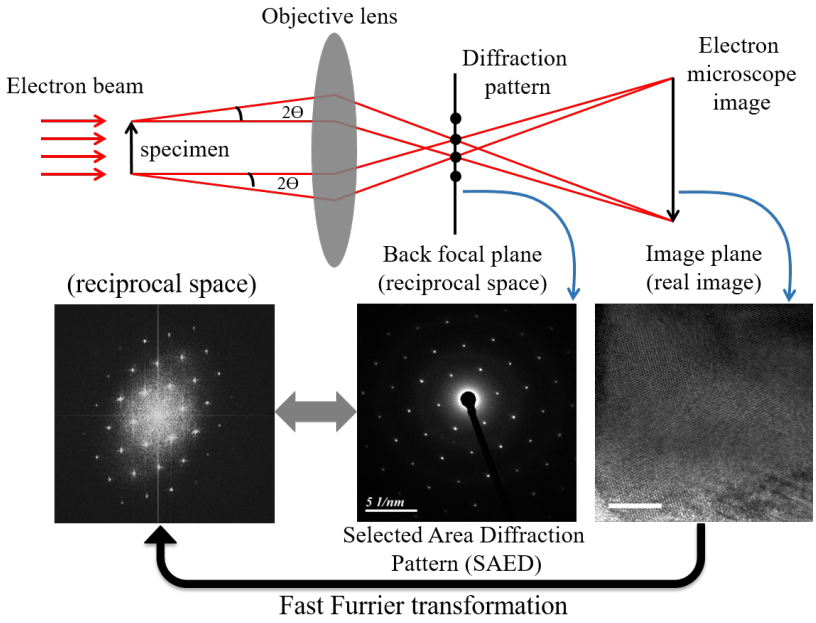

Figure 3.7: Transmission Electron Microscope Schematic diagram (top) represents the electron beam from left passing through lens, sample and collected as diffraction pattern and enhanced real image. Real image along with SAED pattern are shown with correlation between them in the bottom.

work, a free version of GATAN software is used to analyse TEM images.

For the transmission of electron, the sample has to be thin, therefore require special preparation method. Here, we have used drop cast method prepare samples for TEM. Powder samples are dispersed in any organic solvent like, acetone or ethanol and then drop casted on amorphous carbon coated copper grid of 300 mesh size.

3.7 Transport Measurements

3.7.1 Seebeck and Resistivity Measurement

Seebeck and Resistivity measurement is done simultaneously using LSR-3 setup from room temperature to 1000 ^{o}C. The measurement is done in inert atmosphere of He. Figure 3.8 shows the image of sample position and connections for the measurement. The sample is held between two platinum electrodes and two s-type thermocouple connected at the middle. In the Seebeck measurement mode, a platinum heater in the lower electrode generates a tem-

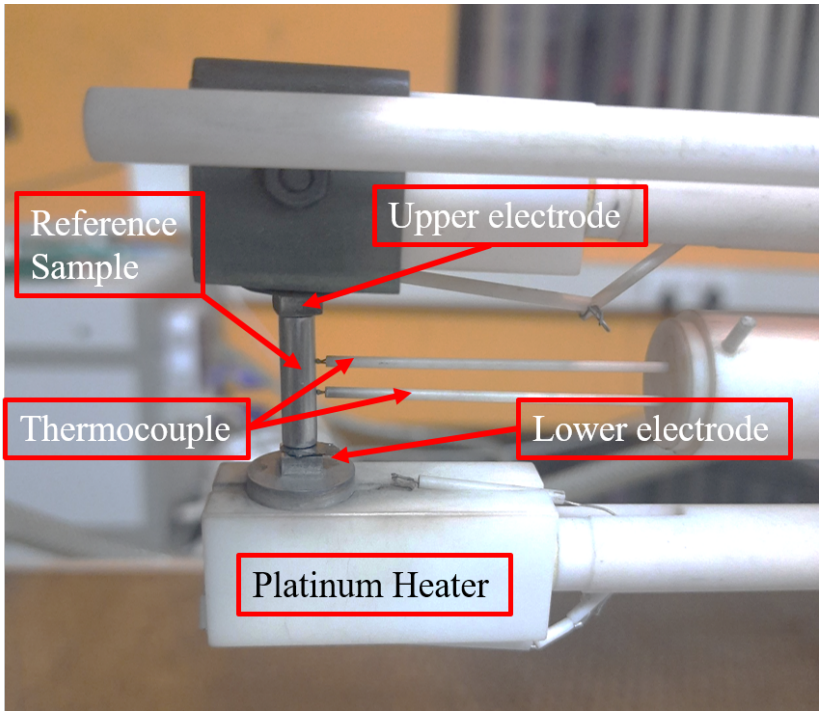

Figure 3.8: Experimental configuration for the simultaneous measurement of electrical resistivity and Seebeck coefficient in a commercial LSR set-up (Linseis, Germany).

perature gradient across the sample. The potential generated across the two thermocouple at the middle due to temperature is recorded which provided the Seebeck coefficient value. Just after the Seebeck measurement the two electrodes produce a constant current across the sample and the thermocouples record the potential drop and with provided sample cross section area and distance between the two probes, resistivity of the sample is measured. This is like a four probe resistivity measurement configuration. LSR-3 setup has a Seebeck measurement range of 1 to 2500 μVK^{-1} with maximum uncertainty of 7%. The conductivity measurement limit is from 0.01 Scm^{-1} to 2$\times$10^{5} Scm^{-1} with maximum error of 7%. LAR-3 setup comes with a standard sample of "Constantan", an alloy of Ni and Copper. The standard sample serve as a benchmark to validate the measured data in case of unreported/new sample.

3.7.2 Thermal Conductivity Measurement

Thermal conductivity is estimated by measuring the thermal diffusivity using laser flash technique. The measurement is done using Laser Flash Analyser (LFA). The setup consists

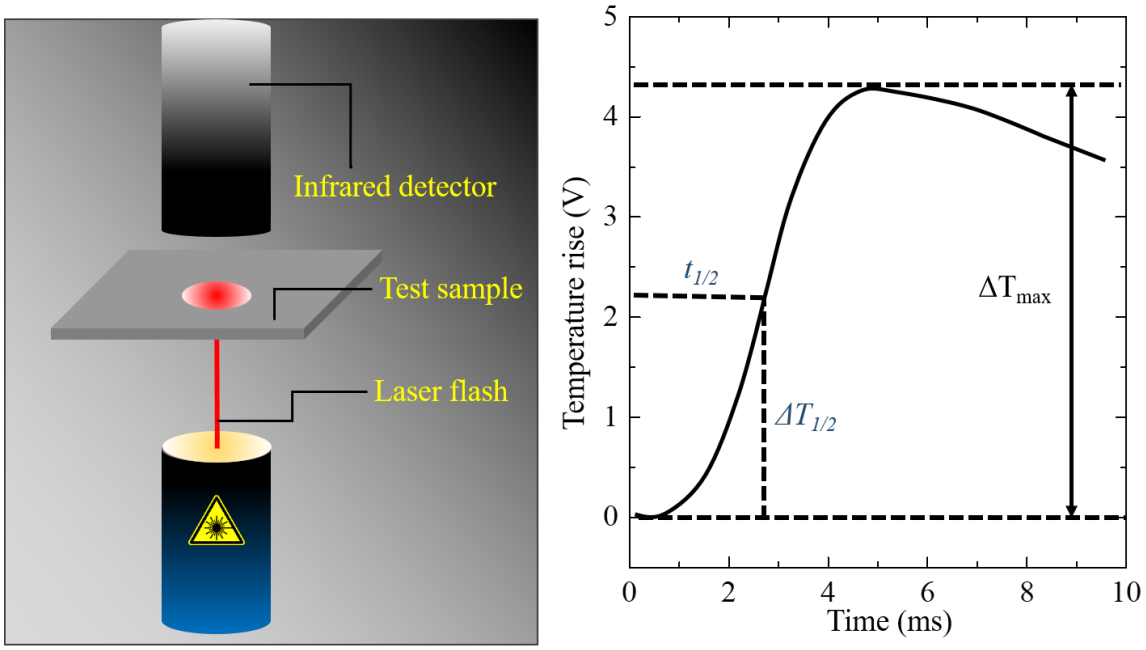

Figure 3.9: LFA working rough sketch (left). The collected signal (right) is shown as a function of time after the laser shot. The $t_{1/2}$ is time required to achieve maximum temperature (ΔT_{max}) at the rear side of the sample.

of a IR pulsed laser focused on the sample from one side. The other side is the IR detector to record the transmitted heat through the sample as a function of time. The Cartoon in Figure 3.9 shows the measurement configuration and obtained data. The diffusivity (d) is estimated using Parker's method given as:

$$d = 0.13879\frac{L^2}{t_{1/2}} \tag{3.5}$$

where L and $t_{1/2}$ is the thickness of the sample. The $t_{1/2}$ depends on the time required to achieve maximum temperature at the rear side of the sample. It is obvious that with increasing thickness, t will increase quadratically.

The thermal conductivity is defined as $\kappa = \rho C_v d$, where ρ and C_v are the material mass density and specific heat.

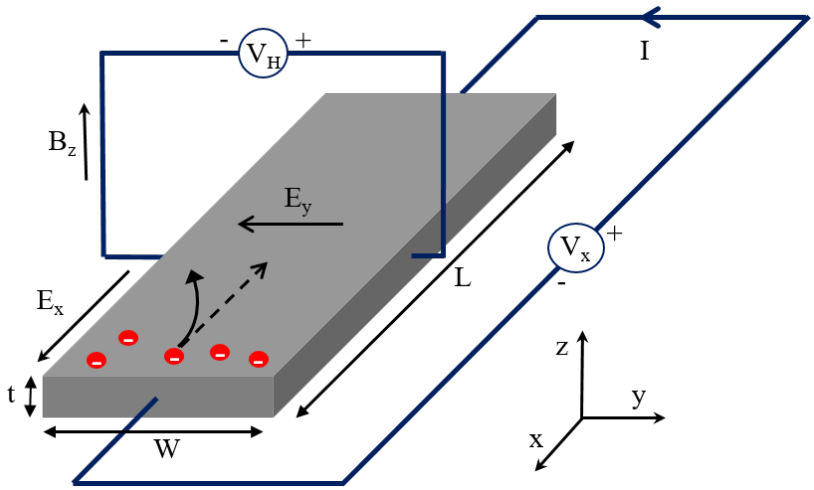

Figure 3.10: Hall measurement schematics (see text for details).

3.7.3 Hall carrier concentration measurement

The actual carrier concentration in a system is a non-measurable quantity. It is possible to get some idea of value using Hall measurement technique therefore called hall carrier concentration (n_H). The method was invented by Edwin Herbert Hall in 1879. Figure 3.10 shows the cartoon of the hall measurement configuration. Sample of thickness t is subjected to constant current I along x direction with a constant magnetic field H along z direction. The electron moving along x-axis will experience a force along y-axis which eventually create voltage across y-axis also called hall voltage (V_H). At the equilibrium the force on the electron due to magnetic field and induced electric filed will be equal. By equating the force the hall voltage can be given as:

$$V_H = \frac{IH}{n_H et} \tag{3.6}$$

Using the above relation, n_H is estimated. For better accuracy the hall voltage is collected as a function of varying magnetic field. The slope of the plot is used to estimate hall carrier concentration. All the carrier concentration measurement in this thesis has been done using our home made Hall setup.

Chapter 4

Band Engineering and Synergistic Modulation Doping for Excellent Thermoelectric Performance in Composites $Ti_{1-x}Nb_xCoSb$ – $Nb_{0.8+\delta}CoSb$

4.1 Introduction

In a recent study, using the density functional theory (DFT)-based ab initio calculations, it was shown that under a compressive strain the valence bands of TiCoSb tend to converge [110], which was confirmed experimentally in a subsequent study [111]. Motivated by these developments, we investigated the effect of tensile or expansive strain on the band structure of TiCoSb. We find that by applying a 10% tensile strain, the bands near the conduction band minimum can be made to converge. Since TiCoSb is intrinsically electron-doped, such a convergence should improve its thermoelectric properties considerably. In experiments, the tensile strain can be produced, for example, by generating a negative chemical

pressure though doping. To test this possibility, we performed electronic band structure calculations with Ti partially substituted with the larger atoms, including Hf, Zr, Nb, and Ta. The Ti-site is chosen for substitution since the electronic states near the conduction band edge of TiCoSb have majority contribution from the Ti d-states [110]. From among the dopants that we examined, the Nb substitution proved to give the best results as far as achieving the desired conduction band convergence is concerned. The full convergence at the conduction band minimum is seen at 25% Nb doping level.

Motivated by the calculated electronic structure, we tried to dope 10% and 15% Nb in TiCoSb experimentally. In both these cases, the arc-melted ingot was found to be phase segregated into phases A and B. While the phase B always turned out to be pure $Nb_{0.8+\delta}CoSb$ ($\delta \leq 0.05$), in phase A $\equiv Ti_{1-x}Nb_xCoSb$, the Nb doping at the Ti site increased from 4.5% to 10%, respectively, from ingot 1 (nominal Nb 10%) to ingot 2 (nominal Nb 15%). Based on these findings, we synthesized a series of composites, $(Ti_{1-x}Nb_xCoSb)_{1-f} \oplus (Nb_{0.8}CoSb)_f$ by arc-melting as discussed under the experimental section. We labelled these composites as: $C_0, C_1, C_2, ..., C_5$. The sample C_0 is pure TiCoSb, which is the control sample. The Nb doping at the Ti site in phase A of our composites gradually increased from 4.5% (C_1) to 22% (C_5) as we increased the quantity of Nb in the starting melt. The composition of phase B, however, remained $Nb_{0.8+\delta}CoSb$ ($\delta \leq 0.05$). It should be pointed out that $Nb_{0.8+\delta}CoSb$ is a well-known 'defective' hH that exhibits a relatively low thermal conductivity due to the presence of Nb vacancies, as is known from the earlier works (see, for example, Ref. [112], [113], [114]). That the quantity of Nb in phase B changes only slightly, consistent with the experimental observation that excess Nb solubility δ in $Nb_{0.8+\delta}CoSb$ is less than 0.05 [112].

Since each Nb atom replacing Ti in TiCoSb dopes an extra electron, the increase in the Nb content of phase A, and at the same time a nearly constant Nb in phase B, implies that from C_0 to C_5, the carrier density (n_A) of phase A gradually builds-up, eventually overwhelming the carrier density (n_B) of phase B. We show that this concentration differential results in 3-D modulation doping, driving excess electrons from phase A into phase B ($n_A > n_B$) or vice-versa ($n_B > n_A$). In particular, for composites with higher Nb doping, the carriers

will be doped from phase A to phase B, thereby, leaving the Fermi level in phase A closer to the conduction band edge. Thus, the Nb doping level in phase A can be raised without increasing the carrier density significantly. This point is important because if the Fermi level in $Ti_{1-x}Nb_xCoSb$ is too high above the conduction band edge, the convergence achieved due to negative chemical pressure will be rendered ineffective. Thus, we show here that through a synergistic combination of band engineering and modulation doping in these composites, we obtained a maximum zT value of 0.81 at 973 K. Further, the temperature variation of zT is shown to exhibit an increasing behaviour with upward curvature, suggesting that even higher zT values can be obtained by extending the measurements to higher temperatures.

4.2 Experimental and computational details

Experimental: Samples were synthesized using the arc-melting technique in an ultra-high-purity argon gas atmosphere. For this purpose, high-purity Ti (Nanoshel 99.95 %), Nb (Sigma Aldrich 99.9%), Co (Sigma Aldrich 99.5%), and Sb (Alfa Aesar 99.9 %)) were used. The precursors were weighed for z = 0, 0.1,..., and 0.5 according to the molar ratio $(TiCoSb)_{1-z}(Nb_{0.8}CoSb)_z$. After melting, the ingots obtained consisted of phases A and B in the ratio A/B $= (1-f)/f$ where A $\equiv Ti_{1-x}Nb_xCoSb$ and B $\equiv Nb_{0.8+\delta}CoSb$, and $f = 0.2z/(0.2-\delta)$ and $x = \delta z/(0.2(z-1)+\delta)$. Here, δ is the amount of excess Nb in $Nb_{0.8+\delta}CoSb$, which is known to have values in the range $0 \leq \delta \leq 0.05$ [112]. The actual values of x were obtained using the EDX analysis. Since the values of δ are small, we used a vs δ plot from Ref. [112] as the calibration to get the values of δ, by using the values of a for phase B from the powder XRD data. The ingots were cut in desired shapes using a low-speed diamond saw for thermoelectric measurements. Powder XRD was done using a Bruker D8 Advance diffractometer. Polished specimens were analyzed using Field Effect Scanning Microscopy (FESEM) technique (Ultra Zeiss plus), equipped with Energy Dispersive x-ray (EDX) analysis probe. The thermopower and resistivity were measured from room-temperature to 973 K using the LSR-3 setup (Linseis) having a maximum uncertainty of 5%. For thermal conductivity (κ) measurements, the LFA-1000 (Linseis) instrument was

used which measures the thermal diffusivity (D) from which the thermal conductivity (κ) is obtained using the formula κ = Dρ_mC$_p$, where ρ_m is samples' mass density that was estimated by measuring the mass and physical dimensions of a rectangular-shaped sample; C$_p$ is the specific heat of the sample, which is taken to be the Dulong-Petit limit ($3nR$). The as-melted samples were free of pores with densities exceeding 93% of theoretical values. The Hall measurements were performed using the highly sensitive lock-in technique. The magnetic field was swept from -10 kOe to +10 kOe and the Hall voltage (V$_H$) was obtained using [V(H) - V(-H)]/2 to eliminate the small, symmetric, MR contribution.

Computational details: Spin-polarized DFT calculations were performed using the Quantum ESPRESSO software [115, 116]. Ultrasoft pseudopotentials were used for valence electron-ion interactions [117]. The valence configurations of $3s^2 3p^6 3d^2 4s^2$, $4s^2 4p^6 4d^2 5s^2$, $5s^2 5p^6 5d^2 6s^2$, $4s^2 4p^6 4d^3 5s^2$, $5s^2 5p^6 5d^3 6s^2$, $3d^8 4s^1$, and $5s^2 5p^3$ had been used for Ti, Zr, Hf, Nb, Ta, Co and Sb, respectively. A kinetic energy cutoff of 55 Ry (550 Ry) had been used to expand the wave function (charge density) in a plane wave basis. Perdew-Burke-Ernzerhof parameterization of the generalized gradient approximation (GGA-PBE) was used to describe the electron-electron exchange and correlation interaction [118]. A 16 $\times$ 16 $\times$ 16 Monkhorst-Pack k-point mesh [92] was used to perform BZ integrations for undoped system. To incorporate the desired doping percentage, a 2$\times$2$\times$2 cubic supercell was considered for which a 8$\times$8$\times$8 Monkhorst-Pack k-point mesh was used for the Brillouin Zone (BZ) integrations. To speed up convergence we have used Marzari-Vanderbilt smearing with a smearing width of 0.005 Ry. The lattice parameters were optimized for the doped systems. To understand the evolution of band structure with various dopings and compare them directly with the undoped one, unfolding of the band structure from the smaller BZ of the supercell onto the bigger BZ of the primitive unit cell was performed using an unfolding method proposed by Boykin [119]. The lattice thermal conductivity was estimated by solving phonon BTE in phono3py [120, 121], which require second and third order force constants. The force constants were calculated using finite-displacement supercell approach. A 2$\times$2$\times$2 supercell was created using python script provided as a part of phono3py package. The atoms were dis-

placed along a particular direction by 0.03Å. Phono3py computes the intrinsic lattice thermal conductivity considering the three-phonon Umklapp and normal processes.

4.3 Results and discussion

4.3.1 Electronic structure and transport

TiCoSb shows a band structure characteristic of an indirect band gap semiconductor with a band gap (E_g) of 0.96 eV, as shown in Figure 4.1a, in agreement with the reported band structure [110]. The valence band maxima (VBM) is located at the Γ-point of the Brillouin zone (BZ) with a second band at the L-point, $\Delta E_V \approx 150$ meV below the VBM. The conduction band minima (CBM), on the other hand, is located at the X-point where a second band can be seen at $\Delta E_C \approx 240$ meV above the CBM. Under a 5% compressive strain, the VBM and the highest occupied state at the L-point become degenerate in energy, resulting in valley degeneracy (Figure 4.1b), which is consistent with earlier work [110]. However, in the case of a tensile strain, which was not previously studied, we find that the higher-lying bands at the X-point tend to converge with the CBM, such that ΔE_C decreases from 240 meV in TiCoSb (unstrained) to 60 meV under a tensile strain of 10% as shown in Figure 4.1c. These results indicate that the application of tensile strain can enhance the transport properties of n-type TiCoSb due to band convergence.

To induce tensile strain experimentally, one can substitute Ti with a larger atom M = Zr, Hf, Nb, or Ta. It should be emphasised that unlike the isovalent dopants Zr and Hf, doping of Nb or Ta at the Ti-site should also result in electron doping. To make the problem computationally tractable, the smallest doping level that we considered here is 12.5%. Depending on the dopant type, the conduction bands at X-point tend to converge by different amounts as shown in Figure 4.2. This is reasonable since the band structure modification under chemical doping depends not only on the steric effect due to ionic size mismatch but also on the electronegativity and ionization energy of the dopants. Typically, doping with an atom with substantially different electronegativity and ionization energy as compared to

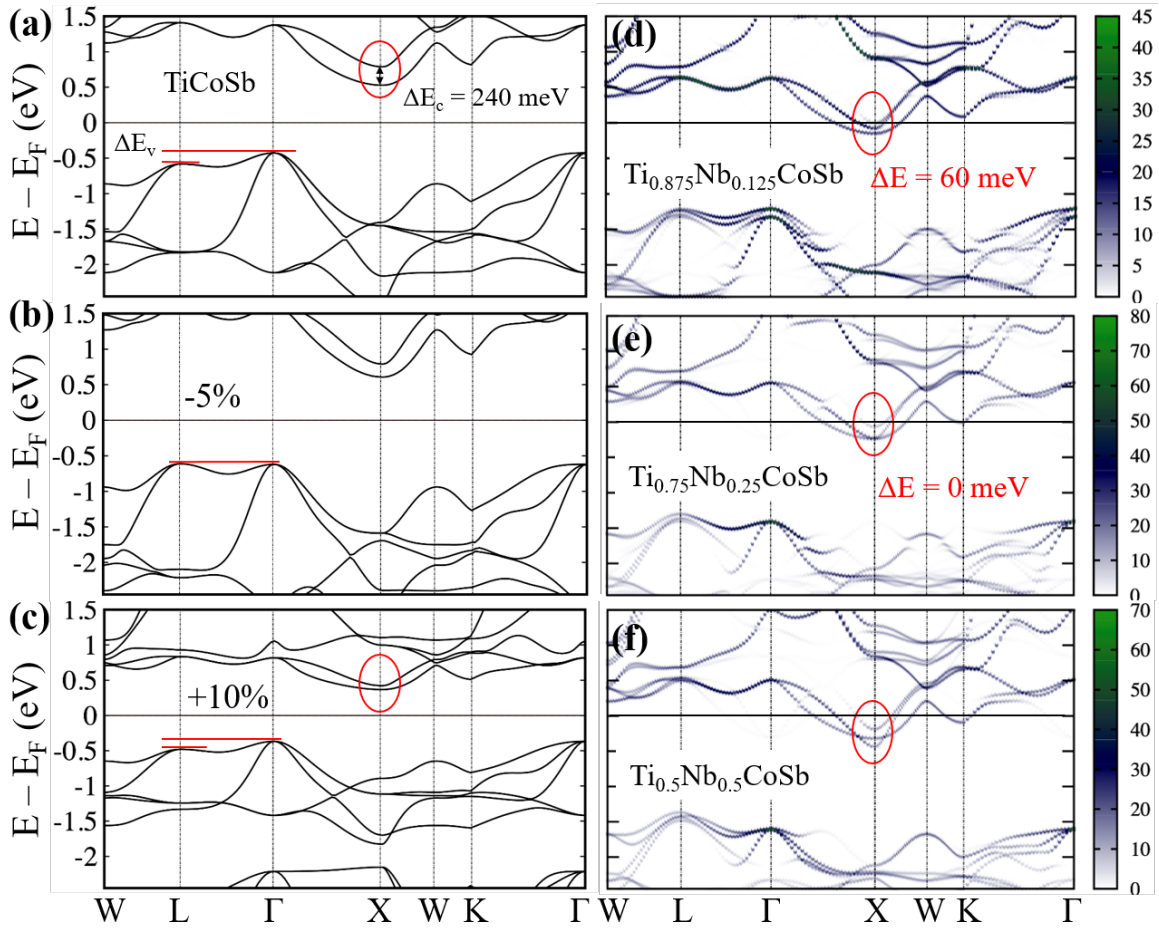

Figure 4.1: Band structure of TiCoSb under different strains: (a) unstrained, (b) under 5 % compressive strain, (c) 10 % tensile strain. (d,e,f) Band structure (Unfolded) of $Ti_{1-x}Nb_xCoSb$ for x = 0.125, 0.25, and 0.5. The scale bar in (d, e and f) is the magnitude (increasing, white-blue-green) of spectral weight, which characterizes the probability of the primitive cell eigenstates contributing to a particular supercell eigenstate of the same energy.

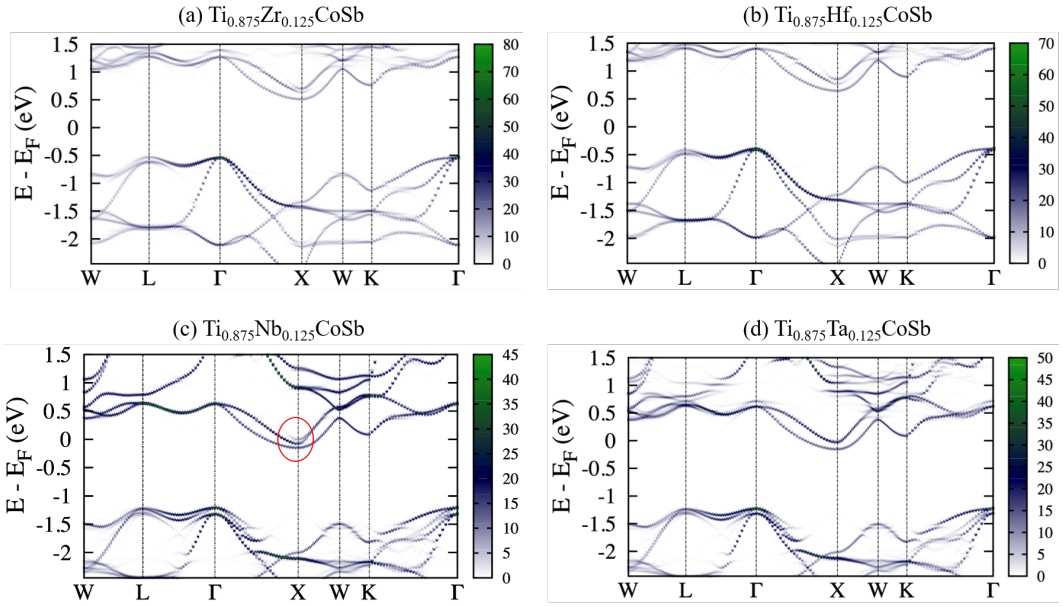

Figure 4.2: Band structure of (a) $Ti_{0.875}Zr_{0.125}CoSb$, (b) $Ti_{0.875}Hf_{0.125}CoSb$, (c)$Ti_{0.875}Nb_{0.125}CoSb$, and (d) $Ti_{0.875}Ta_{0.125}CoSb$.

the host atom can result in a significant band modification without any drastic change in the lattice constant [122]. The case of Nb doping is specifically interesting as Nb is the most electronegative of all the dopants considered here. For 12.5% Nb doping, ΔE_c, which is 240 meV in TiCoSb, reduces to 60 meV in $Ti_{0.875}Nb_{0.125}CoSb$ as shown in Figure 4.1d. The complete band convergence takes place at 25% Nb-doping, as shown in Figure 4.1e. With further increase in Nb-doping, the two bands again separate out but with the upper band becoming the CBM as shown here for the case of 50% Nb-doping in Figure 4.1f. These results suggest that Nb-doping would be an effective strategy to enhance the thermoelectric properties of TiCoSb. Motivated by these findings, we investigate the influence of Nb-doping on the thermoelectric characteristics of TiCoSb experimentally.

4.3.2 Structural characterization

Figure 4.3a shows the powder X-ray diffraction (PXRD) patterns for the composites C_0 to C_5. The pattern for C_0 (TiCoSb) can be indexed satisfactorily based on the cubic hH structure (space group *F-43m*). No detectable extra peaks could be seen, indicating the absence of any

secondary phase(s) in our sample. PXRD patterns for samples C_1 to C_5 are similar to C_0. However, a closer look reveals that each diffraction peak is a superposition of two closely spaced peaks, as shown in the zoomed-in view in the adjacent panel, where the region around the (024) diffraction peak has been expanded, indicating the presence of two hH phases. It should be noted that the diffraction peaks at low 2θ values do not show this splitting clearly, as the angular separation $\Delta\theta$ between the peaks scales with the angle θ as $\tan\theta$. Since $\tan\theta$ is an increasing function of θ, the peaks due to hH phases become well-resolved at higher angles.

The FESEM micrographs further corroborate the presence of two primary phases. A few representative FESEM images for the composites C_1 and C_5 are shown in Figure 4.3c and Figure 4.3e, respectively. The elemental maps for Ti, Nb, Co, and Sb over the scanned area of C_1 and C_5 are shown in Figure 4.3d (C_1) and Figure 4.3f (C_5). Similar elemental maps for the remaining samples are presented in Figures 4.4(a,b,c,d). The FESEM micrographs show the presence of dark and light (grey) regions. Using EDX, these regions are identified as A $\equiv$ ($Ti_{1-x}Nb_x$)CoSb (dark grey) and B $\equiv$ $Nb_{0.8+\delta}CoSb$ (light grey). The composition (x) of Nb in phase A is given in Table. 4.1. The volume fraction f of phase B, is obtained by analyzing the FESEM images using the ImageJ software [123].As x increases from 0 (C_0) to 0.22 (C_5), the value of f increases from 0 to 0.34. In other words, taking composite C_5 as an example, the volume fraction of phase B in C_5 is $\approx$34% and that of A is $\approx$66%, phase A being doped with 22% Nb.

The PXRD peaks are deconvoluted using two Voight line shapes. The peak centred at higher 2θ is due to phase A, and that at lower 2θ due to phase B. This identification is made on the basis of changes in the relative intensities of the two peaks upon going from C_0 to C_5. The intensity of the peak due to phase B gradually increases in agreement with the increase in volume fraction (f) of this phase from C_0 to C_5. Also, note that the position of the peak due to phase A shifts to smaller 2θ values upon going from C_0 to C_5 indicating an increase in the lattice parameter of phase A (a_A) with increasing Nb doping at the Ti-site, which is understandable given that the ionic radius of Nb is larger than that of Ti. The lattice

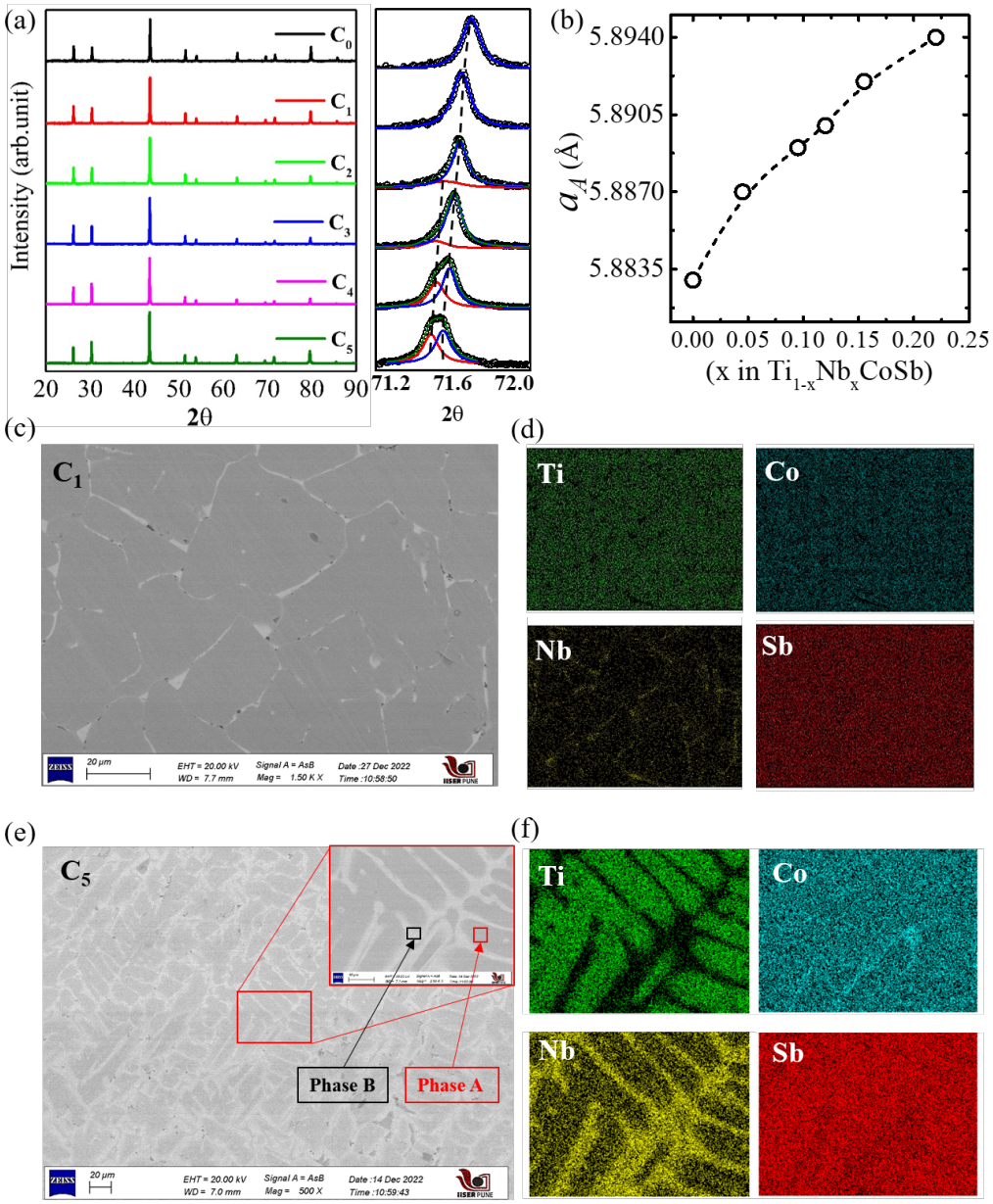

Figure 4.3: (a) Powder XRD of composites C_1, C_2, ..., and C_5. The right panel shows a zoomed-in view of the XRD pattern around the 024 peak. The blue and purple lines represent deconvoluted peaks due to the hH phases A $\equiv Ti_{1-x}Nb_xCoSb$ and B $\equiv Nb_{0.8+\delta}CoSb$. The total intensity is shown using red. The vertical lines trace the position of the 024 peaks due to the two phases and are shown here as a guide to the eye (b) Variation of lattice parameter (a) of phase A as a function of Nb doping x in phase A. (c, e) FESEM micrographs of samples C_1 and C_5 showing the phase segregation. The compositions of the light- and dark-grey regions represent phases A and B whose compositions are given in Table 4.1. (d, f) The elemental chemical maps for Ti, Nb, Co, and Sb are shown corresponding to the FESEM images in (c) and (e), respectively.

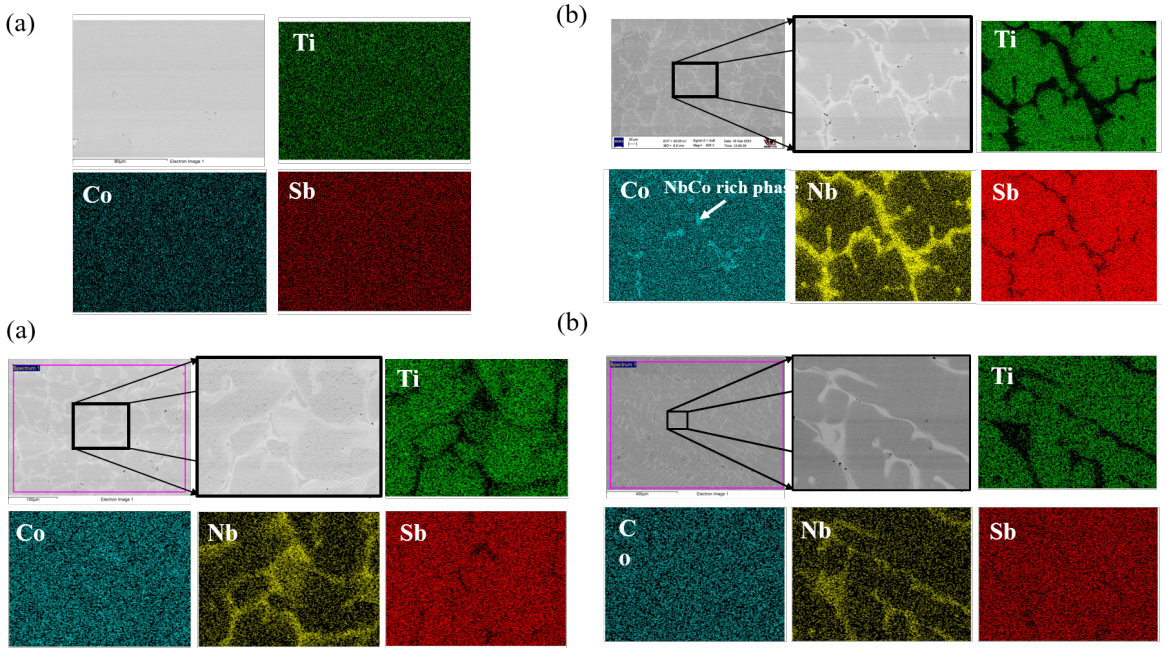

Figure 4.4: FESEM image and chemical mapping of (a,b,c,d) C_0, C_2, C_3, and C_4 respectively.

parameters a_A and a_B are estimated from two-phase refinement using the Highscore plus software. The variation of a_A with x for $Ti_{1-x}Nb_xCoSb$ phase is shown in Figure 4.3b. On the other hand, the position of the peak due to phase B shifts to lower angles by a relatively smaller amount. The lattice parameters (a_A and a_B) for both phases are listed in Table. 4.1. Between C2 and C5, while a_B changes from 5.897 Å to 5.899 Å ($\Delta a_B = 0.002$ Å); over the same range, a_A changes from 5.889 Å to 5.894 Å ($\Delta a_A = 0.005$ Å). From previous work, we know that the lattice parameter of $Nb_{0.8+\delta}CoSb$ increases linearly by an amount 0.01 Å only as δ changes from 0 to 0.05, giving $\Delta a/\Delta\delta \approx 0.2$ [56]. Using this and a vs. δ from Ref. [56], we estimated the value of δ as $\delta \approx 0.03$ for C_2 and 0.04 for C_5. The carrier densities of phase B for these compositions are $\approx 2.4 \times 10^{21}$ cm^{-3} (C_2) and $\approx 3 \times 10^{21}$ cm^{-3} (C_5) [56]. Thus, the carrier concentration between C_2 and C_5 changes by an amount $\approx 0.6 \times 10^{21}$ cm^{-3}. Note that in C_1, the phase fraction of B is rather small and hence a_B was difficult to estimate unambiguously. Therefore in Table. 4.1, the lattice parameter of phase B for this sample is not given.

Table 4.1: Composition (x, f of composites $C_n \equiv (Ti_{1-x}Nb_xCoSb)_{1-f} \oplus (Nb_{0.8}CoSb)_f$); lattice parameters a_A and a_B of phases A $\equiv Ti_{1-x}Nb_xCoSb$ and B $\equiv Nb_{0.8}CoSb$; calculated carrier concentration of phase A (n_{cal}), and the experimentally measured Hall carrier concentration (n_{exp}) of composites C_n.

Sample name	x –	f	a_A (Å)	a_B (Å)	n_{cal} (10^{21} cm^{-3})	n_{exp} (10^{21} cm^{-3})
C_0	0.0	0.0	5.883	–	–	–
C_1	0.045	0.05	5.887	–	0.867	1.30
C_2	0.094	0.114	5.889	5.897	1.80	1.94
C_3	0.12	0.192	5.890	5.898	2.30	2.19
C_4	0.155	0.27	5.892	5.899	2.95	2.48
C_5	0.22	0.343	5.894	5.899	4.20	2.59

4.3.3 Transport properties

Figure 4.5a and Figure 4.5b show the Seebeck coefficient (S) and the electrical conductivity (σ), respectively, for all six samples in the temperature range from 300 K to 973 K. The negative value of S indicates the n-type nature of these composites. TiCoSb (C_0) is intrinsically n-type, possibly due to minor off-stoichiometry leading to self-doping as is typical of small band gap semiconductors. The carrier concentration n of C_0 is $\sim 10^{18}$ cm^{-3}. Its Seebeck coefficient first increases upon heating up to about 600 K and thereafter shows a decreasing behaviour. The peak S value is $-200\ \mu$ V K^{-1} near 600 K. The electrical conductivity for this sample is accordingly small ~ 200 S cm^{-1} showing a weak temperature dependence. A qualitatively similar transport behaviour has been reported previously by Zhou *et al.* [124], but with a higher peak S value of $-350\ \mu$ V K^{-1}, and σ (≈ 100 S cm^{-1}) accordingly less compared to our TiCoSb sample. The difference in the magnitude of S and σ from sample to sample can easily arise due to slight differences in the stoichiometry from one sample to another.

For C_1, a synergistic increase in the Seebeck coefficient and conductivity is observed. The value of S near room temperature increases from $\approx -60\ \mu$ V K^{-1} (C_0) to $\approx -130\ \mu$ V K^{-1}

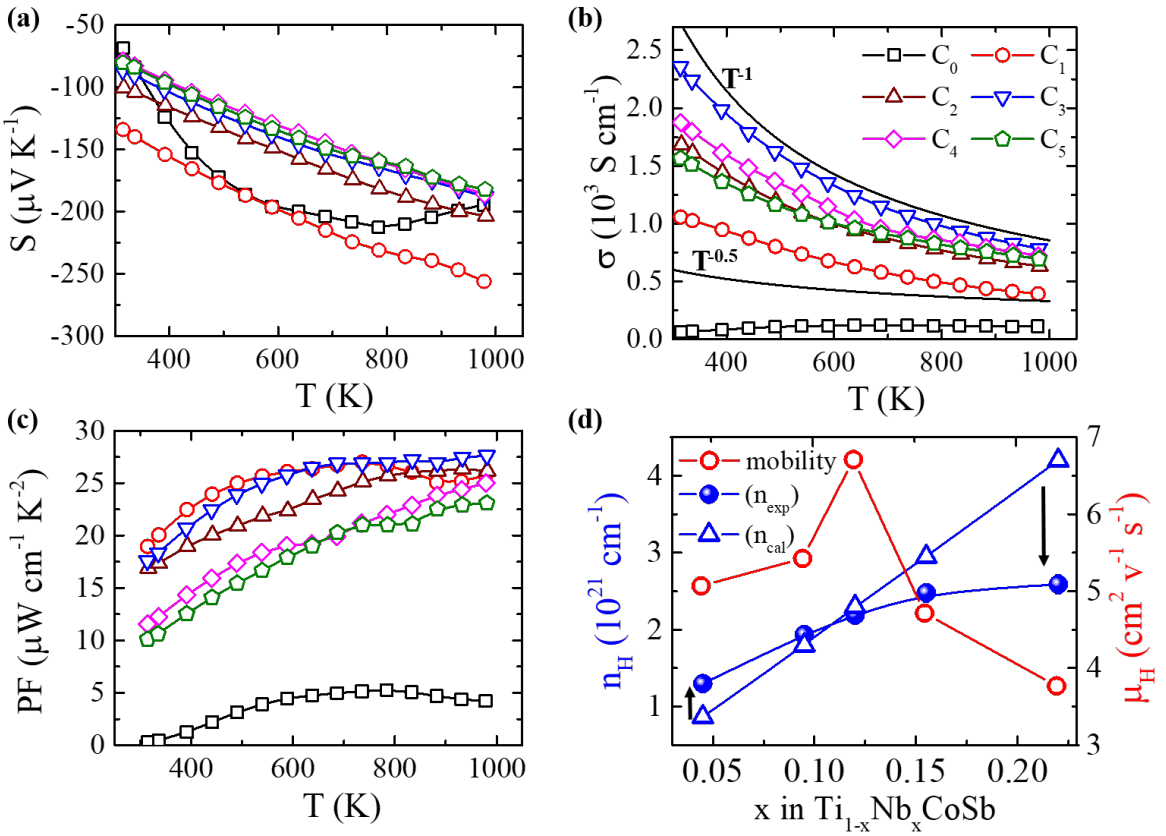

Figure 4.5: The temperature variation of the (a) Seebeck coefficient (S), (b) electrical conductivity (σ), and (c) Power Factor (PF) for the composites C_1, C_2, ..., and C_5. (d) The calculated carrier concentration (n_{cal}) of the phase $Ti_{1-x}Nb_xCoSb$ (open triangle), the experimentally measured Hall carrier concentration (n_{exp}) (blue solid sphere), and the carrier mobility (μ_H) are plotted for various composites at T = 300 K.

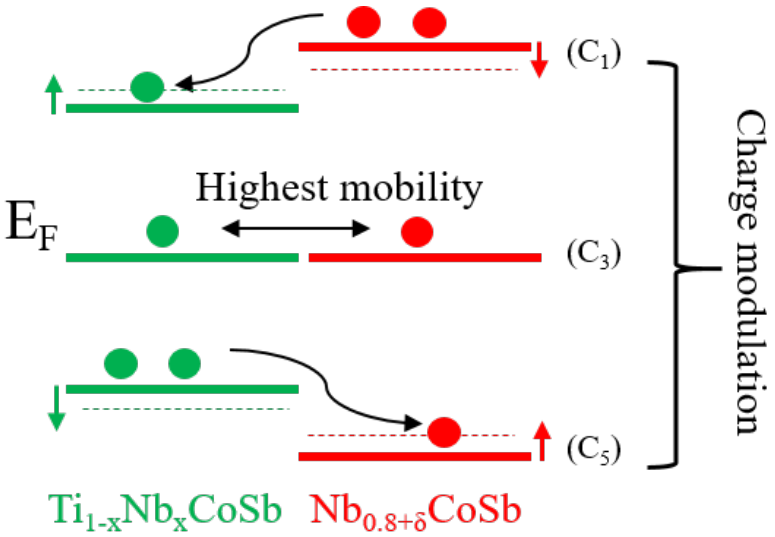

Figure 4.6: A schematic depicting electronic charge transfer between phases A $\equiv$ $Ti_{1-x}Nb_xCoSb$ and B $\equiv$ $Nb_{0.8+\delta}CoSb$. In the composite C_1 (top), the phase B is electron-rich with respect to the phase A, leading to the transfer of electrons from B to A. In C_5 (bottom), the transfer takes place from A to B; and in C_3 (middle), the charge transfer between the two phases is negligible (see text for details). The green and red horizontal lines depict the Fermi levels in the two phases before (bold) and after (dashed) the charge transfer. The red and green vertical arrows depict the shift in the Fermi level upon charge transfer.

(C_1) with a qualitatively changed temperature dependence, characterized by a monotonically increasing behavior up to the highest temperature. Interestingly, σ, which often bears a negative correlation with S, also increases dramatically for C_1, reaching values as high as $1000\ \mathrm{S\ cm^{-1}}$ near room temperature from $< 100\ \mathrm{S\ cm^{-1}}$ for the pristine TiCoSb. This clearly reflects a departure from the commonly observed trend and indicates that along with the increase in the carrier density, the concomitant changes in the band structure upon Nb-doping are also important. Indeed, as shown in Figure 4.1, Nb-doping in TiCoSb enhances the band convergence at the conduction band minimum at point X of the Brillouin zone. σ exhibits a decreasing behaviour with temperature, following approximately a $T^{-\alpha}$ dependence with $0.5 < \alpha < 1$.

A simultaneous increase in both S and σ resulted in a remarkable improvement in the power factor (PF), which increased from a value of less than $5\ \mu\mathrm{W\ cm^{-1}\ K^{-2}}$ (C_0) to $28\ \mu\mathrm{W\ cm^{-1}\ K^{-2}}$ (C_1) at 975 K, i.e., a colossal $\sim$450% increase as shown in Figure 4.5c. A similar increase in σ (and PF) was previously observed using 10% Ta doping at the Ti site [124]. However, unlike the case of Nb-doping where phase segregation occurs, Ta-doping apparently leads to a uniformly doped single-phase sample. This difference is crucial since in the $Ti_{1-x}Ta_xCoSb$ alloys, the electrical conductivity decreases with a further increase in x (i.e., for $x > 0.1$), which can be attributed, at least partly, to the disorder induced by Ta-doping (e.g., $450\ \mathrm{S\ cm^{-1}}$ near 300 K for $x = 0.14$) [124]. However, in the case of Nb-doping, the electrical conductivity increases further, attaining values close to $1900\ \mathrm{S\ cm^{-1}}$ (C_2) and $2300\ \mathrm{S\ cm^{-1}}$ (C_3) near 300 K. These are remarkably high values, which cannot be attained by doping or co-doping Ta, Hf, or Zr [124–126]. Due to increased conductivity, the thermopower of C_2 and C_3 declines slightly to $\approx -100\ \mu\ \mathrm{V\ K^{-1}}$ (C_2) and $\approx -86\ \mu\ \mathrm{V\ K^{-1}}$ (C_3). However, the PF at 300 K remains as high as that of C_1. In fact, above 700 K the PF of C_3 surpasses that of C_1. While this increment is quite nominal, what is important here to note is that the PF of these samples remain high ($\approx 26 - 28\ \mu\mathrm{W\ cm^{-1}\ K^{-2}}$) and almost constant over a very broad temperature range (T > 600 K). In contrast, for the Ta-doped samples the PF drops substantially for $x > 0.1$ (peak PF of $\approx 27\ \mu\mathrm{W\ cm^{-1}\ K^{-2}}$ for

$x = 0.1$ to $\approx 18\ \mu\mathrm{W\ cm^{-1}\ K^{-2}}$ for $x = 0.14$) [126]. For C_4 and C_5, σ decreases slightly to 1875 S cm^{-1} (C_4) and 1560 S cm^{-1} (C_5). The temperature dependence of σ for these samples shows a $T^{-\alpha}$ dependence with α becoming increasingly less than 1 as one moves away from C_3 towards C_5. The PF for these samples has accordingly reduced somewhat: Peak PF $\approx 25\ \mu\mathrm{W\ cm^{-1}\ K^{-2}}$, and $\approx 22\ \mu\mathrm{W\ cm^{-1}\ K^{-2}}$ at 1000 K for C_4, and C_5, respectively.

The variation of Hall carrier concentration ($\mathrm{n_{exp}}$) for these composites is shown in Figure 4.5d. The calculated carrier concentration ($\mathrm{n_{cal}}$) for the main phase (A) $Ti_{1-x}Nb_xCoSb$ as a function of x is also shown.Within the Zintl framework, $\mathrm{n_{cal}}$ due to an aliovalent dopant can be obtained using the formula $\mathrm{Z\Delta_{VEC}/V}$, where Z is the number of formula units per unit cell, V is the unit cell volume, and $\Delta_{\mathrm{VEC}} = (\mathrm{VEC_{Ti_{1-x}Nb_xCoSb}} - 18) = \mathrm{x}$. Had the secondary phase (B) been inert, i.e., acting neither as a donor nor an acceptor, the measured carrier concentration of our composites would have matched $\mathrm{n_{cal}}$. This is generally the case when the secondary phase is either an insulator or a semiconductor with a large band gap such that the Fermi energy in the matrix (phase A) lies in the band gap region of the secondary phase, away from the band edges. On the other hand, if the secondary phase is metallic or a degenerate semiconductor with a relatively smaller band gap, then there is a high possibility that the secondary phase acts either as a donor or an acceptor of carriers, depending on whether its Fermi level lies above or below that of the matrix. In such situations, the carrier concentration of the matrix may increase or decrease due to the 'doping' from the secondary phase. This type of doping is called 3-D modulation doping in analogy with the GaAs-AlGaAs heterostructures [127]. However, as opposed to the GaAs-AlGaAs heterostructures, where the *active* region is physically separated from the ionized dopants; in the composite alloys, the secondary phase is embedded within the main matrix in the form of islands with ionized dopants located mainly at its interface with the matrix. This lowers the carrier mobility somewhat due to the interfacial scattering and charge trapping; nonetheless, it is a useful approach for enhancing the thermoelectric properties, as the scattering from the same concentration of ionized dopants will be much more enhanced if they are doped uniformly in the matrix [127]. In previous works, huge (67%) power factor enhancement has

been reported for the TiNiSn (primary) - MnNiSn (impurity) system via modulation doping, resulting in a peak zT of 0.6 for this system [41]. A similar concept has also been used in other systems including Cu_2Se [128].

We now investigate how n_{exp} and n_{cal} relate to each other in the composites (C_1, C_2, ..., C_5). For C_1, n_{exp} exceeds n_{cal} considerably, but the difference $n_{exp} - n_{cal}$ becomes small for C_2 and even smaller for C_3. In C_4 and C_5, the difference becomes substantial again, but with $n_{exp} < n_{cal}$. n_{exp} in these composites exhibits a tendency towards saturation, hence deviating significantly from n_{cal} which increases linearly with x ($n_{cal} = Z\Delta_{VEC} = Zx$/V). It is interesting to note that despite heavy Nb doping (15% in C_4 and 22% in C_5), the carrier concentration in these samples does not increase but rather saturates. If we consider the two phases individually, then for phase A we expect the carrier concentration to increase with increasing Nb doping (x) as depicted in the variation of n_{cal}. However, as discussed earlier, upon progression from C_0 to C_5, only the volume fraction (f) of phase B increases, whereas the quantity of excess Nb (δ) increases marginally, and hence the carrier concentration of phase B increases by a relatively small amount. In summary, as the quantity of Nb in the initial melt increases, the carrier concentration in phase A increases and eventually overwhelms the carrier concentration in phase B. Thus, C_1, with $n_{cal} < n_{exp}$, represents the scenario where phase B acts as a donor, doping electrons in phase A and hence making $n_{exp} > n_{cal}$. On the other hand, in C_4 and C_5, phase B acts as an acceptor of carriers, removing carriers from the $Ti_{1-x}Nb_xCoSb$ phase and thus making n_{exp} smaller than n_{cal}. In C_2 and C_3, $n_{cal} \approx n_{exp}$ implies that the phase B neither adds nor removes electrons significantly from the phase A. The three cases are depicted schematically in Figure 4.6.

The Hall mobility (μ_H) of our samples is also shown in Figure 4.5d. μ_H increases from C_0 to C_3, reaching a peak value of ~ 6.75 cm^2 V^{-1} s^{-1} for C_3. Thereafter, for C_4 and C_5, a decline in μ_H is observed. In sample C_1, the carrier concentration is high due to both Nb-doping and modulation doping, as discussed above. The high carrier density thus gives rise to a high electrical conductivity, $\sigma = 1050$ S cm^{-1} (near 300 K) compared to the pristine TiCoSb (C_0) with $\sigma \approx 60$ S cm^{-1} (near 300 K). Since Ta has the same number

of valence electrons as Nb, a comparison with Ta-doped TiCoSb should be instructive. In $Ti_{1-x}Ta_xCoSb$ system, to obtain a comparable value of σ one should dope about 10% Ta, which is more than twice the percentage of Nb doping in C_1. In fact, σ in a 5% Ta-doped sample is only 200 S cm^{-1} [124]. This strongly supports our hypothesis that phase A in C_1 has some contribution from the modulation doping in addition to the direct doping due to Nb substitution at the Ti site. The modulation doping also helps in achieving higher mobility of $\mu_H = 5.1\ cm^{-2}\ V^{-1}\ s^{-1}$ compared to $\mu_H = 4.7\ cm^{-2}\ V^{-1}\ s^{-1}$ in $Ti_{0.9}Ta_{0.1}CoSb$ despite its higher conductivity ($\approx 1150\ S\ cm^{-1}$) than C_1 [126]. Furthermore, in $Ti_{1-x}Ta_xCoSb$ system, σ decreases significantly for $x > 0.1$ (for example, $\sigma \approx 400\ S\ cm^{-1}$ for x = 0.14) [126], which shows that in the $Ti_{1-x}Ta_xCoSb$ system, above 10% Ta doping, the gain due to increased carrier concentration is outweighed by the decrease due to Ti-Ta disorder. On the other hand, the composites C_2 and C_3 in our study, where the Nb doping in phase A is $x = 0.09$ (C_2) and $x = 0.12$ (C_3), respectively, exhibit high σ and μ_H. We argue that these samples show high conductivity ($\sigma = 1685\ S\ cm^{-1}$ and 2300 S cm^{-1} for C_2 and C_3 respectively) by virtue of their high carrier concentration due to Nb doping. For these samples $n_{cal} \approx n_{exp}$, hence the modulation doping is not expected. Consequently, both regions remain charge neutral with no immobile interfacial charges, which minimizes the interfacial scattering resulting in the highest μ_H (in C_3) and also a nearly T^{-1} dependence of σ, which is a characteristic feature of the electron-phonon scattering.

We now turn our attention to the composites C_4 and C_5 where the modulation doping is in action again. For these composites, the doping concentration of Nb in phase A has increased to 15% and 22%, respectively. As discussed earlier, in these composites the carriers diffuse in opposite directions, from phase A to phase B, resulting in a lesser carrier density in phase A than n_{cal}. Additionally, we note that the volume fraction of phase B has increased significantly in these composites (respectively, 27% and 34% in C_4 and C_5) and their direct influence (i.e., beyond their role as donor or acceptor) on the transport properties cannot be overlooked. Due to a copious amount of Nb vacancies, the phase B $\equiv Nb_{0.8+\delta}CoSb$ exhibits low μ_H (σ), ranging between $\approx$ 2.1 $cm^{-2}\ V^{-1}\ s^{-1}$ and 4.2 $cm^{-2}\ V^{-1}\ s^{-1}$ (1000 -

2000 S cm^{-1}) depending on the value of δ [129]. Both these factors, (a) a decrease in the carrier concentration of phase A and (b) an increase in the volume fraction of phase B, result in the observed decrease in μ_H and σ for these samples.

We now discuss the magnitude of the Seebeck coefficient which is important for obtaining the high PF. Concerning the enhancement of the Seebeck coefficient upon Nb doping, we attribute this to the band engineering due to Nb doping as discussed in the computational section. As shown there, Nb doping enhances the band convergence, which is likely the reason why the Seebeck coefficient also increases along with a increase in σ. The Seebeck coefficient for C_4 and C_5 remains high due to the charge-draining effect discussed earlier, which leaves the phase A in these samples with lower carrier density than n_{cal}, despite an increased Nb doping. The growing fraction of $Nb_{0.8+\delta}CoSb$ phase also contributes to their high Seebeck as the Seebeck coefficient for $Nb_{0.8+\delta}CoSb$ is of the order of 10^2 $\mu V\ K^{-1}$ [56].

4.3.4 Reproducibility and thermal cycling

Finally, to verify the reproducibility of our results, we synthesized a new sample C_5 (labelled at C'$_5$). The temperature variation of S and σ for C_5 and C'$_5$ are in excellent agreement with each other shown in Figure 4.7(a,b). The results of the thermal cycling tests, taking sample C_1 as a representative case, are shown in Figure 4.7(c,d). No significant changes could be seen between multiple cycles during the measurements, indicating that the material is thermally stable.

4.3.5 Thermal conductivity

Figure 4.8a shows the total measured thermal conductivity (κ) for all the samples investigated here. C_0 (TiCoSb) has the highest thermal conductivity with values ranging from $\approx 18\ W\ m^{-1}\ K^{-1}$ (300 K) to $\approx 7\ W\ m^{-1}\ K^{-1}$ (1000 K) in good agreement with the previous report [124]. κ vs T plots for the defective hHs $Nb_{0.80}CoSb$ and $Nb_{0.85}CoSb$ are also shown for comparison [112]. These samples have a significantly lower κ compared to TiCoSb due to the presence of a copious amount of Nb vacancies. However, a comparison among these samples shows that κ slowly increases upon increasing the Nb concentration (for example,

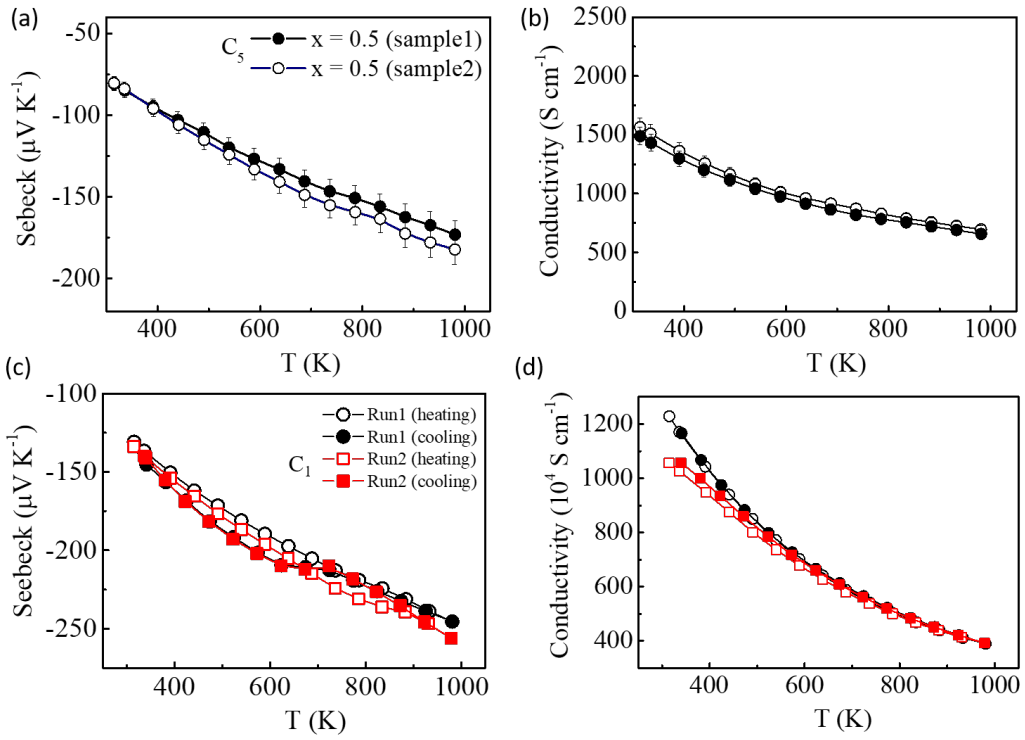

Figure 4.7: (a,b) Seebeck and Conductivity data comparison for to separately prepared samples, (c,d) Seebeck and Conductivity data with multiple heating cooling cycle

from 4.3 W m^{-1} K^{-1} for $\delta = 0$ to 6 W m^{-1} K^{-1} for 0.84). This is primarily due to the increase in the lattice component (κ_l) as a result of the filling up of a fraction of Nb vacancies upon increasing δ. κ for composites C_1, C_2, ..., and C_5 lies between those of TiCoSb and $Nb_{0.8}CoSb$. Upon going from C_1 to C_4, κ shows a decreasing trend. However, for C_5, κ is slightly higher than that for C_4. This appears anomalous, as the Nb doping in C_5 (22%) is higher than that in C_4 (15.5%) which should enhance the point-mass fluctuation; however one has to consider the growing fraction of the phase $Nb_{0.8+\delta}CoSb$, whose volume fraction increases from 27% in C_4 to 34.3% in C_5, which would increase the thermal conductivity. For $Nb_{0.84}CoSb$ (the approximate composition of phase B in C_5), κ near room-temperature is close to 6 W m^{-1} K^{-1}. We should include here the contribution due to charge transfer from phase A to phase B (recall that n_{exp} becomes increasingly smaller than n_{cal} for the samples C_4 and C_5). We believe, these factors together allow C_5 to have a slightly higher κ.

For C_1, the reduction in κ with respect to C_0 is rather significant ($\approx 30\%$). This is interesting given that $\sigma(C_1)$ is almost an order of magnitude higher compared to $\sigma(C_0)$. This suggests that the electronic component, κ_e, of the thermal conductivity of TiCoSb is very small. The κ_l component, on the other hand, is sensitive to the presence of lattice defects. To deal with these aspects more rigorously, we estimated the components, κ_e and κ_l. For this, we first used the single parabolic band (SPB) model to estimate the Lorentz number (L). Using this, the component κ_l is extracted by making use of the relation: $\kappa_l = \kappa - \kappa_e$, where κ_e is related to the electrical conductivity σ through the Wiedemann-Franz law, $\kappa_e = L\sigma T$. The details of Lorentz number calculations are given in the Supporting Information. κ_e for various samples thus obtained is shown in Figure 4.8b. As it turned out, the component κ_e is only a very small fraction of the total measured κ, as anticipated above based on the comparison of κ's for the composites C_0 and C_1. This conclusion is in agreement with the previous report [112].

To analyze these results theoretically, we calculate the lattice thermal conductivity of undoped TiCoSb using two different approaches: (i) by solving the Boltzmann Transport Equation (BTE) using *phono3py* package that computes the anharmonicity using the finite

Table 4.2: Elastic constants, bulk(B_H) and shear (G_H) moduli of TiCoSb. v_L, v_T, and v_{av} are the longitudnal , transverse and average phonon velocities. Gruneisen parameter and Debye temperature are represented as γ and Θ_D respectively.

Parameters	TiCoSb
G_H (GPa/m^2)	75.9
B_H (GPa/m^2)	140.8
v_L (m/s)	5720
v_T (m/s)	3204
v_{av} (m/s)	3565
γ	1.6
Θ_D (K)	412.2

displacement supercell approach [104, 130], and (ii) using the Slack's equation [131]. The different parameters that we have computed to estimate the lattice thermal conductivity is given in the Table 4.2.

The lattice thermal conductivity estimated using Slack's equation turned out to be in close agreement with that calculated by solving the BTE using *phono3py* as shown in Figure 4.8c. The calculated κ_l from either method, however, significantly exceeds the experimentally estimated κ_l. This is not surprising as the calculated κ_l assumes an idealized lattice with no defects (hence the notation κ_l^0). For real materials, κ_l is given by $\kappa_l = \eta(T)\kappa_l^0$ where $\eta(T) < 1$ is a temperature-dependent attenuation factor which depends on the nature of defects present in the sample. In an ingot sample, the point defects, e.g., antisite disorder, off-stoichiometry, etc., are more effective in suppressing κ_l. The factor $\eta(T)$ for the point defects can be estimated using the Klemens model [109]. Assuming 1% of Co-Sb antisite disorder in our TiCoSb ingot, the calculated κ_l shows a good agreement with the experimental κ_l as depicted in Figure 4.8c. The actual antisite disorder in our TiCoSb ingot might be much less than 1%, as a small concentration of other lattice defects (e.g., vacant sites, strain, dislocations, grain boundaries, etc), which we have not considered, may also statistically be present in the sample and would contribute to the lowering of thermal conductivity.

In order to calculate κ_l for the composites C_1, C_2, ..., C_5, we used similar approach but with κ_l^0 replaced by the thermal conductivity of C_0 by tacitly assuming that in C_1 the point-defect concentration is same as that in C_0. In reality, this may not be true, but for the purpose of a rough estimation, we use this as an approximation. For ΔM we use the atomic mass difference between Nb and Ti, and for x_a we used the values of x as given in Table. 4.1. The simulated κ_l, shown in Fig. 4.8(c) is systematically suppressed upon increasing the disorder in a good qualitative agreement with the experimental data. The growing volume fraction of phase B which impacts the experimentally estimated κ_l, and other scattering factors that we ignored should also be considered for a more realistic modelling of the thermal conductivity of these composites.

4.3.6 Thermoelectric figure-of-merit

The temperature variation of figure-of-merit (zT) for all the composites along with that of TiCoSb, $Nb_{0.80}CoSb$, and $Nb_{083}CoSb$ is shown in Figure 4.8d. The zT in all cases shows an increasing behaviour upon heating above the room temperature with no signs of saturation; in fact, zT vs T curves bend upwards (except in C_0) indicating a higher rate of increase of zT with respect to T at high temperatures. At 975 K, the highest temperature in our experiments, the maximum zT of 0.81 is obtained for the composite C_4. This is significantly higher than the zT $\approx$ 0.06 of TiCoSb or zT $\approx$ 0.3 of Ta-doped TiCoSb [124]. Thus, even though Ta and Nb are isovalent, the zT in the Nb-doped TiCoSb is significantly higher which underscores the concept of using composites for increasing the zT further. This is further supported by the observation that the highest zT in our composites is also almost 20% enhanced with respect to the highest zT at 975 K for the $Nb_{0.80+\delta}CoSb$ ($\delta = 0.83$) [112] samples. The enhancement of zT in these composites can be attributed to the synergistic increase in electrical conductivity and thermopower leading to a high value of power factor (PF). A high PF combined with the low values of thermal conductivity led to the high values of zT. In particular, the highest zT of C_4 among all the composites investigated here can be attributed to its lowest κ ($3\ \mathrm{W\ m^{-1}\ K^{-1}}$

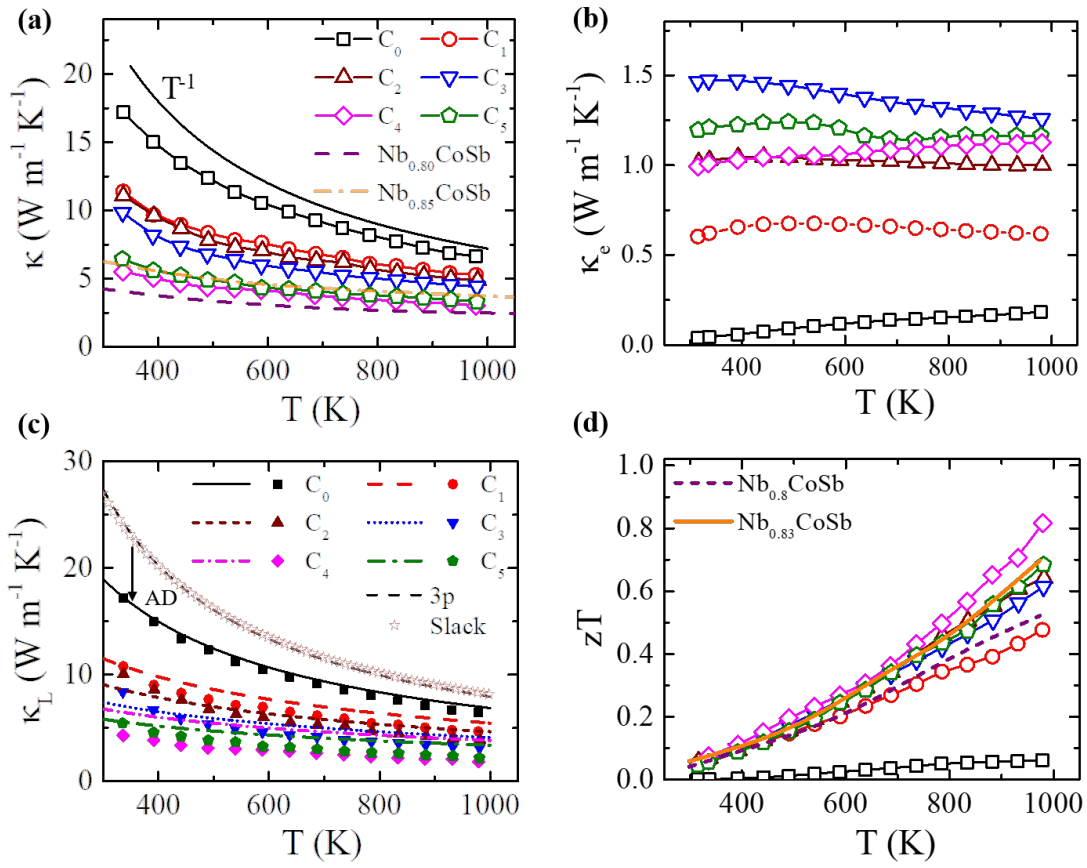

Figure 4.8: (a) The temperature variation of total measured thermal conductivity (κ), (b) the electronic component (κ_e, and (c) the lattice component (κ_l). (d) the thermoelectric figure of merit (zT) plotted as a function of temperature for composites C_0, C_1, ..., and C_5. The zT of $Nb_{0.80}CoSb$ and $Nb_{0.83}CoSb$ (the sample with the highest zT in $Nb_{0.8+\delta}CoSb$ family) is also included for comparison. In (c), legends '3P' and 'Slack' represent the lattice thermal conductivity computed from the 3-phonon scattering processes using the *phono3py* package and the Slack equation for a perfect lattice. The lines (data point) represent the calculated (experimental) lattice thermal conductivity for the composite C_0, C_1, C_4, and C_5. Data for C_2 and C_3 are not shown for clarity. The calculation of κ_l for C_0 is done using the Klemens model by considering 1% AD (see text for details). The grey-coloured downward arrow (top left) shows the effect of including 1% Co-Sb antisite disorder (see text for details). The symbols used in (b) and (d) are same as in (a).

at 975 K) and a reasonably high PF ($\approx$ 25 μW cm^{-1} K^{-2} at 975 K). The composition C_3 which exhibits the highest power factor over a broad temperature range has a high zT of 0.6 (975 K). In future, the zT of C_3 can possibly be enhanced by isovalent doping at the Ti site to lower κ_l further.

4.4 Summary and Conclusions

The experimental work presented here was motivated by our DFT calculations based prediction of conduction band degeneracy in TiCoSb under tensile strain. To realize the tensile strain experimentally, we introduced negative chemical pressure by substituting a fraction of Ti with M = Zr, Hf, Nb or Ta, the ions with a larger ionic radius compared to Ti. The computed band structure showed that Nb-doping is particularly effective in achieving the desired band convergence. Hence, (Ti, Nb)CoSb-type alloys were synthesized by melting Ti, Nb, Co, and Sb. The microstructure of these alloys revealed the presence of two competing phases, the majority or primary phase A $\equiv$ $Ti_{1-x}Nb_xCoSb$ and a secondary phase B $\equiv$ $Nb_{0.8+\delta}CoSb$. We thus synthesized composite samples C_0, C_1, C_2,..., and C_5 comprising A and B as $(1-f)$A + fB. The Nb doping level (x) in phase A, and the volume fraction (f) of phase B in these composites varied as follows: $C_0 : x = 0, f = 0$; $C_1 : x = 4.5, f = 5$; $C_2 : x = 9.4, f = 11.4$; $C_3 : x = 12, f = 19.2$; $C_4 : x = 15.5, f = 27$; and $C_5 : x = 22, f = 34$, where x and f are expressed in %. The structural investigation reveals that while the Nb doping level (x) in phase A increases from C_1 to C_5, the Nb content of phase B increases by only a small amount, consistent with a previous report where the solid-solubility (δ) of Nb in $Nb_{0.8+\delta}CoSb$ was found to range from $0 \leq \delta \leq 0.05$. For composite C_1 (f = 5%), the experimentally measured carrier concentration is found to be significantly higher than what one would calculate using the Zintl concept (n_{cal} in the text). We explain this using the concept of 3-D modulation doping where the excess carriers from the secondary phase B are doped in phase A, enhancing the carrier density in phase A, leading to the observation $n_{exp} > n_{cal}$. As a consequence of this, there is a sharp increase in the value of σ from $\sim$ 60 S cm^{-1} in C_0 to $\sim$ 1050 S cm^{-1} in C_1, at 300 K. At the same

time, a significant enhancement is observed in the Seebeck coefficient from $< 60\ \mu\mathrm{V\ K^{-1}}$ to $\approx 130\ \mu\mathrm{V\ K^{-1}}$ due to improved band degeneracy at the conduction band minimum (X-point in the Brillouin zone). As a result of simultaneous increase in σ and S, the PF of C_1 exhibits a considerable increment from $0.3\ \mu\mathrm{W\ cm^{-1}\ K^{-2}}$ for C_0 to $19\ \mu\mathrm{W\ cm^{-1}\ K^{-2}}$ for C_1 (300 K). On the other hand, in composites C_4 and C_5, due to a high level of Nb doping at the Ti-site in phase A, the calculated carrier concentration of phase A ($\mathrm{n_{cal}}$) exceeds the experimental density by a significant amount. In this case, the electron transfer happens from phase A to phase B resulting in the Fermi level in phase A remaining closer to the conduction band edge. Thus, benefiting from the conduction band degeneracy at the band edge due to tensile strain generated by Nb-doping, the Seebeck for these samples decreases only slightly even though Nb-doping at the Ti site becomes as high as 22% (C_5). In the intermediate sample C_3, the carrier concentration of both phases is well-matched, which reduced the interfacial boundary scattering, resulting in the highest μ_H and hence the highest σ with σ(300 K) for C_3 taking values as high as 2300 S $\mathrm{cm^{-1}}$, which is highest among all the samples investigated. For this sample the PF of $\approx 28\ \mu\mathrm{W\ cm^{-1}\ K^{-2}}$ is not only very high but also remains constant over a broad temperature range. The thermal conductivity of these composites decreases systematically upon going from C_0 to C_4, which can be attributed to the increase in the alloy scattering due to Nb doping at the Ti-site. The higher thermal conductivity of C_5 compared to C_4 is attributed to an increase in the volume fraction of the phase $\mathrm{Nb_{0.8+\delta}CoSb}$ which has a thermal conductivity of about $\approx 6\ \mathrm{W\ m^{-1}\ K^{-1}}$ near 300 K for $\delta = 0.04 - 0.05$. The zT vs T plots for C_1, C_2,..., C_5 exhibit an increasing behaviour with the rate of increase of zT with respect to temperature showing an increasing behaviour upon heating above 700 K, suggesting that even higher zT can be expected upon further heating. The highest zT of 0.81 is observed for C_4 at 975 K. In conclusion, we show here that by synergistic band engineering, modulation doping and alloying, the PF (thermal conductivity) can be enhanced (diminished), which in turn augments the zT.

Chapter 5

Elucidating the role of hierarchical bonding, electronegativity and chemical pressure on thermoelectric properties of double Half Heuslers

5.1 Introduction

The most common approach to address the challenge of high lattice thermal conductivity in hHs is to alloy with elements that have a significantly large difference in atomic mass and size compared to the parent elements; eg, alloying Hf with Ti and Zr containing elements [132–135]. The heavier alloying element acts as a scattering centre for phonons, thereby reducing the lattice thermal conductivity. An alternative approach to enhance the phonon scattering was the simultaneous introduction of full Heusler nanoprecipitates (by slightly increasing the Y-element) and antisite defects [136–143] However, the enhancement of zT achieved by this method is still limited because it affects the electronic conductivity due to scattering of charge carriers at the interface of these nano precipitates. Moreover, as these nano precipitates grows in size, the effectiveness of the localized modes decreases.

Couple of years ago Anand *et al.* proposed a novel idea of enhancing the complexity of the crystal structure of the half Heusler alloys by introducing quaternary double half Heuslers (dhHs) [144]. While half Heuslers have a chemical formula of XYZ, the dhHs can be represented with a nominal formula of $X_{0.5}X'_{0.5}YZ$, $XY_{0.5}Y'_{0.5}Z$, and $XYZ_{0.5}Z'_{0.5}$. A double half Heusler can be made by combining two half Heuslers. For example, a $XY_{0.5}Y'_{0.5}Z$ dhH can be made up of two half Heuslers XYZ and XY′Z with one having a valence electron count (VEC) of 17 while the other has a VEC of 19 such that the newly formed dhH has a VEC of 18. It is important to note that the stability of these alloys depend on their VEC. For these family of materials VEC=18 denotes that the alloys are stable. This opened up a large compositional space compared to half Heuslers, with about 7719 possible candidates for dhHs as opposed to 715 candidates for hHs.

Amongst the dhHs proposed by Anand et al., $TiFe_{0.5}Ni_{0.5}Sb$ (TFNS) is the most widely studied one [126, 132, 145, 146]. The disordered structure of this dhH has a lattice thermal conductivity of 7.3 W m^{-1} K^{-1} [132] at room temperature, which is much lower than that of TiCoSb (18 W m^{-1} K^{-1}) [42]. Though this has a low lattice thermal conductivity (3.8 W m^{-1} K^{-1} at 973 K), the intrinsic value of zT is extremely low (maximum $zT =$ of 0.05 at 973 K), that has been attributed to its poor electrical conductivity of 10 Scm^{-1} at 973 K [145]. Over the last few years there has been enormous effort to increase the value of zT of this material. For example, in a recent work, Hasan et al. induced formation of nanoprecipitates of full Heuslers in $TiFe_{0.5}Ni_{0.5}Sb$ by synthesizing these materials in excess Ni [147]. They added up to 10% of excess Ni. Their samples containing 5% excess Ni exhibited an enhanced zT of 0.31 at 973 K. In another work by Hasan et al., the effects of doping Co and Bi at the Fe and Sb sites, respectively were investigated [148]. For $Ti_2Fe_{0.9}Co_{0.1}NiSb_2$ they obtained a zT of 0.69 at 973 K that is approximately *fourteen* times higher than that of pristine $TiFe_{0.5}Ni_0.5Sb$. They attributed this enhancement to the bypassing of the trade off between Seebeck coefficient and electrical conductivity due to targeted atomic site doping. In another recent work Mishra et al. doped $TiNi_{0.5}Co_{0.5}Sn_{0.5}Sb_{0.5}$ dhH with heavy (Ta, Zr) and light (Al) dopants at the X site. They found that at an optimum dopant level of 25% Zr,

7.5% Ta, and 10% Al, their samples had the maximum zT of 0.29 at 823 K [149].

In addition to $TiFe_{0.5}Ni_{0.5}Sb$, if one replaces Ti by Zr or Hf, it is possible to form $ZrFe_{0.5}Ni_{0.5}Sb$ (ZFNS) and $HfFe_{0.5}Ni_{0.5}Sb$ (HFNS), respectively. However, in contrast to $TiFe_{0.5}Ni_{0.5}Sb$, these two compounds are not well studied. Only recently Kahiu et al. showed that tuning the Fe:Ni ratio, one can prepare both p and n-type $ZrFe_xNi_{1-x}Sb$ double half Heusler material [150]. Their best n (p) type sample with x =0.35 (0.55) exhibited maximum zT of 0.43 (0.06). In another work Kahiu et al. studied the effect of Co doping at the Fe site in $ZrFe_{0.4-y}Co_yNi_{0.6}Sb$ [151]. Their samples exhibited phase separation into dhH and ZrNiSb phase. They could obtain only a marginal enhancement of zT. Hassan et al. studied the effect of Ti-doping in $Hf_{2-x}Ti_xFeNiSb_2$ [152]. They obtained highest value of the thermoelectric figure of merit of 0.28 at 800 K $Hf_{1.75}Ti_{0.25}FeNiSb_2$.

The discussions in the previous paragraphs suggests that there is still enormous room for improving the zT of the DHHs. However, to do so through rational modifications of the parent dhHs, it is imperative to have a proper understanding of the chemical interactions between the different elements that form the dhH and how these interactions affect their stability, electronic and transport properties. Moreover, it is also interesting to understand the trends in the transport properties by replacing the X or Y or Z elements of the parent dhH with other elements in the periodic table, by moving systematically along the group or along a row. However, to the best of our knowledge, such systematic computational study is missing in these cases. Hence, in this work, using DFT based calculations we studied the stability and electronic properties of $XFe_{0.5}Ni_{0.5}Sb$, where X=Ti, Zr and Hf, which belong to the family of $XY_{0.5}Y'_{0.5}Z$ dhH. $TiFe_{0.5}Ni_{0.5}Sb$ was chosen because it is one of the most well studied member of this family. We replaced Ti (X) with Zr and Hf. All these elements belong to Group IV of the periodic table. However, we note that as we move down the periodic table, the atomic size increases (though Zr and Hf have similar atomic sizes) while the electronegativity decreases. The change in atomic size introduces local strain in the lattice. Additionaly, it is also unclear that upon formation of the dhH whether the nature of the chemical bonds between the atomic species are similar or different compared to the

hHs. Hence, through our study, we have elucidated the role of bonding, effect of local strain and electronegativity in their stability and electronic properties. Further, we have used semiclassical Boltzmann Transport theory to study how the above mentioned effects are translated to their transport properties. The rest of the manuscript is divided as follows. In Section 5.2 we present the Computational details. Section 5.3 contains the results and discussions. Finally we summarize and conclude in Section 5.4.

5.2 Computational Details

The DFT calculations have been performed using the Quantum ESPRESSO software [115, 116]. The electron-ion interactions are described using ultrasoft pseudopotentials [117]. Valence configurations of $3s^2 4s^2 3p^6 3d^2$, $4s^2 5s^2 4p^6 4d^2$, $5s^2 6s^2 5p^6 5d^2$, $3s^2 3p^6 3d^6 4s^2$, $4s^2 3d^8$, $5s^2 5p^3$ have been used for Ti, Zr, Hf, Fe, Ni and Sb. Kinetic energy cutoff of 55 Ry (550 Ry) is used for expanding the wave functions (charge density) on a plane wave basis. The electron-electron exchange and correlation was described using Perdew-Burke-Ernzerhof parametrization of generalized gradient approximation (PBE-GGA) [118]. A $8\times8\times8$ Monkhorst-Pack k-point mesh was used for Brillouin zone (BZ) integration [92].

For the dhHs with the chemical formula $XFe_{1-x}Ni_xSb$ and $0 \leq x \leq 1.0$, the random structures were obtained using the special quasi-random structure (SQS) method as implemented in the mcsqs code [153]. In order to generate these structures, we have considered the conventional cubic unit cell containing 12 atoms and allowed the possibility of random arrangement of Fe and Ni at 4c cite. The atomic positions and lattice parameters of these structures were relaxed before further calculations.

TE transport properties were calculated by solving the Boltzmann transport equation (BTE) under constant relaxation time approximation and the rigid band approximation, using the BoltzTraP code [154]. In order to compute the transport coefficients, we have computed the electronic structure with a denser $20 \times 20 \times 20$ k-grid. Since BoltzTraP calculates electrical conductivity and electronic thermal conductivity in terms of relaxation time (τ) as σ/τ and κ_e/τ, to estimate the absolute values of the transport coefficients, one has to compute

the relaxation time explicitly. We have estimated the relaxation time using the deformation potential (DP) theory [155] and the parabolic band approximation. Previous works have shown that these approximations predicts the relaxation time for the hH systems within a reasonable accuracy [156, 157]. Within the DP theory, τ is given by:

$$\tau = \frac{2\sqrt{2\pi}\hbar^4 c_{11}}{3(m^* k_B T)^{3/2} V_{DP}^2}, \tag{5.1}$$

where $\hbar$ is the reduced Planck's constant, c_{11} is the elastic constant, k_B is the Boltzmann constant and m^* is the effective mass of electron/hole. V_{DP} represents the deformation potential and is given by:

$$V_{DP} = \frac{\partial E_{edge}}{\partial \alpha}, \qquad \alpha = \frac{a - a_0}{a_0}, \tag{5.2}$$

where E_{edge} is the position of the valance band maximum (VBM) or conduction band minimum (CBM) and α is the uniaxial strain along the direction of lattice vector a with a_0 being the equilibrium lattice parameter.

m^* in Eqn. 5.1 has be computed at the VBM and CBM as:

$$\left(\frac{1}{m^*}\right)_{ij} = \frac{1}{\hbar^2}\frac{\partial E_{edge}(k)}{\partial k_i \partial k_j}, \qquad i, j = x, y, z \tag{5.3}$$

where k_i is the direction of the k-path in the BZ along which the derivative is computed.

We have computed the lattice thermal conductivity (κ_l) using Slack's equation [131], which is given as:

$$\kappa_l = A\frac{\Theta_D^3 V_a^{1/3} m_{av}}{\gamma^2 n^{2/3} T}, \tag{5.4}$$

where Θ_D, V_a, m_{av}, γ and n are the Debye temperature, the volume per atom (in Å^3), average atomic mass (in amu) and the Grüneisen parameter, respectively. n is number of atoms in unit cell. A and Θ_D in Eqn. 5.4 are given by:

$$A = \frac{2.43 \times 10^{-6}}{1 - \frac{0.514}{\gamma} + \frac{0.228}{\gamma^2}} \tag{5.5}$$

$$\Theta_D = \frac{\hbar}{k_B} v_{av} \left(\frac{6\pi^2 n}{V} \right)^{\frac{1}{3}} \tag{5.6}$$

where V is the volume of unit cell. The average sound velocity (v_{av}) has been computed from longitudinal (v_L) and transverse (v_T) velocities of the long wavelength acoustic modes. v_{av} is given by:

$$v_{av} = \left[\frac{1}{3} \left(\frac{1}{v_L^3} + \frac{2}{v_T^3} \right) \right]^{-1/3} \tag{5.7}$$

The Grüneisen parameter is estimated as:

$$\gamma = \frac{3}{2} \left(\frac{1+u}{2-3u} \right), \tag{5.8}$$

where the Poisson ratio (u) is given as:

$$u = \frac{1 - 2\left(\frac{v_T}{v_L}\right)^2}{2 - 2\left(\frac{v_T}{v_L}\right)^2} \tag{5.9}$$

We note that Slack's equation has been widely used to determine κ_l in hH systems and is known to provide estimates of κ_l which are in reasonably good agreement with those obtained from the more computationally demanding but accurate method of solving the Boltzmann transport equations for phonons [157]. Moreover, we compared the values of κ_l obtained from the Slack's equation with that computed by solving the phonon BTE for TiCoSb hH and dhH $TiFe_{0.5}Ni_{0.5}Sb$ [145]. We found that both the methods yield similar results as shown in Figure 5.1. Hence, to reduce the computational cost, for the other dhHs, i.e. $ZrFe_{0.5}Ni_{0.5}Sb$ and $HfFe_{0.5}Ni_{0.5}Sb$, we have used the Slack's equation to compute κ_l.

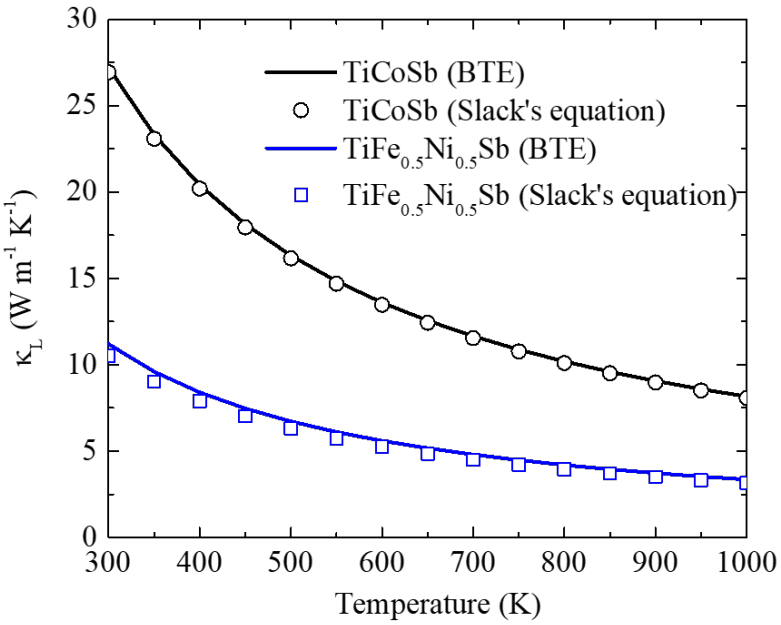

Figure 5.1: Lattice thermal conductivity comparison calculated by solving phonon BTE and Slack's equation.

Table 5.1: Lattice parameters (a_0) and corresponding E^{mix} of the dhHs at different values of x.

Compounds	$TiFe_{1-x}Ni_xSb$		$ZrFe_{1-x}Ni_xSb$		$HfFe_{1-x}Ni_xSb$	
Concentration x	a_0 (Å)	E^{mix} (eV/fu)	a_0 (Å)	E^{mix} (eV/fu)	a_0 (Å)	E^{mix} (eV/fu)
0.00	5.930	0.00	6.128	0.00	6.091	0.00
0.25	5.926	-1.89	6.126	-2.09	6.087	-1.92
0.50	5.919	-2.13	6.120	-2.34	6.081	-2.16
0.75	5.937	-1.88	6.134	-2.15	6.093	-1.92
1.00	5.954	0.00	6.146	0.00	6.104	0.00

5.3 Results and discussion

5.3.1 Structure and stability

Figure 5.2(a, b, c) show the lowest energy configurations of $XFe_{1-x}Ni_xSb$ for $x = 0$, 0.25/0.75 and 0.5, respectively, while the corresponding lattice parameters are summarized in Table 5.1. At each value of x, as we move from Ti to Zr the lattice parameter increases while from Zr to Hf there is a reduction. With increasing Ni content the lattice parameters show a non-monotonous trend. From $x = 0$ to $x = 0.5$, the lattice parameter decreases while for $x > 0.5$ it increases. The lattice parameters of the compounds for which all the Fe atoms are replaced with Ni, i.e. $x = 1.0$, are larger than those obtained for $x = 0$. This trend can be understood from the filling of the bonding and anti-bonding orbitals as explained later. Our computed lattice parameters of 5.919, 6.120 and 6.080 Å for TFNS, ZFNS and HFNS, respectively, are in good agreement with the experimentally reported values of 5.912 [158], 6.091 [150] and 6.058 Å [152].

In order to determine the relative stability of these materials with respect to the parent compounds, namely, XFeSb and XNiSb, we have computed mixing energy ($E^{mix}_{XFe_{1-x}Ni_xSb}$), which is defined as:

$$E^{mix}_{XFe_{1-x}Ni_xSb} = E_{XFe_{1-x}Ni_xSb} - (1-x)E_{XFeSb} - xE_{XNiSb} \tag{5.10}$$

where the first, second and third terms on the right hand side of Equation 5.10 denote the total energies of $XFe_{1-x}Ni_xSb$, XFeSb and XNiSb, respectively. By definition, E^{mix} for the parent compounds, i.e., $x = 0/1$ are zero. A negative value of E^{mix} for $0 < x < 1$ will indicate that the Ni/Fe-substituted compounds are thermodynamically more stable than the parent hHs, i.e., XFeSb and XNiSb. Figure 5.2d shows the plot of $E^{mix}_{XFe_{1-x}Ni_xSb}$ as a function of x. We find that the compounds containing a mixture of Fe and Ni are more stable compared to the parent ones. Amongst the different values of x, $x = 0.50$ is the most stable composition. The order of their stability is in accordance with that predicted by the

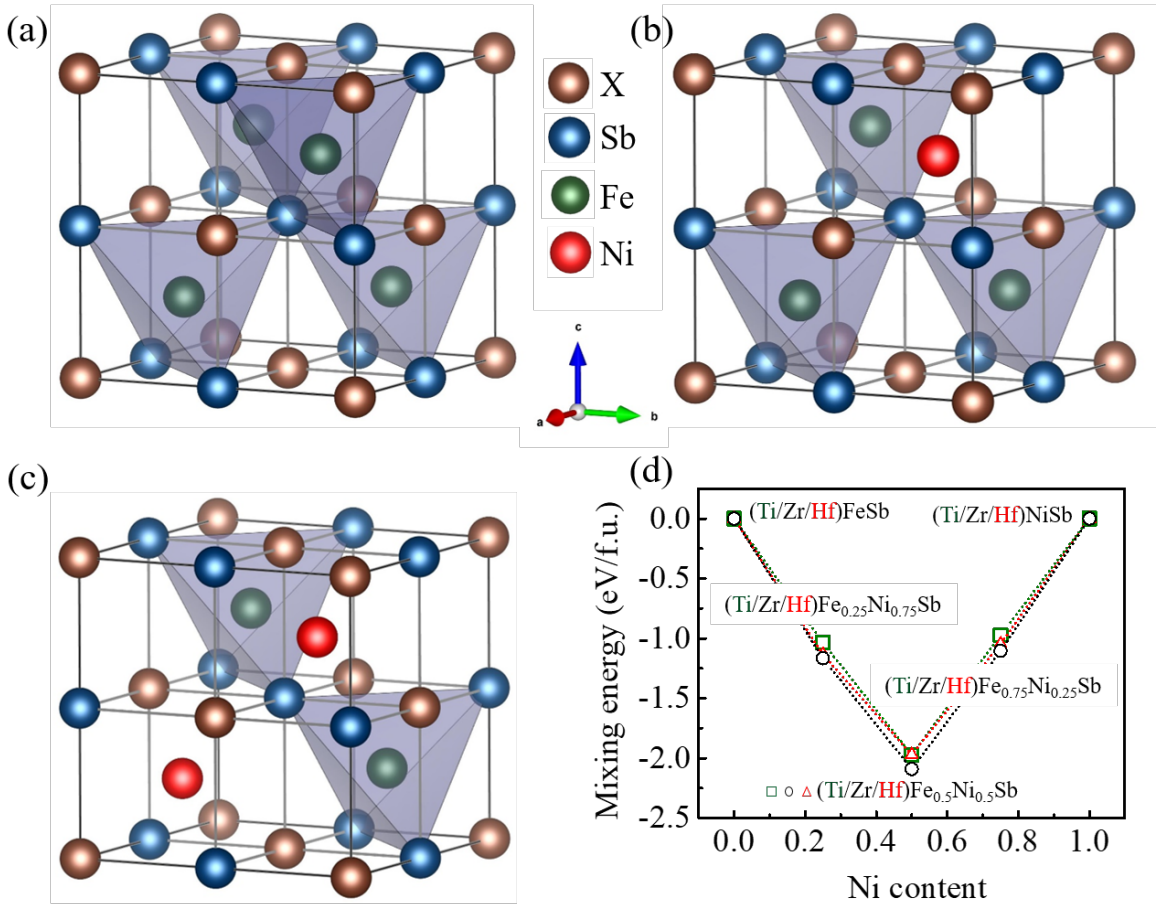

Figure 5.2: Structure of (a) XFeSb, (b) $XFe_{0.75}Ni_{0.25}Sb$, and (c) $XFe_{0.5}Ni_{0.5}Sb$ respectively. (d) Mixing energy as a function of Ni content. In all these and subsequent figures the X, Sb, Fe and Ni atoms are represented with brown, blue, green and red spheres, respectively.

valence electron count (VEC). For eg. the parent compounds XFeSb ($x = 0.00$) and XNiSb ($x = 1.00$) with VEC of 17 and 19, respectively are most unstable. This is followed by those corresponding to $x = 0.25$ and 0.75 (VEC= 17.5 and 18.5). The dhHs with $x = 0.50$ and corresponding to a VEC of 18 are the most stable ones with mixing energies lying between -2.34 and -2.13 eV/fu (Table 5.1). The dhH containing Zr is slightly more stable towards decomposition to the parent compounds compared to that of the Ti and Hf containing ones. Since the dhHs are thermodynamically the most stable ones, in the remaining part of this work, we focus on the electronic and transport properties of these compounds.

5.3.2 Bonding analysis

In order to understand the electronic density redistribution when the elements interact to form the dhH and thereby the interatomic bonding, and how these differ from the parent compounds, we have computed the charge density difference ($\Delta\rho$) which is given as:

$$\Delta\rho(r) = \rho_{system}(r) - \sum_i \rho_i^{atom}(r) \tag{5.11}$$

where the first term on the right hand side of equation 5.11 is the charge density of the system at a point r while the second is the charge density computed by the superposition of the atomic charge densities; the summation i runs over all the atoms in the system. The isosurfaces corresponding to $\Delta\rho$ for the parent and the dhHs are shown in Figure 5.3. For all the systems we observe that close to the X and Y atoms there is both accumulation and depletion of charges upon formation of the hHs. However, there is a striking difference in the charge density change in the spatial region between the X and Y elements and Y and Z elements of the hHs. For XFeSb (Figure 5.3(a, d, g)) we observe that there is accumulation of charge density between X-Fe and Fe-Sb; the charge cloud surrounds the Fe atom and is slightly directed towards X. In contrast for XNiSb (Figure 5.3(c, f,i)), we observe that the accumulated charge is highly localized between the X-Ni atoms, with a larger weight towards the Ni atom. This suggests that the X-Co bond is more covalent than the X-Ni bond. Upon formation of the dhHs, we observe that the characteristic features of the charge density

accumulation and depletion around the X-Fe and X-Ni bonds in the parent compounds are also present in the dhH with slight modifications.

To further quantify the above observations, we have computed the bond-orders (BO) between the X-Y and Y-Z elements using the density derived electrostatic and chemical (DDEC) charges as proposed by Manz et al. [159–161]. The BOs between two atoms is a measure of the overlap of the charge density basins of the two atoms. Larger is the value, more is the overlap, thereby suggesting that the bond is covalent in nature. Smaller values of BO are suggestive of ionic bonds. Figure 5.4 shows the variation of BOs between X-Y and Y-Z elements for the parent compounds and the dhHs. We observe that for the Ti containing compounds, the Fe-Sb (X-Fe) and Ni-Sb (X-Ni) bonds have the most (least) covalent character. However, as we move down the Group 4 in the periodic table, i.e., replace Ti with Zr and Hf, we observe that both the X-Y and Y-Z bonds become more ionic. This is true for the parent as well as the dhHs. On formation of the dhHs, we observe that the Ni-Sb bonds become more ionic in character compared to the parent compounds. In contrast, the Fe-Sb bonds become more covalent. These changes in the character of these bonds are more in case of Zr and Hf than that in Ti. Moreover, while the character of the X-Ni bonds are not significantly affected by the formation of dhH, the X-Fe bonds also become more covalent on dhH formation. Thus, the overall effect of the dhH formation is that there is a much greater variation in the nature of the bonding resulting in the formation of hierarchical bonding in the lattice.

5.3.3 Electronic properties

Figure 5.5 shows the band structure (unfolded on the BZ of the primitive fcc unit cell of respective conventional cell) and density of states (DOS) of the three dhHs. Our calculations show that all the three materials are semiconductors with indirect band gaps. For each of these, the valence band maxima (VBM) is at the L-point of the BZ while the conduction band minima (CBM) is at the Γ-point. We note that our result about the position of the VBM of $TiFe_{0.5}Ni_{0.5}Sb$ is in variance with that reported by Liu *et al.* [158] where they find that

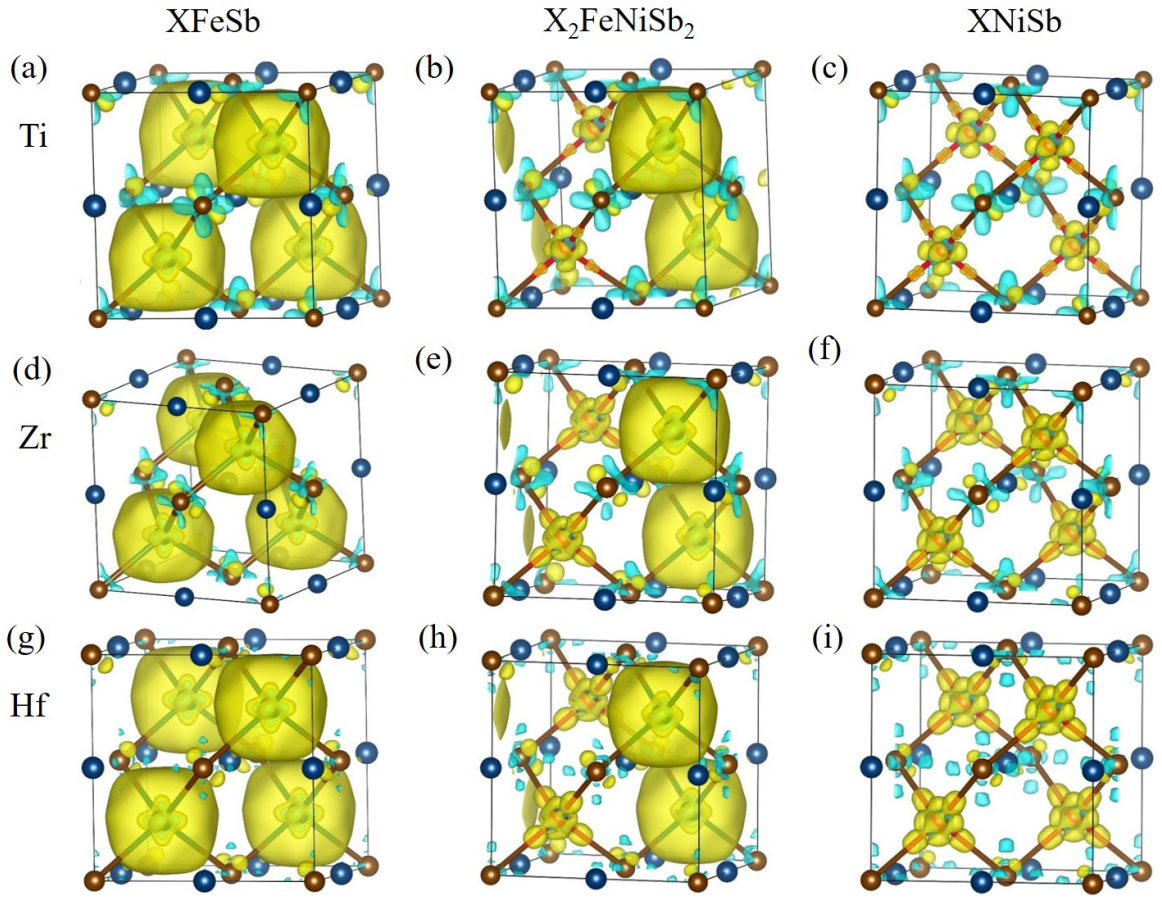

Figure 5.3: Isosurfaces showing charge density difference between the charge density of the system and the charge density obtained by superposition of the atomic charge density of the constituent atoms. The left panel [(a),(d) and (g)] are for XFeSb, the right panel [(c), (f) and (i)] are for XNiSb while the middle one [(b), (e) and (h)] are for the dhHs. The top, middle and bottom rows are for X=Ti, Zr and Hf, respectively. The isosurfaces are plotted with isovalues of 0.01 electrons/bohr^{-3}. The yellow isosurfaces represent charge accumulation while the turquoise ones represent charge depletion.

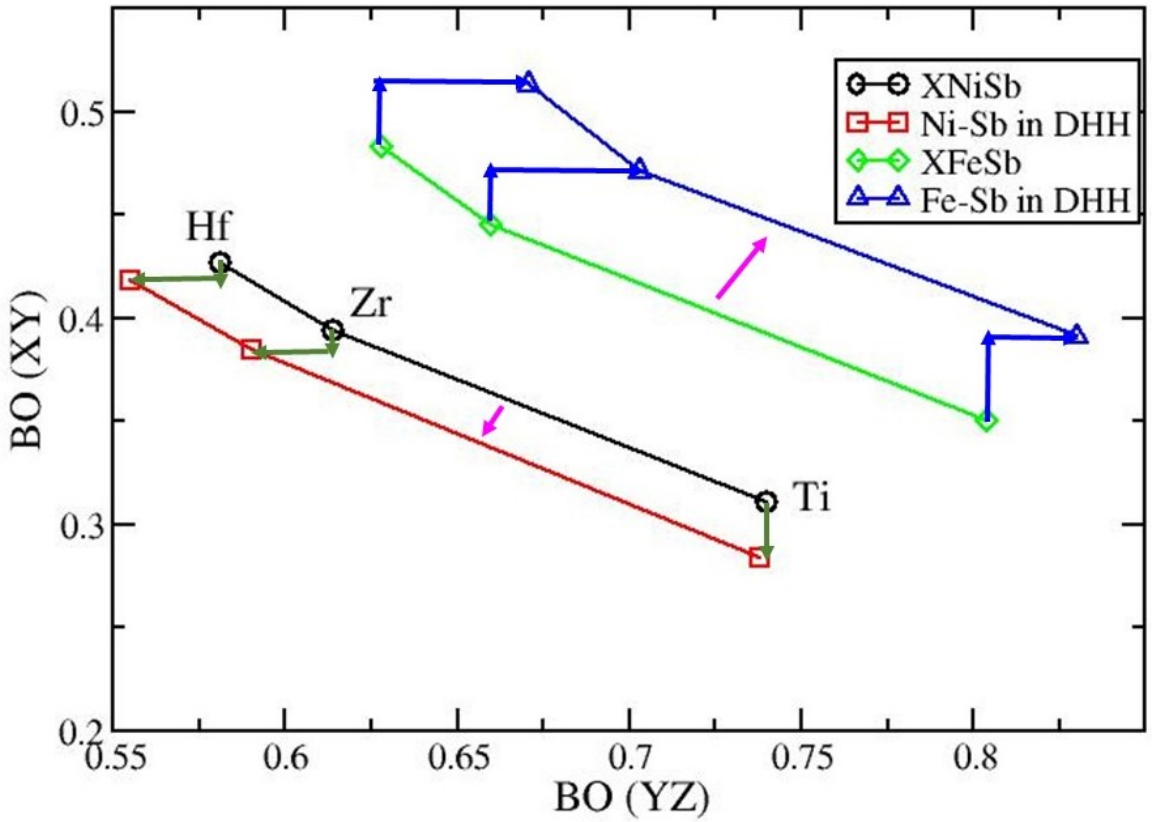

Figure 5.4: Bond orders (BO) between X-Y and Y-Z for the parent and double hHs. The black and red plots are for Y=Ni while the blue plots are for Y=Fe. The magenta arrows show the overall direction of the shift of the plots on formation of dhHs, while the dark green and blue arrows show for the individual ones. On formation of the dhHs, we observe that the X-Ni and Ni-Sb bonds become more ionic while the X-Fe and Fe-Sb bonds become more covalent.

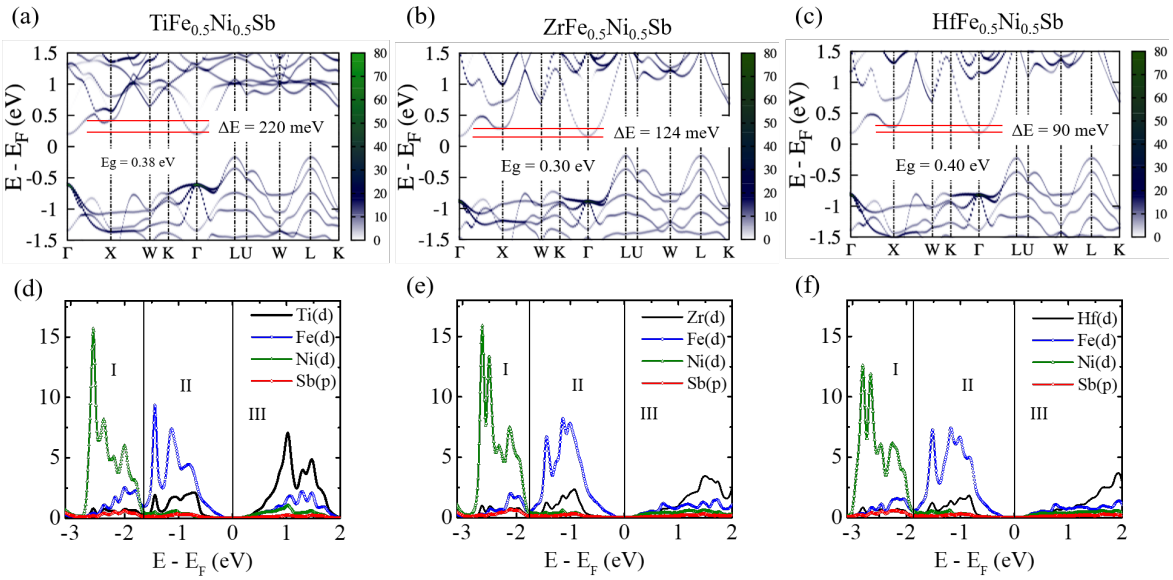

Figure 5.5: Electronic band structure and partial dos of $TiFe_{0.5}Ni_{0.5}Sb$ (a,d) $ZrFe_{0.5}Ni_{0.5}Sb$ (b,e), and $HfFe_{0.5}Ni_{0.5}Sb$ (c,f).

the VBM is at Γ-point of the BZ while the secondary maxima at L point is very close to the VBM. For $TiFe_{0.5}Ni_{0.5}Sb$ we obtain a band gap of 0.38 eV, which is slightly smaller than that of 0.44 eV reported by Liu *et al.* [158]. These differences may be due to the fact that the authors used a larger disordered supercell consisting of 48 atoms in their calculations. Upon replacing Ti with Zr (Hf), the band gap is reduced (increased) to 0.30 eV (0.40 eV).

In TFNS, in addition to the CBM at the Γ-point, there is a valley at the X-point of the BZ that is about 220 meV higher in energy compared to the CBM (Figure 5.5a). As we replace Ti by Zr and Hf, we observe that the energy difference between these two states (ΔE) are reduced to 124 meV and 90 meV, respectively, suggesting that substituting Ti with Zr and Hf helps in achieving valley convergence in the conduction band. The X-point has a six-fold valley degeneracy. We note that such valley convergence helps in enhancing the transport properties [42].

The above mentioned valley convergence can be due to the effect of strain induced by the mismatch of atomic sizes and/or the enhancement in the electropositivity of the X cation as we move down the periodic table. To filter out these effects, we computed the band struc-

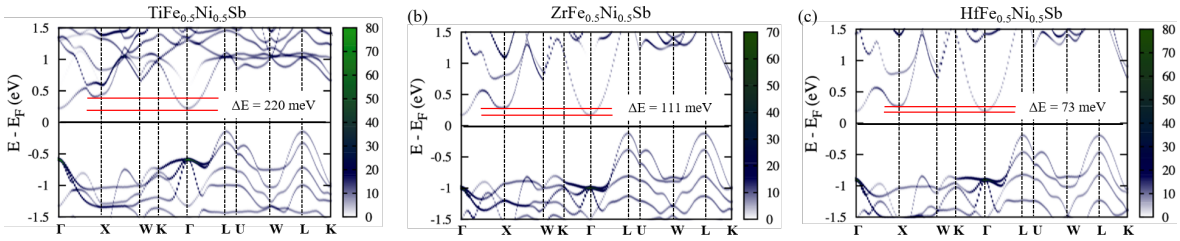

Figure 5.6: Band structure of (a) $TiFe_{0.5}Ni_{0.5}Sb$, (b) $ZrFe_{0.5}Ni_{0.5}Sb$ and (c) $HfFe_{0.5}Ni_{0.5}Sb$ calculated at $TiFe_{0.5}Ni_{0.5}Sb$ lattice parameter.

ture by replacing Ti of TFNS with Zr and Hf at TFNS lattice parameters. We optimize the atomic positions, thereby relaxing the local strain. Since moving down the periodic table, X becomes more electropositive, these calculations will throw light on the effect of enhanced electropositivity on ΔE. The results are shown in Figure 5.6. We observe that when Ti is replaced with Zr (Hf), ΔE is reduced from 220 meV to 111 meV (73 meV). These results suggests that more electropositive is the X element, larger is the band convergence. On optimizing the lattice parameters of ZFNS and HFNS (this amounts to a tensile strain of 2.74% for HFNS and 3.4% for ZFNS compared to that of TFNS), we observe that ΔE is enhanced by 13 meV (17 meV) for HFNS (ZFNS). These results show that the change in ΔE and the resulting tensile strain due to the change in atomic size affects the band convergence in opposite ways. While reduced electronegativity of X favours band convergence by reducing the hybridization between the X and the Y and Y′ atoms, strain enhances the value of ΔE. Moreover, we observe that the former has a stronger effect on band convergence.

The density of states (DOS) and their contributions from different atomic orbitals of the constituent elements (projected density of states, PDOS) are shown in Figure 5.5(d-f). We observe that for all the three materials the DOS can be split into three regions. Region I, deep inside the valence band (from -3 eV to about -1.6 eV) has primary contributions from the Ni-d states. Some contributions are also observed from X-d, Fe-d and Sb-p orbitals. Interestingly, the peak positions of the PDOS of each of the constituent elements overlap, suggesting some hybridization between them. However, the large differences between their contributions are indicative of the ionic nature of the bonds.

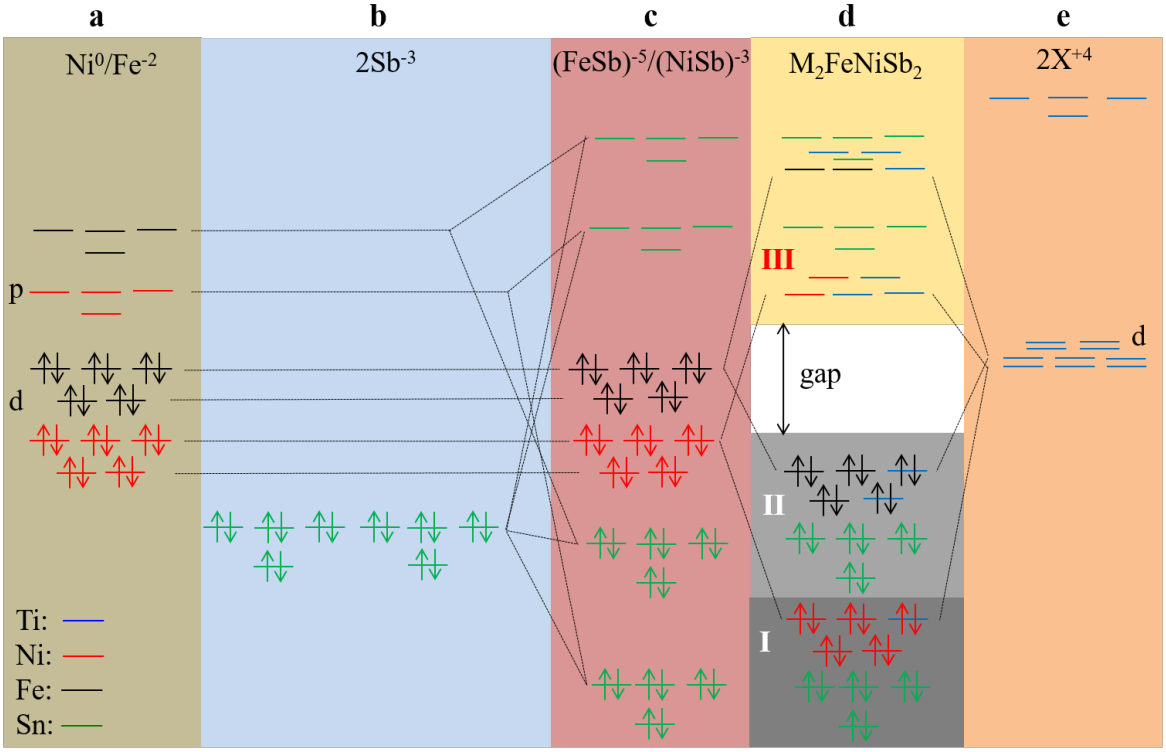

Figure 5.7: Atomic and Molecular orbitals of $X_2FeNiSb_2$ (two formula unit of $XFe_{0.5}Ni_{0.5}Sb$).

In region II (from -0.5 eV to the VBM) Fe-d states have the dominant contributions. For all the double Heuslers, the VBM is localized primarily on the Fe-d orbitals as is evident from the plots of the wavefunctions corresponding to the VBM at the L-point of the BZ as shown in Figure 5.8a. For TFNS slight weight is also observed on the Ti atoms. Though the X-d orbitals have the second largest contribution in this region, they contribute upto states that are 1.6 eV below the VBM. Further, some small contributions are also observed from the Ni-d and Sb-p states. In contrast with the VBM, the CBM (region III) has contributions from all the three transition metals and is also more delocalized as shown in Figure 5.8c. The conduction band is dominated with contributions from X-d states. The bottom of the conduction band (0.2 to 0.4 eV for TFNS, 0.15 to 1.05 eV for ZFNS and 0.2 to 1.2 eV for HFNS) have similar contributions from X, Fe and Ni. However, as one moves to higher energy, the dominating contribution is from the X-d states followed by those from the Fe-d states.

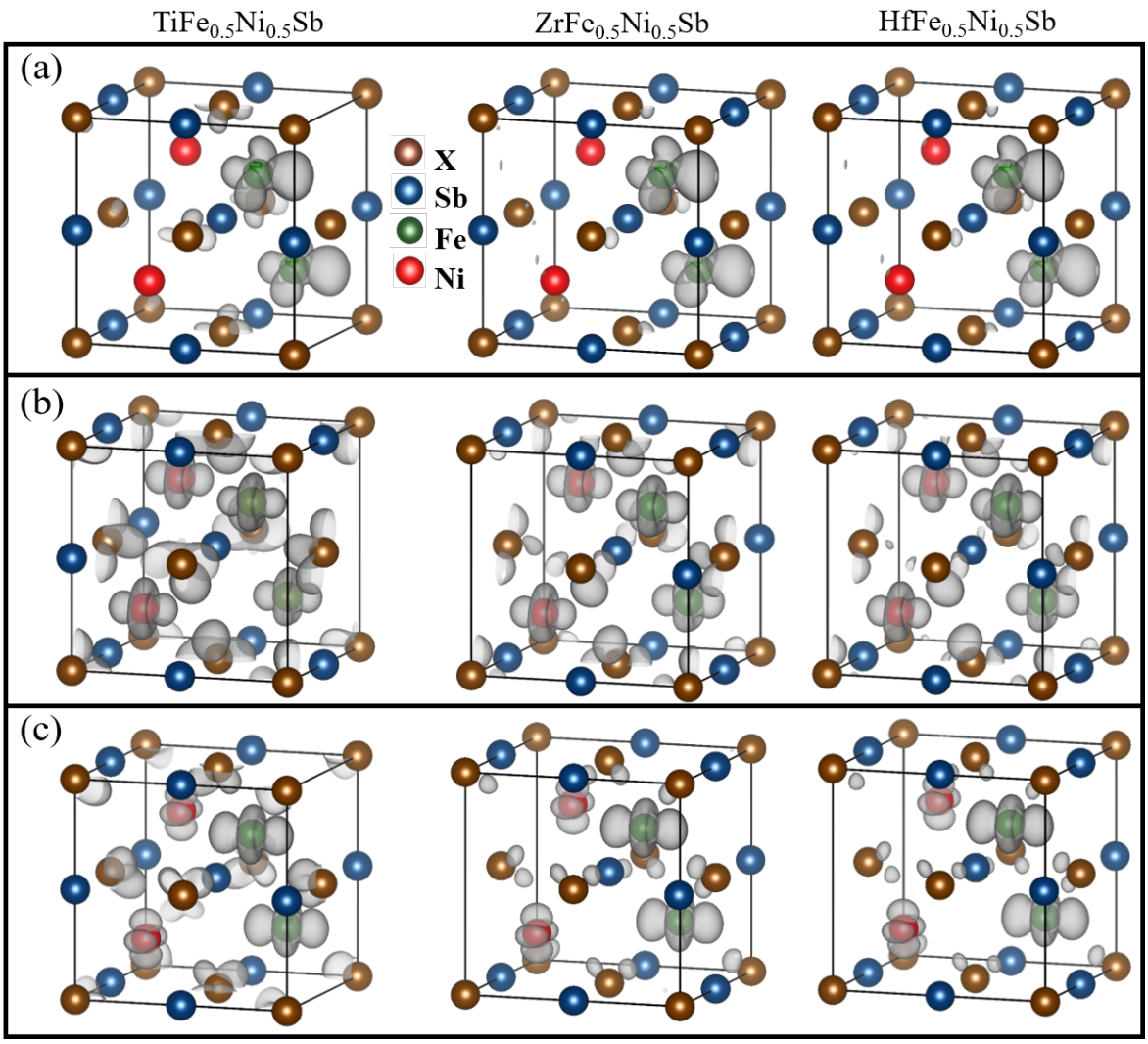

Figure 5.8: Wavefunctions corresponding to the (a) VBM at the L-point, (b,c) CBM at X and Γ-point of the BZ.

These features of the DOS of the double half-Heuslers can be explained from a molecular orbital picture. We note that similar concept had been used to explain properties of Zintl compounds and transition metal containing half Heuslers [162]. The anion network of these dhHs consists of FeSb and NiSb, which requires 5 and 3 electrons, respectively, to complete their octet structure. Hence, two X atoms, which is the most electropositive element in XFNS, donate all their four valence electrons (8 in total) to the anion network comprising of $(FeSb)^{5-}$ and $(NiSb)^{3-}$ to stabilize the structure. Figure 5.7 shows the schematics of the formation of the molecular orbitals from the atomic constituents. Ni being more electronegative than that of Fe, its d orbitals are lower in energy than those of Fe (Figure 5.7a). Moreover, since both of them are in a tetrahedral crystal field of Sb anions, they are split into t_{2g} (d_{xy}, d_{xz} and d_{yz}) and e_g (d_{z^2} and $d_{x^2-y^2}$). Due to the tetrahedral nature of the bonding environment, the Sb s and p (shown in Figure 5.7b) states will primarily hybridize with the empty p-states of Ni and Fe resulting in completely occupied bonding and empty antibonding orbitals (Figure 5.7c). The Fe/Ni d states are relatively unperturbed in the $(FeSb)^{5-}$/$(NiSb)^{3-}$ network. The d orbitals of the most electropositive X are higher in energy than those of relatively less electropositive Fe and Ni (Figure 5.7e). Also, X experiences an octahedral crystal field of the Sb anions due to which the positions of the e_g and t_{2g} orbitals are now reversed. These d-orbitals of X and Fe/Ni hybridize to form antibonding and bonding orbitals with the former having dominant contributions from the X-d states and the latter with dominant contribution from Fe/Ni d states. Due to the differences in electronegativity between Fe and Ni, the bonding orbitals having dominant contributions from Ni are lower in energy than those from Fe. Figure 5.7d shows the schematics of the molecular orbitals. Now based on the number of valence electrons available, we find that all the bonding orbitals are completely filled while the antibonding orbitals are empty giving rise to a gap and stabilizing the system.

5.3.4 Dynamic stability and lattice thermal conductivity

The phonon dispersion and the density of states (phDOS) plots for the three systems are shown in Figure 5.9. The absence of imaginary frequencies in all the plots confirms the

dynamical stability of these materials. We observe stark differences between the phonon dispersion plots of TFNS and ZFNS/HFNS. Unlike the other two systems, TFNS phonon spectrum has a gap (varying between 25 to 50 cm^{-1} in the BZ) at around 150 cm^{-1} (Figure 5.9a). The atomic contributions to the phDOS for the modes lying below the phonon gap show that these are primarily associated with the vibrations of the heavy Sb atoms while the optical modes above the phonon gap have contributions from Ti, Fe and Ni, all having similar atomic masses. On replacing Ti with heavier Zr and Hf, we observe an overall softening of the optical phonon modes that results in closing of this phonon gap in ZFNS and HFNS. Additionally, in HFNS there is opening of a small gaps of 8 cm^{-1} at around 204 cm^{-1}. These changes indicate that ZFNS and HFNS exhibits enhanced mixing of the acoustic and optical phonons. As a consequence the heat carrying acoustic phonons in these materials will be more scattered by the optical ones compared to TFNS. Additionally in ZFNS, in the low frequency region (less than 150 cm^{-1}) of the phonon spectra, we observe that there are contributions from both the Sb and Zr atoms with the former dominating. However, in case of HFNS, Hf being heavier than Sb, the vibrations originating from the Hf atoms have much larger contribution than Sb in the low frequency window. Further, for ZFNS and HFNS, the high frequency modes are primarily due to vibrations of Fe atoms in the lattice.

The softening of the phonon modes as one moves from Ti to Zr to Hf also results in diminution of the phonon dispersion, a consequence of which is the lowering in the sound velocity as we move down the periodic table (Table 5.2). Analogously the Debye temperature is also reduced as one moves down the periodic table. In contrast, the Grüneissan parameter (γ) changes non-monotonously, increasing from TFNS to ZFNS and reducing when Zr is replaced by Hf.

The calculated lattice thermal conductivity as a function of temperature is shown in Figure 5.9d. As we move down the periodic table, we observe that the κ_l decreases monotonously. For TFNS we obtained a κ_l of 10.5 W m^{-1} K^{-1} at 300 K. We note that this is in reasonably good agreement with of previously computed and experimentally measured values of 11.2 and 7.9 W m^{-1} K^{-1}, respectively [145, 158]. With increase in temperature, the calculated

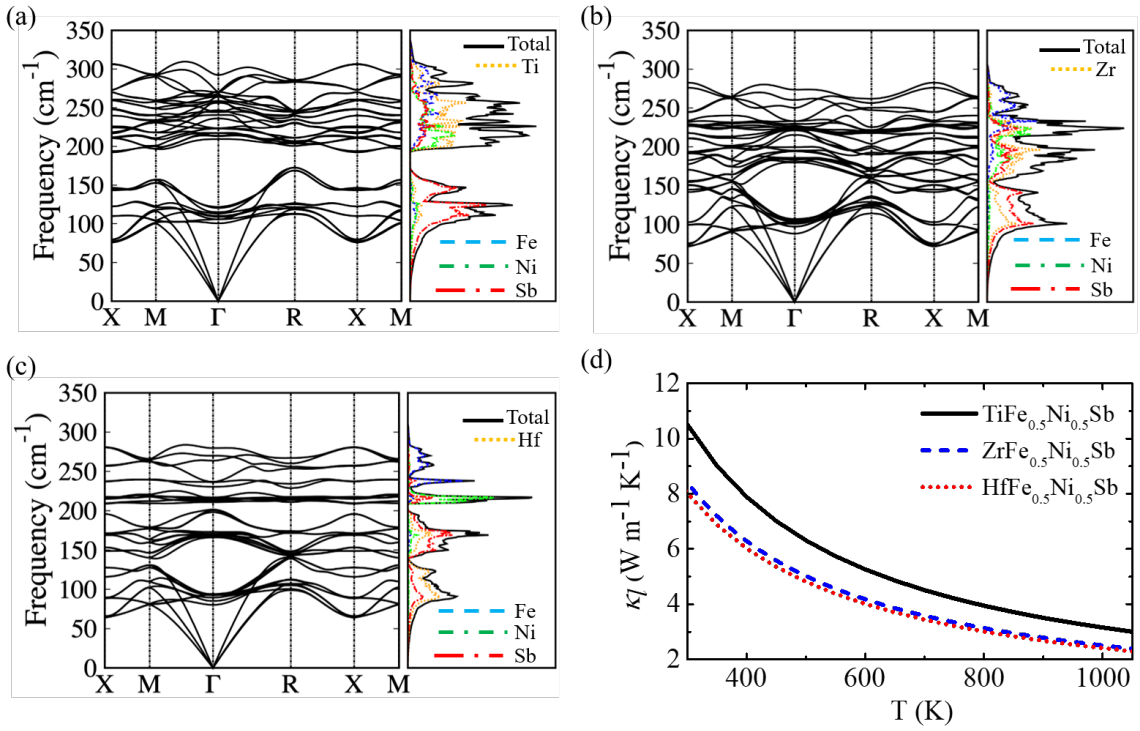

Figure 5.9: Phonon dispersion (left panel) and density of states (right panel) of (a) TFNS, (b) ZFNS and (c) HFNS. (d) Plot of κ_l as a function of T.

Table 5.2: Velocity of phonon modes (longitudinal (v_L), transverse (v_T) and average (v_{avg})), Gruneissan parameter (γ), Debye temperature (Θ_D) and lattice thermal conductivity (κ_l) at 300 K of TFNS, ZFNS and HFNS.

Compounds	$TiFe_{0.5}Ni_{0.5}Sb$	$ZrFe_{0.5}Ni_{0.5}Sb$	$HfFe_{0.5}Ni_{0.5}Sb$
v_L (ms^{-1})	7561	7359	6380
v_T (ms^{-1})	3738	3500	3087
v_{av} (ms^{-1})	4159	3937	3469
γ	2.04	2.16	2.10
Θ_D	483	438	389
k_l (W m^{-1} K^{-1})	10.52 (7.3[a], 11.24[b])	8.34 (7.0[a])	8.02 (5.8[a])

[a] experimental report [150, 152, 158]
[b] Computational report [145]

value reduces to 3.27 W m^{-1} K^{-1} at 1000 K. We note that these values are significantly less than what is generally observed for half-Heuslers (20 to 25 W m^{-1} K^{-1} at 300 K) [157]. On replacing Ti with Zr, we observed a further reduction of κ_l to 8.3 W m^{-1} K^{-1} at 300 K. This is also in very good agreement with a recent experimental measurement by Lee *et al.* where they obtained $\kappa_l \simeq 7$ W m^{-1} K^{-1} [150]. In contrast, when Zr is replaced with Hf we observe only a slight reduction in the value of κ_l (8.0 W m^{-1} K^{-1} at 300 K). Recent measurements by Hassan et al., obtained κ_l to be about 6 Wm^{-1} K^{-1} at 300 K. For all these systems we observe that our values of κ_l are overestimated compared to the existing experimental reports. We believe that this over estimation is due to the neglect of phonon scattering by defects and grain boundary in our calculations.

5.3.5 Electronic transport properties

The parameters needed to estimate the relaxation time are given in Table 5.3. The deformation potentials for electrons and holes are similar across different systems. However, V_{DP} of holes are slightly larger compared to that of electrons, suggesting that holes are more strongly coupled with the acoustic phonons than the electrons. Further, m_e^* (m_h^*) is largest for TFNS (HFNS) and smallest for HFNS (ZFNS). Moreover, in HFNS we observe that the holes are heavier than electrons. Using these parameters we find that the computed τ for holes are larger than that of electrons in TFNS and ZFNS while the trend is reversed for

Table 5.3: Deformation potentials (V_{DP}), effective masses (m^*) of electrons and holes, elastic constants (c_{11}), and their relaxation times (τ) at 300 K. The subscript/superscripts 'e' and 'h' represent electrons and holes, respectively.

Compounds	$TiFe_{0.5}Ni_{0.5}Sb$	$ZrFe_{0.5}Ni_{0.5}Sb$	$HfFe_{0.5}Ni_{0.5}Sb$
c_{11} (GPa)	1239	1193	1244
V_{DP}^h	15.44	15.76	15.89
m_h^*	1.67	1.55	1.49
τ_h	8.37	8.65	9.40
$V_{DP}^e(\Gamma)$	15.59	15.62	15.75
m_e^* (Γ)	2.41	1.70	1.45
τ_e (Γ)	4.76	7.66	9.93

HFNS. Largest value of τ_h (τ_e) is observed for ZFNS (HFNS) while HFNS (TFNS) have the smallest value.

Figure 5.10 and 5.11 show the transport properties calculated in a typical carrier concentration range of 10^{20} to 10^{21} cm^{-3} for both n (electrons) and p-type (holes) carriers. Consistent with the smallest value of ΔE, the energy difference between two conduction band valleys at X and Γ points of the BZ, HFNS has the maximum Seebeck coefficient of -327 μV/K for n-type carriers at around 750 K and 10^{20} cm^{-3}, which is highest amongst the three systems considered in this study. Maximum S of -305 μV/K (670 K) and -253 μV/K (670 K) are obtained for TFNS and ZFNS, respectively, at similar n-type carrier concentration. Additionally, $|S|$ for n-type carriers are larger than that of p-type carriers for all the systems. We note that this is consistent with that observed experimentally in TFNS [158].

The electrical conductivity, σ for the three systems as a function of temperature and carrier concentration are plotted in Figure 5.12. Since in TFNS and ZFNS $m_h^* < m_e^*$ and $\tau_h > \tau_e$, holes will be more conductive than electrons in these systems. In contrast the reverse is expected for HFNS. In accordance with the trends observed in m^* and τ we find that in TFNS and ZFNS (HFNS) p-type (n-type) carriers have larger values of σ compared to that of n-type (p-type) carriers. Infact, amongst the three systems HFNS exhibit largest conductivity for electrons. Moreover, the trends in the electronic contribution to lattice thermal

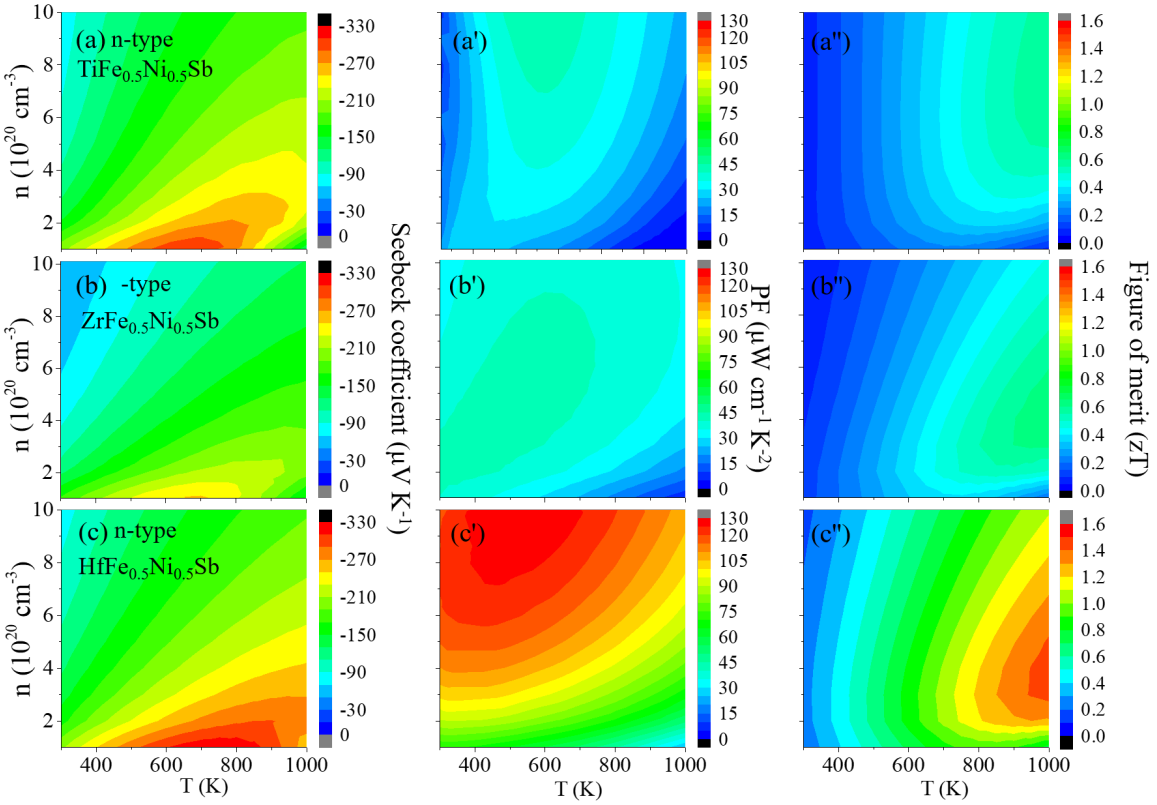

Figure 5.10: Seebeck coefficient, power factor and zT of n-type $TiFe_{0.5}Ni_{0.5}Sb$ (a, a′, a″), $ZrFe_{0.5}Ni_{0.5}Sb$ (b, b′, b″), $HfFe_{0.5}Ni_{0.5}Sb$ (c, c′, c″).

conductivity κ_e follows that observed in σ and is shown in Figure 5.13.

Due to large values of S and σ, electrons in HFNS show PF aslarge as 129 μWcm^{-1}K^{-2} at 10^{21} carrier concentration and 530 K temperature. These values are comparable to that observed in the state of the art HH thermoelectric materials like TaFeSb (160 μWcm^{-1}K^{-2} at 300 K) and NbFeSb (91.5 μWcm^{-1}K^{-2} at 300 K) [157]. Maximum power factors of 43 μWcm^{-1}K^{-2} at 10^{21} cm^{-3} electron concentration and 500 K temperature and 42 μWcm^{-1}K^{-2} at 4$\times$ 10^{20} cm^{-3} electron concentration and 400 K temperature are obtained for TFNS and ZFNS respectively. For TFNS and ZFNS p-type carriers yield better values of power factors with TFNS (ZFNS) having a value of 95 μWcm^{-1}K^{-2} at 10^{21} cm^{-3} and 650 K temperature (90 μWcm^{-1}K^{-2} at 10^{21} cm^{-3} and 670 K temperature). However HFNS is also have comparable value of 90 μWcm^{-1}K^{-2} at 10^{21} cm^{-3} and 650 K temperature.

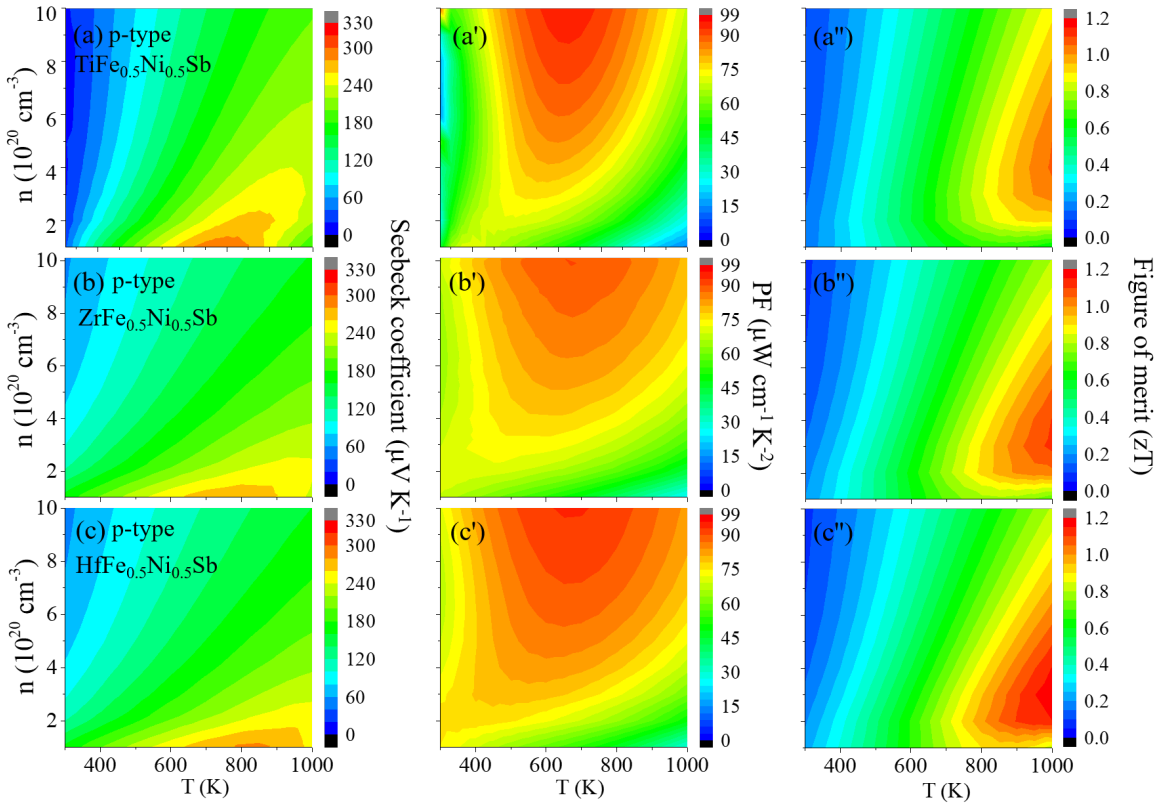

Figure 5.11: Seebeck coefficient, power factor and zT of p-type $TiFe_{0.5}Ni_{0.5}Sb$ (a, a′, a″), $ZrFe_{0.5}Ni_{0.5}Sb$ (b, b′, b″), $HfFe_{0.5}Ni_{0.5}Sb$ (c, c′, c″).

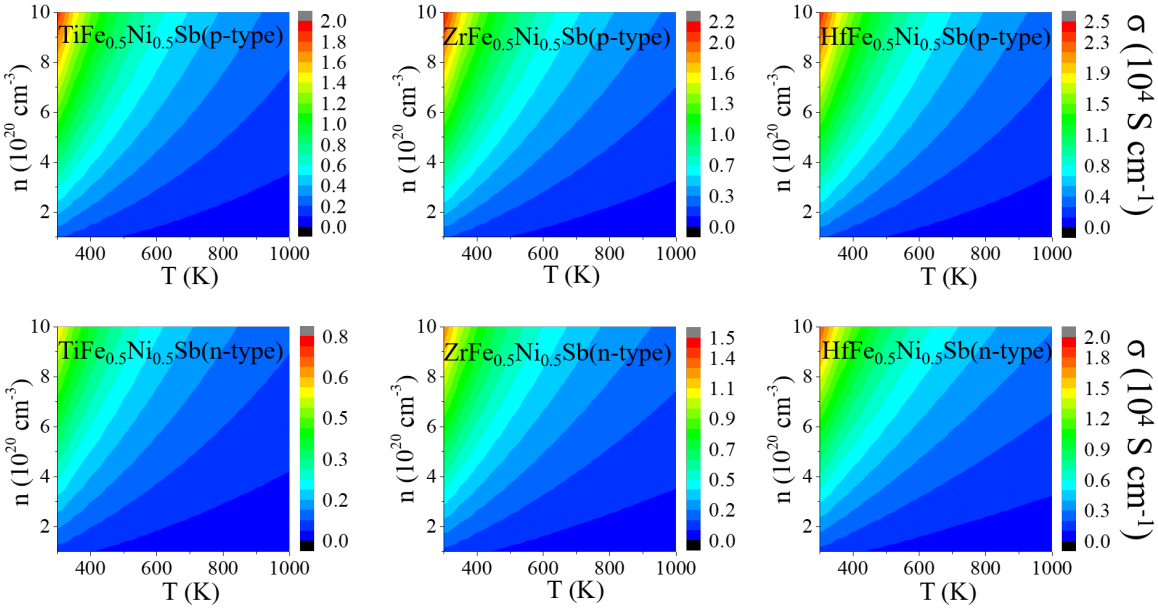

Figure 5.12: Electronic conductivity (σ) as a function of carrier concentration and temperature.

Our computed values of zT for all three system as shown in Fig 5.11(a″, b″, c″), 5.10(a″, b″, c″). For TFNS we obtained the maximum value of zT of 0.59 at 1000 K and 8$\times$ 10^{20} cm^{-3} (1.05 at 1000 K and 6$\times$ 10^{20} cm^{-3}) for n-type at (p-type) carriers. We note that this is in close agreement with that of 0.5 (0.75) at 973 K (973 K) obtained experimentally by Liu *et al.* [158] for p-type (n-type) carriers in TFNS. For ZFNS the zT values are 1.12 at 1000 K and 0.64 at 1000 K for p (3$\times$ 10^{20} cm^{-3}) and n-type (4$\times$ 10^{20} cm^{-3}) carriers, respectively. Amongst the three systems, HFNS exhibit the maximum value of zT for both p and n-type carriers. While a maximum zT of 1.45 at 1000 K was obtained for n-type carriers at 4$\times$ 10^{20} cm^{-3} , the p-type carriers exhibited a maximum value of zT of 1.19 at 1000 K and 3$\times$ 10^{20} cm^{-3}.

Apart from high lattice thermal conductivity, another important challenge in the use of hH materials is to find a candidate that has high zT for both n and p-type charge carriers. For example, though certain hH compounds like TaFeSb [66] , NbFeSb [163], ZrCoBi [68] are reported to have zT above unity when p-doped, their n-type counterparts do not have significant zT values in order to use the same material to make both the legs of the devices.

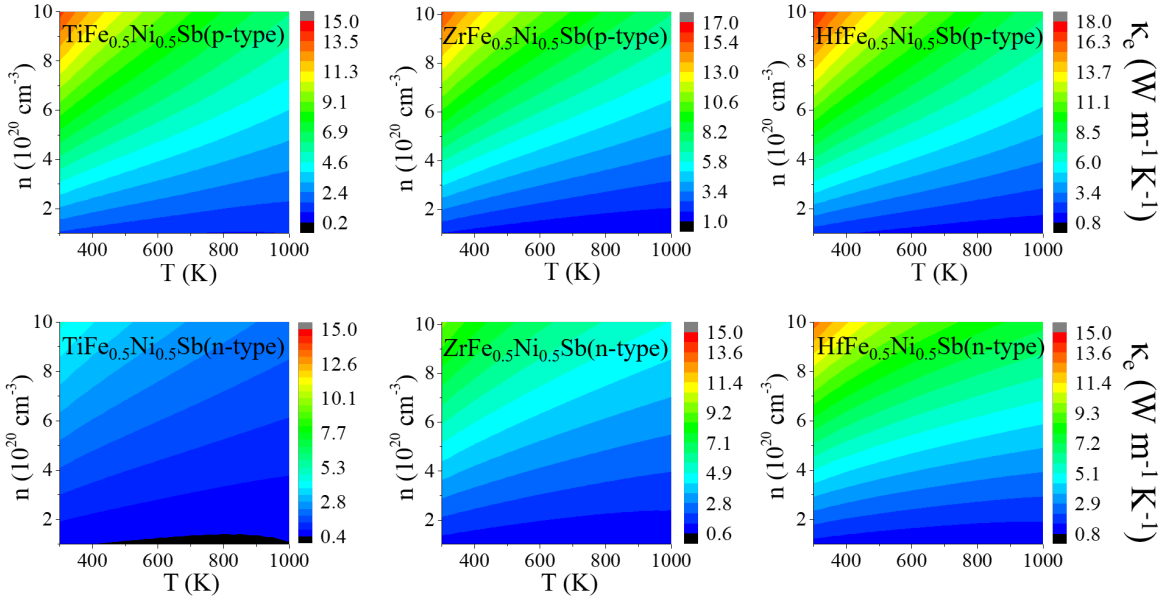

Figure 5.13: Electronic contribution to thermal conductivity (κ_e) as a function of carrier concentration and temperature.

Similarly, defective $Nb_{0.8}CoSb$ [69], TiCoSb and its composite [42, 126], MCoSb [73], and MNiSn [70,71] based hH has zT near and above unity in the n-type region. The zT exhibited by their p-type counterparts are quite low. In contrast, our calculations show that both n and p type HFNS have $zT > 1$ at round 1000 K. Hence, this material can be used to manufacture both the p and n-legs of the thermoelectric device.

5.4 Summary and Conclusions

In summary, using first principles DFT based calculations we have studied $XFe_{0.5}Ni_{0.5}Sb$ double half Heusler thermoelectric materials, where X belong to the group 4 elements of the periodic table. A detailed analysis of the nature of the bonding in these dhHs show that there is a presence of hierarchical bonding, i.e., varying degree of covalent and ionic bonds, in these systems that results in changes in electronic structure and lowering of lattice thermal conductivity. We observe that replacing Ti with Zr or Hf facilitates band convergence in the conduction band of these materials. Our calculations show that reduction of electronegativity and tensile strain induced due to change in atomic size have opposite ef-

fects on band convergence in these materials. While the former favours band convergence, the latter is detrimental for it. Additionally, electronegativity has a stronger effect than the chemical pressure. In accordance with the observed band convergence, we find that in these materials n-type carriers have larger Seebeck coefficient than there p-type counterparts, with $HfFe_{0.5}Ni_{0.5}Sb$ showing the largest value. Amongst the three materials considered in our study, $HfFe_{0.5}Ni_{0.5}Sb$ exhibits the largest value of zT for n-type carriers at around 1000 K. Moreover, p-doped $HfFe_{0.5}Ni_{0.5}Sb$ also have $zT > 1$ at 1000 K. We anticipate that our work will provide a guideline for the experimentalists in rational design of dhHs with high zT.

Chapter 6

Entropy-stabilized half-Heusler alloys $(TiHf)_{1/2}(Fe_{1-x}CoNi_{1+x})_{1/3}Sb$ with highly reduced lattice thermal conductivity

6.1 Introduction

Alloying to obtain desirable properties has long been a benchmark in materials science. In its traditional form, alloying involves partially substituting one of the elements in the parent composition with a foreign element to induce new properties. This classical approach has been extensively used to develop materials with improved strength, ductility, corrosion resistance, and other desirable attributes. However, to go beyond the realm of classical alloys, a novel 'high-entropy' alloying principle has recently garnered significant interest [164–166]. In a high-entropy alloy (HEA), three to five or even more elements substitute one of the elements of the parent composition in an equal or relatively large proportion to form a single-phase alloy. This results in a high configurational entropy, $\Delta S_{conf} = -R \sum_i x_i ln(x_i)$, where x_i denotes the mole fraction of the i^{th} substituent and R is the universal gas constant.

Interestingly, in certain cases, the high configurational entropy itself becomes the driving force in stabilizing a single phase alloy [167]. If the product $\mathrm{T}\Delta\mathrm{S}_{\mathrm{conf}}$, where T is absolute temperature, is large enough to overwhelm the enthalpy $\Delta\mathrm{H} > 0$, the Gibbs free energy $\Delta\mathrm{G} = \Delta\mathrm{H} - \mathrm{T}\Delta\mathrm{S}_{\mathrm{conf}}$ becomes negative, making it feasible for the alloy to form in a single-phase. Such alloys whose formation is driven primarily by the entropic consideration are called entropy-stabilized alloys (ESA) to distinguish them from other more conventional multicomponent alloys or solid-solutions, where the configurational entropy might be high but the phase stability need not be solely entropic driven. To exemplify this, consider a set of structurally analogous compounds $\mathrm{X}_n\mathrm{Y}_m$, where X = A, B, C, D, and E. Then, the alloy whose composition is $(\mathrm{A}_{1/5}\mathrm{B}_{1/5}\mathrm{C}_{1/5}\mathrm{D}_{1/5}\mathrm{E}_{1/5})_n\mathrm{Y}_m$ is highly probable to form as a single phase alloy since each of $\mathrm{X}_n\mathrm{Y}_m$ are known to form stable isostructural phases. Such an alloy will have a reasonably high configurational entropy (1.6R to be more precise) and should as such be labeled as a 'high-entropy alloy' since $\Delta\mathrm{S}_{\mathrm{conf}}$ exceeds 1.5R, which is the generally accepted lower limit. On the other hand, if some of the $\mathrm{X}_n\mathrm{Y}_m$ do not form, or form with a different crystal structure, then $(\mathrm{A}_{1/5}\mathrm{B}_{1/5}\mathrm{C}_{1/5}\mathrm{D}_{1/5}\mathrm{E}_{1/5})_n\mathrm{Y}_m$, should it form as a single-phase alloy is likely entropy-stabilized, which can be verified by performing an annealing procedure [167]. The entropy-stabilized high-entropy alloys have been demonstrated to have exceptional properties that surpass those of traditional alloys [165].

The high-entropy materials as high-performing thermoelectrics has recently generated lot of interest [168–172]. In HEAs, the presence of multiple elements at a single lattice site enhances lattice strain and point-defect scattering, lowering the lattice thermal conductivity, κ_l, which in turn aids in enhancing their thermoelectric performance. The compositional flexibility of HEAs can simultaneously be exploited to improve the transport properties, leading to high-performance thermoelectric materials.

In this study, we explore entropy-stabilization approach to designing a new entropy-stabilized half-Heusler material with ultra-low lattice thermal conductivity. The half-Heusler (hH) alloys have been extensively investigated for their thermoelectric properties. [173–177]. While they are highly favorable due to their structural robustness and superior electronic

properties, hHs also have an intrinsically high lattice thermal conductivity (κ_l), which limits their potential for thermoelectric applications. The conventional doping approach can lower κ_l up to some extent. For example, in the alloy $TiFe_{1/2}Ni_{1/2}Sb$, obtained from TiCoSb by replacing Co with Fe and Ni, $\kappa_l \approx 4$ W m^{-1} K^{-1} near 1000 K [57], which is almost 33% lower than κ_l of TiCoSb around the same temperature [178]. The question is, can one use the high-entropy route to reduce κ_l in hHs to values as low as in some of the well-known traditional chalcogenides thermoelectrics [179]?

Here, we combine theoretical and experimental approaches to obtain a new entropy-stabilized hH alloys with remarkably low values of κ_l. We demonstrate that the composition $(TiHf)_{1/2}(FeCoNi)_{1/3}Sb$, for which $\Delta S_{conf} = 1.79R$, is a entropy-stabilized, high-entropy hH alloy with a very low κ_l value of 1.8 W m^{-1} K^{-1} at 973 K, which is one of the lowest κ_l values known within the hH family of alloys [180]. κ_l is further reduced by tuning the Fe/Ni ratio in $(TiHf)_{1/2}(Fe_{1-x}CoNi_{1+x})_{1/3}Sb$. With increasing x, κ_l systematically decreases, approaching the theoretical minimum ($\kappa_{min} \approx 1$ W m^{-1} K^{-1}) for x = 0.5 near T = 973 K. This is one of the rare cases in hH alloys where κ_l becomes as low as κ_{min}, underpinning the effectiveness of entropy stabilization in designing novel thermoelectric materials. Since $(TiHf)_{1/2}(FeCoNi)_{1/3}Sb$ has a nominal valence electron count (VEC) of 18, the carrier density is also optimized by tuning the Fe/Ni ratio, which changes the VEC to $18 + \delta$ ($\delta > 0$ for Fe/Ni < 1). We observed a seven-fold increase in the electrical conductivity of the alloy $x = 0.5$ as compared to $x = 0$. This causes the Seebeck coefficient to decrease systematically, but the power factor showed a significant increase from 7μW cm^{-1} K^{-2} to 16μW cm^{-1} K^{-2} at 973 K, leading to high zT value of 0.55.

6.2 Experimental and computational Details

Experimental details: All the samples were prepared by arc-melting the constituent elements under an inert atmosphere of high-purity Ar gas. The high-purity Ti (Nanoshel 99.9% or Sigma Aldrich 99.9%), Hf (Sigma Aldrich 99.9%), Fe (Sigma Aldrich 99.9%), Co (Sigma Aldrich 99.5%), and Sb (Alfa Aesar 99.98%) were used. These elements were weighed ac-

cording to the desired stoichiometry, and loaded on the water-cooled copper hearth of the arc-furnace that was subsequently pumped (rotary vacuum) and flushed with Ar-gas several times before striking the arc. About 10 % excess Sb was added to compensate for the weight loss due to its low boiling point.

A Zr-getter was employed to minimize any residual oxygen in the chamber. The ingot was remelted 3-4 times, with each remelting involving flipping the ingot to ensure chemical homogeneity. After being removed from the furnace, the ingot was hand-ground for 1 hour using an agate mortar and pestle. The resulting fine powder was subjected to hot-pressing at 57 MPa and 1343 K for 300 seconds. The hot-pressed pellets achieved high density. The room-temperature density was calculated using the formula: $\rho_{\mathrm{m}} = \mathrm{M}/\pi\mathrm{R}^2\mathrm{H}$, where R, H, and M represent the radius, height, and mass of the hot-pressed pellet, respectively. The phase purity of the samples was verified via powder X-ray diffraction (XRD) using a Bruker D8 Advance diffractometer. Structural parameters were derived from Rietveld refinement of the XRD data. High-resolution transmission electron microscopy (HRTEM) was employed to capture high-resolution electron micrographs and selected area electron diffraction (SAED) patterns using a JEOL JEM 2200FS at 200 keV. For imaging, the samples were ground in ethanol and drop-cast onto a copper grid coated with amorphous carbon using a micropipette. The sample was then oven-dried at 80°C, followed by plasma cleaning to remove any residual organic solvent. Thermal diffusivity (D) was measured using a laser flash analyzer (Linseis LFA-1000), and thermal conductivity was calculated from the thermal diffusivity using the equation $\kappa = \mathrm{DC_p}\rho_{\mathrm{m}}$, where ρ_m is the mass density and $\mathrm{C_p}$ is the specific heat. The specific heat above 300 K was assumed to follow the Dulong-Petit limit, $3nR$, where n is the number of atoms per formula unit and R is the universal gas constant (8.314 J mol^{-1}). The Seebeck coefficient and electrical conductivity were measured simultaneously using a Linseis LSR-3 on rectangular-shaped samples. Charge carrier concentration was estimated by measuring the Hall coefficient with an ac transport option in a custom-built setup. The transverse (ν_t) and longitudinal (ν_l) sound velocities were measured on a disk-shaped sample using an Epoch 650 Ultrasonic Flaw Detector (Olympus) with a 5 MHz transducer

Computational details: DFT based calculations were performed using the Quantum ESPRESSO software [115, 116]. Ultrasoft pseudopotentials were used for valence electron-ion interactions [117]. The valence configurations of $3s^2 3p^6 3d^2 4s^2$, $5s^2 5p^6 5d^2 6s^2$, $3d^7 4s^1$, $3d^8 4s^1$, $3d^9 4s^1$ and $5s^2 5p^3$ had been used for Ti, Hf, Fe, Co, Ni and Sb, respectively. A kinetic energy cutoff of 65 Ry (650 Ry) had been used to expand the wave function (charge density) in a plane wave basis. Perdew-Burke-Ernzerhof parameterization of the generalized gradient approximation (GGA-PBE) was used to describe the electron-electron exchange and correlation interaction [118]. Conventional cubic unit cell was used to calculate the electronic state of Ti$(FeNi)_{1/2}$Sb, Hf$(FeNi)_{1/2}$Sb, and $(TiHf)_{1/2}(FeNi)_{1/2}$Sb. For additional incorporation Co in place of Fe and Ni we created a super cell of 2 $\times$ 2 $\times$ 3 starting from primitive fcc unit cell, thus having 36 atoms ($Ti_6Hf_6Fe_4Co_4Ni_4Sb_{12}$). A shifted 8 $\times$ 8 $\times$ 8 Monkhorst-Pack k-point mesh [92] was used to perform BZ integrations for Ti$(FeNi)_{1/2}$Sb, Hf$(FeNi)_{1/2}$Sb, and $(TiHf)_{1/2}(FeNi)_{1/2}$Sb where a conventional fcc structure with 12 atoms is considered for calculation. For $Ti_6Hf_6Fe_4Co_4Ni_4Sb_{12}$, a 6 $\times$ 6 $\times$ 4 k-point mesh was used. To speed up convergence we have used Marzari-Vanderbilt smearing with a smearing width of 0.005 Ry. To understand the evolution of band structure with various composition unfolding of the band structure from the smaller BZ of the supercell onto the bigger BZ of the primitive unit cell was performed using an unfolding method proposed by Boykin [119]. We have used Special Quasi-random Structure(SQS) generated using mcsqs code (a part of ATAT toolkit) to get a random structure of $Ti_6Hf_6Fe_4Co_4Ni_4Sb_{12}$ [181]. We have used a 2 $\times$ 2 $\times$ 3 supercell having 36 total atoms with 6 of Ti and Hf each, 4 of Fe, Co, and Ni each and 12 of Sb. By changing the Fe and Ni atoms to 2 and 6 we will have another composition which is x = 0.5. Random structure were generated using SQS. All the generated structures were relaxed before considering the most energetically favorable for further calculation. The cutoff radius of the randomization was taken to be 3 times the lattice parameter of premittive cell as we are using a supercell of 2 $\times$ 2 $\times$ 3. The Enthalpy of formation (ΔH) of the

compositions are calculated using the following expression:

$$\Delta H = E_{total} - \sum_{i=1}^{n} E_i \tag{6.1}$$

where E_i and E_{total} represents the total energy of individual component in bulk form and total energy of composition respectively. Change in Gibbs free energy of formation (ΔG) at any temperature (T) is estimated using the expression:

$$\Delta G = \Delta H - T\Delta S \tag{6.2}$$

The elastic coefficients are calculated using open source Thermo-PW package (a driver of QE routines). The symmetry of the most stable SQS was obtained using seek-path package [182]. The same SQS structure with new lattice parameter and symmetry is then used as an input for elastic constant calculation.

6.3 Results and discussion

6.3.1 Realization of a new entropy stabilized half-Heusler $(TiHf)_{1/2}(FeCoNi)_{1/3}Sb$

Synthesis and structural characterization

X-ray diffraction

The alloy $Ti(FeNi)_{1/2}Sb$ has been reported to be stable in cubic *F-43m* hH structure with an intrinsic *p*-type behaviour and a thermal conductivity of around 10 W m^{-1} K^{-1} at 300 K [57]. In this work, we have successfully synthesized its Hf analog $Hf(FeNi)_{1/2}Sb$. Figure 6.1a shows the powder X-ray diffraction (PXRD) patterns of our $Ti(FeNi)_{1/2}Sb$ and $Hf(FeNi)_{1/2}Sb$ samples. Both the samples show the requisite diffraction patterns, conforming fully to the hH structure with no extra (secondary) diffraction peaks present, indicating

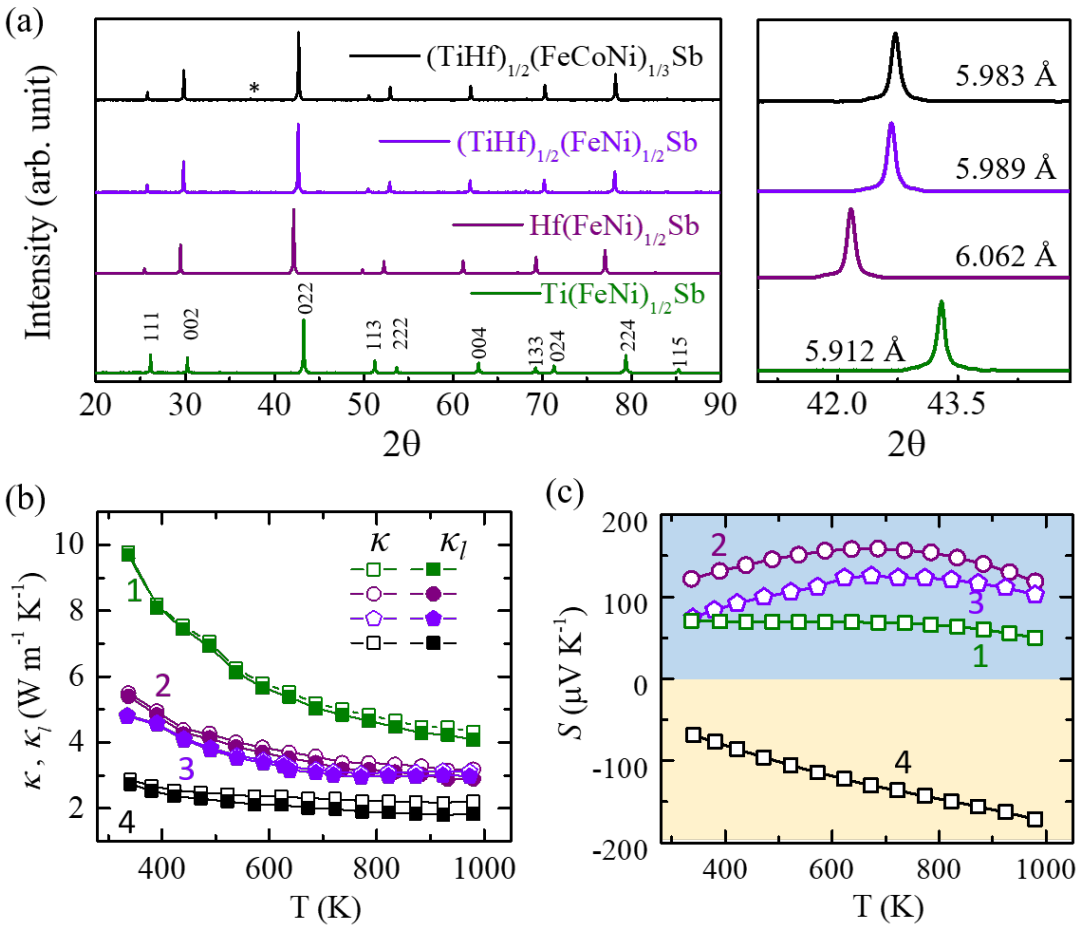

Figure 6.1: (a) Powder x-ray diffraction of $Ti(FeNi)_{1/2}Sb$, $Hf(FeNi)_{1/2}Sb$, $(TiHf)_{1/2}(FeNi)_{1/2}Sb$, and $(TiHf)_{1/2}(FeCoNi)_{1/3}Sb$ labelled as 1, 2, 3, and 4, respectively. The right panel shows a zoomed-in view of the (022) peak with lattice parameters shown for each alloy; (b) As-measured or total, κ (open symbol), and lattice, κ_l, thermal conductivity; and (c) the temperature variation of Seebeck coefficient, S for the four alloys.

that these sample are phase pure. The PXRD pattern for $Hf(FeNi)_{1/2}Sb$ is shifted towards smaller 2θ values consistent with the bigger ionic radius of Hf compared to Ti. The lattice parameters of the two alloys are, respectively, 5.912 Å (Ti) and 6.062 Å (Hf).

The PXRD patterns of $(TiHf)_{1/2}(FeNi)_{1/2}Sb$ and $(TiHf)_{1/2}(FeCoNi)_{1/3}Sb$ are, synthesized in this work, are also shown in Figure 6.1a. The observed patterns are analogous to $Ti(FeNi)_{1/2}Sb$, showing that they also form in the desired hH structure. The absence of any extra peak in their PXRD patterns indicate that no impurity of secondary phase(s) precipitate or form during their synthesis. The lattice parameter of $(TiHf)_{1/2}(FeNi)_{1/2}Sb$ 5.989 Åis intermediate between that of $Ti(FeNi)_{1/2}Sb$ and $Hf(FeNi)_{1/2}Sb$. Upon Co incorporation, the lattice parameter remains nearly unchanged since the size of Co is intermediate between that of Ni and Fe. This is shown in the right panel of Figure 6.1a, where a zoomed-in view of the (224) peak is shown. The diffraction peaks of $(TiHf)_{1/2}(FeCoNi)_{1/3}Sb$ are somewhat broadened compared to $(TiHf)_{1/2}(FeNi)_{1/2}Sb$, which may be due to the presence of lattice strain. The lattice parameter (calculated and experimental), mass density, and relative density of all the samples are listed in Table 6.1.

Table 6.1: Experimental, calculated lattice parameter and density (relative density).

Composition	a/b/c (Å) (experimental)	a/b/c (Å) (calculated)	Density (g cm^{-3})
$Ti(FeNi)_{1/2}Sb$	5.912	5.919	7.0 (93 %)
$Hf(FeNi)_{1/2}Sb$	6.062	6.081	9.8 (93 %)
$(TiHf)_{1/2}(FeNi)_{1/2}Sb$	5.989	6.006	8.3 (93 %)
$(TiHf)_{1/2}(FeCoNi)_{1/3}Sb$	5.983	5.998	8.3 (93 %)

SEM and TEM analysis

The single phase nature of $(TiHf)_{1/2}(FeCoNi)_{1/3}Sb$ is further confirmed by analyzing the microstructure under a scanning electron microscope. The chemical mapping and elemental composition is obtained using the EDS probe. The results are shown in Figure 6.3. The elemental distribution appears homogeneous with no sign of decomposition or phase segregation, consistent with PXRD result. A high resolution TEM image is shown in Figure 6.2a

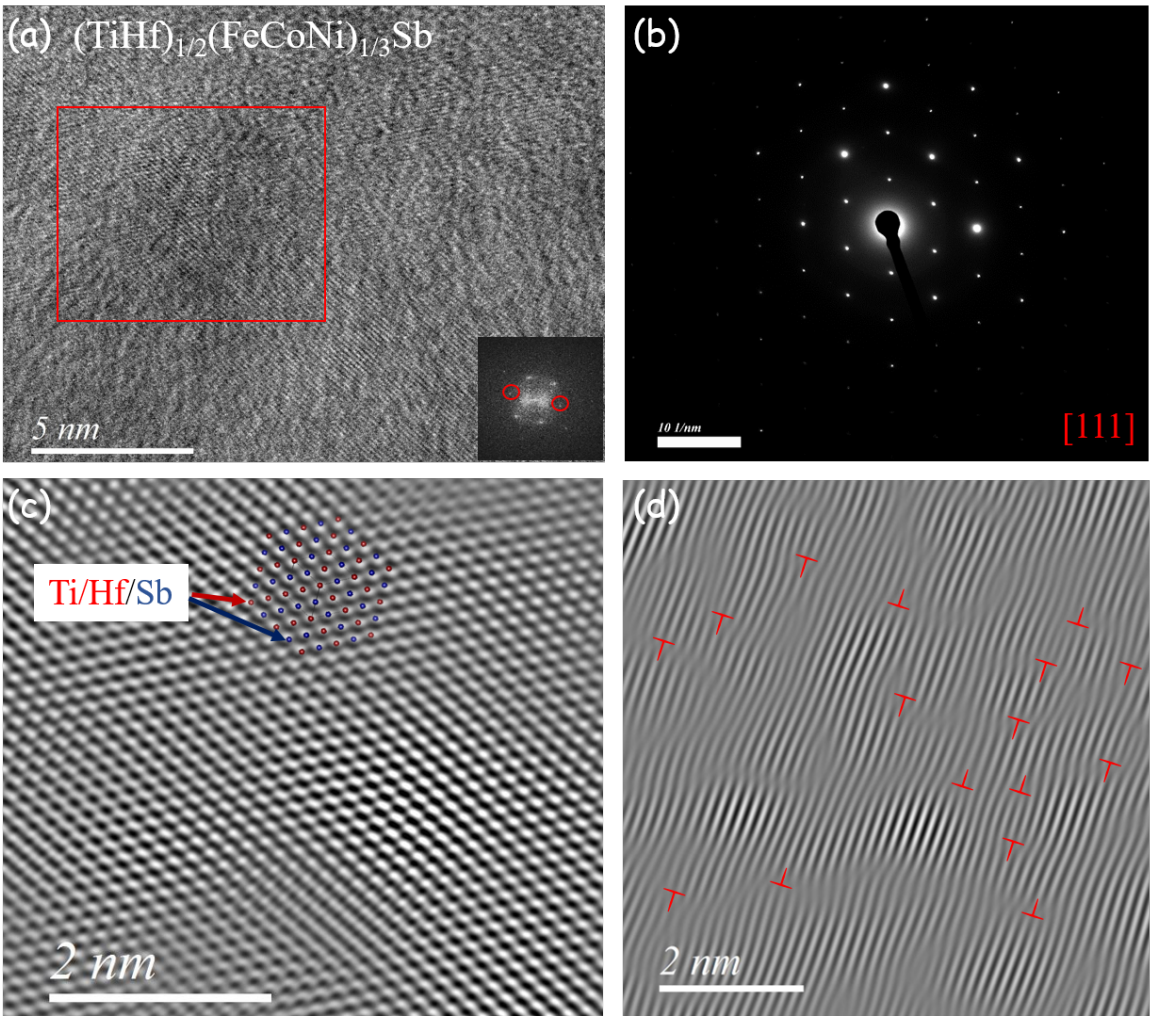

Figure 6.2: (a) high resolution TEM image with FFT in inset, (b) SAED pattern, (c) IFFT image of the selected region in (a), and (d) defects in plain [220]

in real space. The fast Fourier transformed (FFT) image agrees well with the corresponding selected area diffraction (SAED) pattern shown in Figure 6.2b. Despite having multiple atoms occupying the same site the material is highly crystalline and the presence of sharp diffraction spots in the SAED pattern are indicative of high-crystallinity of our samples. The inverse of FFT of the selected area (red box) is shown in Figure 6.2c where the arrangement of Ti/Hf and Sb is shown. Plain [220] is shown in Figure 6.2d where the defects are shown by burger vectors and has an important role in reduction of thermal conductivity. As discussed in the main text, strain gets doubled with Co incorporation which can be seen in Figure 6.2d.

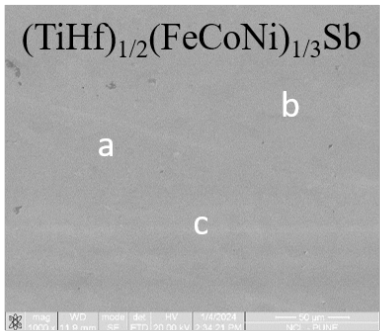

Fe (%)	Co (%)	Ni (%)
[a]12.19	12.42	14.20
[b]12.78	13.17	13.86
[c]13.60	14.40	14.73

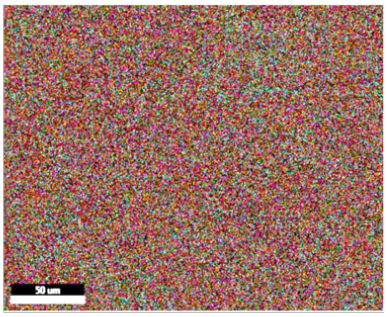

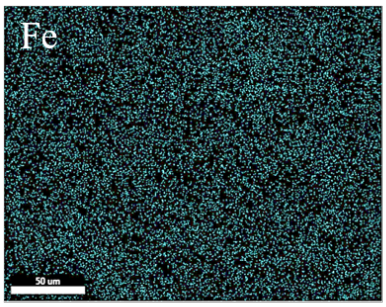

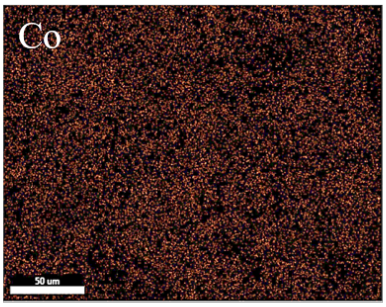

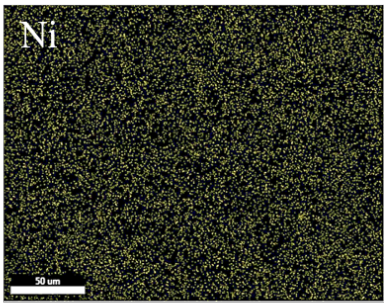

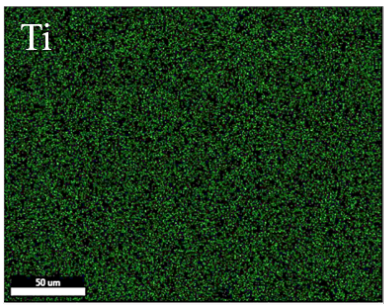

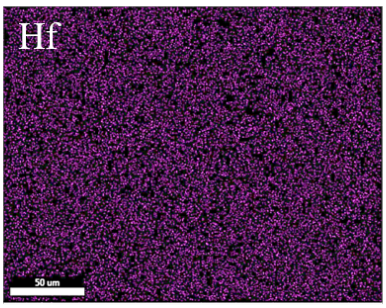

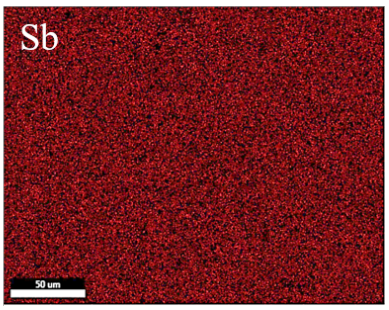

Figure 6.3: A representative electron micrograph of the alloy $(TiHf)_{1/2}(FeCoNi)_{1/3}Sb$ along with elemental chemical mapping and elemental composition at points labeled a, b and c.

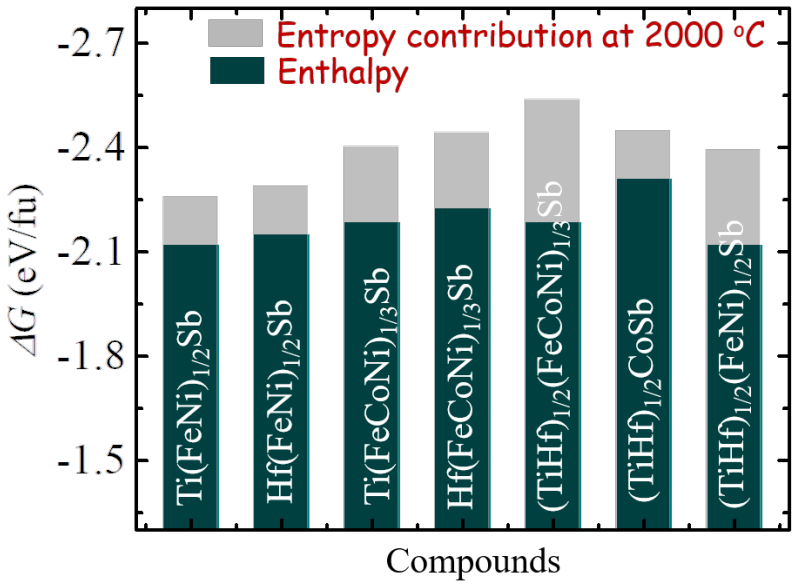

Figure 6.4: Enthalpy of formation and Gibbs free energy of formation (ΔG) contribution at 2000 ^{o}C

Entropy effect

To quantify the configurational entropy of the alloy $(TiHf)_{1/2}(FeCoNi)_{1/3}Sb$, the ΔS_{conf} is obtained using the expression [7]:

$$\Delta S_{conf} = -R\left[\left(\sum_{i=1}^{m} x_i \ln x_i\right)_X + \left(\sum_{j=1}^{n} x_j \ln x_j\right)_Y + \left(\sum_{k=1}^{l} x_k \ln x_k\right)_Z\right], \qquad (6.3)$$

where m, n, and l are the number of constituent elements at the site X, Y, and Z, respectively, and x_i, x_j, and x_k are their respective mole fractions. The calculated ΔS_{conf} for $(TiHf)_{1/2}(FeCoNi)_{1/3}Sb$ is $1.79R$, which exceeds the generally accepted threshold value of $1.5R$ used for classifying the high-entropy alloys.

In Figure 6.4, the calculated Gibbs free energy of formation (ΔG) is shown for a number of alloys of our interest that can potentially form using the elements Ti, Hf, Fe, Ni, Co, and Sb. ΔG at zero-temperature is found to be the lowest for the alloy $Ti_{1/2}Hf_{1/2}CoSb$ (≈ -2.3 eV), indicating that this is the most stable alloy amongst the alloys considered. Interestingly, upon incorporating the $T\Delta S_{conf}$ term, taking T = 2273 K, ΔG becomes lowest

for the alloy $(TiHf)_{1/2}(FeCoNi)_{1/3}Sb$, suggesting that entropic considerations must be taken into account to understand the experimentally observed stability of $(TiHf)_{1/2}(FeCoNi)_{1/3}Sb$. To estimate the temperature T_0 above which the phase $(TiHf)_{1/2}(FeCoNi)_{1/3}Sb$ becomes stable, we plot ΔG as a function of temperature shown in Figure 6.5a. The linearly varying ΔG versus T plots for $Ti(FeNi)_{1/2}Sb$ and $(TiHf)_{1/2}(FeCoNi)_{1/3}Sb$, cross each other near T_0 = 1450 K, indicating that $(TiHf)_{1/2}(FeCoNi)_{1/3}Sb$ is entropy-stabilized above this temperature; or equivalently, if $(TiHf)_{1/2}(FeCoNi)_{1/3}Sb$ is indeed entropy stabilized, we expect it to decompose when annealed at some temperature $T < T_0$ for a sufficient length of time [164]. We should emphasize here that our synthesis method involves arc-melting the constituents on a water-cooled hearth (see Section Experimental and computational details). Thus, when the arc is turned-off, the melt freezes-out rapidly, which is akin to quenching the sample from a high temperature (above T_0), kinetically arresting the high-entropy phase. The subsequent hot-pressing at 1343 K (see Section Experimental and computational details) is slightly below T_0, but the duration of this process (300 s) is not long enough to dissociate the entropy-stabilized phase.

To corroborate this, we annealed a small section of $(TiHf)_{1/2}(FeCoNi)_{1/3}Sb$ at 1173 K for seven days. The annealed specimen shows clear signs of decomposition, as the diffraction peaks in the PXRD pattern split upon annealing. This is demonstrated in Figure 6.5b, where a zoomed-in view of the (224) peak is shown. However, upon remelting the annealed specimen, the splitting disappeared, as shown in the bottom panel of Figure 6.5b. This observation strongly supports our conclusion that the alloy $(TiHf)_{1/2}(FeCoNi)_{1/3}Sb$ is not only a high-entropy alloy (ΔS_{conf} = 1.79R ¿ 1.5R) but is also entropy-stabilized. A section of the specimen annealed @1173K, when examined under an electron microscope, revealed the presence of Co-rich $(TiHf)_{1/2}CoSb$ and Co-deficient $(TiHf)_{1/2}(FeNi)_{1/2}Sb$ phases to which the alloy $(TiHf)_{1/2}(FeCoNi)_{1/3}Sb$ is expected to decomposes upon annealing as shown in Figure 6.6.

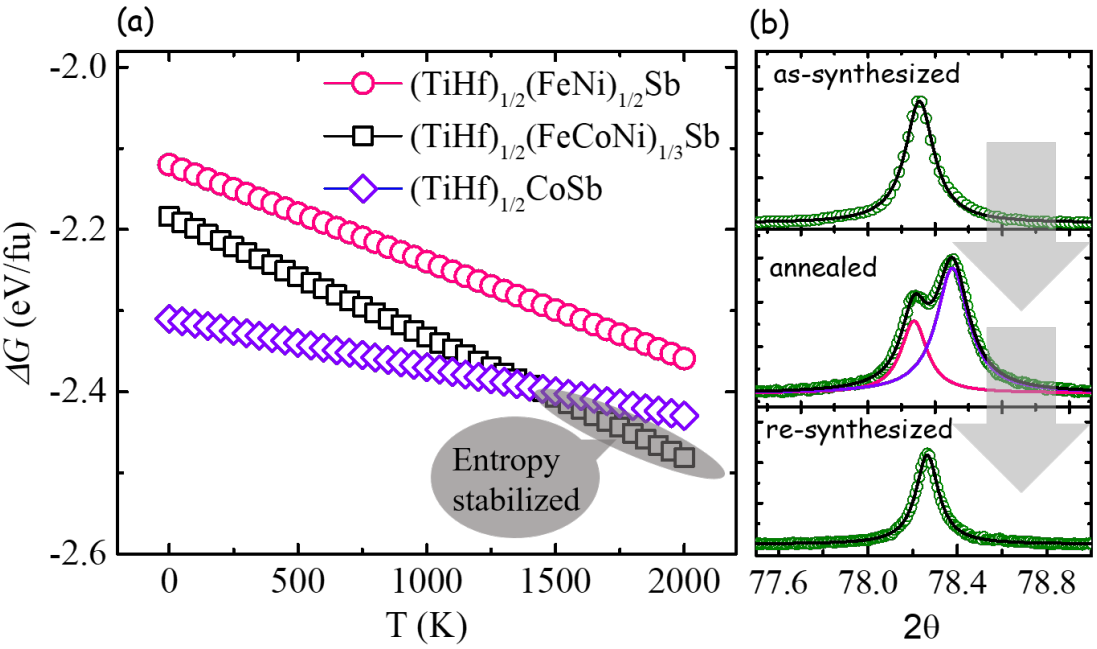

Figure 6.5: (a) Variation of Gibbs free energy of formation, ΔG, with temperature (b) A zoomed-in view of the (224) diffraction peak in the as-synthesized, annealed, and re-synthesized $(TiHf)_{1/2}(FeCoNi)_{1/3}Sb$ samples. The line trough the data points are a guide to the eye. The two deconvoluted peaks in the diffraction pattern of annealed sample correspond to the phases $(TiHf)_{1/2}(FeNi)_{1/2}Sb$ (pink) and $(TiHf)_{1/2}CoSb$ (violet). See text for details.

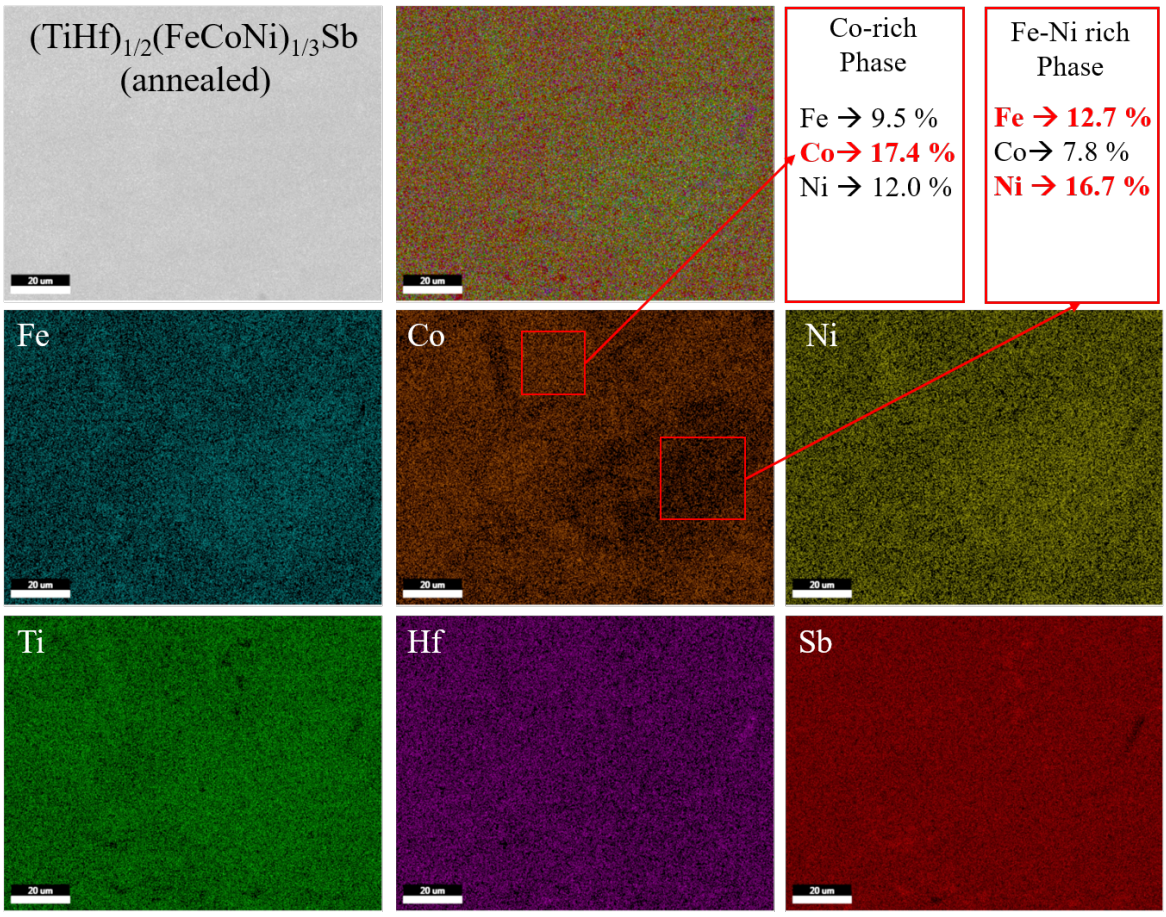

Figure 6.6: chemical mapping of annealed $(TiHf)_{1/2}(FeCoNi)_{1/3}Sb$.

Ultra-low lattice thermal conductivity of entropy-stabilized $(TiHf)_{1/2}(FeCoNi)_{1/3}Sb$

The thermal conductivity of $Hf(FeNi)_{1/2}Sb$ is observed to be 5.4 W m^{-1} K^{-1} around room-temperature (RT), as shown in Figure 6.1b, which is almost half that of $Ti(FeNi)_{1/2}Sb$. Note that κ_e for these materials is marginally small, making $\kappa_l \approx \kappa$. This massive reduction is caused by the heavier mass of Hf compared to Ti, resulting in a softening of the phonon modes. In $(TiHf)Fe_{0.5}Ni_{0.5}Sb$, κ_l reduces further to 4.8 W m^{-1} K^{-1} at 300 K, which can be attributed to the increased point-mass fluctuations upon random occupation of the $4a$ site by Ti and Hf. Finally, upon going from $(TiHf)_{1/2}(FeNi)_{1/2}Sb$ to $(TiHf)_{1/2}(FeCoNi)_{1/3}Sb$, κ_l diminishes further by a significant amount, with the room-temperature value of κ_l decreasing to 3 W m^{-1} K^{-1}. In order get some insight into this, we measured the longitudinal (v_L) and transverse (v_T) sound velocities for $Ti(FeNi)_{1/2}Sb$, $Hf(FeNi)_{1/2}Sb$, $(TiHf)_{1/2}(FeNi)_{1/2}Sb$, and $(TiHf)_{1/2}(FeCoNi)_{1/3}Sb$. The measure results are tabulated in Table 6.2. In $Ti(FeNi)_{1/2}Sb$, $v_L \approx 5500$ m s^{-1} and $v_T \approx 3100$ m s^{-1} are in good agreement with Ref. [57]. In $(TiHf)_{1/2}(FeNi)_{1/2}Sb$, both v_L and v_T decrease by $15 - 18\%$, due to the heavier Hf replacing a part of Ti. In $Hf(FeNi)_{1/2}Sb$, the sound velocity decreases further by $7 - 9\%$. The decrease from Ti to $Ti_{0.5}Hf_{0.5}$ is larger than from $Ti_{0.5}Hf_{0.5}$ to Hf due to the reduced atomic disorder in $Hf(FeNi)_{1/2}Sb$ compared to $(TiHf)_{1/2}(FeNi)_{1/2}Sb$. Remarkably, in $(TiHf)_{1/2}(FeCoNi)_{1/3}Sb$, the average sound velocity [with respect to $(TiHf)_{1/2}(FeNi)_{1/2}Sb$] reduces even further by almost 20%. Since the average mass of Fe and Ni is nearly the same as that of Co, one cannot attribute the observed large reduction of sound velocity to the average atomic mass of the Y-site.

The reduction of sound velocity can also be due to the reduced dispersion of the heat carrying acoustic phonon modes because of the change in the nature of the chemical bonds. In order to understand whether the introduction of Co results in change of the nature of bonding we have computed the charge density difference ($\Delta\rho$), which is given as:

$$\Delta\rho(r) = \rho_{system}(r) - \sum_i \rho_i^{atom} \tag{6.4}$$

where the first term on the right hand side of the above equation is the charge density of the material at a point *r* while the second term is the charge density computed by the superposition of the atomic charge densities; the summation *i* runs over all the atoms in the material. A positive (negative) value of $\Delta\rho$ implies charge accumulation (depletion) in space upon compound formation. The isosurfaces for $(TiHf)_{1/2}(FeNi)_{1/2}Sb$ and $(TiHf)_{1/2}(FeCoNi)_{1/3}Sb$ are shown in Figure 6.7. For the double Heusler we observe that there is charge accumulation is between Fe and X (Ti/Hf), with the charge density localized closer to Fe. In contrast, the charge density of the Ni atom is localized on the atom itself (Figure 6.7a). However, on introduction of Co, we observe that there is charge depletion from the Co atoms in $(TiHf)_{1/2}(FeCoNi)_{1/3}Sb$ (Figure 6.7b). The distribution of the accumulated/depleted electron density on Fe/Ni remains similar to that of the double Heusler. These results suggest that the introduction of Co in the Y sublattice enhances the heterogeneity in the degree of ionicity in the X-Y sublattice resulting in hierarchical bonding in the crystal that might affect the lattice vibrations and thereby the lattice thermal conductivity. This further underpins the dominating influence of the nature of bonding, atomic disorder and lattice strain on phonon scattering. The highly reduced thermal conductivity of $(TiHf)_{1/2}(FeCoNi)_{1/3}Sb$ is an evidence of the effectiveness of the high-entropy principle in reducing the lattice thermal conductivity (κ_l) to very low values. .

Table 6.2: Measured sound velocity, v_L, and v_T are the longitudinal and transverse sound velocities (in ms^{-1}).

Compositions	v_L	v_T
$Ti(FeNi)_{1/2}Sb$	5512	3129
$Hf(FeNi)_{1/2}Sb$	4202	2646
$(TiHf)_{1/2}(FeNi)_{1/2}Sb$	4541	2916
$(TiHf)_{1/2}(FeCoNi)_{1/3}Sb$	3667	2379

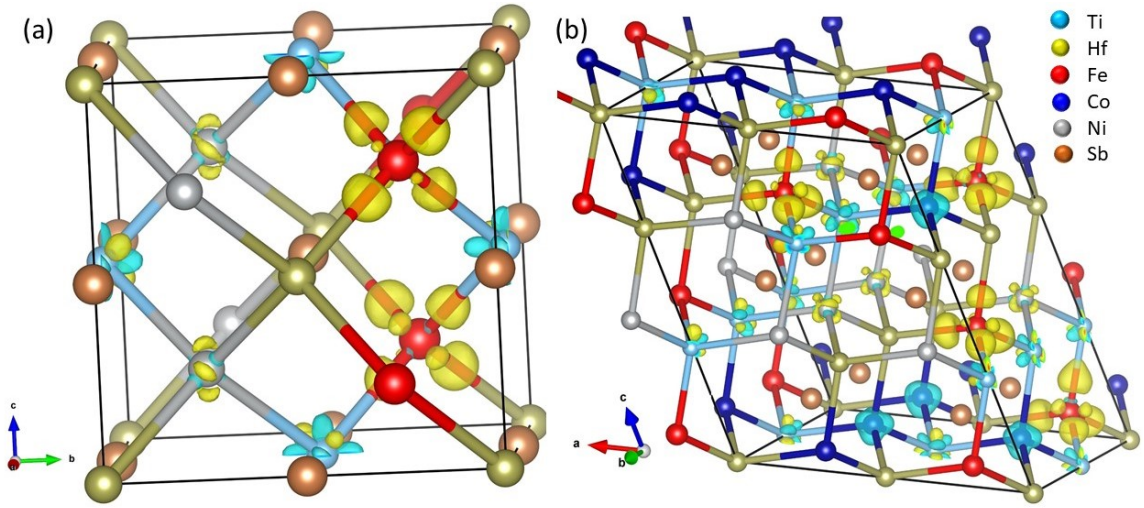

Figure 6.7: Isosurfaces showing charge density rearrangement after the formation of the half Heuslers for (a) $(TiHf)_{1/2}(FeNi)_{1/2}Sb$ and (b) $(TiHf)_{1/2}(FeCoNi)_{1/3}Sb$. Blue (yellow) isosurfaces show charge depletion (accumulation).

Electronic transport in $Ti(FeNi)_{1/2}Sb$, $Hf(FeNi)_{1/2}Sb$, $(TiHf)_{1/2}(FeNi)_{1/2}Sb$, and $(TiHf)_{1/2}(FeCoNi)_{1/3}Sb$

The density functional theory based first-principles calculations show that $Ti(FeNi)_{1/2}Sb$, $Hf(FeNi)_{1/2}Sb$, and $(TiHf)_{1/2}(FeNi)_{1/2}Sb$ have similar band structures. All three of them exhibit an indirect band gap (≈ 0.4 eV) between the conduction band minimum at the Γ-point and valence band maximum at the R-point of the Brillouin zone, as shown in Figure 6.10. Due to a small band gap, these alloys exhibit bipolarity at high temperatures, which is manifested as a decrease in the thermopower at high temperatures, as shown in Figure 6.1c. It is, therefore, imperative to increase the band gap to reduce the bipolarity.

Interestingly, the Seebeck coefficient of $(TiHf)_{1/2}(FeCoNi)_{1/3}Sb$ shows a monotonically increasing behavior up to the highest temperature, as shown in Figure 6.1c, suggesting that the incorporation of Co in the structure suppresses bipolarity. Additionally, Co substitution also changes the sign of the Seebeck coefficient from positive in $(TiHf)_{1/2}(FeNi)_{1/2}Sb$ to negative in $(TiHf)_{1/2}(FeCoNi)_{1/3}Sb$. This can be attributed to a small off-set in the valence electron count, say from $18-\delta$ in $(TiHf)_{1/2}(FeNi)_{1/2}Sb$ to $18+\delta$ in $(TiHf)_{1/2}(FeCoNi)_{1/3}Sb$, due to minor off-stoichiometry leading to self-doping. As we will see in the next section, the elec-

tron or hole doping is sensitive to the $\mathrm{Fe/Ni}$ ratio: $\mathrm{Fe/Ni} < 1$ (electron-doping) and $\mathrm{Fe/Ni} > 1$ (hole-doping). The calculated electronic band structure of $(TiHf)_{1/2}(FeCoNi)_{1/3}Sb$ is shown in Figure 6.10d. The indirect band gap increases to 0.7 eV from its value of 0.4 eV in $(TiHf)_{1/2}(FeNi)_{1/2}Sb$. This is in good empirical agreement with the fact that the measured Seebeck coefficient does not show bipolarity up to the highest temperature in our Seebeck measurement. As discussed in Section below, Co addition stabilizes the disordered structures. In absence of Co, it is imperative for the double Heusler to have an ordered arrangement of Fe and Ni to maintain zero-net valence throughout the crystal. However, on addition of Co this restriction is lifted and thereby stabilizing the disordered structures.

Effect of disorder on the band gap of the high entropy half Heusler

As described in the main text, we observe that the band gap of $(TiHf)_{1/2}(FeCoNi)_{1/3}Sb$ is increased by about 0.3 eV compared to that of $Ti(FeNi)_{1/2}Sb$ and $(TiHf)_{1/2}(FeNi)_{1/2}Sb$. In order to understand the origin of the enhancement of the band gap, we compared the structure of $(TiHf)_{1/2}(FeNi)_{1/2}Sb$ with the Co containing one. Since the valence and the conduction bands in these materials are due to the hybridization of the Ti/Hf-d orbitals, we focus only on the X-Y sublattice where each X atom is tetrahedrally coordinated to four Y atoms and vice-versa. In the double half Heuslers $(TiHf)_{1/2}(FeNi)_{1/2}Sb$, the vertices of the tetrahedron in which Ti/Hf resides are occupied by two Fe and Ni atoms each, forming an ordered Y sublattice (Figgure 6.8(a)). In contrast, upon adding Co, we observe a disorder in the Y sublattice where the vertices are occupied by different number of Fe/Co/Ni atoms (Figure 6.8b). For example, there are tetrahedra that are formed by three Fe and one Co atoms or one Fe, one Co and two Ni atoms, etc. It is this disorder that enhances the band gap. To prove this, we considered a $2\times2\times3$ supercell of the fcc unit cell and generated 53 SQS structures of $Ti(FeNi)_{1/2}Sb$, where the Y site has been randomly occupied by Fe/Ni, maintaining 1:1 stoichiometry in the unit cell, and computed the band gap for each case. These structures have different local coordination of the Ti atoms with Fe/Ni based on the occupation of the Y sublattice by Fe/Ni. Given that there are 4 sites that can be occupied by Fe/Ni, there are 5 possibilities, namely, each tetrahedra occupied by (a) 2 Fe and 2 Ni

atoms, (b) 3 Fe and 1 Ni atom, (c) 1 Fe and 3 Ni atom, (d) 4 Fe atoms and (e) 4 Ni atoms. In this supercell there are 12 such Ti-Fe/Ni tetrahedra and if all of them have an occupancy of type (a), then the structure is fully ordered. The computed band gaps as a function of number of octahedra with 2Fe and 2Ti are shown in Figure 6.9. We observe that for all the disordered cases the band gap is much larger compared to the ordered configuration. Further to understand the role of disorder on the X site due to introduction of Hf, we considered 5 configurations from the above SQS structures and randomly replaced 50% of the Ti with Hf at the X site, maintaining the same arrangement of the atoms in the Y sublattice. We find that the band gaps either remain similar to those without Hf (Figure 6.9). This suggests that it is the disorder in the Y sublattice that is primarily responsible for enhancement of band gap.

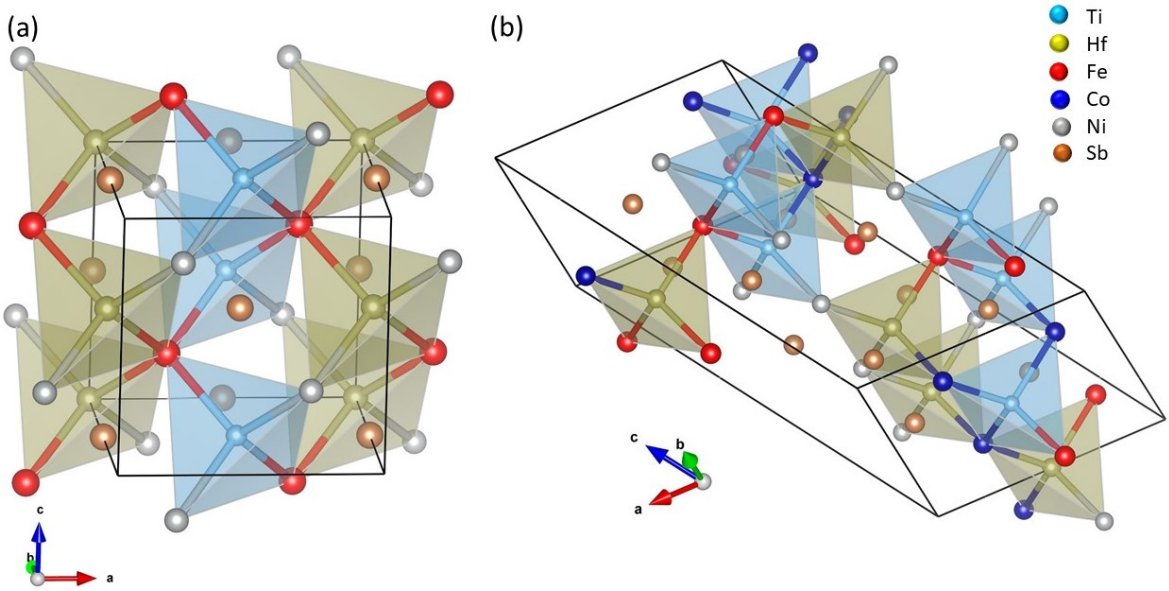

Figure 6.8: Structure of (a)$(TiHf)_{1/2}(FeNi)_{1/2}Sb$ and (b) $(TiHf)_{1/2}(FeCoNi)_{1/3}Sb$.

To understand the role of Co, we chose 4 SQS structures from those generated for $Ti(FeNi)_{1/2}Sb$ and randomly replaced the Fe/Ni with Co maintaining the 1:1:1 stoichiometry of Fe, Co and Ni and computed their formation energies with respect to the bulk form of the constituent elements and their band gap. The results are listed in Tables 6.3 and 6.4. We observe that upon introduction of Co there are slight changes in the band gap. However, these changes are much smaller compared to the changes observed due to disorder in the

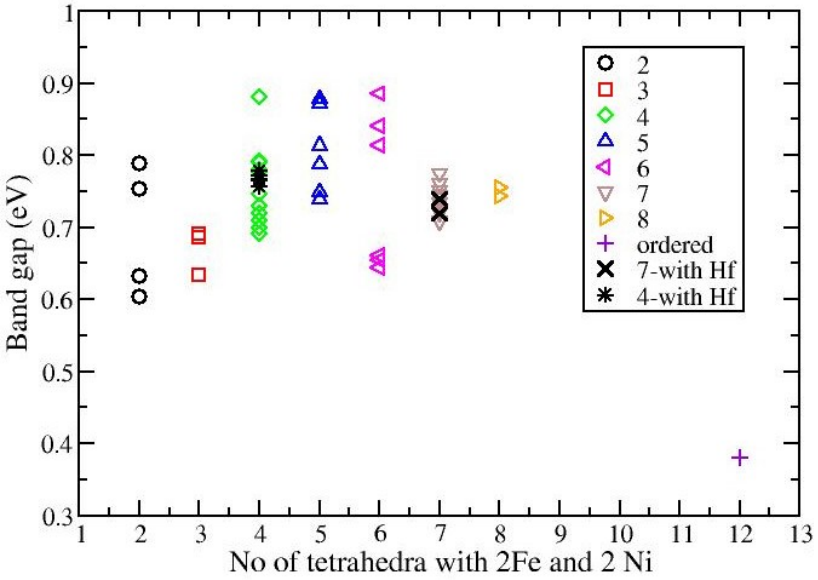

Figure 6.9: Variation of band gap with increasing disorder in the Y sublattice of $Ti(FeNi)_{1/2}Sb$.

Y sublattice. Moreover, we also note that the formation energy of the Co containing half Heuslers are more negative than those of the ones without Co, suggesting that Co is stabilizing the disordered structures. In absence of Co, it is imperative for the double Heusler to have an ordered arrangement of Fe and Ni to maintain zero-net valence throughout the crystal. However, on addition of Co this restriction is lifted and thereby stabilizing the disordered structures.

6.3.2 Electron-doping in $(TiHf)_{1/2}(FeCoNi)_{1/3}Sb$

Synthesis and structural characterizations of $(TiHf)_{1/2}(Fe_{1-x}CoNi_{1+x})_{1/3}Sb$

Even though $(TiHf)_{1/2}(FeCoNi)_{1/3}Sb$ has a remarkably low thermal conductivity, its electronic properties should be further optimized to turn it into a useful thermoelectric material. The electrical conductivity of the alloy $(TiHf)_{1/2}(FeCoNi)_{1/3}Sb$ near room temperature is low (less than 200 S cm^{-1}), and it remains low over the whole temperature range. However, one can easily dope $(TiHf)_{1/2}(FeCoNi)_{1/3}Sb$ to enhance its electrical conductivity. In fact, it can be doped either with electrons or holes simply by tuning the Fe/Ni ratio as alluded to above. With this spirit, we synthesized electron-doped alloys $(TiHf)_{1/2}(Fe_{1-x}CoNi_{1+x})_{1/3}Sb$ for

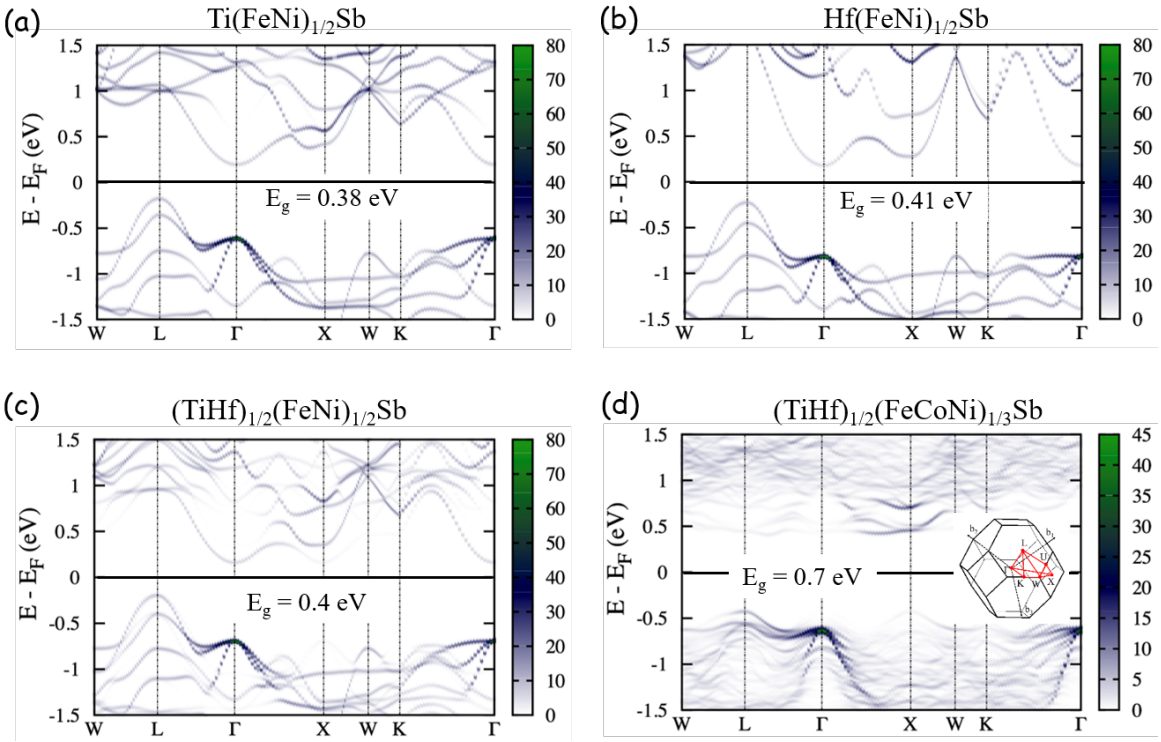

Figure 6.10: Band structure of (a) $Ti(FeNi)_{1/2}Sb$, (b) $Hf(FeNi)_{1/2}Sb$, (c) $(TiH)_{1/2}(FeNi)_{1/2}Sb$, and (d) $(TiHf)_{1/2}(FeCoNi)_{1/3}Sb$. The scale bar is the magnitude (increasing, white-blue-green) of spectral weight, which characterizes the probability of the primitive cell eigenstates contributing to a particular supercell eigenstate of the same energy.

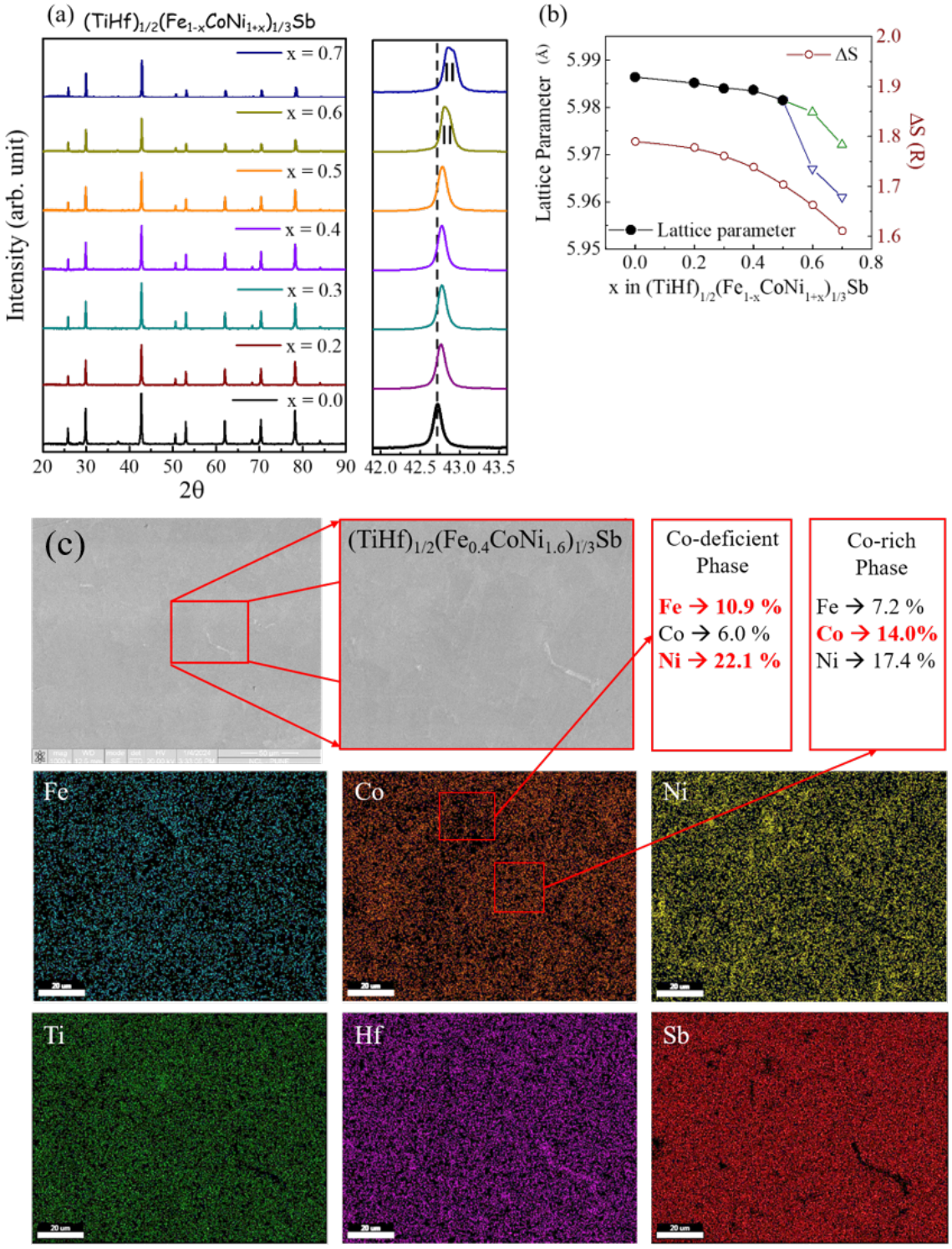

Figure 6.11: (a) XRD pattern of all the compositions, (b) lattice parameter and entropy, and (c) Chemical mapping for x = 0.6

Table 6.3: Computed band gap and formation energy (ΔH) of different disordered configurations of Ti(FeNi)$_{1/2}$Sb.

Strucuture No	Band gap (eV)	Formation energy (eV/formula unit)
01	0.85	-2.17
02	0.84	-2.18
03	0.74	-2.16
04	0.81	-2.17
05	0.91	-2.18
06	0.84	-2.18
07	0.78	-2.18
08	0.90	-2.18
09	0.90	-2.18
10	0.78	-2.18
11	0.78	-2.18
12	0.84	-2.18
13	0.72	-2.18
14	0.78	-2.18
15	0.91	-2.18
16	0.96	-2.18
15	0.89	-2.18
18	0.78	-2.18
19	0.88	-2.18
20	0.77	-2.18
21	0.81	-2.18
22	0.79	-2.18
23	0.84	-2.18

$x = 0, 0.2, 0.3, 0.4, 0.5, 0.6,$ and 0.7.

Figure 6.11a shows the PXRD patterns of our Ni excess samples. Up to x = 0.5, a single phase sample is obtained. The lattice constant, shown in Figure 6.11b, decreases systematically with increasing x due to the smaller ionic radius of Ni compared to Fe. The samples $x = 0.6,$ and 0.7 decompose into a Co-rich (TiHf)$_{1/2}$CoSb and Co-poor (TiHf)$_{1/2}$(FeNi)$_{1/2}$Sb phases. The electron microscope images in conjunction with the EDS probe, corroborate these findings further, as shown in Figure 6.11c. The ΔS_{conf} computed for these alloys shows a decreasing trend with an increase in x, see Figure 6.11b, consistent with the observation that a

Table 6.4: Computed band gap and formation energy (ΔH) of different disordered configurations of Ti(FeCoNi)$_{1/3}$Sb.

Strucuture No	Band gap (eV)	Formation energy (eV/formula unit)
01	0.74	-2.12
02	0.79	-2.12
03	0.69	-2.12
04	0.74	-2.12
05	0.69	-2.12
06	0.79	-2.12
07	0.74	-2.12
08	0.74	-2.12
09	0.79	-2.12
10	0.69	-2.12

single-phase hH alloy does not stabilize for higher values of x.

Electronic properties of (TiHf)$_{1/2}$(Fe$_{1-x}$CoNi$_{1+x}$)$_{1/3}$Sb; $x = 0.0 - 0.5$ alloys

Figure 6.12a shows the temperature dependent electrical conductivity for the compositions $x = 0.0 - 0.5$. Upon increasing x, σ increases markedly from $\approx$ 200 S cm^{-1} near 300 K for $x = 0$ to $\approx$ 1500 S cm^{-1} for $x = 0.5$ at the same temperature. This increase can be attributed to the increase in the carrier concentration as Fe/Ni ratio decreases. This is discussed further in the next paragraph. Generally, the increase in σ is accompanied by a concomitant decrease in the Seebeck coefficient. In (TiHf)$_{1/2}$(Fe$_{1-x}$CoNi$_{1+x}$)$_{1/3}$Sb alloys, Seebeck coefficient indeed decreases, but compared to σ, which increases by a factor of five between $x = 0$ and 0.5, the Seebeck coefficient decreases from a value near 973 K of $\approx$ 180 μV K^{-1} ($x = 0$) to $\approx$ 120 μV K^{-1} ($x = 0.5$) (see, Figure 6.12b.

To understand this, we estimated the temperature dependent weighted mobility (μ_W) of these alloys [183]. As shown in Figure 6.12d, μ_W shows a significant increase upon doping, which points to an increase in carrier effective mass (m*) with an increase in x, explaining why the decrease in Seebeck coefficient with increasing x is not as large as one may expect from the overall marked increase in the value of σ.

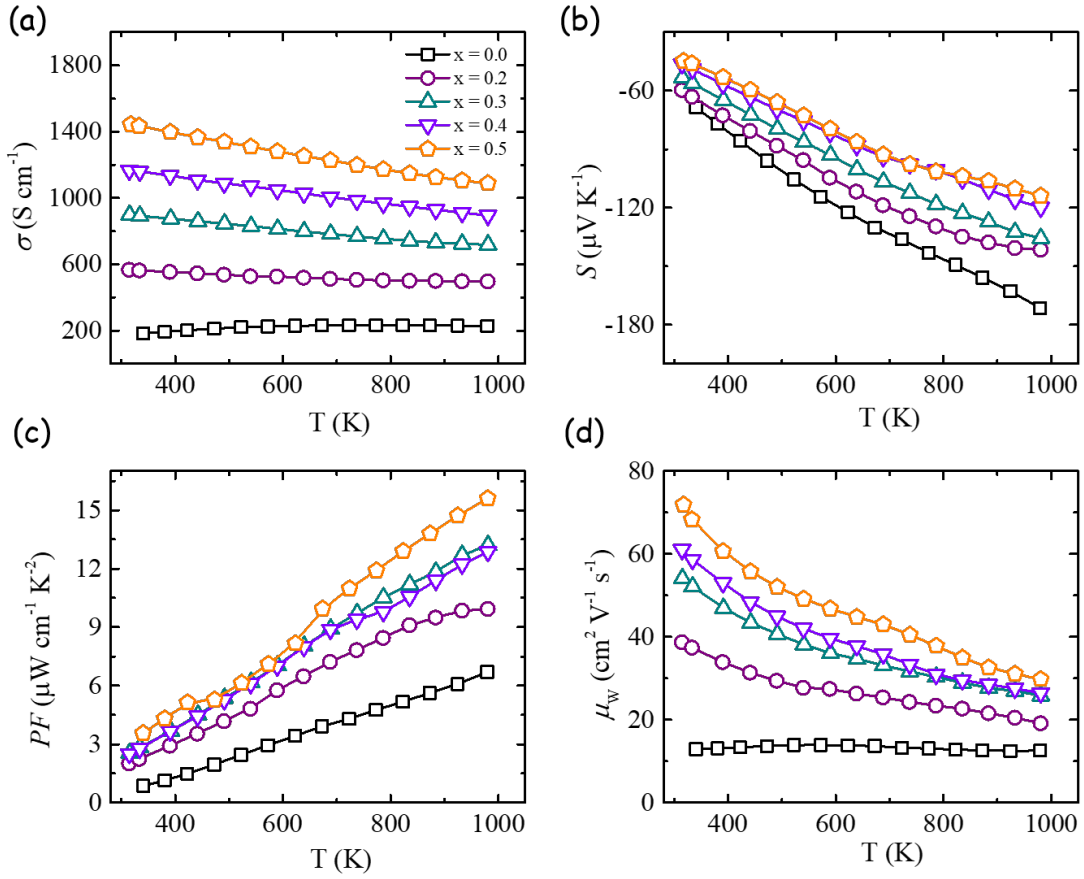

Figure 6.12: The temperature variation of (a) electrical conductivity (σ), (b) Seebeck coefficient (S), (c) power factor (PF), and (d) weighted mobility (μ_{W}) of the alloys $(\mathrm{TiHf})_{1/2}(\mathrm{Fe}_{1-x}\mathrm{CoNi}_{1+x})_{1/3}\mathrm{Sb}$ for various x.

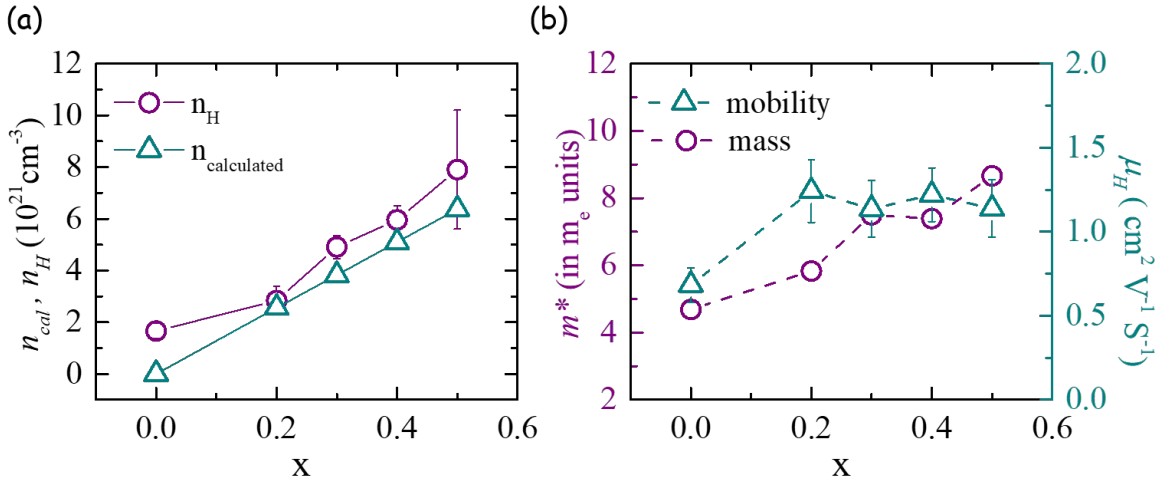

Figure 6.13: The variation of (a) carrier concentration, calculated (n_{cal}), and experimental, (n_H); (b) Hall mobility (μ_H) and carrier effective mass (m^*) as a function of x in the alloys $(TiHf)_{1/2}(Fe_{1-x}CoNi_{1+x})_{1/3}Sb$ for various x.

Figure 6.13a shows the measured (n_H) and calculated (n_{cal}) carrier concentration for all the samples. n_{cal} is estimated from the VEC off-set caused by the increase in x using the formula $n_{cal} = Z\Delta_{VEC}/V$, where Z is the number of formula units per unit cell and V is the unit cell volume [129, 184]. Assuming each excess Ni substituting Fe adds one extra electron to the conduction sea, we get $\Delta_{VEC} = HEA_{VEC} - 18$, where HEA is for our high-entropy alloys $(TiHf)_{1/2}(Fe_{1-x}CoNi_{1+x})_{1/3}Sb$. Thus, $HEA_{VEC} = \frac{54+2x}{3} \Rightarrow \Delta_{VEC} = \frac{2x}{3}$. For $(TiHf)_{1/2}(FeCoNi)_{1/3}Sb$ a n_H value of $\approx 1.7 \times 10^{21}$ cm^{-3} is high, and we attribute this to the self-doping due to off-stoichiometry. It is typical of hH alloys to show a high intrinsic carrier concentration due to off-stoichiometry [185]. In the present case, it is likely that the Fe/Ni ratio in $(TiHf)_{1/2}(FeCoNi)_{1/3}Sb$ is not exactly 1 but less than 1. For $x = 0.2$, $n_H \approx n_{cal} \approx 3 \times 10^{21}$ cm^{-3}. This shows that as small as a few percent of the Fe-Ni offset can result in a high carrier concentration. Deliberate attempts to make the $\frac{Fe}{Ni}$ greater than unity, indeed led to a p-type alloys with a carrier concentration of the same order as here. The p-type doping in these alloys will be discussed elsewhere. With an increase in x, n_H increases linearly, showing a good agreement with n_{cal}.

Figure 6.13b shows the variation of carrier effective mass (m^*) as a function of x, at

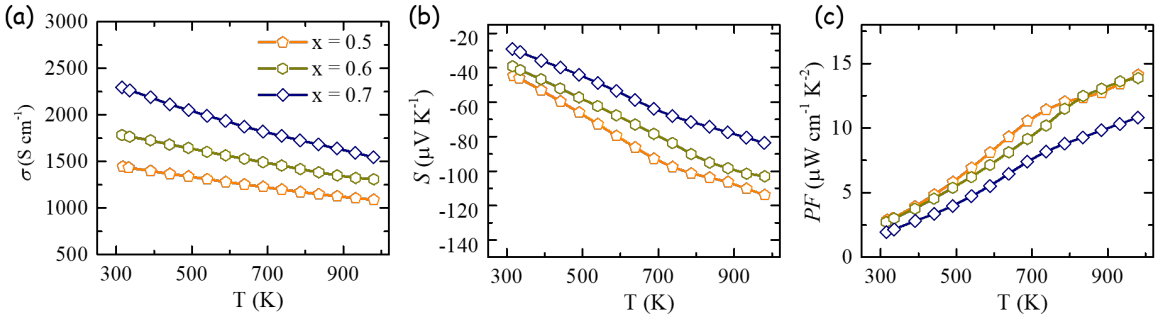

Figure 6.14: Transport properties of $(TiHf)_{1/2}(Fe_{1-x}CoNi_{1+x})_{1/3}Sb$ for x = 0.5, 0.6 and 0.7

300 K, estimated using SBM model assuming auctic phonon as a majior scattering mechanism. With an increase in the value of x, m^* increases from $\approx 5m_e$ ($x = 0$) to $\approx 9m_e$ ($x = 0.5$), where m_e is the bare-electron mass. The increasing trend of m^* is in line with the dependence of the weighted mobility on x. We also computed the Hall mobility at 300 K using the values of n_H for various x. The variation of μ_H with x is shown in Figure 6.13b, which also shows an approximately increasing behaviour. The value of μ_H (0.5 to 1.2 $cm^2\ V^{-1}\ s^{-1}$) is very small compared to the conventional thermoelectrics (for example, doped PbTe samples [186]). This partly explains why the electrical conductivity of these alloys is relatively low despite their high carrier concentration. The temperature variation of power factor ($PF = \sigma S^2$) is shown in Figure 6.12c. For all the alloys, the PF shows a nearly linearly increasing behavior with temperature. Moreover, at any temperature, the PF is found to be higher for a higher value of x, varying from $\approx 7\ \mu W\ cm^{-1}\ K^{-2}$ ($x = 0$) to $\approx 16\ \mu W\ cm^{-1}\ K^{-2}$ ($x = 0.5$)at 973 K, reflecting the trend observed in the variation of m^* with x. The measured transport coefficients for $x = 0.6$ and 0.7 are shown in Figure 6.14.

Thermal conductivity of $(TiHf)_{1/2}(Fe_{1-x}CoNi_{1+x})_{1/3}Sb$ alloys

The as-measured thermal conductivity (κ) of $(TiHf)_{1/2}(Fe_{1-x}CoNi_{1+x})_{1/3}Sb$ alloys is shown in Figure 6.15a. For all the samples, κ shows a decreasing trend upon heating. The thermal conductivity of $(TiHf)_{1/2}(FeCoNi)_{1/3}Sb$ varies between 2.8 $W\ m^{-1}K^{-1}$ (300 K) to 2.1 $W\ m^{-1}K^{-1}$ (973 K). With the increase in x, κ shows an increasing trend dominated by the κ_e component. The lattice part of the thermal conduc-

tivity (κ_l) is obtained by subtracting the electronic part (κ_e) from the total measured κ. The κ_e contribution is obtained using the Wiedmann-Franz law, $\kappa_{\mathrm{e}} = \sigma \mathrm{L} \mathrm{T}$, where L is the Lorentz number, which is estimated using the single parabolic band (SPB) model (see Supporting Information). The κ_l contribution thus obtained is shown in Figure 6.15b. With the increase in the value of x, κ_l further decreases slightly. For $x = 0.5$, $\kappa_l \approx$ 3 W m^{-1} K^{-1} at 300 K decreases to $\approx$ 1 W m^{-1} K^{-1} at the highest temperature (973 K) in our measurements. To the best of our knowledge, this is by far the lowest observed κ_l in any hH alloy [180]. The κ_l for a few representative high-performing hH high-entropy alloys are listed in Figure 6.15c for comparison [3–8]. The decreasing trend of κ_l with increasing x can possibly be understood from the fact that as x increases, the Ni ions at the $4c$-site form Ni-rich nanoclusters, scattering the long wavelength phonon. Further experiment, for example X-ray Absorption Spectroscopy (XAS), may be helpful in showing the existence of Ni nanoclusters, if any .

The calculated elastic properties and sound velocities are tabulated for $x = 0.0$ and 0.5 in Table 6.5. The average sound velocity decreases marginally with the increase in x. For $x = 0.5$, κ_l is estimated using Slack's equation, where the calculated elastic properties are used as input. The calculated κ_l is plotted in Figure 6.15b. This exceeds the experimental κ_l, especially near 300 K. However, if one assumes 1.5% vacancies at the $4c$-site, the calculated and experimental values show a close agreement. Given that the undoped composition $x = 0$ has significant carriers, the presence of such vacancies cannot be completely ruled out. The lowest observed κ_l of $\approx$ 1 W m^{-1}K^{-1} at 973 K for $x = 0.5$ is close to the theoretical minimum value of 0.86 W m^{-1} K^{-1}.

The thermoelectric figure-of-merit (zT) of these alloys is shown in the Figure 6.15d. The zT of $(TiHf)_{1/2}(FeCoNi)_{1/3}Sb$ shows an increasing trend over the whole temperature range, attaining a value of 0.3 at the highest temperature. Given that $(TiHf)_{1/2}(FeCoNi)_{1/3}Sb$ has a very low electrical conductivity (< 200 S cm^{-1}), the value of 0.3 is rather impressive and can be attributed to its very low κ_l. The doped samples show a similarly increasing trend, but with zT systematically increasing with an increase in x. A maximum zT value of 0.51 is obtained at 973 K for $x = 0.5$, as shown in Figure 6.15d. This is about 70% enhanced

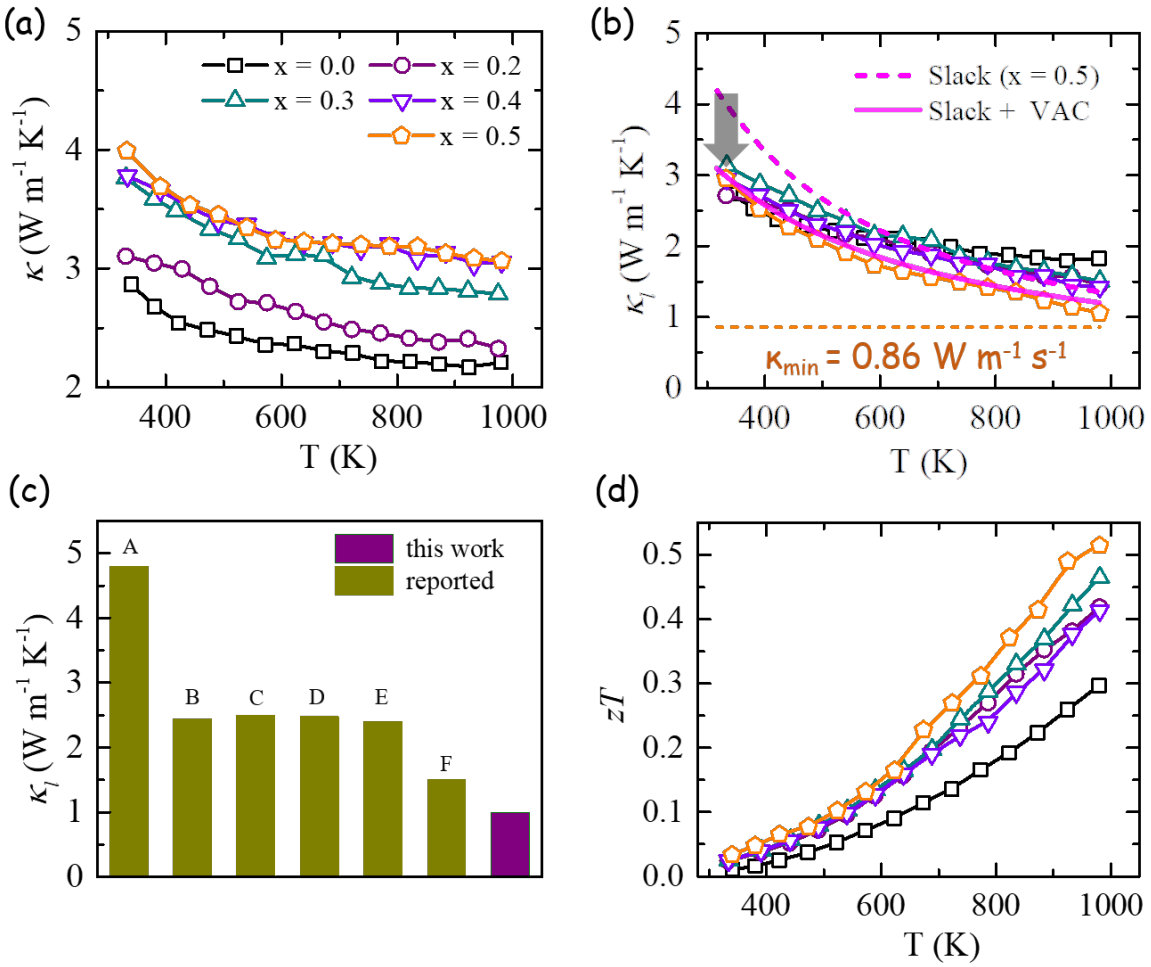

Figure 6.15: The temperature variation of: (a) as-measured or total thermal conductivity (κ), (b) lattice thermal conductivity (κ_l), (c) comparison of κ_l of various high-entropy half-Heusler alloys, A: $Ti_2NiCoSb$ [3] ;
B: $(Zr_{0.88}Ta_{0.12}Co_{0.88}Ni0.12Sb)_{1-y}$
$(Hf_{0.75}Zr_{0.25}NiSn_{0.99}Sb_{0.01})_y$ [4] ; C: $Ti_2NiCoSn_{0.5}Sb_{1.5}$ [5] ; D: $Ti_2Zr_2Hf_2NbVFe_5Ni_3Sb_8$ [6] ; E: MCoSb-based hEAs [7] ; F: $(TiZrHfVNbTa)_{0.1667}FeCoSb$ [8] ; The purple bar represents $(TiHf)_{1/2}(Fe_{0.5}CoNi_{1.5})_{1/3}Sb$ (this work), and (d) thermoelectric figure-of-merit (zT) for the alloys $(TiHf)_{1/2}(Fe_{1-x}CoNi_{1+x})_{1/3}Sb$. The lines connecting the data points in frames (a), (b) and (d) are shown as a guide to the eye. The smooth dashed line in (b) shows the calculated κ_l using Slack's equation, the solid pink line shows the calculated κ_l in the presence of 1.5% vacancies at the $4c$ site.

Table 6.5: Elastic constants, bulk (B_H) and shear (G_H) moduli of (TiHf)$_{1/2}$(Fe$_{1-x}$CoNi$_{1+x}$)$_{1/3}$Sb) (x = 0, 0.5). v_L, v_T, and v_{av} are the longitudnal , transverse and average phonon velocities. Gruneisen parameter and Debye temperature are represented as γ and Θ_D respectively.

Compositions	x = 0.0	x = 0.5
G_H (GPa/m^2)	77.15	72.231
B_H (GPa/m^2)	136.37	135.36
v_L (m/s)	5159	5060
v_T (m/s)	2929	2837
v_{av} (m/s)	3253	3154
γ	1.56	1.60
Θ_D (K)	369	357

with respect to the zT of $x = 0$. In order to see how this value compares with the zT of other reported high-entropy hH alloys, we have listed the zT of a number of such alloys from recent studies in Table 6.6. With the exception of high-entropy alloys M$_{0.85}$Nb$_{0.15}$CoSb (M = Ti, Zr, Hf; equimolar), where the peak zT reported is 0.55 at 923 K, the zT of our (TiHf)$_{1/2}$(Fe$_{1-x}$CoNi$_{1+x}$)$_{1/3}$Sb (x = 0.5) is better than all other reported high-entropy hH alloys. In the same table, one can also see the respective minimum κ_l for all these alloys, where (TiHf)$_{1/2}$(Fe$_{1-x}$CoNi$_{1+x}$)$_{1/3}$Sb ($x = 0.5$) stands out with a considerably lower lattice thermal conductivity compared to all the other alloys, including M$_{0.85}$Nb$_{0.15}$CoSb. This clearly reflects the potential of (TiHf)$_{1/2}$(FeCoNi)$_{1/3}$Sb as a promising thermoelectric material. The PF of this alloy can possibly be further enhanced by doping at Sb site.

Thermal stability and reproducibility

We now come to the most important and often overlooked part concerning samples' reproducibility and thermal stability. In order to verify the observed thermoelectric properties, in particular the ultra-low thermal conductivity, we synthesized a second $x = 0.5$ sample using exactly the same protocol as used in the synthesis of the first sample. The measured transport properties of both samples show excellent agreement with each other as shown in Figure 6.16(a,b,c). We further tested the effect of thermal cycling on the thermoelectric properties. We show that for two successive heating and cooling cycles, these samples does

Table 6.6: Comparison with reported zT and κ_l of a few half Heusler based HEAs.

Composition / type (n/p)	lowest κ_l ($\mathrm{Wm^{-1}K^{-1}}$)	peak zT	ref.
$(TiHf)_{1/3}(Fe_{0.5}CoNi_{1.5})_{1/3}Sb$ (n)	1.05	0.55	this work
$Ti_2NiCoSnSb$ (n)	4.8 at 800 K	0.14	[3]
$(Zr_{0.88}Ta_{0.12}Co_{0.88}Ni_{0.12}Sb)_{1-y}(Hf...)_y$ (n)	2.44 at 923 K	0.38	[4]
$Ti_2NiCoSn_{0.5}Sb_{1.5}$ (n)	2.5 at 873 K	0.29	[5]
$Ti_2Zr_2Hf_2NbVFe_5Ni_3Sb_8$ (p)	2.48 at 800 K	0.027	[6]
MCoSb based alloys (n)	2.4 at 923 K	0.58	[7]
$(TiZrHfVNbTa)_{0.1667}FeCoSb$ (n)	1.5 at 923 K	0.3	[8]

not show any change in their transport properties shown in Figure 6.16d, indicating that the samples are thermally stable as is expected of a hH materials, known for their structural robustness.

6.4 Summary and Conclusions

The combined experimental and theoretical work presented here is motivated by the increasing interest in high-entropy alloys in the field of thermoelectric materials. The high lattice thermal conductivity of the hH alloys is one of their main disadvantages and the high-entropy alloying principle can be useful in overcoming this challenge. In this work, we have synthesized a new hH alloy, namely, $Hf(FeNi)_{1/2}Sb$ and using this as the base material, we introduced Ti at the X-site by substituting 50% of Hf with Ti, and Co at the Y site by replacing $(FeNi)_{1/2}$ by $(FeCoNi)_{1/3}$. This resulted in a high-entropy alloy $(TiHf)_{1/2}(FeCoNi)_{1/3}Sb$ ($\Delta S_{conf} = 1.79R > 1.5R$). Using estiblished annealing protocol, we further show that $(TiHf)_{1/2}(FeCoNi)_{1/3}Sb$ is not only a high-entropy alloy, but it is also belongs to the category of entropy-stabilized alloys. It should be pointed out that while there are several previous studies on high-entropy hH alloys, the entropy stabilized hH alloys are rare. The effect of Co-doping on the band structure was studied using first-principles DFT calculations. We show that Co incorporation in the structure increases the band gap from 0.4 eV in $(TiHf)_{1/2}(FeNi)_{1/2}Sb$ to 0.7 eV in $(TiHf)_{1/2}(FeCoNi)_{1/3}Sb$. This, in turn, helps

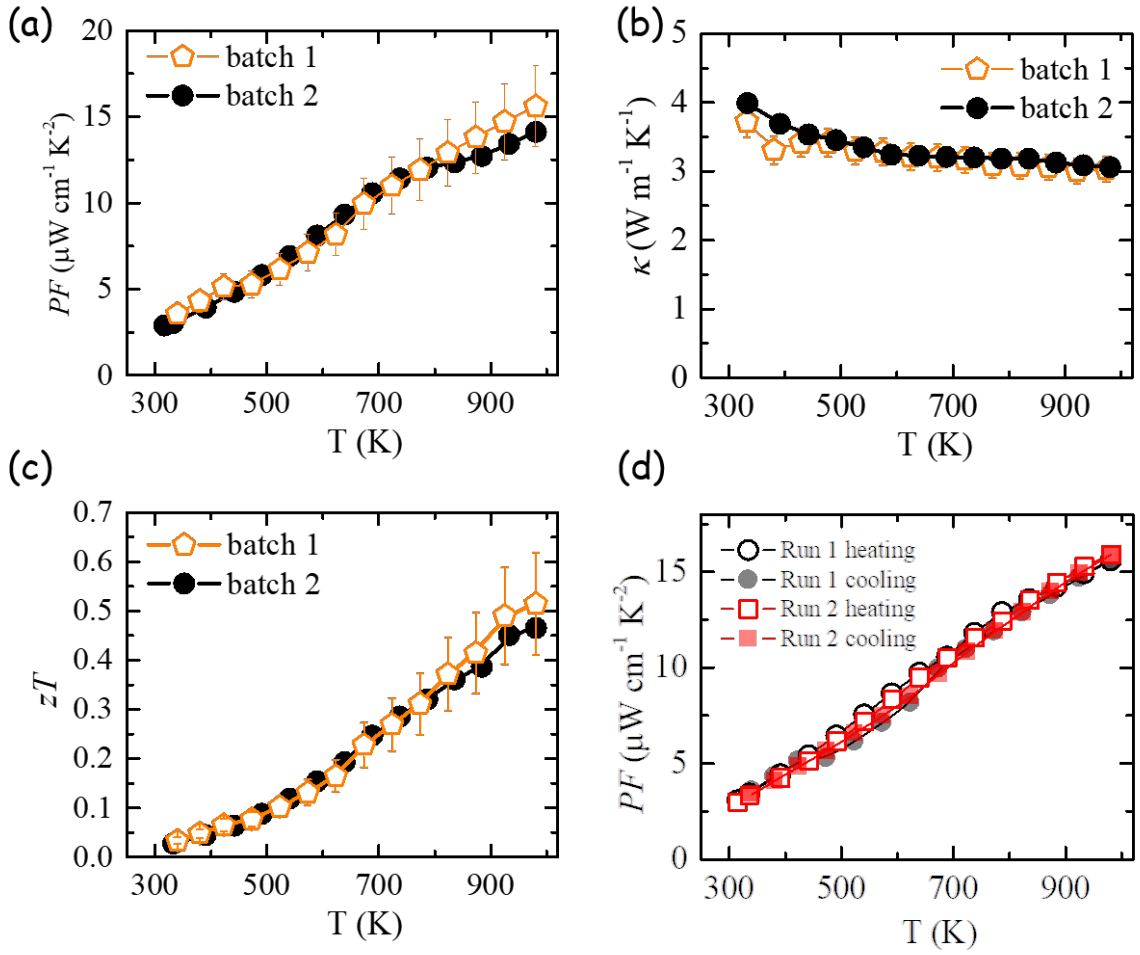

Figure 6.16: (a,b,c) Power factor, thermal conductivity, and zT respectively of the same composition prepared again, and (d) transport after multiple heating cooling cycle.

mitigate the issue of bipolarity. The entropy-stabilized $(TiHf)_{1/2}(FeCoNi)_{1/3}Sb$ is found to exhibit a very low lattice thermal conductivity (1.7 W m^{-1} K^{-1} at 973 K).Further carrier optimization is carried out by tuning Fe and Ni concentrations in $(TiHf)_{1/2}(Fe_{1-x}CoNi_{1+x})_{1/3}Sb$ by varying x up to 0.5, beyond which the sample does not form in a single phase. With increasing x, the PF increases and κ_l decreases, leading to a remarkably low $\kappa_l \sim 1$ W m^{-1} K^{-1} at 973 K. This, to the best of our knowledge, is the lowest value of κ_l ever reported for any hH alloy [180]. A combination of ultra-low thermal conductivity and high PF, the sample with $x = 0.5$ showcases the highest zT of 0.55 at 973 K, up to this temperature, zT exhibits an increasing behavior. The sample's reproducibility and thermal stability were successfully tested. Our work demonstrates the experimental validation of entropy stabilization in hH family for the first time, showcasing the effectiveness of the high-entropy strategy for high-performance thermoelectric materials.

Chapter 7

Defect-assisted ultrahigh zT of TaFeSb based Half-Heuslers

7.1 Introduction

Here we investigate the role of antisite disorder on the thermoelectric behavior of this interesting material. For this purpose, we synthesized $Ta_{1-x}Ti_xFeSb$, $Ta_{1-x}Ti_xFe_{1-\delta}Sb$, and Ti/V co-substituted samples with and without Fe deficiency. We used two different synthesis approaches. In the first one, we used high-temperature (T $>$ 3000°C) arc-melting to first mix Ta/Ti and Fe metal pieces, which was followed by a series of steps involving ball-milling at room-temperature and annealing/hot-pressing at temperatures T $<$ 850°C. This method resulted in a phase-pure samples but with Fe-deficiency due to evaporative losses of Fe during arc-melting, and resulting Ta/Ti-Fe antisite disorder. In the second method, the starting precursors were in their powder form and therefore the entire process, involving ball-milling and hot-pressing/annealing, was carried out at temperatures less than 850°C. This led to samples with effectively zero Fe-loss and minimal Ta/Ti-Fe antisite disorder compared to the samples prepared using the first method. Using the zero-loss powder synthesis method, we also prepared several Fe-deficient samples.

We found that the presence of Fe-deficiency enhances the antisite disorder. The disor-

dered samples are characterized by the presence of "defect" states in the bandgap region that effectively reduces the bandgap to 0.5 eV, in agreement with the bandgap observed experimentally. In the disordered samples, the valence band edge tends to flatten, enhancing the Seebeck coefficient and electrical conductivity simultaneously. The zT enhances significantly for the disordered samples, showing that the antisite disorder is critical for obtaining high zT in Ti-substituted TaFeSb. The carrier optimized Ti-doped TaFeSb with small antisite disorder, together with low value of lattice thermal conductivity, results in high zT of 1.55 at 973 K. Our study provides a novel approach to understand, control and modulate the disorder to further enhance electronic and thermal properties of half-Heusler materials

7.2 Experimental and computational details

Experimental details: Samples were prepared using two different methods. First method, called AM, starts with arc melting of Ta and Fe (Sigma Aldrich 99.9%) to form an ingot. This ingot was then ground along with Sb shots and ball milled for 1 hr. The fine-powder thus obtained was cold-pressed in a KBr die-set, and subjected to a two-step sintering process: 650°C for 24 h, the temperature was then raised to 780°C where it was kept for 40 h. The obtained sintered pellet was re-ground in a mortar-pestle and hot-pressed for 10 min at 800°C under a pressure of 57 MPa. In the final step, the hot-pressed pellet was further annealed for 7 days at 800 °C to obtain phase-pure TaFeSb sample. In the the second synthesis method, called PS, the elements Ta, Ti, V, Fe, and Sb were used in their powder form. The powders were mixed in the desired stoichiometric ratio, ball-milled cold pressed and subjected to the same two-step sintering process as above. The subsequent steps are all exactly the same as outlined above.

The phase purity of the samples was confirmed using the powder X-ray diffraction (XRD) technique a Bruker (D8 Advance) diffractometer. The structural parameters were determined from Rietveld refinement of the XRD data. High-resolution transmission electron microscopy (HRTEM) was performed using a JEOL JEM 2200FS 200 keV microscope. The samples were prepared by dispersing fine powders in ethanol. The solution was drop-casted

on a copper grid with amorphous carbon coating using a micro pipette, and thereafter oven-dried at 80°C for a few hours. The plasma cleaning was done to remove any organic solvent that may have still remained. The Linseis LFA-1000 set-up was used to measure the thermal diffusivity (D) on pellet samples of uniform thickness. The thermal conductivity was obtained from the thermal diffusivity using the formula: $\kappa = DC_p\rho_m$, here ρ_m is the density of the pellet, and $\mathrm{C_p}$ is the specific heat. The specific heat was taken to be equal to the classical Dulong-Petit limit of *3nR*. The Seebeck coefficient and electrical conductivity were measured simultaneously on bar-shaped samples using the Linseis LSR-3 set-up. The temperature dependent charge carrier concentration was estimated from the measurement of the Hall coefficient using a lock-in based technique in a sensitive, home-built setup by varying the magnetic field between $\pm$ 10 kOe.

Computational details: Density Functional theory (DFT) based calculations were performed using the Quantum ESPRESSO software [115,116]. Ultrasoft pseudopotentials were used for valence electron-ion interactions [117]. The valence configurations of $5s^25p^66s^25d^3$, $3s^24s^23p^63d^2$, $3s^23p^63d^64s^2$, and $5s^25p^3$ had been used for Ta, Ti, Fe, and Sb, respectively. A kinetic energy cutoff of 65 Ry (650 Ry) had been used to expand the wave function (charge density) in a plane wave basis. Perdew-Burke-Ernzerhof parameterization of the generalized gradient approximation (GGA-PBE) was used to describe the electron-electron exchange and correlation interaction [118]. A 3$\times$ 3 $\times$ 3 supercell with 81 atoms is used to introduce antisite disorder, Ti doping, and Fe vacancy. A 2 $\times$ 2 $\times$ 2 Monkhorst-Pack k-point mesh [92] was used to perform BZ integration. To speed up convergence we have used Marzari-Vanderbilt smearing with a smearing width of 0.001 Ry.

In order to incorporate disorder Ta/Ti-Fe disorder or Fe-vacancy, a 3 $\times$ 3 $\times$ 3 supercell containing 81 atom was created having 27 atoms of Ta/Ti, Fe, and Sb each. Exchanging one (Ta/Ti) with one Fe site will introduce 3.7 % of (Ta/Ti)-Fe antisite disorder. Removing one Fe will create 3.7 % Fe-vacancy. Doping one Ti in place of Ta in $Ta_{27}Fe_{27}Sb_{27}$ will introduce 3.7 % of Ti doping.We have considered both system (TaFeSb and TiFeSb) separately to understand effect of vacancy. For Ta-Fe and Ti-Fe disorder we have considered end member

TaFeSb and TiFeSb along with a few intermediate structures where Ti is doped at Ta site having Ti-Fe antisite disorder. We have done Ti doping up to 14.81 % having 3.7 % of Ti-Fe disorder in all structures. We also considered multiple possible structure for each doping case. Although, most of the case they have similar Defect Formation Energy (DFE), we considered the most energetically favorable structures. DFE calculation is done using the following formula:

$$DFE_{([Ta/Ti]-Fe\ disorder)} = E([Ta/Ti]FeSb)_{disordered} - E([Ta/Ti]FeSb)_{ordered} \quad (7.1)$$

$$DFE_{(Ti\ doped\ +\ Ti-Fe\ disorder)} = E(Ta_{1-x}Ti_xFeSb) - (1-x)E(TaFeSb)_{ordered} - xE(TiFeSb)_{ordered} \quad (7.2)$$

$$DFE_{(Fe-vacancy)} = E([Ta/Ti]Fe_{1-x}Sb) - E([Ta/Ti]FeSb)_{ordered} - xE(Fe)_{bulk} \quad (7.3)$$

where E represents the total energy of the compositions indicated in the subscript.

7.3 Results

7.3.1 Structural and electronic state analysis

TaFeSb is reported to form with a stable hH XYZ structure (space group: *F-43m*), where the atoms X (Ta), Y (Fe), and Z (Sb) occupy $4a$ (0 0 0), $4c$ $(1/4, 1/4, 1/4)$, and $4b$ $(1/2, 1/2, 1/2)$ sites, respectively. We prepared TaFeSb and its Ti substituted (or Ti/V co-substituted) variants by two methods. In the first method, Ta and Fe chunks were first arc-melted to make a 'TaFe' ingot. The ingot was ground along with a stoichiometric amount of Sb shots to obtain a fine powder. The powder was further ball-milled for 1 h, and subsequently cold-pressed using a KBr press to obtain disc-shaped pellets that were flame-sealed in an evacuated quartz ampule. The ampoule was placed in a muffle furnace whose temperature was gradually raised to 650°C. After waiting there for 24 h, the temperature was raised to 780°C where the sample was allowed to homogenize for 40 h before furnace cooling to room-temperature. After sintering, the pellets were reground using a mortar-pestle set and the resulting powder

was hot-pressed at 800°C for 10 min under a pressure of 57 MPa in a graphite die. In the final step, the hot-pressed pellets were annealed at 800°C for 7 days in an evacuated quartz ampule, leading to the formation of dense and phase-pure TaFeSb pellets for thermoelectric characterization.

In the second synthesis approach, instead of melting Ta and Fe chunks to make a 'TaFe' ingot that was eventually ground and mixed with Sb-powder, all the precursors used were in their powder form. The stoichiometric quantities of Ta, Fe, and Sb (or Ta, V, Fe, and Sb) powders were well-mixed in a ball-mill as above and thereafter subjected to the same sintering and annealing protocol as outlined above in the first method. The samples prepared by first and second method are labeled AM and PS: for example, TaFeSb (AM) and TaFeSb (PS), respectively. The list of samples synthesized and studied in this work is tabulated in Table 7.1.

Due to a relatively very high melting temperature of Ta (3020°C) compared to the boiling point of Fe (2860°C), some evaporative losses of Fe during arc-melting were noted in the first method. Therefore, the samples prepared using the AM method are slightly Fe deficient. On the other hand, no such losses occurred in the powder-synthesized samples (PS) as the highest temperature used in this method remains less than 800°C throughout the synthesis process. Therefore, the composition of samples prepared using the PS method are closer to their respective nominal compositions.

The powder X-ray diffraction (XRD) patterns of our samples are shown in Figure 7.1. With the exception of $Ta_{1-x}Ti_xFeSb$ ($x = 0.20$), all other samples are found to be phase pure, crystallizing with the desired hH structure. In $x = 0.20$, in addition to the main hH phase, a few weak extra reflections are also observed indicating the presence of unidentified minor secondary phase(s). The lattice parameter (a) of all the samples are listed in Table S1 in the Supporting Information. For TaFeSb (AM) and TaFeSb (PS), a = 5.9368 Å and a = 5.9365 Å, respectively, agree well with the previous report (5.938 Å) [66]. Upon substituting Ti for Ta, the XRD peaks for both sets of samples gradually shift towards smaller 2θ values as x increases, showing that the lattice expands with increasing Ti substitution. In the $Ta_{1-x}Ti_xFeSb$

Table 7.1: Starting composition, Arc melted (AM) or Powder Synthesised (PS) and composition obtained from Rietveld refinement of XRD pattern.

Starting composition	Refined composition	a(Å)
TaFeSb(AM)	TaFeSb	5.9368, 5.938[a]
$Ta_{0.88}Ti_{0.12}FeSb$(AM)	$(Ta_{0.887}Ti_{0.110}Fe_{0.003})(Fe_{0.96}Ti_{0.018})Sb$	5.9378
$Ta_{0.84}Ti_{0.16}FeSb$(AM)	$(Ta_{0.822}Ti_{0.135}Fe_{0.009})(Fe_{0.95}Ti_{0.035})Sb$	5.9391
$Ta_{0.80}Ti_{0.20}FeSb$[@](AM)	$(Ta_{0.797}Ti_{0.178}Fe_{0.017})(Fe_{0.913}Ti_{0.057})Sb$	5.9399
TaFeSb(PS)	TaFeSb	5.9365
$Ta_{0.84}Ti_{0.16}FeSb$(PS)	$(Ta_{0.849}Ti_{0.15}Fe_{0.009})(Fe_{0.976}Ti_{0.014})Sb$	5.9376
$Ta_{0.84}Ti_{0.16}Fe_{0.97}Sb$(PS)	$(Ta_{0.842}Ti_{0.12}Fe_{0.019})(Fe_{0.945}Ti_{0.042})Sb$	5.9375
$Ta_{0.84}Ti_{0.16}Fe_{0.95}Sb$ [@](PS)	$(Ta_{0.850}Ti_{0.13}Fe_{0.028})(Fe_{0.93}Ti_{0.043})Sb$	5.9384
$Ta_{0.74}V_{0.1}Ti_{0.16}FeSb$(PS)	——	5.9266
$Ta_{0.74}V_{0.1}Ti_{0.16}Fe_{0.97}Sb$ [@](PS)	——	5.9329

[a] reported experimental value [66]
[@] forms with small impurity phase

(AM) series, *a* increases from $a \sim 5.9368$ ($x = 0$) to $a \sim 5.9399$ ($x = 0.20$). Similar expansion is also observed for the samples of the PS series. The observed trend (expansion upon Ti substitution) is opposite of the trend seen in the homologous $Ti_{1-y}Ta_yCoSb$ series, where *a* increases (decreases) with increasing (decreasing) Ta (Ti) due to slightly larger metallic radius (r_m) of Ta ($r_m = 1.343$ Å) as compared to Ti ($r_m = 1.324$ Å) [187, 188].

To understand this unusual trend in the variation of *a*, we carried out Rietveld refinement on all our Ti-doped samples. The refinement results are shown in Figure 7.2. In all cases, the refinement converged nicely as is evident from the goodness-of-fit parameters and the difference plots in Figure 7.2. The refined occupancies revealed presence of Ti-Fe antisite disorder and Fe-vacancies. The Ti-Fe antisite disorder builds-up progressively as the Ti concentration (x) increases. Also, in the Fe deficient PS samples, the increasing Fe deficiency promotes more Ti occupancy at the Y-site. It should be stressed that the refined compositions shown in the Supporting Information are only indicative of the observed trends, the actual compositions may differ slightly. Since the metallic radius of Fe (r_m = 1.26 Å) is smaller compared to that of Ti, as the quantity of Ti at the Y-site increases with increasing x, *a* shows an increasing trend as observed experimentally. We therefore conclude that the

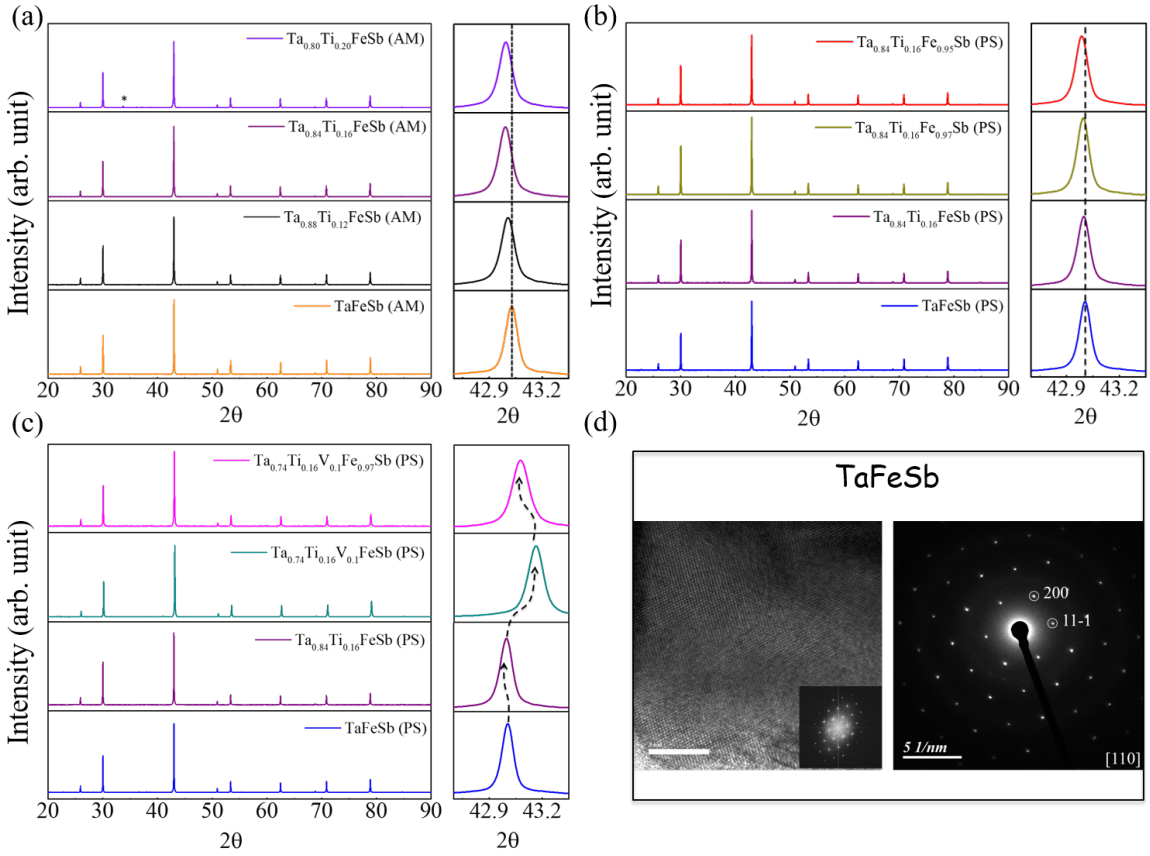

Figure 7.1: X-ray diffraction of $Ta_{1-x}Ti_xFeSb$ with zoomed in peak 022 (a) arc melted sample, (b) Powder synthesized sample, (c) Powder synthesized and V alloyed sample, and (d) real image of TaFeSb (fft in the inset), and SAED pattern (right)

observed increasing trend shown by a is primarily due to the Ti-Fe antisite disorder.

It should be specified that although we did not detect any Ta at the Y-site using our lab-based XRD, a previous NMR study reported the presence of small Ta-Fe antisite disorder even in pristine TaFeSb [189]. In the Ti-substituted samples, clearly the Ti-Fe disorder takes the precedence. This is in agreement with the calculated Defect Formation Energy (DFE) involved in Ti-Fe type antisite disorders shown in Figure 7.3b. We observed the DFE decreasing as the Ti concentration increase at Ta site having a consistent 3.7 % of Ti-Fe disorder. In case of Ti completely replacing Ta, the disorder is highly favorable although TiFeSb does not form in pure phase. Our calculation justifies the increase Ti-Fe antisite disorder with increase in Ti doping at Ta site. See supporting information for details of calculations.

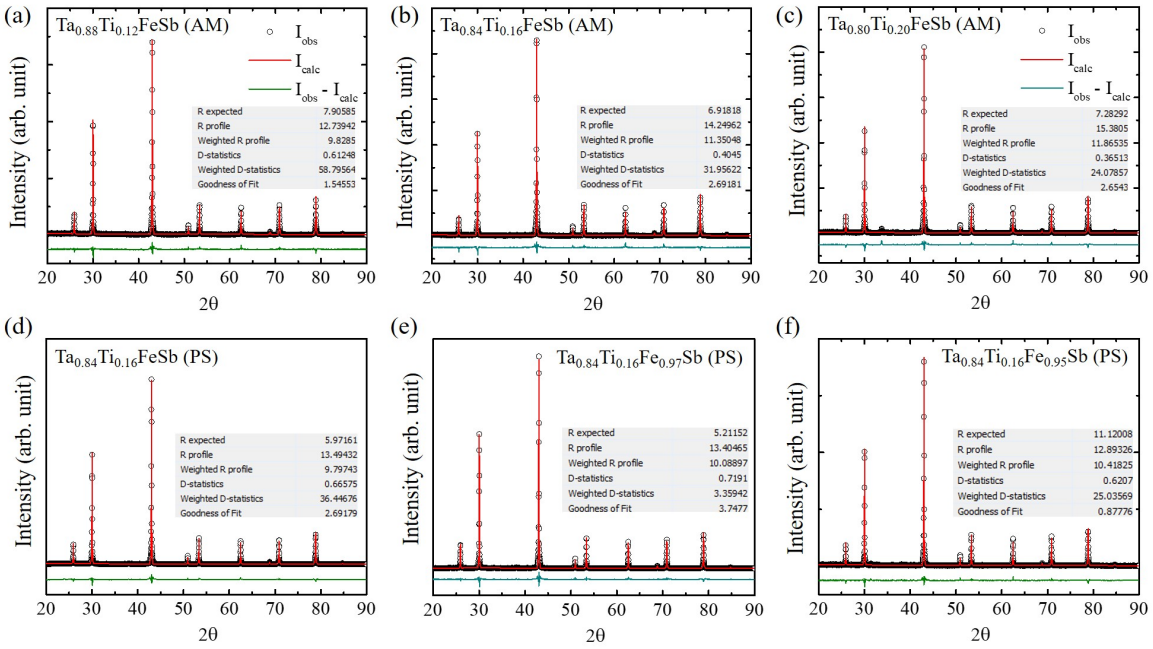

Figure 7.2: Rietveld refinement of XRD pattern for (a,b,c) Arc melted samples and (d, e, f) Powder synthesized samples.

The same way, we also calculated the energy cost for creating a Fe vacancy in TaFeSb and TiFeSb, and Found that Fe-vacancy is again more favorable after Ti doping. The results shown in Figure 7.5. It is easier to create Fe vacancy in the Ti-doped TiFeSb than in TaFeSb. Thus, with increasing Ti at the Ta site, the energy cost of creating a Fe vacancy progressively decreases.

In the Ti/V co-substituted sample, *a* decreased significantly from 5.9365 Å, for $Ta_{0.84}Ti_{0.16}FeSb$ (PS), to 5.9226 Å, for $Ta_{0.74}V_{0.1}Ti_{0.16}FeSb$ (PS). The observed reduction can be attributed to two factors: (a) the smaller size of V compared to Ta, and (b) substitution of V for Ta suppresses the antisite disorder. The Rietveld refinement for the Ti/V co-substituted samples did not yield reliable results due to over-parameterization arising from refining the ocupancies of four elements at the X and Y sites. However, the factor (b) is endorsed by the observation that in a sample prepared with 3% Fe deficiency, $Ta_{0.74}V_{0.1}Ti_{0.16}Fe_{0.97}Sb$ (PS), the lattice parameter increases from 5.9226 Å to 5.9330 Å, as demonstrated in Figure 7.1c, due to increase in the antisite disorder.

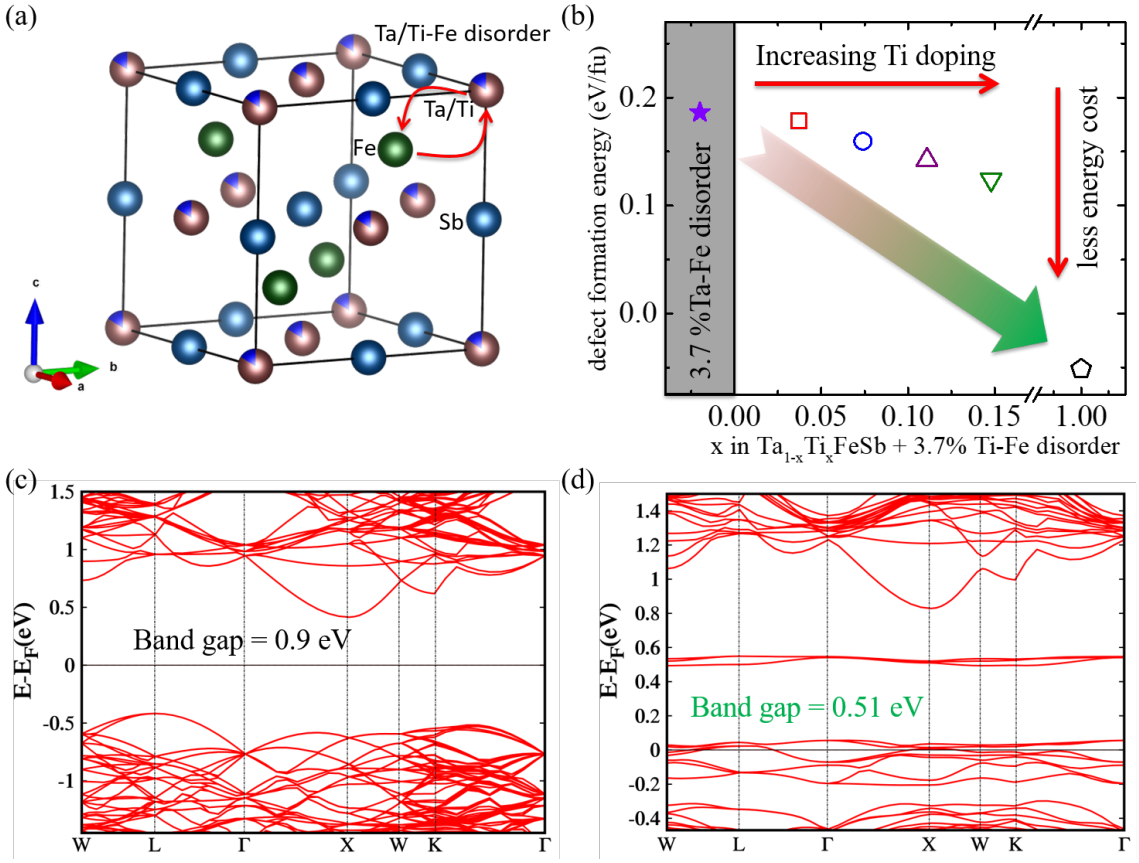

Figure 7.3: (a) Unit cell of $Ta_{(1-x)}Ti_xFeSb$. The red curved arrows show Ti-Fe antisite disorder. See text for details; (b) Defect formation energy for 3.7 % of Ta-Fe disorder in TaFeSb (shaded region), and increasing fraction of Ti doping in TaFeSb with 3.7 % of Ti-Fe disorder; (c) band structure of TaFeSb ordered structure, and (d) band structure considering 3.7 % of Ta-Fe antisite disorder.

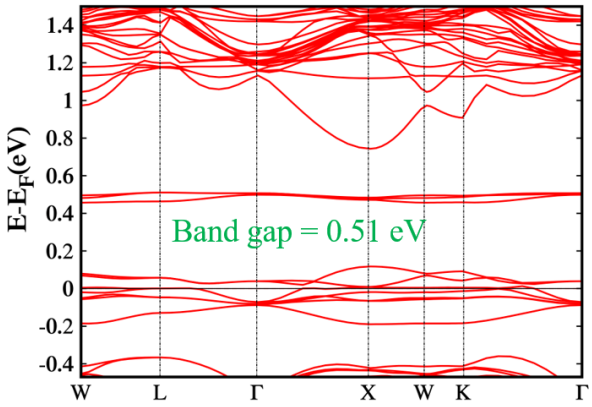

Figure 7.4: Band structure of $(Ta_{26}Fe)(Fe_{26}Ti)Sb_{27}$

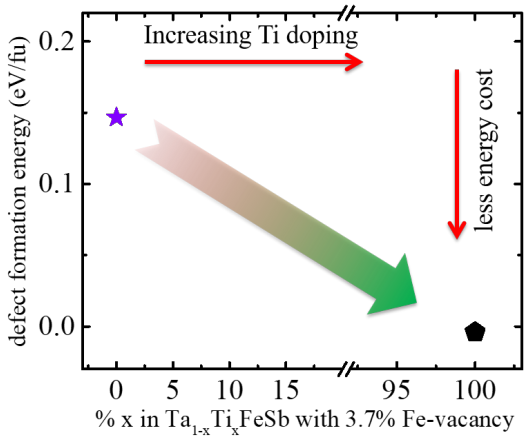

Figure 7.5: Defect formation energy for Structures (TaFeSb and TiFeSb) with 3.7 % Fe-vacancy.

We examined our TaFeSb (AM) sample using high-resolution Transmission Electron Microscopy (HRTEM). A representative HRTEM micrograph is shown in Figure 7.1d. The Selected area diffraction pattern (SAED) exhibit sharp spots, reflecting the high crystallinity of our sample. The symmetry of the spots is in line with the expected hH structure.

The electronic band structure of TaFeSb is shown in Figure 7.3c. The calculated band structure and the band gap of 0.87 eV between points X (conduction band minimum) and L (valence band maximum) of the Brillouin zone are in good agreement with the previous study by Zhu *et al*. [66, 190]. However. the experimentally observed band gap of TaFeSb is only 0.53 eV, which is less than the calculated bandgap [66]. We found that this difference is due to the presence of antisite disorder present in these samples. For example, incorporating Ta-Fe antisite disorder in the calculation results in the appearance of *new* defect states around 0.5 eV above the valence band maximum, reducing the effective bandgap to close to its experimental value, as shown in Figure. 7.3(c,d) where the band structures of pristine TaFeSb (c) and TaFeSb with 3.7% Ta-Fe antisite disorder (d) are plotted. We found a similar result when we incorporated Ti-Fe antisite disorder for Ti-doped TaFeSb, which is more closer to the experimental situation, where the disorder is dominated by Ti occupying to the Y-site (shown in Figure 7.4). In Figure 7.3d, the Fermi energy is also shifted into the valence band, making TaFeSb an intrinsically *p*-type material, which explains why TaFeSb sample

shows a nearly degenerate *p*-type behavior without any external doping. Another interesting consequence of antisite disorder is that it flattens the bands near the valence band maxima, resulting in high effective mass (m_D^*) of charge carriers. This agrees well with our experimental results discussed in the next section. The band structure for Ti substituted sample with Ti-Fe antisite disorder is shown in Figure 7.4, where the effective bandgap is found to be still close to 0.5 eV. The presence of defect states in the forbidden gap due to antisite disorder or interstitial atoms is not unusual. For example, similar defect states are shown for ZrNiSn due to some Ni atoms occupying the interstitial 4*d* site [162]. Manipulating these defect states by substitution is a useful way to enhance the zT of ZrNiSn based alloys [191]. As shown by Bhattacharya *et al*. [192], in TaFeSb the intrinsic defects comprising Fe atoms occupying the tetrahedral 4*d* site is energetically unfavourable, explaining further why TaFeSb is not intrinsically *n*-type.

7.3.2 Electronic Transport Properties

Figure 7.6 shows the transport properties of $Ta_{1-x}Ti_xFeSb$ (AM) (x = 0, 0.12, 0.16, and 0.20), $Ta_{0.84}Ti_{0.16}FeSb$ (PS), $Ta_{0.84}Ti_{0.16}Fe_{0.97}Sb$ (PS), and the Ti/V co-substituted counterparts of the two PS samples. The electrical conductivity (σ) of AM series of samples, shown in Figure **??**a, increases dramatically with increase in x form 0 to 0.12 and thereafter more gradually as x increases further. A value close to 4.5 $\times 10^3$ S cm^{-1} for 16% Ti-doped sample is in a reasonably good agreement with previous study [66]. Simultaneously, the Seebeck coefficient (S), shown in Figure 7.6b, increases equally dramatically with the initial Ti-doping, and thereafter decreases gradually but remains significantly higher than the Seebeck of undoped TaFeSb up to the highest doping. The simultaneous dramatic increase of σ and S is, in fact, one of the most remarkable features of TaFeSb that makes it stand out among the other hH thermeoelectric, and is essentially driven by the Ti-Fe antisite disorder that simultaneously dope holes and makes favorable changes in the band structure leading to the simultaneous increase in two otherwise contra-related transport coefficients. A value of S = 235 μ V K^{-1} at 973 K in $Ta_{0.84}Ti_{0.16}FeSb$ (AM) is in close agreement with previous

study [66]. The power factor (PF = $S^2\sigma$) of the doped AM samples is shown in Figure 7.6c. Both x = 0.12 and 0.16, show high and comparable PF, with a slight upturn for x = 0.16 above 800 K. For x = 0.20, the PF has reduced over the whole temperature range.

The transport properties of the PS samples (including PS samples obtained by Ti/V co-substitution) are also shown in Figure 7.6 (right panels). The electrical conductivity (σ), and Seebeck of these samples follow the same qualitative behavior as seen for the AM samples. The differences between the two series of samples are best highlighted in the temperature variation of PF, shown in Figure 7.6d. The highest PF from in the PS series is shown by $Ta_{0.84}Ti_{0.16}Fe_{0.97}Sb$ (PS), which is comparable in magnitude and behavior to the PF of sample $Ta_{0.84}Ti_{0.16}FeSb$ (AM). The PF of the $Ta_{0.84}Ti_{0.16}FeSb$ (PS) is smaller over the whole temperature compared to its AM analogue, underpinning the role of Ti-Fe antisite disorder. The higher PF of $Ta_{0.86}Ti_{0.16}Fe_{0.97}Sb$ (PS) with respect to $Ta_{0.86}Ti_{0.16}FeSb$ (PS) is because of the increased Seebeck coefficient of Fe deficient sample due to its higher density of state effective mass (m^*_D) discussed next. In Ti/V co-substituted samples, the PF has reduced over the whole temperature range. Near room-temperature, they lag behind due to their lower σ, and at high temperatures, due to reduced S. This trend is consistent with Ref. 66, but the peak PF in their study is 25% higher for the same nominal composition (10%V-16%Ti), and the reason for this is that in their samples S increases with increase in the V-doping concentration, unlike what we see where a small decrease is observed at higher temperatures. The increasing behavior reported in Ref. 66 is somewhat unclear since VFeSb itself is a n-type thermoelectric with a large negative S. Thus, one naively expects V-doping to decrease the Seebeck. Since V-doped TaFeSb has also been studies by Luo *et al.*, they repotr a decreasing trend in the values of S with increasing V-doping [193]. The carrier concentration (n) is estimated from the measured Hall carrier concentration using: $n = r_H n_H$, where r_H is the Hall factor, calculated using the SPB model [194, 195]. The carrier concentration (n), effective mass (m^*_D), and mobility (μ) of the AM samples are plotted in Figure 7.7. As shown in Figure 7.7(a, b), n increases with increase in Ti-content, but remains almost constant at high temperatures. In $Ta_{0.84}Ti_{0.16}FeSb$ (PS), $n \approx 9.2 \times 10^{20}$ cm^{-3}, which is smaller than

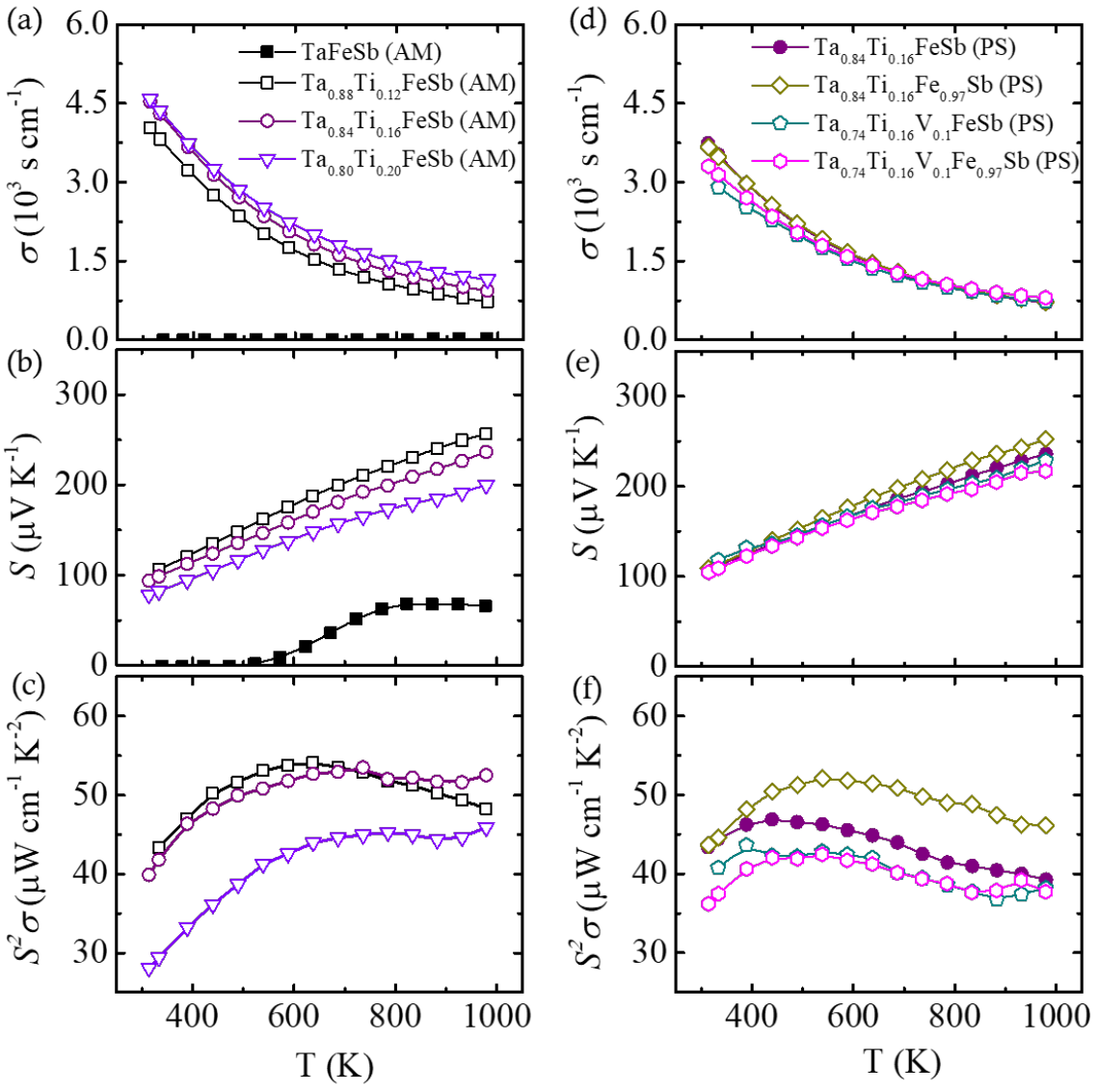

Figure 7.6: Seebeck coefficient, electrical conductivity, and power factor of (a,b,c) arc melted samples, and (d,e,f) powder synthesised samples.

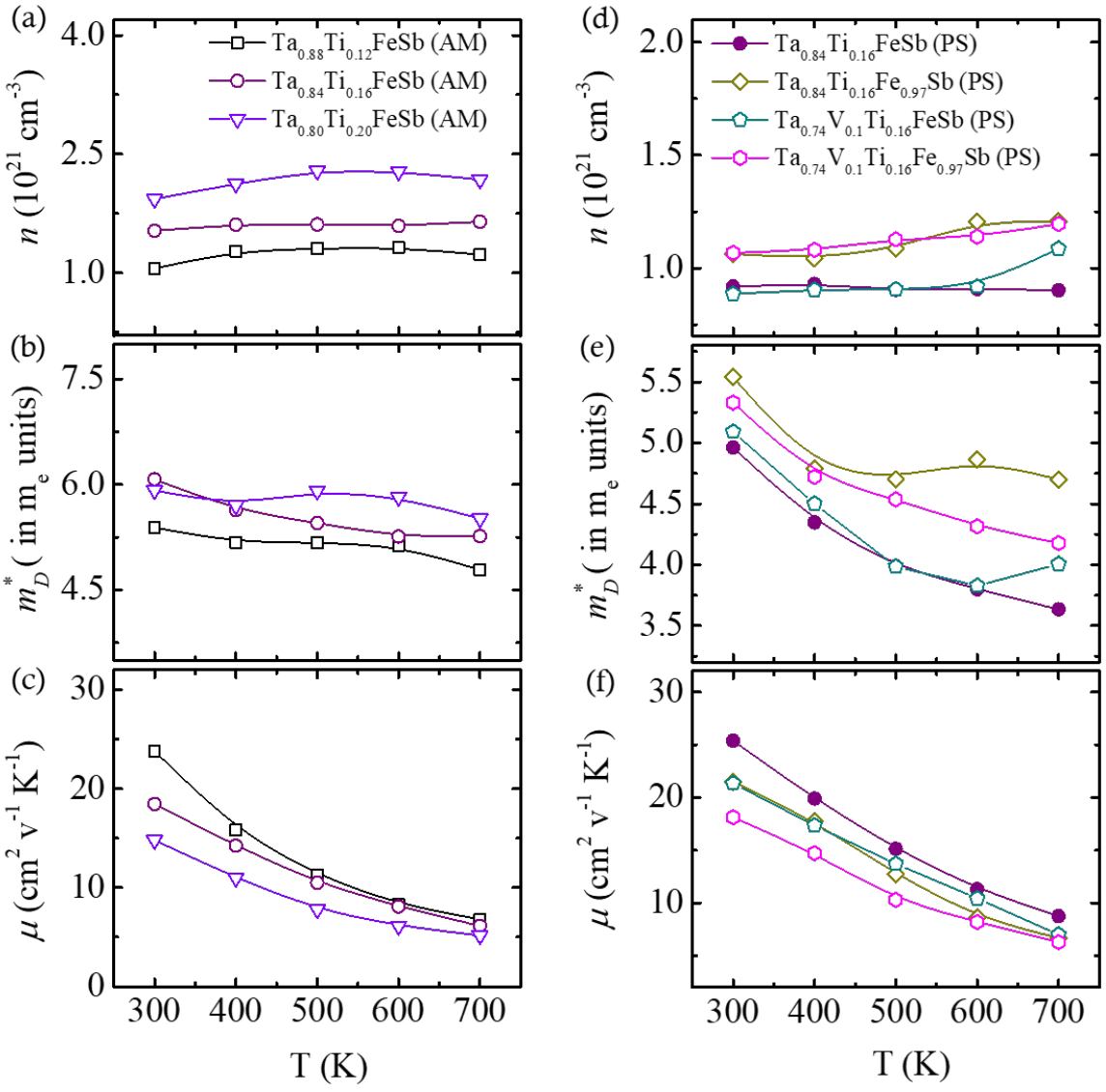

Figure 7.7: carrier concentration, Seebeck effective mass, and mobility of (a,b,c) AM samples, and (d,e,f) PS samples.

$n \approx 15.4 \times 10^{20}$ cm^{-3} in $Ta_{0.84}Ti_{0.16}FeSb$ (AM). In Fe-deficient $Ta_{0.84}Ti_{0.16}Fe_{0.97}Sb$ (PS), n increases to $\approx 10.6 \times 10^{20}$cm^{-3}. Thus, Fe-deficiency along with the Ti-Fe antisite disorder results in excess carrier doping than what Ti-doping alone will achieve.

The density of state effective mass estimated using SPB model for the AM and PS samples is shown in Figure 7.7(b, d). While m_D^* is 5m_e for $Ta_{0.84}Ti_{0.16}FeSb$ (PS), it is 5.9m_e for its AM counterpart. m_D^* also shows a stronger decreasing trend with temperature for PS samples prepared without the Fe deficiency. On the other hand, for Fe-deficient $Ta_{0.84}Ti_{0.16}Fe_{0.97}Sb$ (PS), m_D^* increases to $5.6m_e$, closer to that for $Ta_{0.84}Ti_{0.16}FeSb$ (AM). For this sample, the temperature dependence of m_D^* is also qualitatively similar to that for the AM sample, as for both these samples m_D^* plot tends to become flatter after an initial decreases as the temperature increases. The higher value of m_D^* for the Fe-deficient PS sample or for $Ta_{0.84}Ti_{0.16}FeSb$ (AM) aligns well with our band structure calculation that shows flattening of the valence bands in the presence of Ti-Fe antisite disorder. As shown earlier, in both $Ta_{0.84}Ti_{0.16}FeSb$ (AM) and $Ta_{0.84}Ti_{0.16}Fe_{0.97}Sb$ (PS), the Fe-deficiency in the starting melt, promotes Ti-Fe antisite disorder–in AM the the Fe deficiency is due to evaportive losses and in PS due to starting with some lesser amount of Fe than required.

The mobility (μ) of AM and PS samples are shown in Figure 7.7(c, f). Since n is relatively temperature independent, the temperature dependence of μ is similar to that of σ. At any temperature, as x increases, μ decreases due to increase in the impurity scattering. For $Ta_{0.84}Ti_{0.16}FeSb$ (PS), the mobility is $\approx$ 26 cm^2 V^{-1} k^{-1} at 300 K is clearly larger than $\approx$ 19 cm^2 V^{-1} k^{-1} of $Ta_{0.84}Ti_{0.16}FeSb$ (AM). This is consistent with the fact that the antisite disorder is more pronounced in the AM sample. Compared to $Ta_{0.84}Ti_{0.16}FeSb$ (PS), for the Fe-deficient sample $Ta_{0.84}Ti_{0.16}Fe_{0.97}Sb$ (PS), μ reduces to $\approx$ 21 cm^2 V^{-1} k^{-1}. Similalry, with respect to $Ta_{0.84}Ti_{0.16}FeSb$ (PS), in the Ti/V co-doping [$Ta_{0.74}V_{0.10}Ti_{0.16}FeSb$ (PS)], reduces μ. Along the predictable line, a further reduction is seen in the Fe-deficient sample $Ta_{0.74}V_{0.10}Ti_{0.16}Fe_{0.97}Sb$ (PS).

7.3.3 Lattice thermal conductivity

Figure 7.8a shows the lattice thermal conductivity (κ_l) of $Ta_{1-x}Ti_xFeSb$ (AM) for x = 0.12, 0.16, and 0.20. The κ_l component is estimated by subtracting the electronic part (κ_e) using the Wiedemann-Franz law [18]. The Lorentz number is estimated using the SPB model considering the acoustic phonon scattering mechanism [195]. As expected, κ_l decreases with increase in Ti doping from 5.4 W m^{-1} K^{-1} for $x = 0.12$ to 3.9 W m^{-1} K^{-1} for $x = 0.16$, and 2.85 W m^{-1} K^{-1} for $x = 0.20$. This reduction is due to increased point-defect scattering when Ti is substituted for Ta, which also increases the antisite disorder that further contributes to the suppression of κ_l. A comparison of $Ta_{0.84}Ti_{0.16}FeSb$ (AM) and $Ta_{0.84}Ti_{0.16}FeSb$ (PS) shows that the PS sample has $\approx 55\%$ higher κ_l as compared to its AM counterpart, as shown in Figure 7.8b. However, in the Fe-deficient $Ta_{0.84}Ti_{0.16}Fe_{0.97}Sb$ (PS) sample, κ_l has lowered again. The Ti/V co-substitution [$Ta_{0.74}V_{0.1}Ti_{0.16}FeSb$ (PS)], similarly has a reduced κ_l. A further reduction, leading to the lowest κ_l of 2.56 W m^{-1} K^{-1} at 300 K in our study, is achieved in the Fe-deficient, Ti/V-co-substituted sample $Ta_{0.74}V_{0.1}Ti_{0.16}Fe_{0.97}Sb$ (PS).

7.3.4 Thermoelectric figure-of-merit zT

The thermoelectric figure-of-merit (zT) of our AM and PS samples is shown in Figure 7.8(c, d). In all cases, zT shows a increasing trend up to the highest measured temperature (973 K). A maximum zT of $\sim$ 1.5 is recorded for $Ta_{0.84}Ti_{0.16}FeSb$ (AM), as shown in Figure 7.8b. This value is higher than that previously reported for the same composition in Ref. [66] (zT $\sim$ 1.4 at 973 K). As for the two PS samples, a maximum zT of $\sim$1 is obtained for the sample $Ta_{0.84}Ti_{0.16}FeSb$ (PS), but for the Fe-deficient sample $Ta_{0.84}Ti_{0.16}Fe_{0.97}Sb$ (PS) that has substantially higher Ti-Fe disorder, the observed maximum zT value of 1.35 is considerably higher.

Upon Ti/V co-substitution, κ_l reduces, but the maximum zT value remains close to 1 because of the low power factor. However, in the Fe-deficient $Ta_{0.74}Ti_{0.16}V_{0.10}Fe_{0.97}Sb$ (PS), zT value rises to 1.28 at 973 K. Zhu *et al*. [66] had reported their maximum zT of 1.5 for

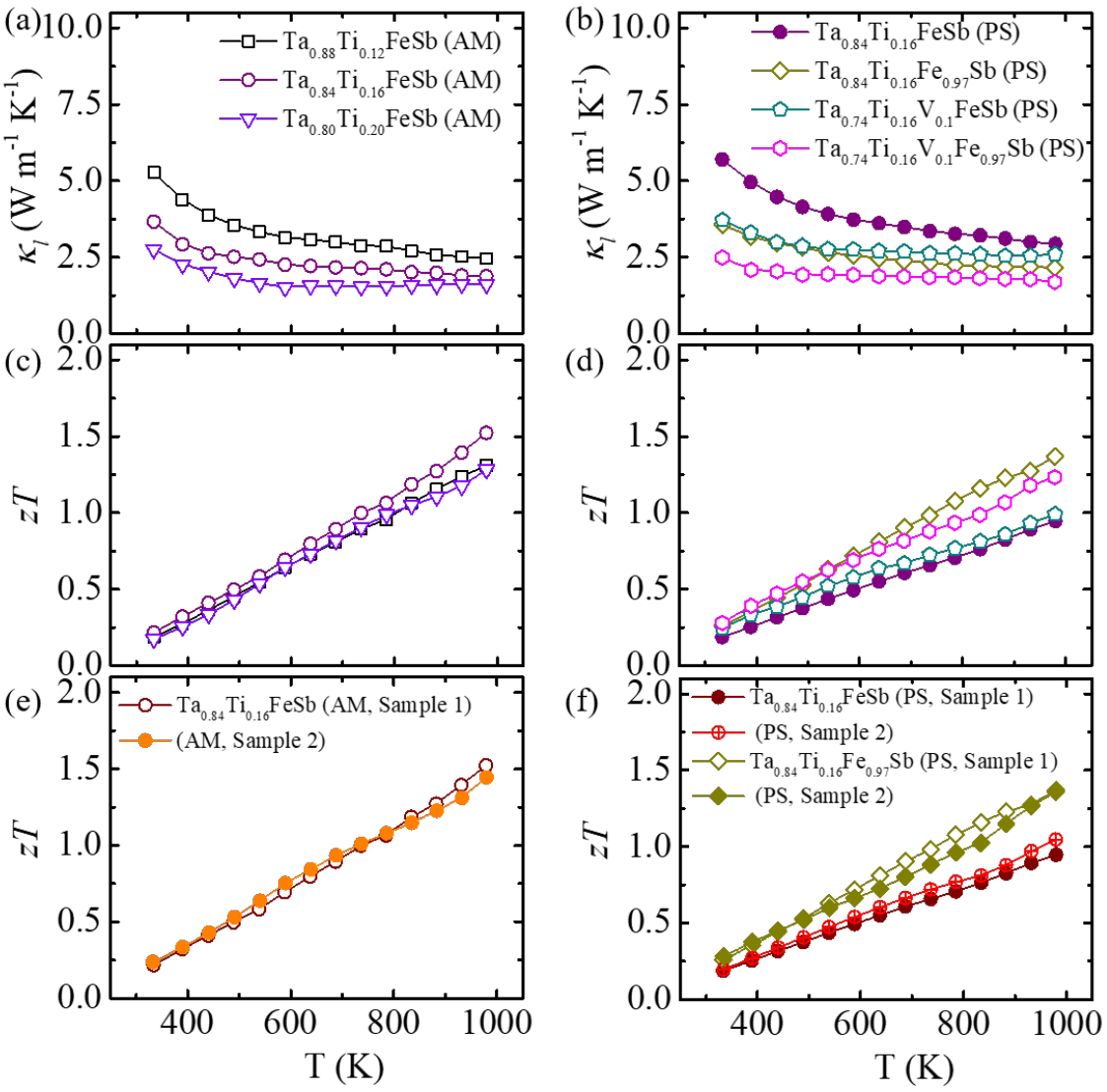

Figure 7.8: Lattice thermal conductivity and zT of (a,c) arc melted sample and (b, d) powder synthesised sample

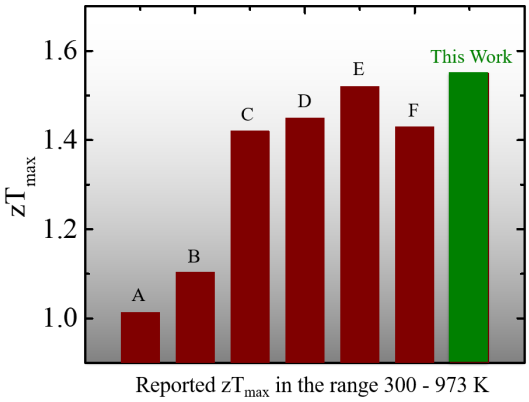

Figure 7.9: zT_{max} comparison with a few state of the art hH thermoelectric materials.

the Ti/V co-substituted sample. However, we could not reproduce their result. It maybe that we need further optimization of the composition for the co-doped samples. However, as it stands our observation is consistent with the more recent study by Luo *et al.* who found a maximum zT of 1.2 in Ti/V co-substituted sample. Since VFeSb in intrinsically *n*-type and hence shows a negative Seebeck coefficient, introducing V in (Ta,Ti)FeSb is naively expected to reduce the Seebeck, which is what is found experimentally in the present study and study by Luo *et al*. [193]. Further scrutiny is therefore necessary and the current study should motivate further research on TaFeSb-based materials. Nonetheless we have compared zT_{max} with a few state of the art hH thermoelectric materials are shown in Figure 7.9. The the samples are represented as: A $\equiv Hf_{0.8}Ti_{0.2}FeSb_{0.8}Sn_{0.2}$ [73], B $\equiv Nb_{0.8}Ti_{0.2}FeSb$ [163], C $\equiv Zr_{0.8}CoBi_{0.65}Sb_{0.15}Sn_{0.2}$ [68], D $\equiv Nb_{0.8}Hf_{0.2}FeSb$ [64], E $\equiv Ta_{0.74}V_{0.1}Ti_{0.16}FeSb$ [66], F $\equiv Ta_{0.42}Nb_{0.3}V_{0.15}Ti_{0.13}FeSb\text{-}(InSb)_{0.015}$ [196].

7.3.5 Reproducibility and thermal cycling

In order to confirm that zT of 1.5 at 973 K is reproducible, we prepared a second $Ta_{0.84}Ti_{0.16}FeSb$ (AM) sample using exactly the same synthesis protocol as used before. The results, plotted in Figure 7.10a, shows that the high zT value is well reproducible. Similarly, we prepared a second set of $Ta_{0.84}Ti_{0.16}FeSb$ (PS) and $Ta_{0.84}Ti_{0.16}Fe_{0.97}Sb$ samples using exactly the same

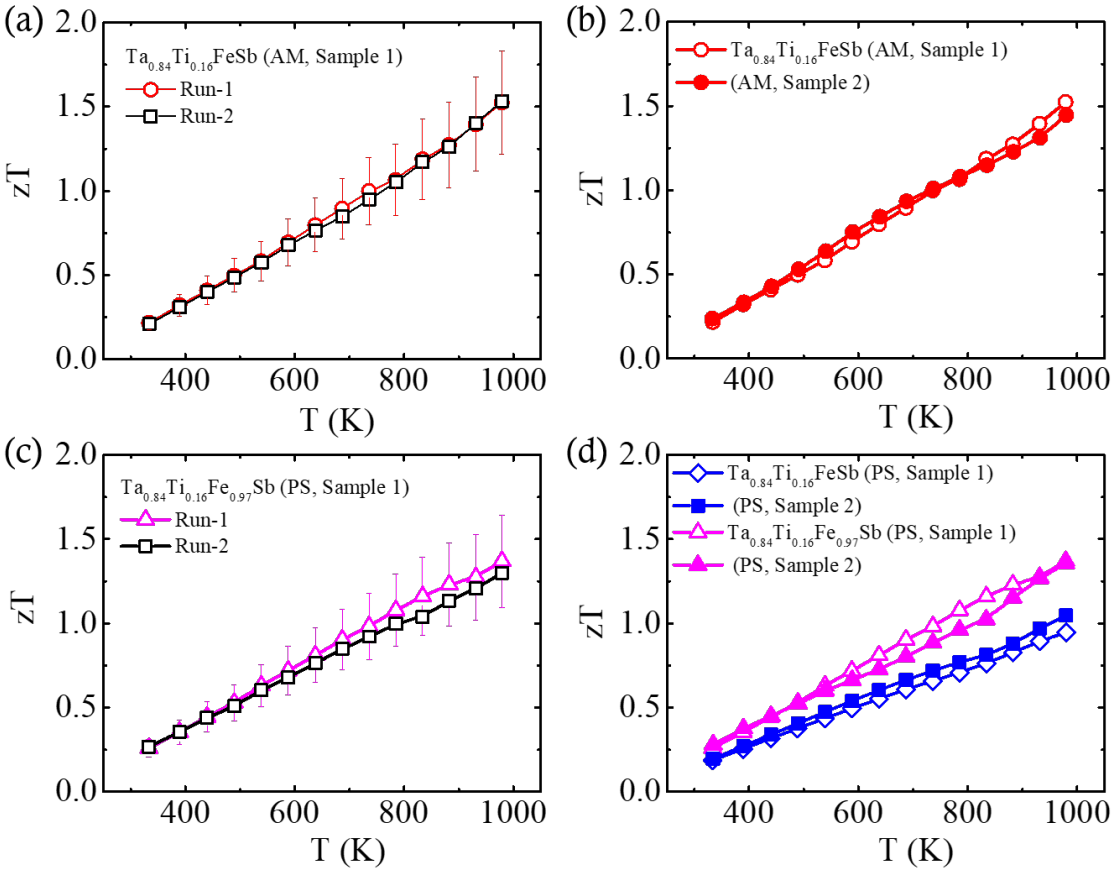

Figure 7.10: Reproducible zT of AM and PS samples (a,b) and Thermal cycling (c,d)

protocol as before. The zT of these new samples, shown in Figure 7.10b, matches fairly nicely with the zT of the first set of samples. To verify the thermal stability, we have also dine multiple heating cooling measurements as shown in Figure 7.10(c,d).

7.4 Summary and Conclusions

We studied the role of antisite disorder and Fe-deficiency in giving rise to high zT in the Ti substituted TaFeSb samples. For this we prepared, a series of Ti substituted, Ti/V co-substituted samples, and their counterparts with or without Fe deficiency. Our study reveal that antisite disorder is crucial for obtaining a high zT, exceeding 1.5. In a sample with no Fe deficiency and minimal Ti-Fe disorder, the maximum zT at 973 K did not increase above a value of zT = 1. Our density functional theory based electronic structure calculations show that the Ti-Fe antisite disorder results in defect states within the bandgap, effectively narrowing it to about 0.5 eV–a value closer to the experimental bandgap. The antisite disorder also pushes the Fermi energy into the valence band, leading to the observed *p*-type behavior of TaFeSb-based materials. The defect/disorder assisted lowering of the lattice thermal conductivity, and high value of power-factor due to carrier optimization through Ti content tuning results in high zT exceeding 1.5. These findings offer valuable insights into optimizing the thermoelectric performance of half-Heuslers through controlled defect engineering.

Chapter 8

Summary and Conclusion

In this thesis, we have explored the thermoelectric properties of some new half Heusler (hH) materials. Half-Heuslers are structurally stable, mechanically strong, and can sustain high temperatures, which makes them suitable candidates for high temperature thermoelectric device for heat to electricity conversion. They are generally represented as XYZ, where X is the most electropositive element, Z is the most electronegative and Y has intermediate electonegativity. The thesis mainly focuses on the design and development of new hH materials and methods to enhance thermoelectric performance.

We have done band engineering along with modulation doping to enhance the thermoelectric figure-of-merit (zT) of TiCoSb, which is a well known hH material with intrinsic n-type properties. DFT calculation suggests the convergence of two conduction band near the conduction band minima when the material is subjected to a tensile strain. To achieve this chemically, we tried various substituents for Ti and found Nb to be most favourable for the conduction band convergence. Up untill this point we managed to engineer the band in favour of better thermolectric performance but Nb doping brings one extra electron into the matrix. The convergence was achieved at 25 % Nb doping which means 25 % electron doping too. Even though bands converged , the carriers near the band edge could not participating in transport as Fermi energy was too high up into the conduction band due to large Nb doping required for the band convergence. We mitigate this issue by using the concept

of modulation doping as explained below.

We found that our 10% and 15% Nb substituted samples undergo phase segregated into phases $Ti_{1-x}Nb_xCoSb$ and $Nb_{0.8+\delta}CoSb$ ($\delta \leq 0.05$). Based on these findings, we synthesized a series of composites, $(Ti_{1-x}Nb_xCoSb)_{1-f} \oplus (Nb_{0.8}CoSb)_f$ by arc-melting. With increase in x the band convergence was achieved and the secondary phase, $Nb_{0.8+\delta}CoSb$, having less carrier density than $Ti_{1-x}Nb_xCoSb$, accepted the addtional electrons from Nb-doped TiCoSb phase in order to bring the Fermi energy so that the band convergence can be exploited. We show in this chapter that through a synergistic combination of band engineering and modulation doping in these composites, we obtained a maximum zT value of 0.81 at 973 K. Further, the temperature variation of zT is shown to exhibit an increasing behavior with upward curvature, suggesting that even higher zT values can be obtained by extending the measurements to higher temperatures.

In another project, using using DFT based calculations we studied the stability and electronic properties of $XFe_{0.5}Ni_{0.5}Sb$, where X = Ti, Zr and Hf, which belong to the family of $XY_{0.5}Y'_{0.5}Z$ dhH. $TiFe_{0.5}Ni_{0.5}Sb$ was chosen because it is one of the most well studied member of this family. We replaced Ti (X) with Zr and Hf. All these elements belong to Group IV of the periodic table. However, we note that as we move down the periodic table, the atomic size increases (though Zr and Hf have similar atomic sizes) while the electronegativity decreases. The change in atomic size introduces local strain in the lattice. Additionaly, it is also unclear that upon formation of the DHH whether the nature of the chemical bonds between the atomic species are similar or different compared to the HHs. Hence, through our study, we have elucidated the role of bonding, effect of local strain and electronegativity on their stability and electronic properties. Further, we used semiclassical Boltzmann Transport theory to study how the above mentioned effects are translated to their transport properties.

A detailed analysis of the nature of the bonding in these DHHs show that there is a presence of hierarchical bonding, i.e., varying degree of covalent and ionic bonds, in these systems that results in changes in electronic structure and lowering of lattice thermal conductivity. We observe that replacing Ti with Zr or Hf facilitates band convergence in the

conduction band of these materials. Our calculations show that reduction of electronegativity and tensile strain induced due to change in atomic size have opposite effects on band convergence in these materials. While the former favours band convergence, the latter is detrimental for it. Additionally, electronegativity has a stronger effect than the chemical pressure. In accordance with the observed band convergence, we find that in these materials n-type carriers have larger Seebeck coefficient than there p-type counterparts, with $HfFe_{0.5}Ni_{0.5}Sb$ showing the largest value. Amongst the three materials considered in our study, $HfFe_{0.5}Ni_{0.5}Sb$ exhibits the largest value of zT for n-type carriers at around 1000 K. Moreover, p-doped $HfFe_{0.5}Ni_{0.5}Sb$ also have $zT > 1$ at 1000 K. We anticipate that our work will provide a guideline for the experimentalists in rational design of DHHs with high zT.

We then started a combined experimental and theoretical project motivated by the increasing interest in high-entropy alloys in the field of thermoelectric materials. The high lattice thermal conductivity of the hH alloys is one of their main disadvantages and the high-entropy alloying principle can be useful in overcoming this challenge. In this work, we have synthesized a new hH alloy, namely, $Hf(FeNi)_{1/2}Sb$ and using this as the base material, we introduced Ti at the X-site by substituting 50% of Hf with Ti, and Co at the Y site by replacing $(FeNi)_{1/2}$ by $(FeCoNi)_{1/3}$. This resulted in a high-entropy alloy $(TiHf)_{1/2}(FeCoNi)_{1/3}Sb$ ($\Delta S_{conf} = 1.79R > 1.5R$). Using estiblished annealing protocol, we further show that $(TiHf)_{1/2}(FeCoNi)_{1/3}Sb$ is not only a high-entropy alloy, but it also belongs to the small subgroup of entropy-stabilized alloys, where the high configurational entropy becomes the driving force in stabilizing a homogenous single-phase alloy. It should be pointed out that while there are several previous studies on high-entropy hH alloys, the entropy stabilized hH alloys are rare. The effect of Co-doping on the band structure was studied using first-principles DFT calculations. We show that Co incorporation in the structure increases the band gap from 0.4 eV in $(TiHf)_{1/2}(FeNi)_{1/2}Sb$ to 0.7 eV in $(TiHf)_{1/2}(FeCoNi)_{1/3}Sb$. This, in turn, helps mitigate the issue of bipolarity. The entropy-stabilized $(TiHf)_{1/2}(FeCoNi)_{1/3}Sb$ is found to exhibit a very low lattice thermal conductivity (1.7 W m^{-1} K^{-1} at 973 K). Further carrier optimization is carried out by tuning Fe and Ni

concentrations in $(TiHf)_{1/2}(Fe_{1-x}CoNi_{1+x})_{1/3}Sb$ by varying x up to 0.5, beyond which the sample does not form in a single phase. With increasing x, the PF increases and κ_l decreases, leading to a remarkably low $\kappa_l \sim 1$ W m^{-1} K^{-1} at 973 K. This, to the best of our knowledge, is the lowest value of κ_l ever reported for any hH alloy [180]. A combination of ultra-low thermal conductivity and high PF, the sample with $x = 0.5$ showcases the highest zT of 0.55 at 973 K, up to this temperature, zT exhibits an increasing behavior. The sample's reproducibility and thermal stability were successfully tested. Our work demonstrates the experimental validation of entropy stabilization in hH family for the first time, showcasing the effectiveness of the high-entropy strategy for high-performance thermoelectric materials.

Finally, we studied the role of antisite disorder and Fe-deficiency in giving rise to record high zT value in Ti substituted TaFeSb samples. For this we prepared, a series of Ti substituted and Ti/V co-substituted samples. Alongside, we also synthesized their counterparts with or without Fe deficiency. Our study reveals that antisite disorder is crucial for obtaining a high zT, exceeding 1.5. In a sample with no Fe deficiency and minimal Ti-Fe disorder, the maximum zT at 973 K did not increase above a value of zT = 1. Our density functional theory based electronic structure calculations show that the Ti-Fe antisite disorder results in defect states within the bandgap, effectively narrowing it to about 0.5 eV–a value closer to the experimental bandgap. The antisite disorder also pushes the Fermi energy into the valence band, leading to the observed *p*-type behavior of TaFeSb-based materials. The defect/disorder assisted lowering of the lattice thermal conductivity, and high value of power-factor due to carrier optimization through Ti content tuning results in high zT exceeding 1.5. These findings offer valuable insights into optimizing the thermoelectric performance of half-Heuslers through controlled defect engineering.

Appendix A

Simplified approach to estimate Lorenz number using experimental Seebeck coefficient for non parabolic band

Reduction of lattice thermal conductivity (κ_L) is one of the most effective ways of improving thermoelectric properties [197]. However extraction of κ_L from the total measured thermal conductivity can be misleading if Lorenz (L) number is not estimated correctly. The κ_L is obtained using Wiedemann-Franz law which estimates electronic part of thermal conductivity κ_e = $L\sigma$T where, σ and T are electrical conductivity and temperature. The κ_L is then estimated as κ_L = κ_T - $L\sigma$T. For the metallic system the Lorenz number has universal value of 2.44 $\times$ 10^{-8} WΩK^{-2} (degenerate limit), but for no-degenerate semiconductors, the value can deviate significantly for acoustic phonon scattering, the most common scattering mechanism for thermoelectric above room temperatures. Up till now, L is estimated by solving a series of equation derived form Boltzmann transport equations. For the single parabolic band (SPB) an equation was proposed to estimate L directly from the experimental Seebeck coefficient. However using SPB model will lead to overestimation of L in case of low band gap semiconductors which result in underestimation of κ_L sometimes even negative κ_L. In this letter we propose a simpler equation to estimate L for a non parabolic band. Experimental

Seebeck coefficient, band gap(E_g), and Temperature (T) are the main inputs in the equation which nearly eliminates the need of solving multiple Fermi integrals besides giving accurate values of L. For example, incautious determination of L in case of lanthanum telluride can even cause κ_L to be negative, which is not physical [198]. Therefore, careful evaluation of L is critical in characterizing enhancements in zT due to κ_L reduction.

In case of metals, charge carriers are free-electrons like, where L converges to 2.44 $\times$ 10^{-8} WΩ K^{-2} (degenerate limit). However, heavily doped semiconductors will have L very close to the degenerate limit. From thermoelectric point of view, most good thermoelectric materials have their carrier densities between lightly doped and heavily doped regions. In such cases the error in L could be as much as 40 % [199]. Measuring L directly requires high mobility which is beyond attainable above room temperature [200]. So far, L is taken as a constant (2.44 10^{-8} WΩ K^{-2}) or estimated using various band models such as the single parabolic band model (SPB) and single Kane band model (SKB) which considers non parabolic nature of bands. Although both SPB and SKB models work well to estimate L, a transcendental set of equations is needs to be solved for L in terms of S that require a numerical solution. By assuming that the carrier relaxation time is limited by acoustic phonon scattering (APS), one of the most relevant scattering mechanisms for thermoelectric materials above room temperature, followings are the equations that needs to be solved for SPB-APS model [194, 195]:

$$S = \frac{k_{\mathrm{B}}}{e}\left[\frac{2F_1(\eta)}{F_0(\eta)} - \eta\right], \tag{A.1}$$

$$L = \left(\frac{k_{\mathrm{B}}}{e}\right)^2\left[\frac{3F_2(\eta)}{F_0(\eta)} - \left(\frac{2F_1(\eta)}{F_0(\eta)}\right)^2\right] \tag{A.2}$$

$$\eta = \frac{E_{\mathrm{F}}}{k_{\mathrm{B}}T}, \tag{A.3}$$

where, η is the reduced Fermi energy, E_F the Fermi energy, $F_n(\eta)$ is the Fermi integral, k_B is the Boltzmann constant , and e is the electronic charge.

$$F_k(\eta) = \int_0^\infty \frac{e^k \partial\varepsilon}{1 + exp(E - \eta)} \tag{A.4}$$

For SPB model, a much simpler form is proposed by Hyun-Sik Kim et.al which estimated L within 5 % error with respect to actual value estimated using SPB model [201]. The expression for L as derived by Kim et.al. is given as:

$$L = 1.5 + exp\left(-\frac{|S|}{116}\right) \tag{A.5}$$

However, the SPB model with acoustic phonon scattering does not produce correct results in case of low band gap semiconductors where non-parabolic band structure come into picture. PbTe [194, 202], PbSe [203], and PbS [204] are a few examples with narrow band gap described by non-parabolic Kane band model. The non-parabolicity parameter is determined as: $\alpha = k_B T/E_g$, where E_g is the band gap [24,205]. Estimation of L using SPB model produced value 26 % less [201] than actual. With overestimated L, κ_e will be overestimated too. Therefore when κ_e is subtracted from κ_T to get κ_L, it will be highly underestimated. Considering non parabilicity into account provides the correct estimation. The Seebeck coefficient and L for for a non-parabolic band is given as:

$$S = \frac{k_B}{e}\left[\frac{{}^0F^1_{-2}(\eta,\alpha)}{{}^1F^1_{-2}(\eta,\alpha)} - \eta\right] \tag{A.6}$$

$$L = \left(\frac{k_B}{e}\right)^2 \left[\frac{{}^2F^1_{-2}(\eta,\alpha)}{{}^0F^1_{-2}(\eta,\alpha)} - \left(\frac{{}^1F^1_{-2}(\eta,\alpha)}{{}^0F^1_{-2}(\eta,\alpha)}\right)^2\right] \tag{A.7}$$

$$\eta = \frac{E_F}{k_B T}, \quad and \;\; \alpha = \frac{k_B T}{E_g} \tag{A.8}$$

The function ${}^nF^m_k(\eta,\alpha)$ is the generalized Fermi integral given as:

$${}^nF^m_k(\eta,\alpha) = \int_0^\infty -\left(\frac{\partial f}{\partial\varepsilon}\right)\varepsilon^{\mathrm{n}}(\varepsilon + \alpha\varepsilon^2)^{\mathrm{m}}(1 + 2\alpha\varepsilon^2)^{\mathrm{k}}\partial\varepsilon \tag{A.9}$$

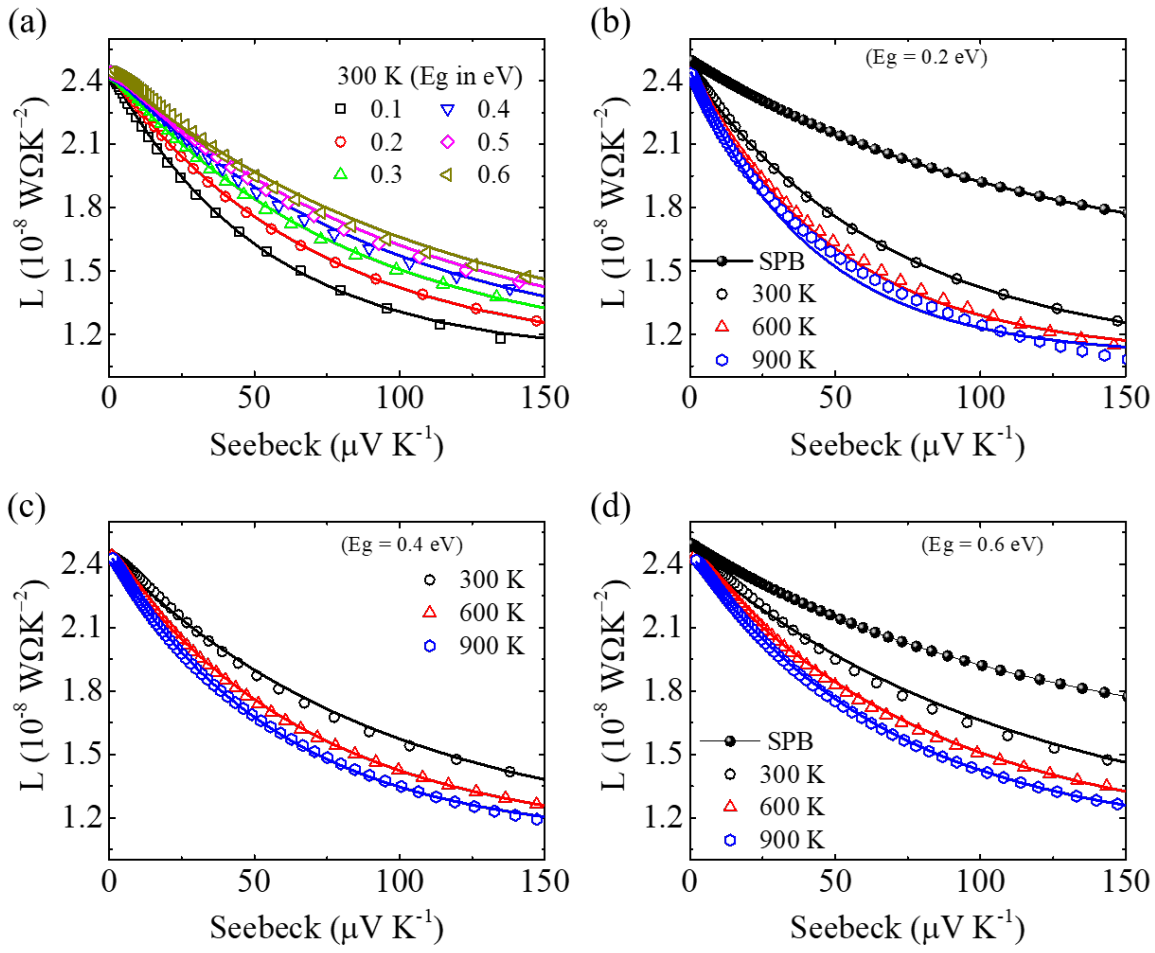

Figure A.1: (a) Lorenz number for different E_g at 300 K, and (b, c, d) L for different E_g at different temperatures. Dots are the calculated date using the SKB model and the solid lines are using equation A.11

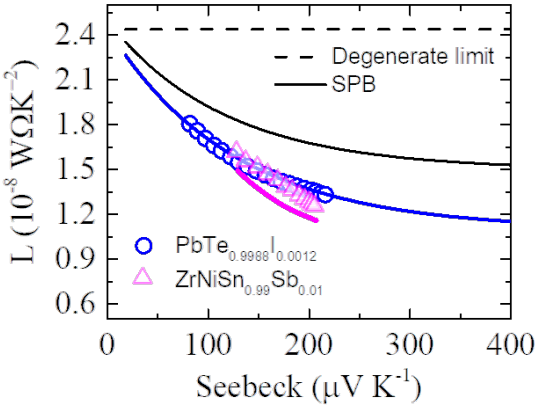

Figure A.2: Reported Lorenz number (points) and calculated using equation **??**(lines). The dotted line represents the degenerate limit whereas the solid black line represents the value of L considering the SPB model.

where ε is the reduced energy E/k_BT, and f is the Fermi distribution function. The parameter n, m and k are the indices of the integral whose value depend on the transport property and scattering mechanism.

The SKB model is much more complex than the SPB model as it has additional parameter of non parabolicity (α). Considering the exponential form of L for the SPB model, we assumed a similar function of L for SKB with additional parameter of temperature (T) and band gap (E_g) or in other words α. The assumed form for L is given as:

$$L = A + Bexp\left[\frac{-|S|}{f(E_g)g(T)}\right] \tag{A.10}$$

where A and B are constants. The T and E_g dependence is accounted by function f and g. In order to find the unknown constants (A, B) and functional form (f, g), we have generated a data set using equation A.6 and A.7 for wide range for E_g and T. A and B are estimated by keeping function f and g as parameters while fitting the L vs S data with the proposed equation. As a result, apart from A and B, we got the information of how f and g are varying as a function of Eg and T and from analyzing that function f and g are determined giving a complete expression of L as function of S with E_g and T as parameters. The final equation

for L can be expressed as:

$$L = 1.1 + 1.35exp\left[\frac{-|S|}{\left[162 + 128exp\left(-\frac{Eg}{0.614}\right)\right]\left[\frac{15.71}{\sqrt{T}} + 0.0925\right]}\right] \tag{A.11}$$

where L is in 10^{-8} WΩK^{-2} and S in μVK^{-1}.

In order to show the validity of proposed equation, we have shown a good agreement between simulated L as a function of S using equation A.6 and A.7 and using our proposed equation A.11. Figure A.1(a) shows the L at 300K with changing band gaps. The dot represents the data obtained by solving equation A.6 and A.7 whereas the line represents value of L generated using equation A.11. The values are in good agreement. Now to see if the equation hold for other temperatures we have done a similar simulation for band gap of 0.2, 0.4 and 0.6 with temperature of 300 K, 600 K, and 900 K as shown in figure A.1(b,c,d). In every case our proposed equation produces value of L close to the value produced by solving equation A.6 and A.7. This concludes the validity of our equation which can be used instead of equation A.6 and A.7.

As a test case, we have considered a few examples where APS is the dominant scattering mechanism. One of the best example is PbTe system as shown in the figure A.2. The L calculated using equation A.11 fits perfectly with the reported value of L obtained using equation A.6 and A.7 [202]. Another example of Sb doped ZrNiSn shows small deviation from the reported value which was calculated by considering Acoustic phonon, Polar and Alloy scattering [70]. In this case just using the SKB model is not so accurate but still the SKB estimate better value of L compared to SPB model as shown with pink (SKB) and black (SPB) lines. Our proposed equation provides an easy way to use SKB model to estimate L for system with small band gaps. The systems with low band gap where complex scattering mechanism are in play, using SKB model with our proposed equation will provide more accurate value than using SPB model. Overall, we have proposed an equation to estimate L considering non parabolicity into account which require, experimental

Seebeck, band gap and measurement temperature. Using our equation one can estimate the lattice thermal conductivity more accurately.

Bibliography

[1] H. Ritchie, M. Roser, and P. Rosado. Energy. our world in data, 2020 (2020).

[2] R. Freer, D. Ekren, T. Ghosh, K. Biswas, P. Qiu, S. Wan, L. Chen, S. Han, C. Fu, T. Zhu, *et al.*, "Key properties of inorganic thermoelectric materials", *Journal of Physics: Energy* **4**(2), 022002 (2022).

[3] A. Karati, M. Nagini, S. Ghosh, R. Shabadi, K. Pradeep, R. C. Mallik, B. Murty, and U. Varadaraju, "Ti2nicosnsb-a new half-heusler type high-entropy alloy showing simultaneous increase in seebeck coefficient and electrical conductivity for thermoelectric applications", *Scientific reports* **9**(1), 5331 (2019).

[4] R. Chen, Y. Yan, G. Li, R. Min, H. Kang, E. Guo, Z. Chen, X. Yang, and T. Wang, "Maximizing the scattering of multiwavelength phonons in novel biphasic high-entropy zrcosb-based half-heusler alloys", *Journal of Materiomics* (2023).

[5] A. Karati, V. Hariharan, S. Ghosh, A. Prasad, M. Nagini, K. Guruvidyathri, R. C. Mallik, R. Shabadi, L. Bichler, B. Murty, *et al.*, "Thermoelectric properties of half-heusler high-entropy ti2nicosn1-xsb1+ x (x= 0.5, 1) alloys with vec¿ 18", *Scripta Materialia* **186**, 375 (2020).

[6] C. Wang, X. Zhou, D. Cong, G. Tang, and J. Yang, "A novel valence-balanced double half-heusler ti2zr2hf2nbvfe5ni3sb8 alloy by high entropy engineering", *Materials Today Physics* **36**, 101172 (2023).

[7] R. Chen, Y. Wang, L. Jiang, R. Min, H. Kang, Z. Chen, E. Guo, X. Yang, X. Jiang, and T. Wang, "Enhancing thermoelectric properties of mcosb-based alloys by entropy-driven energy-filtering effects and band engineering", *Materials Today Physics* **30**, 100957 (2023).

[8] K. Chen, R. Zhang, J.-W. G. Bos, and M. J. Reece, "Synthesis and thermoelectric properties of high-entropy half-heusler mfe1- xcoxsb (m= equimolar ti, zr, hf, v, nb, ta)", *Journal of Alloys and Compounds* **892**, 162045 (2022).

[9] H. Jouhara, N. Khordehgah, S. Almahmoud, B. Delpech, A. Chauhan, and S. A. Tassou, "Waste heat recovery technologies and applications", *Thermal Science and Engineering Progress* **6**, 268 (2018).

[10] T. C. Holgate, R. Bennett, T. Hammel, T. Caillat, S. Keyser, and B. Sievers, "Increasing the efficiency of the multi-mission radioisotope thermoelectric generator", *Journal of Electronic Materials* **44**, 1814 (2015).

[11] T. J. Seebeck, "Magnetic polarization of metals and ores by temperature differences", *Abh. Königlichen Akad. Wiss. Berl* pp. 265–373 (1822).

[12] J. Peltier, "New experiments on the heat effects of electric currents", *Ann. Chim. Phys* **56**, 371 (1834).

[13] W. Thomson, "4. on a mechanical theory of thermo-electric currents", *Proceedings of the Royal society of Edinburgh* **3**, 91 (1857).

[14] H. S. Kim, W. Liu, G. Chen, C.-W. Chu, and Z. Ren, "Relationship between thermoelectric figure of merit and energy conversion efficiency", *Proceedings of the National Academy of Sciences* **112**(27), 8205 (2015).

[15] M. Cutler and N. F. Mott, "Observation of anderson localization in an electron gas", *Physical Review* **181**(3), 1336 (1969).

[16] H. Ibach and H. Lüth. *Solid-state physics: an introduction to principles of materials science* (Springer Science & Business Media, 2013).

[17] G. J. Snyder, A. H. Snyder, M. Wood, R. Gurunathan, B. H. Snyder, and C. Niu, "Weighted mobility", *Advanced Materials* **32**(25), 2001537 (2020).

[18] W. Jones and N. H. March. *Theoretical solid state physics*, vol. 35 (Courier Corporation, 1985).

[19] M. S. Lundstrom and C. Jeong. *Near-equilibrium transport: fundamentals and applications*, vol. 2 (World Scientific Publishing Company, 2012).

[20] H. J. Goldsmid *et al. Introduction to thermoelectricity*, vol. 121 (Springer, 2010).

[21] J. M. Borrego. *Optimum impurity concentration in semiconductor thermoelements* (Massachusetts Institute of Technology, Energy Conversion and Semiconductor, 1962).

[22] H. Goldsmid. Applications of thermoelectricity; butler & tanner ltd (1960).

[23] V. I. Fistul. *Heavily doped semiconductors*, vol. 1 (Springer Science & Business Media, 2012).

[24] I. I. Ravich. *Semiconducting lead chalcogenides*, vol. 5 (Springer Science & Business Media, 2013).

[25] A. Kumar, "Simplified approach to estimate lorenz number using experimental seebeck coefficient for non-parabolic band", *AIP Advances* **14**(10) (2024).

[26] A. F. May, E. S. Toberer, A. Saramat, and G. J. Snyder, "Characterization and analysis of thermoelectric transport in n-type ba 8 ga 16- x ge 30+ x", *Physical Review B* **80**(12), 125205 (2009).

[27] Y. Yu, M. Cagnoni, O. Cojocaru-Mirédin, and M. Wuttig, "Chalcogenide thermoelectrics empowered by an unconventional bonding mechanism", *Advanced Functional Materials* **30**(8), 1904862 (2020).

[28] T. Ghosh, S. Roychowdhury, M. Dutta, and K. Biswas, "High-performance thermoelectric energy conversion: A tale of atomic ordering in agsbte2", *ACS Energy Letters* **6**(8), 2825 (2021).

[29] J. Shuai, H. Geng, Y. Lan, Z. Zhu, C. Wang, Z. Liu, J. Bao, C.-W. Chu, J. Sui, and Z. Ren, "Higher thermoelectric performance of zintl phases (eu0. 5yb0. 5) 1-xcaxmg2bi2 by band engineering and strain fluctuation", *Proceedings of the National Academy of Sciences* **113**(29), E4125 (2016).

[30] J. He and T. M. Tritt, "Advances in thermoelectric materials research: Looking back and moving forward", *Science* **357**(6358), eaak9997 (2017).

[31] P. Jood, J. P. Male, S. Anand, Y. Matsushita, Y. Takagiwa, M. G. Kanatzidis, G. J. Snyder, and M. Ohta, "Na doping in pbte: solubility, band convergence, phase boundary mapping, and thermoelectric properties", *Journal of the American Chemical Society* **142**(36), 15464 (2020).

[32] S. Chen and Z. Ren, "Recent progress of half-heusler for moderate temperature thermoelectric applications", *Materials today* **16**(10), 387 (2013).

[33] J. P. Heremans, B. Wiendlocha, and A. M. Chamoire, "Resonant levels in bulk thermoelectric semiconductors", *Energy & Environmental Science* **5**(2), 5510 (2012).

[34] M. Hong, Z.-G. Chen, L. Yang, Y.-C. Zou, M. S. Dargusch, H. Wang, and J. Zou, "Realizing zt of 2.3 in ge1- x- ysbxinyte via reducing the phase-transition temperature and introducing resonant energy doping", *Advanced materials* **30**(11), 1705942 (2018).

[35] L. Wu, X. Li, S. Wang, T. Zhang, J. Yang, W. Zhang, L. Chen, and J. Yang, "Resonant level-induced high thermoelectric response in indium-doped gete", *NPG Asia Materials* **9**(1), e343 (2017).

[36] D. K. Bhat and S. Shenoy U, "High thermoelectric performance of co-doped tin telluride due to synergistic effect of magnesium and indium", *The Journal of Physical Chemistry C* **121**(13), 7123 (2017).

[37] A. Ioffe, "Semiconductor thermoelements, and thermoelectric", *Cool-ingInfosearch Ltd.: London, UK* (1957).

[38] D. Rowe and G. Min. Multiple potential barriers as a possible mechanism to increase the seebeck coefficient and electrical power factor. In *AIP Conference Proceedings*, vol. 316, pp. 339–342 (American Institute of Physics, 1994).

[39] C. Gayner and Y. Amouyal, "Energy filtering of charge carriers: current trends, challenges, and prospects for thermoelectric materials", *Advanced Functional Materials* **30**(18), 1901789 (2020).

[40] M. Zebarjadi, G. Joshi, G. Zhu, B. Yu, A. Minnich, Y. Lan, X. Wang, M. Dresselhaus, Z. Ren, and G. Chen, "Power factor enhancement by modulation doping in bulk nanocomposites", *Nano letters* **11**(6), 2225 (2011).

[41] T. Berry, C. Fu, G. Auffermann, G. H. Fecher, W. Schnelle, F. Serrano-Sanchez, Y. Yue, H. Liang, and C. Felser, "Enhancing thermoelectric performance of tinisn half-heusler compounds via modulation doping", *Chemistry of Materials* **29**(16), 7042 (2017).

[42] A. Kumar, D. K. Kedia, P. Ghosh, and S. Singh, "Band engineering and synergistic modulation doping for excellent thermoelectric performance in composites ti1–x nb x cosb–nb0. 8+ δcosb", *ACS Applied Energy Materials* **6**(20), 10694 (2023).

[43] D. M. Rowe. *Modules, systems, and applications in thermoelectrics*, vol. 2 (CRC press, 2012).

[44] E. Isotta, S. Jiang, G. Moller, A. Zevalkink, G. J. Snyder, and O. Balogun, "Microscale imaging of thermal conductivity suppression at grain boundaries", *Advanced Materials* **35**(38), 2302777 (2023).

[45] Y. Yin, B. Tudu, and A. Tiwari, "Recent advances in oxide thermoelectric materials and modules", *Vacuum* **146**, 356 (2017).

[46] M. Ohtaki, "Recent aspects of oxide thermoelectric materials for power generation from mid-to-high temperature heat source", *Journal of the Ceramic Society of Japan* **119**(1395), 770 (2011).

[47] H. Yakabe, K. Kikuchi, I. Terasaki, Y. Sasago, and K. Uchinokura. Thermoelectric properties of transition-metal oxide naco/sub 2/o/sub 4/system. In *XVI ICT'97. Proceedings ICT'97. 16th International Conference on Thermoelectrics (Cat. No. 97TH8291)*, pp. 523–527 (IEEE, 1997).

[48] S. I. Kim, K. H. Lee, H. A. Mun, H. S. Kim, S. W. Hwang, J. W. Roh, D. J. Yang, W. H. Shin, X. S. Li, Y. H. Lee, *et al.*, "Dense dislocation arrays embedded in grain boundaries for high-performance bulk thermoelectrics", *Science* **348**(6230), 109 (2015).

[49] L.-D. Zhao, H. Wu, S. Hao, C.-I. Wu, X. Zhou, K. Biswas, J. He, T. P. Hogan, C. Uher, C. Wolverton, *et al.*, "All-scale hierarchical thermoelectrics: Mgte in pbte facilitates valence band convergence and suppresses bipolar thermal transport for high performance", *Energy & Environmental Science* **6**(11), 3346 (2013).

[50] G. Dennler, R. Chmielowski, S. Jacob, F. Capet, P. Roussel, S. Zastrow, K. Nielsch, I. Opahle, and G. K. Madsen, "Are binary copper sulfides/selenides really new and promising thermoelectric materials?", *Advanced Energy Materials* **4**(9), 1301581 (2014).

[51] C. Zhou, Y. K. Lee, Y. Yu, S. Byun, Z.-Z. Luo, H. Lee, B. Ge, Y.-L. Lee, X. Chen, J. Y. Lee, *et al.*, "Polycrystalline snse with a thermoelectric figure of merit greater than the single crystal", *Nature materials* **20**(10), 1378 (2021).

[52] R. J. Korkosz, T. C. Chasapis, S.-h. Lo, J. W. Doak, Y. J. Kim, C.-I. Wu, E. Hatzikraniotis, T. P. Hogan, D. N. Seidman, C. Wolverton, *et al.*, "High zt in p-type (pbte) 1–2 x (pbse) x (pbs) x thermoelectric materials", *Journal of the American Chemical Society* **136**(8), 3225 (2014).

[53] S. Roychowdhury, T. Ghosh, R. Arora, M. Samanta, L. Xie, N. K. Singh, A. Soni, J. He, U. V. Waghmare, and K. Biswas, "Enhanced atomic ordering leads to high thermoelectric performance in agsbte2", *Science* **371**(6530), 722 (2021).

[54] S. Anand, K. Xia, V. I. Hegde, U. Aydemir, V. Kocevski, T. Zhu, C. Wolverton, and G. J. Snyder, "A valence balanced rule for discovery of 18-electron half-heuslers with defects", *Energy & Environmental Science* **11**(6), 1480 (2018).

[55] N. Naghibolashrafi, S. Keshavarz, V. I. Hegde, A. Gupta, W. Butler, J. Romero, K. Munira, P. LeClair, D. Mazumdar, J. Ma, *et al.*, "Synthesis and characterization of fe-ti-sb intermetallic compounds: Discovery of a new slater-pauling phase", *Physical Review B* **93**(10), 104424 (2016).

[56] K. Xia, Y. Liu, S. Anand, G. J. Snyder, J. Xin, J. Yu, X. Zhao, and T. Zhu, "Enhanced thermoelectric performance in 18-electron nb0.8cosb half-heusler compound with intrinsic nb vacancies", *Advanced Functional Materials* **28**(9), 1705845 (2018).

[57] Z. Liu, S. Guo, Y. Wu, J. Mao, Q. Zhu, H. Zhu, Y. Pei, J. Sui, Y. Zhang, and Z. Ren, "Design of high-performance disordered half-heusler thermoelectric materials using 18-electron rule", *Advanced Functional Materials* **29**(44), 1905044 (2019).

[58] F. Aliev, N. Brandt, V. Moshchalkov, V. Kozyrkov, R. Skolozdra, and A. Belogorokhov, "Gap at the fermi level in the intermetallic vacancy system rbisn (r= ti, zr, hf)", *Zeitschrift für Physik B Condensed Matter* **75**, 167 (1989).

[59] M. Schwall and B. Balke, "Phase separation as a key to a thermoelectric high efficiency", *Physical Chemistry Chemical Physics* **15**(6), 1868 (2013).

[60] C. Yu, T.-J. Zhu, R.-Z. Shi, Y. Zhang, X.-B. Zhao, and J. He, "High-performance half-heusler thermoelectric materials hf1- x zrxnisn1- ysby prepared by levitation melting and spark plasma sintering", *Acta Materialia* **57**(9), 2757 (2009).

[61] E. Rausch, B. Balke, J. M. Stahlhofen, S. Ouardi, U. Burkhardt, and C. Felser, "Fine tuning of thermoelectric performance in phase-separated half-heusler compounds", *Journal of Materials Chemistry C* **3**(40), 10409 (2015).

[62] R. He, H. Zhu, J. Sun, J. Mao, H. Reith, S. Chen, G. Schierning, K. Nielsch, and Z. Ren, "Improved thermoelectric performance of n-type half-heusler mco1-xnixsb (m= hf, zr)", *Materials Today Physics* **1**, 24 (2017).

[63] C. Fu, T. Zhu, Y. Liu, H. Xie, and X. Zhao, "Band engineering of high performance p-type fenbsb based half-heusler thermoelectric materials for figure of merit zt¿ 1", *Energy & Environmental Science* **8**(1), 216 (2015).

[64] C. Fu, S. Bai, Y. Liu, Y. Tang, L. Chen, X. Zhao, and T. Zhu, "Realizing high figure of merit in heavy-band p-type half-heusler thermoelectric materials", *Nature communications* **6**(1), 8144 (2015).

[65] J. Yu, C. Fu, Y. Liu, K. Xia, U. Aydemir, T. C. Chasapis, G. J. Snyder, X. Zhao, and T. Zhu, "Unique role of refractory ta alloying in enhancing the figure of merit of nbfesb thermoelectric materials", *Advanced Energy Materials* **8**(1), 1701313 (2018).

[66] H. Zhu, J. Mao, Y. Li, J. Sun, Y. Wang, Q. Zhu, G. Li, Q. Song, J. Zhou, Y. Fu, *et al.*, "Discovery of tafesb-based half-heuslers with high thermoelectric performance", *Nature communications* **10**(1), 270 (2019).

[67] H. Zhu, J. Mao, Z. Feng, J. Sun, Q. Zhu, Z. Liu, D. J. Singh, Y. Wang, and Z. Ren, "Understanding the asymmetrical thermoelectric performance for discovering promising thermoelectric materials", *Science advances* **5**(6), eaav5813 (2019).

[68] H. Zhu, R. He, J. Mao, Q. Zhu, C. Li, J. Sun, W. Ren, Y. Wang, Z. Liu, Z. Tang, *et al.*, "Discovery of zrcobi based half heuslers with high thermoelectric conversion efficiency", *Nature Communications* **9**(1), 2497 (2018).

[69] K. Saurabh, V. K. Pandey, A. Kumar, P. Ghosh, and S. Singh, "Enhanced thermoelectric figure-of-merit in 'defective' half-heusler nb0.8cosb", *Materials Today Physics* **38**, 101236 (2023).

[70] H. Xie, H. Wang, C. Fu, Y. Liu, G. J. Snyder, X. Zhao, and T. Zhu, "The intrinsic disorder related alloy scattering in zrnisn half-heusler thermoelectric materials", *Scientific reports* **4**(1), 6888 (2014).

[71] Q. Shen, L. Chen, T. Goto, T. Hirai, J. Yang, G. Meisner, and C. Uher, "Effects of partial substitution of ni by pd on the thermoelectric properties of zrnisn-based half-heusler compounds", *Applied Physics Letters* **79**(25), 4165 (2001).

[72] S. R. Culp, S. J. Poon, N. Hickman, T. M. Tritt, and J. Blumm, "Effect of substitutions on the thermoelectric figure of merit of half-heusler phases at 800 c", *Applied Physics Letters* **88**(4) (2006).

[73] X. Yan, W. Liu, H. Wang, S. Chen, J. Shiomi, K. Esfarjani, H. Wang, D. Wang, G. Chen, and Z. Ren, "Stronger phonon scattering by larger differences in atomic mass and size in p-type half-heuslers hf 1- x ti x cosb 0.8 sn 0.2", *Energy & Environmental Science* **5**(6), 7543 (2012).

[74] Q. Qiu, Y. Liu, K. Xia, T. Fang, J. Yu, X. Zhao, and T. Zhu, "Grain boundary scattering of charge transport in n-type (hf, zr) cosb half-heusler thermoelectric materials", *Advanced Energy Materials* **9**(11), 1803447 (2019).

[75] D. Young, P. Khalifah, R. J. Cava, and A. Ramirez, "Thermoelectric properties of pure and doped femsb (m= v, nb)", *Journal of Applied Physics* **87**(1), 317 (2000).

[76] J. Yu, Y. Xing, C. Hu, Z. Huang, Q. Qiu, C. Wang, K. Xia, Z. Wang, S. Bai, X. Zhao, *et al.*, "Half-heusler thermoelectric module with high conversion efficiency and high power density", *Advanced Energy Materials* **10**(25), 2000888 (2020).

[77] E. Schrödinger, "An undulatory theory of the mechanics of atoms and molecules", *Physical review* **28**(6), 1049 (1926).

[78] M. Born and W. Heisenberg, "Zur quantentheorie der molekeln", *Original Scientific Papers Wissenschaftliche Originalarbeiten* pp. 216–246 (1985).

[79] J. Hartree, "The self-consistent field for molecules and solids", *Proceedings of the Royal Society of London. Series A, Mathematical and Physical Sciences* **151**(873), 89 (1935).

[80] J. C. Slater, "The self-consistent field for atoms and molecules", *Physical Review* **34**(10), 1293 (1929).

[81] P. Hohenberg and W. Kohn, "Inhomogeneous electron gas", *Physical review* **136**(3B), B864 (1964).

[82] W. Kohn and L. J. Sham, "Self-consistent equations including exchange and correlation effects", *Physical review* **140**(4A), A1133 (1965).

[83] R. M. Martin. *Electronic structure: basic theory and practical methods* (Cambridge university press, 2020).

[84] M. Entwistle, M. Hodgson, J. Wetherell, B. Longstaff, J. D. Ramsden, and R. W. Godby, "Local density approximations from finite systems", *Physical Review B* **94**(20), 205134 (2016).

[85] J. P. Perdew and A. Zunger, "Self-interaction correction to density-functional approximations for many-electron systems", *Physical review B* **23**(10), 5048 (1981).

[86] C.-O. Almbladh and U. von Barth, "Exact results for the charge and spin densities, exchange-correlation potentials, and density-functional eigenvalues", *Physical Review B* **31**(6), 3231 (1985).

[87] M. Levy, J. P. Perdew, and V. Sahni, "Exact differential equation for the density and ionization energy of a many-particle system", *Physical Review A* **30**(5), 2745 (1984).

[88] R. Jones and O. Gunnarsson, "Density-functional formalism: Sources of error in local-density approximations", *Physical review letters* **55**(1), 107 (1985).

[89] A. D. Becke, "Density-functional exchange-energy approximation with correct asymptotic behavior", *Physical review A* **38**(6), 3098 (1988).

[90] Y. Wang and J. P. Perdew, "Spin scaling of the electron-gas correlation energy in the high-density limit", *Physical Review B* **43**(11), 8911 (1991).

[91] J. P. Perdew, K. Burke, and M. Ernzerhof, "Generalized gradient approximation made simple", *Physical review letters* **77**(18), 3865 (1996).

[92] H. J. Monkhorst and J. D. Pack, "Special points for brillouin-zone integrations", *Physical review B* **13**(12), 5188 (1976).

[93] D. Hamann, M. Schlüter, and C. Chiang, "Norm-conserving pseudopotentials", *Physical review letters* **43**(20), 1494 (1979).

[94] D. Vanderbilt, "Soft self-consistent pseudopotentials in a generalized eigenvalue formalism", *Physical review B* **41**(11), 7892 (1990).

[95] P. DeCicco and F. Johnson, "The quantum theory of lattice dynamics. iv", *Proceedings of the Royal Society of London. A. Mathematical and Physical Sciences* **310**(1500), 111 (1969).

[96] R. M. Pick, M. H. Cohen, and R. M. Martin, "Microscopic theory of force constants in the adiabatic approximation", *Physical Review B* **1**(2), 910 (1970).

[97] A. Messiah and J. Potter. Quantum mechanics. number v. 2 in quantum mechanics (1962).

[98] S. Baroni, S. De Gironcoli, A. Dal Corso, and P. Giannozzi, "Phonons and related crystal properties from density-functional perturbation theory", *Reviews of modern Physics* **73**(2), 515 (2001).

[99] G. K. Madsen and D. J. Singh, "Boltztrap. a code for calculating band-structure dependent quantities", *Computer Physics Communications* **175**(1), 67 (2006).

[100] J. M. Ziman. *Electrons and phonons: the theory of transport phenomena in solids* (Oxford university press, 2001).

[101] D. A. Broido, M. Malorny, G. Birner, N. Mingo, and D. Stewart, "Intrinsic lattice thermal conductivity of semiconductors from first principles", *Applied Physics Letters* **91**(23) (2007).

[102] A. Ward and D. Broido, "Intrinsic phonon relaxation times from first-principles studies of the thermal conductivities of si and ge", *Physical Review B-Condensed Matter and Materials Physics* **81**(8), 085205 (2010).

[103] X. Tang and J. Dong, "Lattice thermal conductivity of mgo at conditions of earth's interior", *Proceedings of the National Academy of Sciences* **107**(10), 4539 (2010).

[104] A. Togo, L. Chaput, and I. Tanaka, "Distributions of phonon lifetimes in brillouin zones", *Phys. Rev. B* **91**, 094306 (2015).

[105] A. Togo, L. Chaput, T. Tadano, and I. Tanaka, "Implementation strategies in phonopy and phono3py", *J. Phys. Condens. Matter* **35**(35), 353001 (2023).

[106] L. Chaput, "Direct solution to the linearized phonon boltzmann equation", *Physical review letters* **110**(26), 265506 (2013).

[107] G. A. Slack, "Nonmetallic crystals with high thermal conductivity", *Journal of Physics and Chemistry of Solids* **34**(2), 321 (1973).

[108] G. A. Naydenov, P. J. Hasnip, V. Lazarov, and M. Probert, "Huge power factor in p-type half-heusler alloys nbfesb and tafesb", *JPhys Mater.* **2**(3), 035002 (2019).

[109] P. Klemens, "Theory of thermal conduction in thin ceramic films", *International journal of thermophysics* **22**, 265 (2001).

[110] C. Kumarasinghe and N. Neophytou, "Band alignment and scattering considerations for enhancing the thermoelectric power factor of complex materials: The case of co-based half-heusler alloys", *Phys. Rev. B* **99**(19), 195202 (2019).

[111] A. K. Verma, K. K. Johari, P. Dubey, D. K. Sharma, S. Kumar, S. R. Dhakate, C. Candolfi, B. Lenoir, and B. Gahtori, "Realization of band convergence in p-type ticosb half-heusler alloys significantly enhances the thermoelectric performance", *ACS Appl. Mater. Interfaces* **15**(1), 942 (2022).

[112] K. Xia, P. Nan, S. Tan, Y. Wang, B. Ge, W. Zhang, S. Anand, X. Zhao, G. J. Snyder, and T. Zhu, "Short-range order in defective half-heusler thermoelectric crystals", *Energy Environ. Sci.* **12**(5), 1568 (2019).

[113] K. Saurabh and S. Singh, "Crystal growth of "defective" half-heusler nb0.83cosb", *J. Cryst. Growth* **601**, 126957 (2023).

[114] S. Anand, K. Xia, T. Zhu, C. Wolverton, and G. J. Snyder, "Temperature dependent n-type self doping in nominally 19-electron half-heusler thermoelectric materials", *Adv. Energy Mater.* **8**(30), 1801409 (2018).

[115] P. Giannozzi, S. Baroni, N. Bonini, M. Calandra, R. Car, C. Cavazzoni, D. Ceresoli, G. L. Chiarotti, M. Cococcioni, I. Dabo, D. Andrea, C. Andrea, Dal, d. G. Stefano, F. Stefano, F. Guido, G. Ralph, G. Uwe, G. Christos, K. Anton, L. Michele, M.-S. Layla, M. Nicola, M. Francesco, M. Riccardo, P. Stefano, P. Alfredo, P. Lorenzo, S. Carlo, S. Sandro, S. Gabriele, P. S. Ari, S. Alexander, U. Paolo, and M. W. Renata, "Quantum espresso: a modular and open-source software project for quantum simulations of materials", *J. Phys.: Condens.Matter* **21**(39), 395502 (2009).

[116] P. Giannozzi, O. Andreussi, T. Brumme, O. Bunau, M. B. Nardelli, M. Calandra, R. Car, C. Cavazzoni, D. Ceresoli, M. Cococcioni, C. N, C. I, D. C. A, de Gironcoli S, D. P, D. J. R. A, F. A, F. A, F. G, F. G, G. R, G. U, G. F, G. T, J. J, K. M, K. H-Y, K. A, K. E, L. M, M. M, M. N, M. F, N. N. L, N. H-V, O. de-la Roza A, P. L, P. S, R. D, S. R, S. B, S. M, S. A. P, S. A, T. I, T. T, U. P, V. N, W. X, and B. S, "Advanced capabilities for materials modelling with quantum espresso", *J. Phys.: Condens.Matter* **29**(46), 465901 (2017).

[117] D. Vanderbilt, "Soft self-consistent pseudopotentials in a generalized eigenvalue formalism", *Phys. Rev. B* **41**, 7892 (1990). URL https://link.aps.org/doi/10.1103/PhysRevB.41.7892.

[118] J. P. Perdew, K. Burke, and M. Ernzerhof, "Generalized gradient approximation made simple", *Phys. Rev. Lett.* **77**, 3865 (1996).

[119] T. B. Boykin, N. Kharche, G. Klimeck, and M. Korkusinski, "Approximate bandstructures of semiconductor alloys from tight-binding supercell calculations", *J. Phys.: Condens.Matter* **19**(3), 036203 (2007). URL https://dx.doi.org/10.1088/0953-8984/19/3/036203.

[120] L. Chaput, "Direct solution to the linearized phonon boltzmann equation", *Phys. Rev. Lett.* **110**, 265506 (2013). URL https://link.aps.org/doi/10.1103/PhysRevLett.110.265506.

[121] A. Togo, "First-principles phonon calculations with phonopy and phono3py", *J. Phys. Soc. Jpn.* **92**(1), 012001 (2023).

[122] H. Namiki and Y. Ota, "Effects of isovalent doping on the thermoelectric properties of environmentally-friendly phosphide ag6ge10p12", *Jpn. J. Appl. Phys.* **59**(7), 075508 (2020). URL `https://dx.doi.org/10.35848/1347-4065/ab9ef4`.

[123] C. A. Schneider, W. S. Rasband, and K. W. Eliceiri, "Nih image to imagej: 25 years of image analysis", *Nat. Methods* **9**(7), 671 (2012).

[124] M. Zhou, L. Chen, C. Feng, D. Wang, and J.-F. Li, "Moderate-temperature thermoelectric properties of ticosb-based half-heusler compounds ti 1- x ta x co sb", *Journal of Applied Physics* **101**(11), 113714 (2007).

[125] N. S. Chauhan, S. Bathula, B. Gahtori, Y. V. Kolen'ko, and A. Dhar, "Enhanced thermoelectric performance in hf-free p-type (ti, zr)cosb half-heusler alloys", *J. Electron. Mater.* **48**(10), 6700 (2019).

[126] R.-F. Wang, S. Li, W.-H. Xue, C. Chen, Y.-M. Wang, X.-J. Liu, and Q. Zhang, "Enhanced thermoelectric performance of n-type ticosb half-heusler by ta doping and hf alloying", *Rare Metals* **40**, 40 (2021).

[127] M. Zebarjadi, G. Joshi, G. Zhu, B. Yu, A. Minnich, Y. Lan, X. Wang, M. Dresselhaus, Z. Ren, and G. Chen, "Power factor enhancement by modulation doping in bulk nanocomposites", *Nano Lett.* **11**(6), 2225 (2011).

[128] Y. Chen, Y. Zhang, C. Uher, and P. F. Poudeu, "Carrier mobility modulation in cu2se composites using coherent cu4tise4 inclusions leads to enhanced thermoelectric performance", *ACS Appl. Mater. Interfaces* **14**(51), 56817 (2022).

[129] W. G. Zeier, S. Anand, L. Huang, R. He, H. Zhang, Z. Ren, C. Wolverton, and G. J. Snyder, "Using the 18-electron rule to understand the nominal 19-electron half-heusler nbcosb with nb vacancies", *Chem. Mater.* **29**(3), 1210 (2017).

[130] L. Chaput, "Direct solution to the linearized phonon boltzmann equation", *Phys. Rev. Lett.* **110**, 265506 (2013).

[131] G. Slack, "Nonmetallic crystals with high thermal conductivity", *J. Phys. Chem. Solids* **34**(2), 321 (1973).

[132] Z. Liu, S. Guo, Y. Wu, J. Mao, Q. Zhu, H. Zhu, Y. Pei, J. Sui, Y. Zhang, and Z. Ren, "Design of high performance disordered half heusler thermoelectric materials using 18 electron rule", *Advanced Functional Materials* **29** (2019).

[133] S. Chen, K. C. Lukas, W. Liu, C. P. Opeil, G. Chen, and Z. Ren, "Effect of hf concentration on thermoelectric properties of nanostructured n-type half-heusler materials $hf_xzr_{1-x}nisn_{0.99}sb_{0.01}$", *Advanced Energy Materials* **3**(9), 1210 (2013). https://onlinelibrary.wiley.com/doi/pdf/10.1002/aenm.201300336, URL https://onlinelibrary.wiley.com/doi/abs/10.1002/aenm.201300336.

[134] Y. Liu, C. Fu, K. Xia, J. Yu, X. Zhao, H. Pan, C. Felser, and T. Zhu, "Lanthanide contraction as a design factor for high-performance half-heusler thermoelectric materials", *Advanced Materials* **30**(32), 1800881 (2018). https://onlinelibrary.wiley.com/doi/pdf/10.1002/adma.201800881, URL https://onlinelibrary.wiley.com/doi/abs/10.1002/adma.201800881.

[135] X. Yan, W. Liu, H. Wang, S. Chen, J. Shiomi, K. Esfarjani, H. Wang, D. Wang, G. Chen, and Z. Ren, "Stronger phonon scattering by larger differences in atomic mass and size in p-type half-heuslers $hf_{1-x}ti_xcosb_{0.8}sn_{0.2}$", *Energy Environ. Sci.* **5**, 7543 (2012). URL http://dx.doi.org/10.1039/C2EE21554C.

[136] H. Hazama, M. Matsubara, R. Asahi, and T. Takeuchi, "Improvement of thermoelectric properties for half-heusler tinisn by interstitial ni defects", *Journal of Applied Physics* **110**(6) (2011).

[137] J. P. Makongo, D. K. Misra, X. Zhou, A. Pant, M. R. Shabetai, X. Su, C. Uher, K. L. Stokes, and P. F. Poudeu, "Simultaneous large enhancements in thermopower and electrical conductivity of bulk nanostructured half-heusler alloys", *Journal of the American Chemical Society* **133**(46), 18843 (2011).

[138] R. A. Downie, D. MacLaren, R. Smith, and J. Bos, "Enhanced thermoelectric performance in tinisn-based half-heuslers", *Chemical communications* **49**(39), 4184 (2013).

[139] Y. Liu, P. Sahoo, J. P. Makongo, X. Zhou, S.-J. Kim, H. Chi, C. Uher, X. Pan, and P. F. Poudeu, "Large enhancements of thermopower and carrier mobility in quantum dot engineered bulk semiconductors", *Journal of the American Chemical Society* **135**(20), 7486 (2013).

[140] Y. Tang, X. Li, L. H. Martin, E. C. Reyes, T. Ivas, C. Leinenbach, S. Anand, M. Peters, G. J. Snyder, and C. Battaglia, "Impact of ni content on the thermoelectric properties of half-heusler tinisn", *Energy & Environmental Science* **11**(2), 311 (2018).

[141] J.-L. Chen, H. Yang, C. Liu, J. Liang, L. Miao, Z. Zhang, P. Liu, K. Yoshida, C. Chen, Q. Zhang, *et al.*, "Strategy of extra zr doping on the enhancement of thermoelectric performance for tizr$_x$nisn synthesized by a modified solid-state reaction", *ACS applied materials & interfaces* **13**(41), 48801 (2021).

[142] N. S. Chauhan, P. R. Raghuvanshi, K. Tyagi, K. K. Johari, L. Tyagi, B. Gahtori, S. Bathula, A. Bhattacharya, S. D. Mahanti, V. N. Singh, *et al.*, "Defect engineering for enhancement of thermoelectric performance of (zr, hf) nisn-based n-type half-heusler alloys", *The Journal of Physical Chemistry C* **124**(16), 8584 (2020).

[143] N. S. Chauhan, B. Gahtori, B. Sivaiah, S. D. Mahanti, A. Dhar, and A. Bhattacharya, "Modulating the lattice dynamics of n-type heusler compounds via tuning ni concentration", *Applied Physics Letters* **113**(1) (2018).

[144] S. Anand, M. Wood, Y. Xia, C. Wolverton, and G. J. Snyder, "Double half-heuslers", *Joule* **3**(5), 1226 (2019).

[145] Y. Liu, X. Xu, W. Fang, S. Teng, X. Xie, L. Li, S. Fan, J. Li, and J. Li, "Design of half-heusler thermoelectric compound tife$_{0.5}$ni$_{0.5}$sb with special quasi-random structure using 18-electron rule", *Journal of Alloys and Compounds* **858**, 157689 (2021).

[146] N. Li, H. Zhu, W. He, B. Zhang, W. Cui, Z.-Y. Hu, X. Sang, X. Lu, G. Wang, and X. Zhou, "Realizing both n-and p-types of high thermoelectric performance in fe$_{1-x}$ ni$_x$tisb half-heusler compounds", *Journal of Materials Chemistry C* **8**(9), 3156 (2020).

[147] R. Hasan, Y. Gu, S. Y. Kim, D. W. Chun, and K. H. Lee, "Enhancing the thermoelectric performance of a ti$_2$fenisb$_2$ double half-heusler alloy through excess ni-induced full-heusler nanoprecipitates", *Inorganic Chemistry Frontiers* **10**(19), 5662 (2023).

[148] R. Hasan, S. Jo, W. Shi, S. Y. Lee, W.-S. Seo, V. C. Theja, R. A. Vellaisamy, K. T. Kim, S.-i. Kim, S. W. Kim, *et al.*, "Atomic site-targeted doping in ti$_2$fenisb$_2$ double half-heusler alloys: zt improvement via selective band engineering and point defect scattering", *Journal of Alloys and Compounds* **938**, 168572 (2023).

[149] S. R. Mishra, L. P. Tan, V. Trivedi, M. Battabyal, P. Sankara Rama Krishnan, D. V. M. Repaka, S. K. Yadav, R. V. Ramanujan, and B. S. Murty, "Low-lattice thermal conductivity in zr-doped ti2nicosnsb thermoelectric double half-heusler alloys", *ACS Applied Energy Materials* **6**(11), 6262 (2023).

[150] J. N. Kahiu, S. K. Kihoi, H. Kim, U. S. Shenoy, D. K. Bhat, and H. S. Lee, "Asymmetric thermoelectric performance tuning in low-cost zrfe$_x$ni$_{1-x}$sb double half-heusler materials", *ACS Applied Energy Materials* **6**(8), 4305 (2023).

[151] J. N. Kahiu, S. K. Kihoi, H. Kim, and H. S. Lee, "Thermoelectric and magnetic properties of biphasic zrfe$_{0.5}$ni$_{0.5}$sb double half-heusler and zrnisb half-heusler induced by co doping", *ACS Applied Electronic Materials* **6**(3), 1829 (2024).

[152] M. A. Hassan, E. Chernyshova, E. Argunov, A. Khanina, D. Karpenkov, M. Seredina, F. Bochkanov, S. K. Elshamndy, M. Gorshenkov, A. Voronin, *et al.*, "Thermoelectric properties of $hf_{2-x}ti_x$fenisb$_2$ double-half heusler alloys", *Physica Scripta* **98**(8), 085913 (2023).

[153] A. van de Walle, P. Tiwary, M. de Jong, D. Olmsted, M. Asta, A. Dick, D. Shin, Y. Wang, L.-Q. Chen, and Z.-K. Liu, "Efficient stochastic generation of special quasirandom structures", *Calphad* **42**, 13 (2013).

[154] G. K. Madsen and D. J. Singh, "Boltztrap. a code for calculating band-structure dependent quantities", *Comput. Phys. Commun.* **175**(1), 67 (2006).

[155] J. Bardeen and W. Shockley, "Deformation potentials and mobilities in non-polar crystals", *Phys. Rev.* **80**, 72 (1950).

[156] A. Hong, L. Li, R. He, J. Gong, Z. Yan, K. Wang, J.-M. Liu, and Z. Ren, "Full-scale computation for all the thermoelectric property parameters of half-heusler compounds", *Scientific reports* **6**(1), 1 (2016).

[157] G. A. Naydenov, P. J. Hasnip, V. K. Lazarov, and M. I. J. Probert, "Huge power factor in p-type half-heusler alloys nbfesb and tafesb", *Journal of Physics: Materials* **2**(3), 035002 (2019). URL `https://dx.doi.org/10.1088/2515-7639/ab16fb`.

[158] Z. Liu, S. Guo, Y. Wu, J. Mao, Q. Zhu, H. Zhu, Y. Pei, J. Sui, Y. Zhang, and Z. Ren, "Design of high-performance disordered half-heusler thermoelectric materials using 18-electron rule", *Adv. Funct. Mater.* **29**(44), 1905044 (2019).

[159] T. A. Manz and N. G. Limas, "Introducing ddec6 atomic population analysis: part 1. charge partitioning theory and methodology", *RSC Adv.* **6**, 47771 (2016).

[160] N. G. Limas and T. A. Manz, "Introducing ddec6 atomic population analysis: part 2. computed results for a wide range of periodic and nonperiodic materials", *RSC Adv.* **6**, 45727 (2016).

[161] T. A. Manz, "Introducing ddec6 atomic population analysis: part 3. comprehensive method to compute bond orders", *RSC Adv.* **7**, 45552 (2017). URL `http://dx.doi.org/10.1039/C7RA07400J`.

[162] W. G. Zeier, J. Schmitt, G. Hautier, U. Aydemir, Z. M. Gibbs, C. Felser, and G. J. Snyder, "Engineering half-heusler thermoelectric materials using zintl chemistry", *Nature Reviews Materials* **1**(6), 1 (2016).

[163] R. He, D. Kraemer, J. Mao, L. Zeng, Q. Jie, Y. Lan, C. Li, J. Shuai, H. S. Kim, Y. Liu, *et al.*, "Achieving high power factor and output power density in p-type half-heuslers nb$_{1-x}$ti$_x$fesb", *Proceedings of the National Academy of Sciences* **113**(48), 13576 (2016).

[164] N. Dragoe and D. BÃ©rardan, "Order emerging from disorder", *Science* **366**(6465), 573 (2019).

[165] E. P. George, D. Raabe, and R. O. Ritchie, "High-entropy alloys", *Nature reviews materials* **4**(8), 515 (2019).

[166] S. Zhao and Z. Li, "High entropy alloys for extreme load-bearing applications", *Materials Lab* **1**(3), 220035 (2022).

[167] N. Dragoe, "Entropy driven synthesis of new materials", *Materials Lab* **1**(1), 220001 (2022).

[168] B. Jiang, Y. Yu, J. Cui, X. Liu, L. Xie, J. Liao, Q. Zhang, Y. Huang, S. Ning, B. Jia, *et al.*, "High-entropy-stabilized chalcogenides with high thermoelectric performance", *Science* **371**(6531), 830 (2021).

[169] R. Liu, H. Chen, K. Zhao, Y. Qin, B. Jiang, T. Zhang, G. Sha, X. Shi, C. Uher, W. Zhang, *et al.*, "Entropy as a gene-like performance indicator promoting thermoelectric materials", *Advanced Materials* **29**(38), 1702712 (2017).

[170] L. Hu, Y. Zhang, H. Wu, J. Li, Y. Li, M. Mckenna, J. He, F. Liu, S. J. Pennycook, and X. Zeng, "Entropy engineering of snte: multi-principal-element alloying leading to ultralow lattice thermal conductivity and state-of-the-art thermoelectric performance", *Advanced Energy Materials* **8**(29), 1802116 (2018).

[171] C. Chang and M. G. Kanatzidis, "High-entropy thermoelectric materials emerging", *Mater. Lab* **1**(22004810.54227) (2022).

[172] K. Li, L. Sun, W. Bai, N. Ma, C. Zhao, J. Zhao, C. Xiao, and Y. Xie, "High-entropy strategy to achieve electronic band convergence for high-performance thermoelectrics", *Journal of the American Chemical Society* **146**(20), 14318 (2024). PMID: 38718345.

[173] S. Chen and Z. Ren, "Recent progress of half-heusler for moderate temperature thermoelectric applications", *Mater. Today* **16**(10), 387 (2013).

[174] J.-W. G. Bos and R. A. Downie, "Half-heusler thermoelectrics: a complex class of materials", *J. Phys.: Condens.Matter* **26**(43), 433201 (2014). URL `https://dx.doi.org/10.1088/0953-8984/26/43/433201`.

[175] T. Zhu, C. Fu, H. Xie, Y. Liu, and X. Zhao, "High efficiency half-heusler thermoelectric materials for energy harvesting", *Adv. Energy Mater.* **5**(19), 1500588 (2015).

[176] S. J. Poon, "Half heusler compounds: promising materials for mid-to-high temperature thermoelectric conversion", *J. Phys. D: Appl. Phys.* **52**(49), 493001 (2019). URL `https://dx.doi.org/10.1088/1361-6463/ab3d71`.

[177] T. Zhu, C. Fu, H. Xie, Y. Liu, and X. Zhao, "High efficiency half-heusler thermoelectric materials for energy harvesting", *Adv. Energy Mater.* **5**(19), 1500588 (2015).

[178] M. Zhou, L. Chen, C. Feng, D. Wang, and J.-F. Li, "Moderate-temperature thermoelectric properties of ticosb-based half-heusler compounds $\mathrm{ti}_{1-x}\mathrm{ta}_x$cosb", *Journal of Applied Physics* **101**(11), 113714 (2007).

[179] Y. Shi, C. Sturm, and H. Kleinke, "Chalcogenides as thermoelectric materials", *Journal of Solid State Chemistry* **270**, 273 (2019).

[180] G. Rogl and P. F. Rogl, "Development of thermoelectric half-heusler alloys over the past 25 years", *Crystals* **13**(7) (2023).

[181] A. van de Walle, P. Tiwary, M. M. de Jong, D. L. Olmsted, M. D. Asta, A. Dick, D. Shin, Y. Wang, L.-Q. Chen, and Z.-K. Liu, "Efficient stochastic generation of special quasirandom structures", *Calphad* **42**, 13 (2013).

[182] Y. Hinuma, G. Pizzi, Y. Kumagai, F. Oba, and I. Tanaka, "Band structure diagram paths based on crystallography", *Computational Materials Science* **128**, 140 (2017).

[183] G. J. Snyder, A. H. Snyder, M. Wood, R. Gurunathan, B. H. Snyder, and C. Niu, "Weighted mobility", *Advanced Materials* **32**(25), 2001537 (2020).

[184] K. Saurabh, V. K. Pandey, A. Kumar, P. Ghosh, and S. Singh, "Enhanced thermoelectric figure-of-merit in defective half-heusler nb0.8cosb", *Materials Today Physics* **38**, 101236 (2023).

[185] Y. G. Yu, X. Zhang, and A. Zunger, "Natural off-stoichiometry causes carrier doping in half-heusler filled tetrahedral structures", *Phys. Rev. B* **95**, 085201 (2017).

[186] M. Ocio, "Hall coefficient and mobility in $\mathrm{pb}_{1-x}\mathrm{sn}_x$ te with high carrier densities", *Phys. Rev. B* **10**, 4274 (1974).

[187] M. Zhou, L. Chen, C. Feng, D. Wang, and J.-F. Li, "Moderate-temperature thermoelectric properties of ticosb-based half-heusler compounds $\mathrm{ti}_{1-x}\mathrm{ta}_x$cosb", *Journal of Applied Physics* **101**(11), 113714 (2007).

[188] N. Wang, Y. Lei, F. Ye, Y. Li, C. Yong, Z. Chen, S. Zhang, and D. Wang, "Enhanced thermoelectric figure of merit in ta-doped ticosb half-heusler bulks through simultaneously optimising electrical transport property and reducing thermal conductivity", *Journal of Materials Science: Materials in Electronics* **35**(12), 824 (2024).

[189] Y. Tian, N. Ghassemi, W. Ren, H. Zhu, S. Li, Q. Zhang, Z. Wang, Z. Ren, and J. H. Ross, "Half-heusler thermoelectric materials: Nmr studies", *Journal of Applied Physics* **128**(5) (2020).

[190] G. Naydenov, P. Hasnip, V. Lazarov, and M. Probert, "Huge power factor in p-type half-heusler alloys nbfesb and tafesb", *Journal of Physics: Materials* **2** (2019).

[191] X. Ai, B. Lei, M. O. Cichocka, L. Giebeler, R. B. Villoro, S. Zhang, C. Scheu, N. Pérez, Q. Zhang, A. Sotnikov, *et al.*, "Enhancing the thermoelectric properties via modulation of defects in p-type mnisn-based (m= hf, zr, ti) half-heusler materials", *Advanced Functional Materials* **33**(48), 2305582 (2023).

[192] S. Bhattacharya and G. K. H. Madsen, "A novel p-type half-heusler from high-throughput transport and defect calculations", *J. Mater. Chem. C* **4**, 11261 (2016). URL `http://dx.doi.org/10.1039/C6TC04259G`.

[193] P. Luo, C. Lin, Z. Li, J. Zhang, and J. Luo, "Tafesb-based half-heusler thermoelectrics with high zt ¿ 1 through the alloying effect", *ACS Applied Energy Materials* **6**(19), 10070 (2023).

[194] Y. Pei, X. Shi, A. LaLonde, H. Wang, L. Chen, and G. J. Snyder, "Convergence of electronic bands for high performance bulk thermoelectrics", *Nature* **473**(7345), 66 (2011).

[195] C. Wood, "Materials for thermoelectric energy conversion", *Reports on progress in physics* **51**(4), 459 (1988).

[196] R. H. Naderloo, R. B. Villoro, D. A. Mattlat, P. Ying, S. Song, S. Bayesteh, K. Nielsch, C. Scheu, Z. Ren, H. Zhu, *et al.*, "Performance advancements in p-type tafesb-based thermoelectric materials through composition and composite optimizations", *Energy & Environmental Science* (2025).

[197] G. J. Snyder and E. S. Toberer, "Complex thermoelectric materials", *Nature materials* **7**(2), 105 (2008).

[198] A. F. May, J.-P. Fleurial, and G. J. Snyder, "Thermoelectric performance of lanthanum telluride produced via mechanical alloying", *Physical Review B* **78**(12), 125205 (2008).

[199] E. S. Toberer, L. L. Baranowski, and C. Dames, "Advances in thermal conductivity", *Annual Review of Materials Research* **42**, 179 (2012).

[200] K. C. Lukas, W. Liu, G. Joshi, M. Zebarjadi, M. S. Dresselhaus, Z. Ren, G. Chen, and C. P. Opeil, "Experimental determination of the lorenz number in cu 0.01 bi 2 te 2.7 se 0.3 and bi 0.88 sb 0.12", *Physical Review B* **85**(20), 205410 (2012).

[201] H.-S. Kim, Z. M. Gibbs, Y. Tang, H. Wang, and G. J. Snyder, "Characterization of lorenz number with seebeck coefficient measurement", *APL materials* **3**(4) (2015).

[202] A. D. LaLonde, Y. Pei, and G. J. Snyder, "Reevaluation of $\mathrm{pbte}_{1-x}\mathrm{i}_x$ as high performance n-type thermoelectric material", *Energy & Environmental Science* **4**(6), 2090 (2011).

[203] H. Wang, Y. Pei, A. D. LaLonde, and G. J. Snyder, "Weak electron–phonon coupling contributing to high thermoelectric performance in n-type pbse", *Proceedings of the National Academy of Sciences* **109**(25), 9705 (2012).

[204] H. Wang, E. Schechtel, Y. Pei, and G. J. Snyder, "High thermoelectric efficiency of n-type pbs", *Advanced Energy Materials* **3**(4), 488 (2013).

[205] C. Bhandari and D. Rowe, "Electronic contribution to the thermal conductivity of narrow band gap semiconductors-effect of non-parabolicity of bands", *Journal of Physics D: Applied Physics* **18**(5), 873 (1985).